

The American Monsoon System: variability and teleconnections

Jorge Luis García Franco

Wadham College
University of Oxford

*A thesis submitted for the degree of
Doctor of Philosophy*

Michaelmas 2020

Abstract

Your abstract text goes here. Check your departmental regulations, but generally this should be less than 300 words. See the beginning of Chapter 2 for more.

Lorem ipsum dolor sit amet, consectetur adipiscing elit. Pellentesque sit amet nibh volutpat, scelerisque nibh a, vehicula neque. Integer placerat nulla massa, et vestibulum velit dignissim id. Ut eget nisi elementum, consectetur nibh in, condimentum velit. Quisque sodales dui ut tempus mattis. Duis malesuada arcu at ligula egestas egestas. Phasellus interdum odio at sapien fringilla scelerisque. Mauris sagittis eleifend sapien, sit amet laoreet felis mollis quis. Pellentesque dui ante, finibus eget blandit sit amet, tincidunt eu neque. Vivamus rutrum dapibus ligula, ut imperdiet lectus tincidunt ac. Pellentesque ac lorem sed diam egestas lobortis.

Suspendisse leo purus, efficitur mattis urna a, maximus molestie nisl. Aenean porta semper tortor a vestibulum. Suspendisse viverra facilisis lorem, non pretium erat lacinia a. Vestibulum tempus, quam vitae placerat porta, magna risus euismod purus, in viverra lorem dui at metus. Sed ac sollicitudin nunc. In maximus ipsum nunc, placerat maximus tortor gravida varius. Suspendisse pretium, lorem at porttitor rhoncus, nulla urna condimentum tortor, sed suscipit nisi metus ac risus.

Aenean sit amet enim quis lorem tristique commodo vitae ut lorem. Duis vel tincidunt lacus. Sed massa velit, lacinia sed posuere vitae, malesuada vel ante. Praesent a rhoncus leo. Etiam sed rutrum enim. Pellentesque lobortis elementum augue, at suscipit justo malesuada at. Lorem ipsum dolor sit amet, consectetur adipiscing elit. Praesent rhoncus convallis ex. Etiam commodo nunc ex, non consequat diam consectetur ut. Pellentesque vitae est nec enim interdum dapibus. Donec dapibus purus ipsum, eget tincidunt ex gravida eget. Donec luctus nisi eu fringilla mollis. Donec eget lobortis diam.

Suspendisse finibus placerat dolor. Etiam ornare elementum ex ut vehicula. Donec accumsan mattis erat. Quisque cursus fringilla diam, eget placerat neque bibendum eu. Ut faucibus dui vitae dolor porta, at elementum ipsum semper. Sed ultrices dui non arcu pellentesque placerat. Etiam posuere malesuada turpis, nec malesuada tellus malesuada.

The American Monsoon System: variability and teleconnections



Jorge Luis García Franco

Wadham College

University of Oxford

A thesis submitted for the degree of

Doctor of Philosophy

Michaelmas 2020

Acknowledgements

Personal

This is where you thank your advisor, colleagues, and family and friends.

Lorem ipsum dolor sit amet, consectetur adipiscing elit. Vestibulum feugiat et est at accumsan. Praesent sed elit mattis, congue mi sed, porta ipsum. In non ullamcorper lacus. Quisque volutpat tempus ligula ac ultricies. Nam sed erat feugiat, elementum dolor sed, elementum neque. Aliquam eu iaculis est, a sollicitudin augue. Cras id lorem vel purus posuere tempor. Proin tincidunt, sapien non dictum aliquam, ex odio ornare mauris, ultrices viverra nisi magna in lacus. Fusce aliquet molestie massa, ut fringilla purus rutrum consectetur. Nam non nunc tincidunt, rutrum dui sit amet, ornare nunc. Donec cursus tortor vel odio molestie dignissim. Vivamus id mi erat. Duis porttitor diam tempor rutrum porttitor. Lorem ipsum dolor sit amet, consectetur adipiscing elit. Sed condimentum venenatis consectetur. Lorem ipsum dolor sit amet, consectetur adipiscing elit.

Aenean sit amet lectus nec tellus viverra ultrices vitae commodo nunc. Mauris at maximus arcu. Aliquam varius congue orci et ultrices. In non ipsum vel est scelerisque efficitur in at augue. Nullam rhoncus orci velit. Duis ultricies accumsan feugiat. Etiam consectetur ornare velit et eleifend.

Suspendisse sed enim lacinia, pharetra neque ac, ultricies urna. Phasellus sit amet cursus purus. Quisque non odio libero. Etiam iaculis odio a ex volutpat, eget pulvinar augue mollis. Mauris nibh lorem, mollis quis semper quis, consequat nec metus. Etiam dolor mi, cursus a ipsum aliquam, eleifend venenatis ipsum. Maecenas tempus, nibh eget scelerisque feugiat, leo nibh lobortis diam, id laoreet purus dolor eu mauris. Pellentesque habitant morbi tristique senectus et netus et malesuada fames ac turpis egestas. Nulla eget tortor eu arcu sagittis euismod fermentum id neque. In sit amet justo ligula. Donec rutrum ex a aliquet egestas.

Institutional

If you want to separate out your thanks for funding and institutional support, I don't think there's any rule against it. Of course, you could also just remove the subsections and do one big traditional acknowledgement section.

Lorem ipsum dolor sit amet, consectetur adipiscing elit. Ut luctus tempor ex at pretium. Sed varius, mauris at dapibus lobortis, elit purus tempor neque, facilisis sollicitudin felis nunc a urna. Morbi mattis ante non augue blandit pulvinar. Quisque nec euismod mauris. Nulla et tellus eu nibh auctor malesuada quis imperdiet quam. Sed eget tincidunt velit. Cras molestie sem ipsum, at faucibus quam mattis vel. Quisque vel placerat orci, id tempor urna. Vivamus mollis, neque in aliquam consequat, dui sem volutpat lorem, sit amet tempor ipsum felis eget ante. Integer lacinia nulla vitae felis vulputate, at tincidunt ligula maximus. Aenean venenatis dolor ante, euismod ultrices nibh mollis ac. Ut malesuada aliquam urna, ac interdum magna malesuada posuere.

Abstract

Your abstract text goes here. Check your departmental regulations, but generally this should be less than 300 words. See the beginning of Chapter 2 for more.

Lorem ipsum dolor sit amet, consectetur adipiscing elit. Pellentesque sit amet nibh volutpat, scelerisque nibh a, vehicula neque. Integer placerat nulla massa, et vestibulum velit dignissim id. Ut eget nisi elementum, consectetur nibh in, condimentum velit. Quisque sodales dui ut tempus mattis. Duis malesuada arcu at ligula egestas egestas. Phasellus interdum odio at sapien fringilla scelerisque. Mauris sagittis eleifend sapien, sit amet laoreet felis mollis quis. Pellentesque dui ante, finibus eget blandit sit amet, tincidunt eu neque. Vivamus rutrum dapibus ligula, ut imperdiet lectus tincidunt ac. Pellentesque ac lorem sed diam egestas lobortis.

Suspendisse leo purus, efficitur mattis urna a, maximus molestie nisl. Aenean porta semper tortor a vestibulum. Suspendisse viverra facilisis lorem, non pretium erat lacinia a. Vestibulum tempus, quam vitae placerat porta, magna risus euismod purus, in viverra lorem dui at metus. Sed ac sollicitudin nunc. In maximus ipsum nunc, placerat maximus tortor gravida varius. Suspendisse pretium, lorem at porttitor rhoncus, nulla urna condimentum tortor, sed suscipit nisi metus ac risus.

Aenean sit amet enim quis lorem tristique commodo vitae ut lorem. Duis vel tincidunt lacus. Sed massa velit, lacinia sed posuere vitae, malesuada vel ante. Praesent a rhoncus leo. Etiam sed rutrum enim. Pellentesque lobortis elementum augue, at suscipit justo malesuada at. Lorem ipsum dolor sit amet, consectetur adipiscing elit. Praesent rhoncus convallis ex. Etiam commodo nunc ex, non consequat diam consectetur ut. Pellentesque vitae est nec enim interdum dapibus. Donec dapibus purus ipsum, eget tincidunt ex gravida eget. Donec luctus nisi eu fringilla mollis. Donec eget lobortis diam.

Suspendisse finibus placerat dolor. Etiam ornare elementum ex ut vehicula. Donec accumsan mattis erat. Quisque cursus fringilla diam, eget placerat neque bibendum eu. Ut faucibus dui vitae dolor porta, at elementum ipsum semper. Sed ultrices dui non arcu pellentesque placerat. Etiam posuere malesuada turpis, nec malesuada tellus malesuada.

Contents

List of Figures	vii
List of Abbreviations	xiv
1 Introduction	1
1.1 Motivation	1
1.2 Thesis aims and outline	4
2 Background	7
2.1 The tropical circulation and the global monsoon	7
2.2 The American Monsoon System	13
2.3 A review on the proposed mechanisms for the Midsummer drought .	16
2.4 El Niño Southern Oscillation: impacts to the American monsoon system	20
2.5 Stratosphere-Troposphere Coupling in the Tropics	24
2.5.1 The Quasi-biennial oscillation (QBO)	24
2.5.2 Tropical teleconnections of the QBO	26
3 Data and methods	31
3.1 Observations and reanalysis data	31
3.1.1 Gridded precipitation datasets	31
3.1.2 ERA-5	34
3.2 The Unified Model of the Met Office Hadley Centre	35
3.2.1 The Global Coupled Configurations of HadGEM3	35
3.2.2 The CMIP6 experiments	37
3.3 The Moist Static Energy Budget	39
4 The American monsoon system in UKESM1 and HadGEM3	42
4.1 Introduction	43
4.2 Methods and data	45
4.3 Climatological temperature and low-level wind biases	46
4.4 The Atlantic and Pacific ITCZs and the SACZ	52
4.5 Precipitation and convection in the AMS	56

4.5.1	Mean seasonal precipitation	56
4.5.2	The annual cycle of rainfall	60
4.5.3	Characteristics of convective activity	62
4.6	ENSO Teleconnections	64
4.6.1	Canonical teleconnections	65
4.6.2	The role of ENSO flavours	70
4.6.3	A possible influence of the QBO on tropical ENSO teleconnections	73
4.7	Summary and discussion	76
5	A wavelet transform method to determine monsoon onset and retreat from precipitation time-series	82
5.1	Introduction	83
5.2	Data	87
5.2.1	Precipitation datasets and reanalysis data	87
5.2.2	Model data	87
5.3	The wavelet transform method	88
5.3.1	Identification of Monsoon Onset and Retreat	91
5.3.2	Extension for Application to the MSD signal	94
5.3.3	Comparative Methodologies	96
5.4	Results	97
5.4.1	The North American Monsoon	98
5.4.2	The Indian Monsoon	101
5.4.3	The midsummer drought	104
5.5	Summary and discussion	112
6	Mechanisms of the Mesoamerican midsummer drought in the Met Office CMIP6 experiments	117
6.1	Introduction	118
6.2	Data and methods	121
6.2.1	Observations and reanalysis data	121
6.2.2	CMIP6 data	121
6.2.3	Determination of the timings of the MSD	121
6.3	Climatological features	123
6.4	The East Pacific SSTs	129
6.5	On the role of cloud-radiative effects	135
6.5.1	On the role of the Caribbean Low-Level Jet	142
6.5.2	A look at the MSD through the lense of the moist static energy budget	146
6.6	Summary and discussion	146
Bibliography		150

List of Figures

2.1	a) Climatological mean annual rainfall rates in the tropics using data from the Tropical Rainfall Measurement Mission (TRMM) dataset (1999-2018). b) The mean rainfall rate difference between boreal summer (JJAS) and austral summer (DJFM). The red contours highlight the regions where the mean summer rainfall amount accounts for more than 55% of the mean total annual rainfall accumulation.	9
2.2	Climatological mean a) boreal and b) austral summer rainfall (shading), 850 hPa moisture flux (vectors) and geopotential height at 250 hPa (contours) in a) southern North America and b) South America. c) Monthly-mean seasonal march of precipitation in the TRMM dataset for two area-averaged time-series, the North American Monsoon (NAM) and the South American Monsoon System (SAMS) shown in the red rectangles in a-b).	14
2.3	Schematic of the positive (upper) and negative (lower) phases of ENSO. Regions with tall clouds indicate more ascent and convection than normal whereas brown arrows indicate dry descending air. Obtained from the National Oceanic and Atmospheric Administration at https://www.climate.gov/enso	22
2.4	(a) QBO anomalous precipitation as a function of SST forcing. The δ_{sst} are increments over a baseline of 301 K throughout the whole model domain. (b)-(d) The differences of mass flux in cloud cores, cloud fraction, and the parametrized large-scale vertical velocity derived from the weak temperature gradient approximation, respectively, between experiments with the QBOE and QBOW temperature profiles. Figure 3 from Nie and Sobel (2015).	27

4.1 (a, b) Temperature (color-contours in K) and wind speed (vectors) at 850 hPa DJF and JJA climatologies in ERA5. The biases are shown as the differences between the ensemble mean from the historical experiment of (c, d) GC3 and (e, f) UKESM1 and ERA5. The climatogies and biases are shown for (a, c, e) boreal winter (DJF) and (b, d, f) boreal summer (JJA). Only differences statistically significant to the 95% level are shown, according to a Welch t-test for each field. The key for the size of the wind vectors is shown in the top right corner of panels b) and d). The root-mean square error (RMSE) and pattern correlation coefficient (PCC) are shown on the bottom left of c-f.	47
4.2 As in Figure 4.1, but showing the differences between the piControl simulations of (a, b) GC3 N96-pi and (c, d) GC3 N216-pi, and ERA5. (e, f) show the statistically significant differences between the historical (1979-2014) and piControl experiments of GC3. The RMSE and PCC are shown on the bottom left of a-d.	49
4.3 Monthly-mean temperature in the (a) North American Monsoon [19-35°N,110-103°W], (b) the Midsummer drought [11-19°N,95-85°W] (c) Eastern Brazil [20-10°S,60-40°W] and (d) the Amazon basin [-10-0°S,75-50°W] regions. The shadings for the CRU dataset represents the observational uncertainties and for the historical simulations the shading is the ensemble spread. The regions for this plot are shown in Figure 4.1a.	51
4.4 Climatological rainfall [mm day^{-1}] and low-level wind speed (850-hPa) in (a) TRMM and ERA-5, (b) the ensemble-mean UKESM-historical, (c) GC3-amip and (d) GC3 N216-pi. The red line highlights the maximum rainfall for each longitude as a proxy for the position of the ITCZ. .	53
4.5 Time-Latitude plot of daily mean rainfall (colour contours) and low-level wind speed (850 hPa) longitudinally averaged over the (a, c, e, g) East Pacific [150°W-100°W] and (b, d, f, h) Atlantic [40°W-20°W] Oceans. (a, b) show rainfall from TRMM and winds from ERA-5, (c, d) the ensemble-mean UKESM-historical, (e, f) GC3 AMIP, (g, h) N96-pi and (i, j) GC3 N216-pi. The red solid line shows the ITCZ as the latitude of maximum precipitation.	54

4.6 (a, b, c) OLR anomalies during active South Atlantic Convergence Zone (SACZ) events. (d, e) Frequency of active SACZ days and length of active SACZ events in reanalysis and model data, the standard deviation is shown as the error bar. The SACZ active days are constructed by first computing the first EOF of the monthly-mean deseasonalized OLR and then the daily OLR, previously filtered to remove periods higher than 99 days, is projected on the EOF pattern to produce a time-series of pseudo-principal components. Active SACZ days are found when this time-series of pseudo-PCs is greater than 1, and the persistence is measured as the number of continuous days where the time-series is greater than 1.	56
4.7 DJF mean rainfall [mm day ⁻¹] from (a) TRMM, (b) UKESM1-historical, (c) GC3 N216-pi and (d) GC3-amip. (e, f, g) show the statistically significant differences between panels (b, c ,d) and (a) TRMM, respectively. (h) Precipitation difference between UKESM-historical and UKESM1-pi, only statistically significant differences (95%) confidence level is shown. The biases in the 850-hPa winds are shown as vectors.	57
4.8 As in Figure 4.7 but for JJA in the northern part of subtropical America.	59
4.9 Annual cycle of pentad-mean rainfall in the regions (a) the Midsummer drought, (b) the North American Monsoon, (c) Eastern Brazil and (d) the Amazon Basin. The regions are defined as in Figure 4.3 and are illustrated in Figure 4.8b and Figure 4.9b. The shaded regions represent observational uncertainty for TRMM and ensemble spread for the historical experiments. The correlation coefficient for each of the simulated seasonal cycles with TRMM is given in brackets in each panel.	60
4.10 Pentad-mean (upper) outgoing long-wave radiation (OLR), (middle) specific humidity at 500-hPa and (lower) ω 500-hPa. These are shown from left to right for the North American Monsoon, the Midsummer drought, southeastern Brazil and the core Amazon. The uncertainty in ERA-5 data, shown as faint gray shading was estimating by bootstrapping with replacement the ERA-5 record 10,000 times.	63
4.11 DJF Temperature anomalies (colour contours in K) and SLP (line contours in hPa) during (a, c, e, g) El Niño and (b, d, f, h) La Niña events. Results are shown for (a, b) ERA-5, (c, d) UKESM1-hist, (e, f) GC3 N96-pi and (g, h) GC3 N216-pi. The hatched regions denote differences between ENSO phases and the climatological state with significance to the 99% confidence level from a Welch t-test for the temperature field.	66

4.12 As in Figure 4.11 but for the rainfall response [mm day ⁻¹] using GPCP as the observational dataset.	67
4.13 DJF Longitude-height Walker circulation anomalies of specific humidity (colour-contours), ω (vectors) and zonal wind (line-contours) during El Niño events (left) and La Niña events (right). Results are shown for ERA-5 (upper), UKESM-pi (middle) and HadGEM3 piControl (lower).	68
4.14 Precipitation response [mm day ⁻¹] as a function of the El Niño 3.4 index (see text) for (a) southwestern North America [20-37°N, 112-98°W], (b) Central America and southern Mexico [5-19°N, 95-83°W], (c) South Eastern South America [35-25°S, 60-50°W], and (d) the Amazon [10-0°S, 70-45°W]. The observation scatter points are from GPCC in the period of 1940-2013.	69
4.15 SST anomalies [K] for East Pacific (EP) and Central Pacific El Niño events in HadSST, GC3 N216 and UKESM piControl. EP (CP) events were defined where the E-index (C-index) was greater than 1. In the bottom panel, the frequency of events per decade (with standard deviation as error bar) is shown for HadSST and the simulations used in this study. The E-index is computed from $(PC1 - PC2)/\sqrt{2}$ and the C-index from $(PC1 + PC2)/\sqrt{2}$	71
4.16 Precipitation anomalies in GPCC 1940-2013, GC3 N216-pi, GC3 N96-pi and GC3 AMIP for the four different types of ENSO events, as defined by Cai et al. (2020). Statistically significant anomalies (95% confidence level) are hatched.	72
4.17 Composite precipitation differences during JFMA in GPCP (1979-2018), GC3 N216-pi and GC3 N96-pi between (top) La Niña and Neutral ENSO conditions. The two middle panels show a subset of the top panel, by separating the La Niña composite based on the phase of the QBO. The lower panel shows the differences QBO E-W during La Niña periods. Statistically significant anomalies (95% confidence level) are hatched.	74
4.18 Longitude-height differences (JFMA) of equatorial (10S-10N) air temperature (color shading), zonal wind (contours) and vertical velocity (ω - vectors). The differences shown from top to bottom are between all La Niña (LN) periods and Neutral conditions (NN), between LN and NN during QBOw, LN-NN during QBOe, and the difference between LN events on different QBO phases (LN QBOe-QBOw).	75

4.19 Schematics of (a) the main features in the AMS and (b) the main biases in UKESM1 and HadGEM3. In (a) the boreal summer easterlies (red) and austral summer circulation (blue) are shown with the Caribbean and Bolivian Low-level Jets (CLLJ and BLLJ, respectively). In (b) the biases are shown for the respective northern and southern Hemisphere summers. The ITCZ bias in (b) refers to the southward displacement bias of the Atlantic ITCZ in the simulations.	78
5.1 Haar wavelet exmaple	89
5.2 Wavelet transform coefficient in North American Monsoon	90
5.3 Example determination of onset and retreat in TRMM	92
5.4 Example determination of onset and retreat in HadGEM3 N216	93
5.5 Wavelet transform characterisation of Midsummer drought	95
5.6 Comparison of methods in 2010 in the North American Monsoon	99
5.7 Precipitation anomalies during North American monsoon onset	100
5.8 Onset and retreat spatial distribution in North American Monsoon	101
5.9 Precipitation anomalies during Indian monsoon onset	103
5.10 Indian monsoon precipitation anomalies associated with onset	104
5.11 Onset and retreat dates spatial distribution in Indian monsoon	105
5.12 Precipitation anomalies after MSD	107
5.13 Seasonal cycle of precipitation for various MSD categories	108
5.14 Determination of MSD timings and coefficients	109
5.15 Map of MSD significant regions	111
5.16 Spatial distribution of MSD timings	112
6.1 Pentad-mean precipitation in southern Mexico and northern Central America [95-86°W,11-19°N]. The shading for the TRMM dataset is a meausre of observational uncertainty obtained by bootstrapping the interannual variability 10000 times whereas the shading for the CMIP6 experiments show the ensemble spread where multiple ensembles where available.	120
6.2 Pentad-mean precipitation the study region [95-86°W,11-19°N] in the TRMM dataset for the summer of 2017. The timings of the onset (MSDO) and end (MSDE) of the MSD, as well as the first (P1) and second (P2) peak periods and the MSD periods are highlighted.	122
6.3 (a, d, g) Climatological JJAS rainfall and the difference between (b, e, h) the midsummer drought and the first peak periods and (c, f, i) between the second peak and the midsummer drought periods for (a-c) TRMM, (d-f) ERA5 and (g-i) CHIRPS. The climatological low-level winds (at 850 hPa) for JJAS in ERA5 are shown in c).	124

6.4	(a, d, g, j) JJAS model bias compared to TRMM and the difference between (b, e, h, k) the midsummer drought and the first peak periods and (c, f, i, l) between the second peak and the midsummer drought periods for four different simulations.	125
6.5	(a, b) Scatter plots of the mean values of precipitation [mm day ⁻¹] for TRMM, ERA5, CHIRPS and the experiments during the first peak (P1), the MSD and the second peak (P2) periods and (c, d) the precipitation differences between the three periods.	126
6.6	Outgoing long-wave radiation (OLR) [W m ⁻²] (shaded) and ω 500-hPa [10 ⁻² Pa s ⁻¹] (line contours) differences between the MSD and MSDO and the MSDE and MSD.	127
6.7	Pentad-mean seasonal march of the (a, b) SSTs [°C] and (c, d) the low-level (925-hPa) zonal wind flow [m s ⁻¹] in (a) the easternmost equatorial Pacific and (b, d) the Caribbean Sea. The transparent shading is as in Figure 6.1.	128
6.8	As in Figure 6.6 but the anomalies are shown for SSTs [K] (contours) and surface humidity [g kg ⁻¹] (line-contours).	130
6.9	Scatterplots of yearly timings in the MSD precipitation time-series diagnosed by the WT method for (a) monsoon onset (MO), (b) monsoon retreat (MR), (c) MSDO and (d) MSDE comparing the results of the CHIRPS dataset with ERA5, TRMM and the GC3-amip simulation. The legend shows the Pearson r coefficient for each comparison.	132
6.10	Scatterplots of the mean changes in the East Pacific (a, b) sea-surface temperatures (SSTs) and (c, d) surface saturation specific humidity q_{sat} in the x-axis with respect to precipitation variations in the MSD region on the y-axis for the (a, c) MSD-P1 and (b, d) P2-MSD periods. The correlation coefficient of the interannual spread in ERA5 and the multi-experiment correlation coefficient are shown in each panel.	133
6.11	Lagged correlations between East Pacific SSTs and precipitation in the MSD region for (a) ERA-5 where the lag 0 date was used in four different ways: first, all the boreal summer JJAS SSTs and precipitation pairings, then lag 0 represents the monsoon onset (MO), MSD onset (MSDO) and MSDE dates. (b-d) as in (a) but for the simulations where the correlations are computed with the SST-precipitation timeseries lagged with respect to the b) monsoon onset date, the c) MSDO date and the d) MSDE date.	134
6.12	Composite mean cloud radiative effect (CRE) [W m ⁻²] during the periods of onset of the MSD, the MSD and the end of the MSD for (a-c) ERA5, and the ensemble mean of (d-f) GC3-hist and (g-h) N216-hist.	136

6.13 As in Fig. 6.12 but for the short-wave radiative effect.	137
6.14 As in Fig. 6.12 but for the long-wave CRE.	138
6.15 Pentad-mean seasonal cycle of the (a) SW and (b) LW CREs, (c) the net CRE, and (d) the net SW at the surface, signed positive to indicate surface absorption of SW radiation.	139
6.16 As in Fig. 6.6, but for the net shortwave radiation [W m^{-2}] at the surface.	140
6.17 Scatter of	141
6.18 Composite mean precipitation (shading), vertical velocity (contours) and 850 hPa wind speed (vectors) for the P1, MSD and P2 periods in the (a-c) GC3-amip and (d-f) GC3-amip lwoff experiment. (g-i) shows the difference between the lwoff-amip and the amip experiments.	142
6.19 As in Figure ?? but showing wind vectors at the 850 hPa level.	143
6.20 As in Figure ?? but showing in shading, moisture flux divergence $\nabla \cdot \vec{u}q$ at the 850 hPa level with units of $10^{-7} \text{ s}^{-1} \text{ kg / kg}$ and zonal wind anomalies (line contours) in m s^{-1}	143
6.21 Scatter plot of the (a, b) area-averaged precipitation over land (Box in Figure 4.8) during the different stages of the MSD. (c) scatter of the East Pacific SSTs against the precipitation over land during the first peak period. (d-l) show the scatter differences in several variables between the different stages of onset of the MSD (MSDO), the drier MSD and the end of the MSDE. The differences are shown for area-averaged quantities in the East Pacific (EP), the Caribbean Sea (CSEA) and overland (MSD) as above. The units for ΔU are [m s^{-1}], ΔMFC [10^{-11} s^{-1}], ΔSW and ΔLHF [W m^{-2}] and Δpr mm d^{-1} . The Pearson correlation coefficient for the 38 yr of reanalysis or observations (r_{obs}) is shown for each panel.	145

List of Abbreviations

- 1-D, 2-D** . . . One- or two-dimensional, referring in this thesis to spatial dimensions in an image.
- Otter** One of the finest of water mammals.
- Hedgehog** . . . Quite a nice prickly friend.

1

Introduction

The American Monsoon System (AMS) is the main source of rainfall for the most part of Latin America and the southwestern United States, which are regions where agricultural activity is economically crucial and where a vast wealth of ecosystems and biodiversity are present. Changes to the amount, timings and location of rainfall over different temporal scales has direct consequences for the livelihood of the people and for ecosystems in the regions. Improving our physical understanding of the mechanisms that cause temporal changes to the AMS rainfall is crucial to improve our medium-range forecasts and our climate predictions which could ultimately render key information for risk assessments, climate adaptation and agricultural strategies. In this context, this thesis aims to tackle outstanding questions in the American Monsoons in a global climate model with particular interest in better understanding the physical mechanisms associated with variability and teleconnections of this monsoon.

1.1 Motivation

Temporal and spatial variability of rainfall is important for society throughout the planet for various reasons, but the relevance of the timing and strength of rainfall is emphasized in agriculturally active and biodiversity hotspot tropical regions (Sultan et al., 2005; Jain et al., 2015). In the AMS, changes to rainfall on inter-annual scales

can produce long-lived droughts that are associated with crop loss and forest fire intensification (Chen et al., 2009; Harvey et al., 2018). But shorter-term changes can also produce profound effects such as flash floods and intense rainfall periods that cause crop loss (Devereux, 2007; Ávila et al., 2016). A large body of monsoon research is consequently focused on understanding the physical mechanisms responsible for precipitation variability across temporal and spatial scales, i.e., the causes for variability of the monsoon (Wang et al., 2017; Gadgil, 2018).

The AMS was recognized as a monsoon only after the 1990s, which is relatively recent, as the definition for a monsoon has evolved from an initial dynamical definition based on a reversal of the prevailing winds to an agronomical definition that recognizes the seasonality of precipitation as the dominant feature of a monsoon (Wang et al., 2017; Gadgil, 2018). This fact, however, means that our understanding of the AMS is more limited compared to other monsoons given the lower number of studies on the AMS from a monsoon perspective when compared to other monsoons such as the Indian monsoons where monsoon forecasts exist since the 19th century (Blanford, 1886) produced the first monsoon forecast in 1886. For this reason, several primary questions about general aspects of the AMS remain open including unknown mechanisms for interannual variability and teleconnections.

Recently, theories for general or global monsoon dynamics have arisen in an effort to coherently explain the monsoons observed in Earth through a general physical mechanism. Several characteristics of the North and South American monsoons challenge the basic physical inferences or predictions of most of these theories, which means that these newly developed frameworks cannot easily be applied to the AMS to further understand their variability.

The lack of understanding of the basic physical mechanisms that drive the seasonal cycle of rainfall in the southern Mexico and Central America is one example of the gaps in the literature of the AMS. The so-called Midsummer drought is a robust bimodal feature of the seasonal cycle of precipitation during the wet season that has had implications for agricultural practices in the region since the Mayan Empire (Jobbová et al., 2018). In spite of the importance for region-wide agricultural practices,

the physical mechanisms that can explain this seasonal variation of rainfall has elluded research over recent years.

Climate research in South America has recently focused to investigate the non-linear responses of precipitation of the AMS to teleconnections from the El Niño-Southern Oscillation (ENSO), which occurs just on the western coast of the continent. ENSO phenomena has been well-known by Peruvian fishermen for centuries and has shaped agricultural practices and caused mass migrations (Caramanica et al., 2020). Nevertheless, the understanding of the effect of ENSO over South America and the AMS in general is still somewhat limited. For example, two ENSO events that are very similar in the central Pacific can cause teleconnections with different locations and strengths and the reasons behind these varying effects are not well understood.

One key tool to understand the causes for regional changes to monsoon rainfall are general circulation models (GCMs). These models are useful to evaluate the roles of climate features such as orography, vegetation-atmosphere and ocean-atmosphere feedbacks, ENSO and their impacts over many aspects of Earth's climate including monsoons (Zhou et al., 2016). However, the use of GCMs to address key questions of the AMS has been scarce. In fact, detailed accounts of the biases –differences between the simulated climate of a model and the real world – are rarely done with explicit emphasis on the AMS. In other words, GCMs are rarely evaluated in the AMS, so our the understanding lacks both in knowledge of the GCM biases relevant for the AMS but also because of a lack of use of GCMs to address scientific questions of the AMS.

This thesis focuses on the AMS and the outstanding questions regarding the climate variability and teleconnections affecting this monsoon. This thesis begins by evaluating a state-of-the-art climate model in the AMS region, assessing the roles of biases in the large-scale circulation that affect regional monsoon rainfall biases. This assessment highlights that the GCM used in this thesis is fit for the purpose of investigating two outstanding research questions in the AMS literature. The first chapter also highlights the lack of relevant methods to compare and contrast the timings of rainy seasons in the AMS in both GCM and observed datasets. Therefore, the following chapter describes a new method to determine monsoon timings. This method is then

used in the following two chapters which address the scientific questions, the MSD of Central America and Southern Mexico, as well as the effects of the stratospheric-tropospheric coupling in modulating ENSO teleconnections. In a way, each chapter of this thesis builds on the previous chapters.

1.2 Thesis aims and outline

The main aim of this thesis is to investigate the physical causes of variability and the mechanisms associated with teleconnections to the AMS. In particular, this thesis first evaluates a GCM which shows a reliable representation of the seasonal cycle of rainfall and of ENSO teleconnections, both characteristics of the model that motivate the remaining questions of the thesis.

The specific key aims of this thesis are:

1. To characterize the large-scale biases in a state-of-the-art GCM that are relevant for the representation of rainfall in the AMS.
 - (a) Characterize the main biases in the thermodynamical and dynamical features over the large scale tropical domain and the regional AMS sub-domains.
 - (b) Evaluate the roles of the role of large-scale biases, horizontal resolution and the use of Earth system processes for regional monsoon representation.
 - (c) Assess the representation of the teleconnection associated with the main driver of interannual variability, i.e., ENSO in a GCM with specific emphasis on the causes for non-linearity and non-asymmetry in the teleconnections.
2. Evaluate the seasonal variability of the monsoon onset, withdrawal and intra-seasonal changes in the GCM and compare to observational datasets.
3. Describe and investigate the physical mechanisms associated with the seasonal cycle of rainfall in Central America and southern Mexico by testing previous hypothesis of physical mechanisms within the model.

4. To investigate the role of stratospheric-tropospheric coupling in the tropics and the role of the tropopause for convection in the AMS and for ENSO teleconnections.

The remainder of this thesis is structured as follows:

- Chapter 2 provides a review of the literature on key aspects of the American monsoons. The chapter begins by introducing the concepts of monsoons, their different physical interpretations as a global phenomena and the place of regional monsoons in the global scale. Then, the North and South American monsoons are introduced and detail is given on the applicability of large-scale monsoon theories to these regional monsoons. This section is followed by a literature review of the proposed physical mechanisms that drive the unique monsoon-like seasonal cycle of rainfall in Central America, southern Mexico and the Caribbean. Then, El Niño-Southern Oscillation is introduced and their impacts over North and South America are described with key emphasis on questions. Finally, the chapter summarises how the effect of the stratosphere for tropical convection has recently regained attention by providing a literature review of tropical teleconnections of the stratospheric quasi-biennial oscillation.
- Chapter 3 describes the observational datasets used in this thesis, composed of four gridded precipitation datasets and one reanalysis dataset: ERA5. The chapter also described the UK Met Office Hadley Centre Unified Model (UM) and the configurations of the UM used in this thesis and in the Coupled Model Intercomparison Project phase 6 (CMIP6).
- Chapter 4 evaluates three configurations of the UM model submitted to CMIP6 for their representation of the AMS. The chapter describes large-scale biases over the tropics and local scale biases in the precipitation amount and seasonality in key regions of the AMS. The representation of ENSO teleconnections is also evaluated for their mean impacts over the AMS but also analysis is done on the non-linearity of simulated and observed teleconnections and the role of ENSO

flavours for this non-linearity. This chapter highlights relevant questions that are of interest to the wider AMS community and that can be pursued given the model biases and skill to reproduce aspects of the AMS. In particular, two aspects are emphasized that are tackled in the remaining chapters: first, the skill of the models in reproducing a bimodal signal in the seasonal cycle of rainfall in Central America and southern Mexico and second, a possible effect of the stratospheric quasi-biennial oscillation in modulating ENSO teleconnections to the AMS. The majority of this work has been published in *Weather and Climate Dynamics* García-Franco et al. (2020).

- Chapter 5 details a wavelet covariant transform method used to diagnose changes to the timings of the monsoon by determining the onset and retreat dates from precipitation time-series. The method is extended to be used to determine the timings of bimodal regimes, and even whether or not a bimodal regime exists or not in a given region. This chapter has been submitted to *The International Journal of Climatology*.
- Chapter 6 builds on the two previous chapters by further investigating the physical mechanisms that cause the bimodal regime of precipitation in southern Mexico in the UM CMIP6 models. The chapter relies on the wavelet transform method to differentiate the ocean-atmosphere states during the different stages of the seasonal cycle. The roles of the East Pacific sea-surface temperatures, the cloud-radiative feedback and the Caribbean Low-Level Jet are investigated in various CMIP6 experiments and compared to what is observed in ERA5.

2

Background

This chapter provides the necessary background for the topics of the thesis; first by summarising the main aspects of the tropical circulation and of the global monsoon and discussing the existing theories to explain the monsoon phenomena. Then, the American Monsoon System is introduced and detail is given on the Midsummer drought of southern Mexico and Central America and El Niño Southern Oscillation teleconnections to this monsoon. Finally, a summary of the literature on the role of stratospheric-tropospheric coupling in the tropics for monsoon variability is given.

2.1 The tropical circulation and the global monsoon

Tropical climate is a result of the strong solar insolation received year-round that generally provides a stronger heating of the surface compared to extra-tropical latitudes. These latitudinal differences in insolation generate a meridional heat transport by the coupled atmosphere-ocean system. This means that the tropics have a positive annual net energy and the extra-tropics show a negative net energy.

The dynamics in the tropics is also distinct from extra-tropical latitudes due to other physical features such as the relative extent and location of the continents, the way in which gravity waves propagate throughout the atmosphere and a different

impact of Earth's rotation upon the dynamics of parcels. Generally, tropical dynamics is considered to be less understood than mid-latitude dynamics, because most of the assumptions of mid-latitude dynamical frameworks break down in the tropics, but also because reliable data in the tropics was scarce until satellites began providing continuous reliable observations of the tropics in the 1980s (Emanuel, 2007; Webster, 2020).

Moist convection is arguably one of the characteristic traits of tropical climate as the dynamics and thermodynamic effects of deep moist convection has relevant feedbacks with the regional and large-scale circulation (Emanuel et al., 1994; Webster, 2020) and produces long-distance effects through propagating waves and anomalous circulations (Hartmann, 2015; Li and Hsu, 2018). Moist convective systems span different spatial and temporal scales, from short-lived cumulonimbus showers to tropical cyclones that can survive more than a week on the open ocean. Over sufficiently long scales, the mean deep moist convective activity also plays a significant role in determining the large-scale tropical circulation typically divided into meridional and zonal overturning circulations, the Hadley and Walker circulations.

The Hadley cell is the meridional overturning circulation that arises from the differential heating between the tropics and the midlatitudes. The Hadley cell is characterized by ascending motions in the tropics and descending motions in the subtropics, and acts to transport heat poleward from the equator (Lorenz, 1967). This Hadley cell migrates meridionally with the seasonal cycle, the winter and summer cells interact with each other but also with the midlatitudes through eddy momentum fluxes (Bordoni and Schneider, 2008). The Hadley cell is not zonally symmetric; the boreal summer Hadley cell, for instance, is primarily a result of ascent in the Indian Ocean and the west Pacific regions with a minor contribution from ascending motions in Central and North America (Hoskins et al., 2020).

In spite of the fact that the large input of solar radiation is roughly uniformly distributed throughout the tropics on an annual mean average at the top of the atmosphere, the energy balance at the surface and the tropical circulation are not zonally symmetric. The prominent example of zonal asymmetry in the tropics is the Walker circulation. The Walker circulation is the zonal overturning circulation

found in the equatorial Pacific Ocean characterized by ascending motion over the West Pacific and descending motions over the East Pacific (Walker, 1924; Bjerknes, 1969; Gill, 1980). The dynamic and thermodynamic effects of the location and strength of convection associated with the Walker circulation have strong impacts across all the tropics and also the extratropics, known as teleconnections (Cai et al., 2019).

The Inter-tropical Convergence Zone (ITCZ) is a tropical band of convective clouds and precipitation that migrates meridionally with the seasons (Schneider et al., 2014). The ITCZ is arguably one of the most relevant features of tropical climate due to the strong influence on the low- and upper-level circulation associated with ITCZ, the high tropospheric heating due to deep moist convection in the ITCZ and the largest precipitation rates in the tropics are found in the ITCZ. The ITCZ is characterized by a strong convergent flow in the low levels and a strong divergent flow at upper levels. The meridional migration of the ITCZ, as well as the mean latitude of the ITCZ,

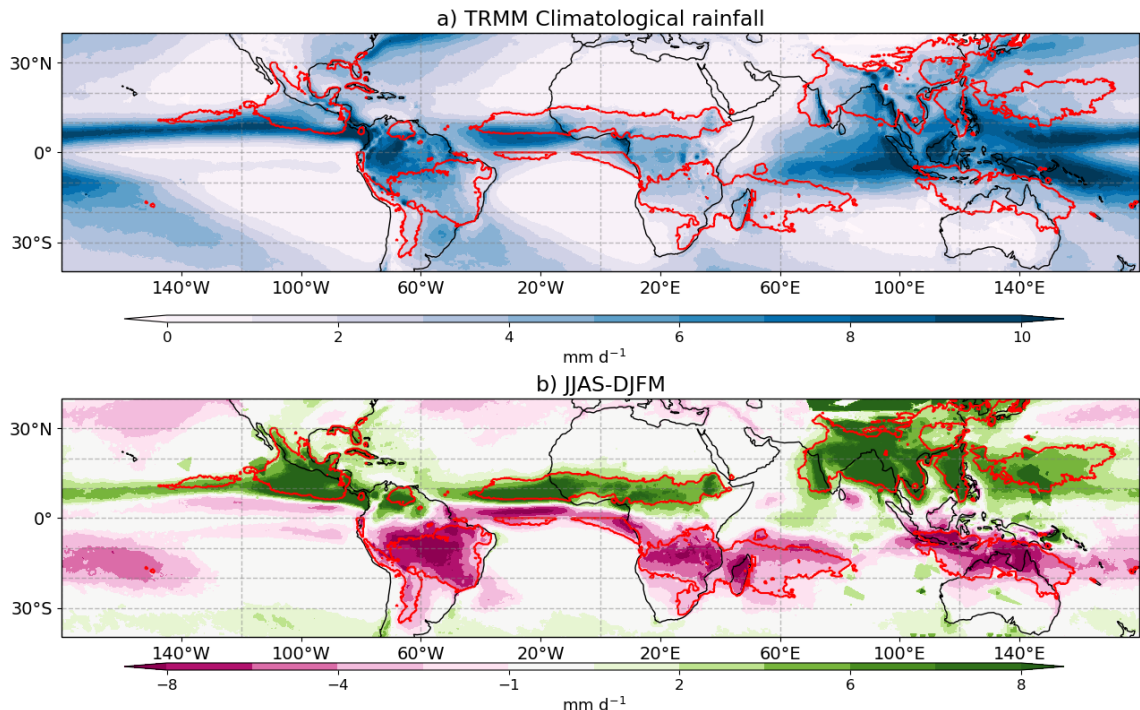


Figure 2.1: a) Climatological mean annual rainfall rates in the tropics using data from the Tropical Rainfall Measurement Mission (TRMM) dataset (1999–2018). b) The mean rainfall rate difference between boreal summer (JJAS) and austral summer (DJFM). The red contours highlight the regions where the mean summer rainfall amount accounts for more than 55% of the mean total annual rainfall accumulation.

results from the energy and momentum balances so that the ITCZ is predominantly north of the equator because of the inter-hemispheric temperature contrast (Donohoe et al., 2013; Bischoff and Schneider, 2016).

One of the phenomena of tropical climate that first generated interest in climate research are monsoons (Halley, 1687). The word *monsoon* stems from the Arabic word for *season* and is closely associated with the very first conceptions of a monsoon. The first widely accepted view of a monsoon was that of a large-scale land-sea breeze associated with the differential warming of the land and the ocean that force a seasonal reversal of the low-level wind flow that brought seasonal rainfall (Halley, 1687).

The traditional land-sea breeze definition of monsoon is now known to present several shortcomings. Firstly, several mid-latitude regions would fit a monsoon definition based solely on a seasonal reversal of the wind (Gadgil, 2018), and secondly, regions that are now recognized as a monsoons, in South America for example, do not show a seasonal reversal of the winds, *per se*, rather just a seasonal change in direction and strength of the zonal winds (Vera et al., 2006). For these reasons, the land-sea breeze view of monsoons has recently been replaced by three alternative conceptions, an ITCZ-monsoon framework, a convective quasi-equilibrium interpretation and a moist static energy (MSE) zonal-mean energetic interpretation (Biasutti et al., 2018; Hill, 2019; Geen et al., 2020). The MSE budget and methodology is detailed in section 3.3 but a broad description of the method and summary of results arising from the MSE budget is given below.

The first framework explains monsoons as a poleward extension of the ITCZ into land generalizing all monsoons as an expression of global tropical convergence resulting from the energy balance (Chao and Chen, 2001; Gadgil, 2018). This interpretation has led to the concept of *the global monsoon*, a term that encompasses all the regions in the tropics that exhibit a strong seasonality in precipitation (Zhou et al., 2016; Gadgil, 2018). In practice, the global monsoon refers to the those regions of the planet where more than 70% of the total annual rainfall falls during the summer season, in several recognizing the seasonality of precipitation as the key feature to diagnose a monsoon (Zhou et al., 2016; Wang et al., 2017).

Figure 2.1 shows the global monsoon as depicted by the TRMM dataset. By this definition, the majority of the regions over land between 5 and 10 degrees away from the equator are part of the global monsoon. A regional monsoon, such as the Indian Monsoon, is then a subset of the global monsoon with unique regional characteristics that shape this monsoon different to other regional monsoons in terms of the seasonality, the strength and the dynamics. The American Monsoon System is then the regional monsoon that is located in the subtropics of North and South America.

Bordoni and Schneider (2008) provide an alternative conceptual view of monsoons, describing the characteristic rapid onset of a monsoon as a regime transition of the Hadley cell from a edddy-momentum driven circulation, which resembles a canonical ITCZ regime, to a thermally direct circulation which resembles a monsoon-like circulation. The zonal mean MSE meridional gradient drives the ITCZ location and determines the strength of the overturning circulation by modulating the ventilation from midlatitude cooler and drier air in a feedback mechanism (Geen et al., 2020). Even though this framework is posited as an axisymmetric framework, their predictions were broadly consistent with the Asian monsoon circulation.

Convective quasi-equilibrium (CQE) is a theory for moist convection where convection sets the vertical temperature and moisture profiles to a convectively neutral state, thereby setting the free tropospheric temperature (Neelin, 2007). For a monsoonal circulation, this theory emphasizes the coupling of convection and dynamics predicting that the subcloud layer equivalent potential temperature maxima must be collocated with the free tropospheric saturation equivalent potential temperature (Nie et al., 2010; Geen et al., 2020). The rapid onset of the Asian monsoon has been shown to be associated with the boundary layer moist entropy distribution, in agreement with predictions of CQE (Nie et al., 2010; Boos, 2015; Ma et al., 2019).

Several studies examine the monsoon phenomena through an axi-symmetric framework that assumes zonal symmetry and aims to understand the large-scale dynamical influence over the extent and strength of the axi-symmetric monsoon through global energetic diagnostics (e.g. Faulk et al., 2017; Geen et al., 2019; Byrne and Zanna, 2020). The zonal-mean framework is common to the Hadley cell interpretation

of monsoons (Bordoni and Schneider, 2008), as well as the ITCZ-monsoon theory. However, regional monsoons are shaped by the asymmetries imposed by the orography, the characteristics of the surrounding ocean basins, land-sea contrasts and also the role of vegetation-hydrology coupling (Wang et al., 2017; Pascale et al., 2019). The importance of zonal asymmetries has raised multiple issues with large-scale so-called monsoon dynamics theories, as several predictions of these theories are not consistent with observations of regional monsoons (e.g. Nie et al., 2010; Smyth et al., 2018; Biasutti et al., 2018; Pascale et al., 2019).

Recent reviews acknowledge that all these frameworks have significant shortcomings to be applied to regional local monsoons (Biasutti et al., 2018; Hill, 2019; Geen et al., 2020). These reviews conclude that a framework that reconciles the global energetic perspective with the characteristics of regional monsoons would be crucially important and very useful, but as several authors point out (e.g. Biasutti et al., 2018; Hill, 2019), also very hard to formulate. For example, the North and South American Monsoons depart from CQE, as precipitation does not follow the maxima in subcloud equivalent potential temperature (Nie et al., 2010; Geen et al., 2020).

The MSE budget framework suffers both from theoretical and practical shortcomings. One practical shortcoming is that the calculation of the budget terms post hoc in reanalysis or models results in very large residuals (Hill, 2019), so these frameworks work best when the calculations are done inside the budget terms to be integrated online at each time-step (e.g. Ma et al., 2019). The theoretical shortcoming is that the surface fluxes over land, e.g., in the Sonoran and Saharan deserts and the deep Amazon make the estimations of the roles of hydrology-vegetation feedbacks and their potential contributions to the MSE budget in observations very difficult to assess (Boos and Korty, 2016; Pascale et al., 2019). The use of simpler moisture budgets has proven useful in a regional monsoon context to investigate the sources of moisture for a monsoon in current (Ordoñez et al., 2019; Martinez et al., 2019) and future climates (Smyth and Ming, 2020), but this budget is mostly a tool and not a coherent theory for process-level understanding of monsoons.

The Hadley cell interpretation of monsoons has significant shortcomings to depict some regional monsoons, particularly those that are not the Asian monsoon as the overturning circulation in the South Asian monsoon is strong enough to be represented by a clear thermally direct regime. However, this energetic framework assumes no zonal transport of energy, which minimizes the role of orography and land-sea interaction (Biasutti et al., 2018). One might reasonably infer from these results that the timing of transition in zonal mean overturning cells would be similar for monsoons at different longitudes but similar latitudes, which is not the case (Wang et al., 2017). Furthermore, a monsoon restricted to a small area, such as the North American and African monsoons may not present a clear zonally averaged overturning regime, and may be significantly affected by local zonal shallow and deep circulations (Zhai and Boos, 2015). For instance, Smyth et al. (2018) shows that the simulated West African monsoon when forced with different solar forcings exhibits a decoupling between the zonal-mean ITCZ location, the strength of the local Hadley cell and the monsoon rainfall, in opposition to the predictions of this framework (Bordoni and Schneider, 2008).

In short, despite significant progress in our understanding of the monsoon phenomena at the planetary-scale through zonal mean energetic frameworks, there is an important gap between large-scale theories of monsoon dynamics and the observed regional monsoons. The next section presents a summary of the American Monsoon literature, which explains the characteristics of these monsoons through the effect of regional features and dynamics, seemingly detached from the literature in this section. The AMS literature is therefore, seemingly, detached from the literature in this section.

2.2 The American Monsoon System

The American Monsoon System (AMS) is the main source of rainfall for tropical Latin America and is typically subdivided into the North and South American monsoon systems (Vera et al., 2006). Although the spatial definition of the AMS is quite varied amongst studies, a general consensus is that the North American Monsoon is found in south-western North America (Figure 2.2a) extending north from central-west Mexico

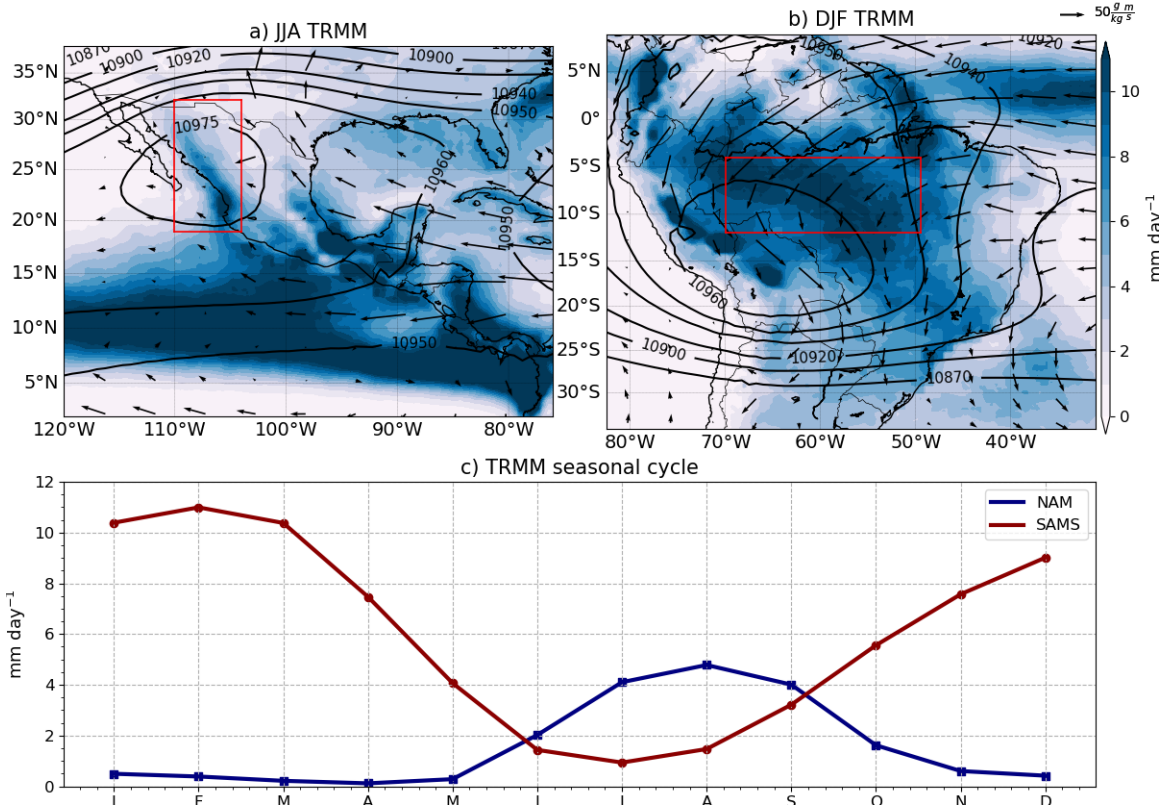


Figure 2.2: Climatological mean a) boreal and b) austral summer rainfall (shading), 850 hPa moisture flux (vectors) and geopotential height at 250 hPa (contours) in a) southern North America and b) South America. c) Monthly-mean seasonal march of precipitation in the TRMM dataset for two area-averaged time-series, the North American Monsoon (NAM) and the South American Monsoon System (SAMS) shown in the red rectangles in a-b).

into the southwestern United States and the South American Monsoon is centred in the deep Amazon south to the river mouth (Figure 2.2b) (Adams and Comrie, 1997; Stensrud et al., 1997; Vera et al., 2006).

The seasonal cycle of rainfall in the North American Monsoon is characterised by a wet July-August-September season and significantly drier conditions during the rest of the year (Adams and Comrie, 1997) (Figure 2.2c). Three temporal stages describe the evolution of the North American Monsoon (Adams and Comrie, 1997; Geil et al., 2013). First, the onset stage (May-June) starts with a strong surface warming that leads to very high temperatures in the desert region. Simultaneously, the sub-tropical jet weakens and migrates north decreasing the frequency of mid-latitude disturbances in the monsoon region (Douglas et al., 1993; Turrent and Cavazos, 2009). These

factors combine to develop a low-level (upper-level) thermal surface low (anticyclone) and moisture influx from the nearby Gulf of California and easternmost Pacific Ocean (Douglas et al., 1993; Geil et al., 2013). Maturity (July-August) is the peak period of monsoon rainfall characterised by sustained deep convection (Barlow et al., 1998) and significant increases in low and mid-level moisture flux convergence and mid-level latent heating (Adams and Comrie, 1997; Cook and Seager, 2013). This latent heating caused by deep convection can be diagnosed in the upper-level geopotential height (Figure 2.2a) in the form of an anticyclone centred on the monsoon region.

The moisture flux convergence decreases in August, after which precipitation recycling (Dominguez et al., 2008) plays an important role in keeping deep convection active until September. Decay (September-October) is the last stage of the monsoon, in many ways opposite to the onset stage, as is characterised by the equatorward migration of the sub-tropical jet (Higgins et al., 1997; Geil et al., 2013), evaporation in the nearby basins decreases and deep convection in the monsoon region gradually disappears (Douglas et al., 1993).

The origin of the high levels of moisture at low and midlevels in the monsoon region has been a matter of debate for a long time (Adams and Comrie, 1997; Barlow et al., 1998; Vera et al., 2006; Ordoñez et al., 2019). A large number of studies acknowledge that the main source of moisture for the North American Monsoon is the East Pacific Ocean and to a second order, mid-level moisture advected from the Gulf of California can mix in the column (e.g. Adams and Comrie, 1997; Stensrud et al., 1997; Vera et al., 2006; Turrent and Cavazos, 2009; Ordoñez et al., 2019).

The South American Monsoon is a primary source of precipitation for South America, especially in the Amazon region (Gan et al., 2004; Vera et al., 2006; Jones and Carvalho, 2013). During austral summer (DJF), monsoon rainfall accounts for over 60% of the total annual precipitation in the Amazon (Gan et al., 2004; Marengo et al., 2012), whereas austral winter rainfall accounts for less than 5% of the total annual rainfall (Vera et al., 2006). In the central Amazon, convective precipitation is observed from early October but the main rainy season extends from December to April (Machado et al., 2004; Adams et al., 2013), whereas convection in southeastern

Brazil and Paraguay starts in November and peaks in January and February (Marengo et al., 2001; Nieto-Ferreira and Rickenbach, 2011).

A surface heat low appears in Bolivia in early austral summer, known as El Chaco Low, as a result of strong warming in austral spring (Marengo et al., 2012; Sulca et al., 2018). As this surface heat-low strengthens, low-level convergence drives the circulation into the low region. Simultaneously, an upper-level anti-cyclone (Fig. 2.2b), known as the Bolivian High, develops in the same region as a signature of strong deep convection and latent heating (Marengo et al., 2001; Vera et al., 2006).

This low-level wind circulation importing moisture from the Atlantic is one of the most important features of the SAMS (Marengo et al., 2012; Wang et al., 2017) as the flow modulates the moisture flux to the mainland and influences the occurrence of active and break phases of the SAMS (Jones and Carvalho, 2002), as well as changes in the temporal and spatial distribution of rainfall (e.g. Giannini et al., 2004; Bombardi and Carvalho, 2011).

As described in the previous sections, both the North and South American monsoon thermodynamics do not follow the CQE propositions, i.e., the maximum low-level moist static energy is not collocated with the maximum free tropospheric temperature. One possible reason for this is that the free-troposphere over southwestern North America is significantly drier than in other monsoon regions, decoupling the free troposphere from the boundary layer. One alternative hypothesis is that ventilation of low moist entropy air from the midlatitudes is responsible for this decoupling of the boundary layer and the free troposphere in the American monsoons (Boos, 2015).

2.3 A review on the proposed mechanisms for the Midsummer drought

The characteristics of the seasonal cycle of precipitation in northwestern Central America, the Caribbean and southern Mexico fit the definition of a monsoon climate (Wang et al., 2017) with a clear separation of the wet and dry seasons. However, this region shows a unique climatological precipitation feature. After monsoon onset,

rainfall decreases considerably around the midsummer; this decrease is followed by a secondary increase in precipitation in the late summer (Mosiño and García, 1966), and for this reason this feature of the seasonal cycle is most commonly referred to in the literature as Midsummer drought (MSD) (Magaña et al., 1999).

The intraseasonal variations of precipitation associated with the MSD have been known for centuries and have shaped agricultural practices in the region. For example, ancient mayan texts suggest that agricultural rituals associated with the plea for rain-bearing clouds to the gods were significantly more frequent during the drier MSD period (Jobbová et al., 2018). In current days, the MSD is well known by local farmers who refer to the drier midsummer period as ‘El Veranillo’ in Central America and ‘canícula’ in southern Mexico because the drier period coincides with the Canis Major constellation appearing in the sky (Dilley, 1996).

The two peak structure of the MSD has been diagnosed in the observed climatological precipitation of several regions of Mexico, El Salvador, Belize, Guatemala, Costa Rica and Cuba (e.g. Mosiño and García, 1966; Magaña et al., 1999; Durán-Quesada et al., 2017; Perdigón-Morales et al., 2018; Martinez et al., 2019). However, notable differences in the seasonal cycle of precipitation have been found between the mainland Central America and the Caribbean islands. The so-called first peak of precipitation occurs in June and the second peak in September in northern Central America whereas the two peaks are observed in May and October in the Caribbean.

In spite of extensive research to understand the physical mechanisms associated with the MSD (e.g. Magaña et al., 1999; Giannini et al., 2000; Gamble et al., 2008; Herrera et al., 2015; Maldonado et al., 2017; Straffon et al., 2019), debate remains over which is the leading-order mechanism that causes rainfall to decrease at midsummer and increase again at the end of the summer. Fundamental questions remain unclear such as whether the MSD is caused by two precipitation enhancing mechanisms (Karnauskas et al., 2013) or a mechanism that inhibits rainfall at midsummer (Durán-Quesada et al., 2017). Furthermore, the association between the MSD in Central America and in the Caribbean is still disputed (Gamble et al., 2008), as most studies

suggest that the two regimes are unrelated and therefore two different explanations are required to account for the two MSDs in these regions.

One of the first hypotheses to account for the bi-modal distribution of rainfall was proposed by Hastenrath (1967) who argue that a double crossing of the ITCZ can explain the MSD so that the first peak of precipitation is associated with early summer northward crossing of the ITCZ and the second peak the return or southward displacement of the ITCZ during late summer. However, this theory fails to explain the MSD signal seen at latitudes as high as 29°N (Perdigón-Morales et al., 2018; Zhao et al., 2020), a feature that will be shown in this thesis, which is further north than the northernmost extension of the ITCZ (Schneider et al., 2014), and certainly the ITCZ does not cross twice so far from the equator.

Magaña et al. (1999) and Magaña and Caetano (2005) proposed a mechanism driven by radiative-convective feedbacks between the East Pacific (EP) sea-surface temperatures (SSTs) and deep tropical convective clouds. The coupling between the height and strength of convection, the incoming shortwave radiation and the SSTs are the key features of their framework. The EP SSTs peak in May triggering large evaporative fluxes and deep convection in the EP ITCZ and the western coast of Central America. The high convective clouds produce a radiative cooling effect at the surface due to a decreased incoming shortwave radiation associated with the reflectance of shortwave radiation by clouds. This cooling decreases SSTs and deep convective activity and thus accounts for the decrease of rainfall during the midsummer. The second peak in September is driven by an opposite mechanism, i.e., the decreased frequency of deep convective clouds during the MSD period in July and August reduce the cooling effect of the anvil clouds and increase the incoming shortwave radiation at the surface, SSTs and surface fluxes, all of which leads to an precipitation during late August and September (Magaña et al., 1999).

A large number of studies, in contrast, propose that the seasonal evolution of the North Atlantic Subtropical High (NASH) is the leading mechanism for the MSD (e.g. Mapes et al., 2005; Small et al., 2007; Gamble et al., 2008; Curtis and Gamble, 2008; Muñoz et al., 2008; Martinez et al., 2019; Corrales-Suastegui et al., 2020). The NASH

is the subtropical anticyclone in the North Atlantic Ocean that migrates southwest during early boreal summer. The expansion and intensification of the NASH in boreal summer, according to these studies, strengthens the low-level trade winds, controlling the seasonal cycle of a low-level jet found in the core of the Caribbean Sea known as the Caribbean Low-Level Jet (CLLJ). The CLLJ is a key regional feature of the climate of the Caribbean and the Intra-Americas Sea because the strength and direction of the flow in the Caribbean controls the underlying Caribbean SSTs and the regional moisture transport (Giannini et al., 2000; Mestas-Nuñez et al., 2007; Martinez et al., 2019; García-Martínez and Bollasina, 2020).

However, studies disagree on the specific roles that the CLLJ and the NASH play for the precipitation over the Mesoamerican region. For example, some studies (e.g. Giannini et al., 2000; Mestas-Nuñez et al., 2007; Gamble et al., 2008) suggest that the expansion of the western flank of the NASH strengthens the CLLJ which cools the SSTs, through the effect of wind stress and mixed-layer mixing. The cooling of SSTs diminishes evaporation and therefore low-level moisture which ultimately leads to less precipitation.

In contrast, other studies propose that the CLLJ and NASH affect the seasonal cycle of precipitation through their effects on the regional moisture transport (Small et al., 2007; Muñoz et al., 2008; Herrera et al., 2015; Durán-Quesada et al., 2017; Martinez et al., 2019). In this second hypothesis, the changes to the intensity of CLLJ influenced by the NASH modify the convergence and divergence patterns in the Intra-Americas Sea. In other words, the midsummer strengthening of the CLLJ increases moisture divergence, drying the atmospheric column over the Caribbean.

Herrera et al. (2015) shows that during the drier months in Central America in the Midsummer, convective west of the central American continent gets stronger with heavier precipitation. Their evidence suggests that the gap flow that originated from the CLLJ in the Caribbean Sea controls the location of ascending and descending motions, and the MSD may be explained by the seasonal variations and the coupling of the low-level wind flow with the underlying EP SSTs. Herrera et al. (2015) further argued that the exit region of the CLLJ is located to the east of the region of

strongest MSD signal, which suggests that the moisture divergence effect over the central American MSD is minimal.

A different mechanism, proposed by Karnauskas et al. (2013), argues that the biannual crossing of the solar declination angle can control precipitation and explains the bimodal characteristics of the seasonal cycle. In this mechanism, the MSD is driven by two precipitation enhancing periods that are separated by a relatively normal, and drier, period. This theory differs from those previously discussed which explained the MSD through mechanisms that inhibit convective activity in the midsummer whereas Karnauskas et al. (2013) argues that the solar declination angle that crosses twice through Central America, once during June and a second time during September, increases convective activity during each crossing.

The variations of incoming shortwave radiation associated with the declination angle modulate the SSTs, surface fluxes and therefore convective activity. In other words, the first crossing of the solar declination angle increases the incoming shortwave radiation which increases the SSTs, evaporation and leads to a peak of precipitation, i.e., the first peak. After the shortwave radiation is reduced the MSD period appears. The second crossing of the solar declination angle, similarly, explains the second peak as the second increase in incoming shortwave promotes more deep convection than during the MSD.

Other mechanisms have been proposed arguing that the MSD is a result of vertical wind shear affecting convective instability or the Saharan dust controlling the microphysics of clouds (Angeles et al., 2010). For instance, Perdigón-Morales et al. (2019) also finds a link between the frequency and spatial distribution of the first peak rainfall rates and the Madden-Julian Oscillation.

2.4 El Niño Southern Oscillation: impacts to the American monsoon system

El Niño-Southern Oscillation (ENSO) is a phenomena that primarily affects the local ocean and atmosphere of the equatorial Pacific Ocean, but these changes are profoundly important for the global climate system, which is why ENSO is commonly

known as the leading mode of interannual variability. The term '*El Niño*' was initially coined by Spanish colonizers when they learnt from Peruvian fishermen that the ocean surface temperatures in the easternmost Pacific Ocean increased notably in some years around December time. For religious reasons, the colonizers termed the SST increase as Christ Child – *El Niño*.

Later on, sir Gilbert Walker (1924) coined the term *Southern Oscillation* to describe the synchronous changes to the sea-level pressure of the Indo-Pacific region and South America. Walker (1924) and Walker (1932) are the first analyses of synchronous effects of the tropical circulation over local precipitation, temperature and pressure. Further research (e.g. Troup, 1965) would highlight that these remote changes in pressure were driven by the east-west pressure gradient in the equatorial Pacific.

The changes in the pressure field associated with the Southern Oscillation (SO) are now part of what is known as the Walker circulation, which intertwines the dynamics of the zonal circulation in the East Pacific with the SSTs over the underlying ocean. ENSO is then characterized as a coupled phenomena composed of an oceanic part, *El Niño*, and an atmospheric component associated with the zonal circulation but best characterized by changes to the surface pressure field, the Southern Oscillation.

ENSO has several unique features, such as no robust periodicity as events may occur every 2 to 7 years and a seasonal phase-locking that are associated with ENSO events peaking in boreal winter in observations (Wang and Picaut, 2004). Even though the underlying physics that cause ENSO and explain the variability in the periodicity of the phenomena is still debated (Wang and Picaut, 2004; Christensen et al., 2017), several aspects are now better understood. For example, the local effect that ENSO events have over on the location and strength of deep convection in the equatorial Pacific have long been thoroughly described (Trenberth, 1997; Neelin et al., 1998).

During a neutral state of ENSO, the Walker circulation is found in the climatological state, with ascent and wet conditions in the West Pacific and descent and drier conditions in the East Pacific. During El Niño the Walker circulation and low-level trade winds weaken which is associated with an eastward shift of deep convection along the equatorial Pacific (Figure 2.3), with convective rainfall becoming more

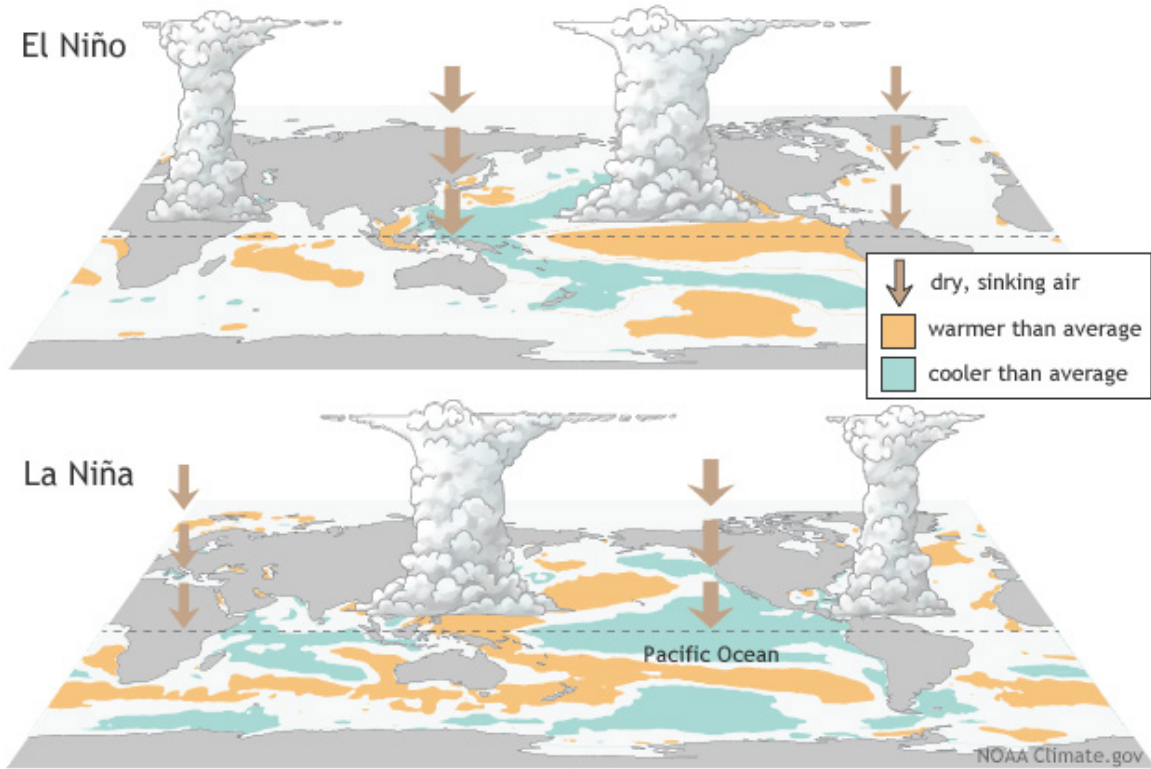


Figure 2.3: Schematic of the positive (upper) and negative (lower) phases of ENSO. Regions with tall clouds indicate more ascent and convection than normal whereas brown arrows indicate dry descending air. Obtained from the National Oceanic and Atmospheric Administration at <https://www.climate.gov/enso>.

frequent in the central and even eastern Pacific than normal (Neelin et al., 1998; Wang and Picaut, 2004). During La Niña the opposite happens and the Walker circulation strengthens which leads to stronger convection in the West Pacific and stronger ascent on the East Pacific (Figure 2.3).

In other words, ENSO imposes a strong control on the location and strength of the Walker circulation (Figure 2.3). These changes to the strength and position of the convective regions in the Pacific Ocean can then propagate to other regions of the planet; these far-distant effects are commonly known as *teleconnections*. For example, ENSO has a direct effect over other tropical regions outside of the Pacific through the Walker circulation, see Figure 2.3, as upper-level wind anomalies induce anomalous vertical motions over the monsoons in West Africa (Ropelewski and Halpert, 1986, 1987) or South America (Sulca et al., 2018). Other mechanisms of ENSO teleconnections to higher latitudes include changes to the position and strength

of sub-tropical jets (Fereday et al., 2020), changes to the Pacific and North American circulation patterns (Bayr et al., 2019) as well as impacts to the North Atlantic via the stratospheric polar vortex (Domeisen et al., 2019).

In South America, the effects of ENSO are felt throughout the continent and throughout economic sectors from Peruvian fishermen (Takahashi, 2004) to the Amazon rain-forest and the plainlands in South-eastern South America(Grimm, 2011; Marengo et al., 2012). One key aspect of current research on ENSO impacts to South America is the observed non-linearity and non-symmetry in the teleconnections, which has mainly been attributed to ENSO diversity (Tedeschi et al., 2015; Cai et al., 2020). A non-linear teleconnection refers to a non-linear scaling between the strength of an ENSO event, typically measured by an SST index, and the magnitude of the response, in most cases precipitation response.

Observations have shown that the maximum SST anomaly does not always appear in the same region of the Pacific Ocean (Ashok and Yamagata, 2009; Dommeneget et al., 2013). These differences in the SST patterns are referred to as ENSO *diversity* or *flavours* which can be broadly summarized as two flavours for each phase, based on the location of the SST anomaly these events are commonly separated into Central and Eastern Pacific events. In observations, each type of event is usually also associated with the strength of the event (Dommeneget et al., 2013).

The strength and patterns of ENSO teleconnections have been shown to depend on the type of event for the South American monsoon (Rodrigues et al., 2011; Sulca et al., 2018). Cai et al. (2020) provides a recent review on the differences in the impacts that Central and Eastern Pacific (CP and EP) events have on South America. The observed record shows that the teleconnections affecting the Amazon and northeastern Brazil are most pronounced during EP El Niño events and CP La Niña events than the CP El Niño events and EP La Niña events. This recent review also highlights the need for further modelling work to test observation-driven hypothesis, as the observed record is too short to make confident statements about the mechanisms associated with ENSO teleconnections.

2.5 Stratosphere-Troposphere Coupling in the Tropics

The troposphere is the lowermost layer of the atmosphere ranging from the surface up to 10-15 km where the vertical temperature profile is characterized by a decrease of temperature with height. The layer above the troposphere is called the *stratosphere* where the vertical temperature gradient is reversed and temperatures increase with height, this layer spans from 10-20 km up to 50 km in altitude (Andrews et al., 1987). The layer in between the troposphere and the stratosphere is the tropopause, which is a transition region where the vertical temperature gradient reverses and the atmosphere is stable to upward motions.

Stratosphere-troposphere coupling refers to events or processes where the two layers are notably affected by each other so that the temperature or wind flow of the two layers vary together, or *couple*. One prominent example of this coupling is the effect of the stratospheric polar vortices over the zonal flow in the troposphere (Thompson et al., 2005; Domeisen et al., 2019). However, semi-periodic climatic variability in either layer can also have effects over the other layer. The dominant mode of interannual variability in the equatorial stratosphere is such an example and is introduced in the following section.

2.5.1 The Quasi-biennial oscillation (QBO)

The stratospheric quasi-biennial oscillation (QBO) was discovered 60 years ago through balloon observations that revealed that the zonal winds reverse direction in a semi-periodic way with accompanying temperature variations (Ebdon, 1960; Reed, 1964). The QBO has then been characterized by further observations as alternating easterly and westerly wind regimes associated with a descending zonal wind shear from up to 50 km down to 10 km, with a mean oscillatory period of 28 months (Baldwin et al., 2001). The downward propagation of the easterly and westerly wind regimes, amplitude and the mean period have been explained by the interaction of a broad

spectrum of gravity and Kelvin waves of tropospheric origin with the equatorial stratospheric zonal mean flow (Baldwin et al., 2001).

The wind variation in the middle stratosphere associated with the QBO are greater than the seasonal cycle (Andrews et al., 1987) and this vertical wind shear imposes a temperature signal through the thermal wind relationship, which can be expressed as:

$$\frac{\partial u}{\partial z} = \frac{-R}{H\beta} \frac{\partial^2 T}{\partial y^2}, \quad (2.1)$$

where $\partial u / \partial z$ is the vertical shear of the zonal wind, R is the ideal gas constant, y is the latitude, H is a scale height of the atmosphere (7-8 km) and β is the first derivative of the Coriolis term in the meridional coordinate y .

Through this thermal wind relationship a westerly shear would have warm anomalies beneath whereas an easterly shear would impose cold temperature anomalies. In turn, these temperature anomalies couple to the mean meridional circulation (Baldwin et al., 2001) causing an anomaly on this circulation, an effect which is often referred as the secondary circulation of the QBO (Plumb and Bell, 1982; Li et al., 1995; Ribera et al., 2004). This anomalous circulation is characterized by reduced upwelling during westerly shear phases and increased upwelling during the easterly phase. These meridional circulation perturbations adiabatically warm (anomalous descent at the equator) and cool (anomalous ascent) for westerly and easterly shears, respectively, at the equator.

The combination of dynamic and thermodynamic effects of the QBO in the equatorial stratosphere are associated with long-distance impacts across the stratosphere (Holton and Tan, 1980; Lu et al., 2020) and down to the surface (Garfinkel and Hartmann, 2010; Gray et al., 2018). Even though the domain of the QBO is in the tropics, the better recognized effects of the QBO are in the extra tropics, particular how the direction of the zonal mean flow in the equatorial stratosphere modulates the propagation of extratropical waves and therefore also influences the wintertime stratospheric polar vortex (Lu et al., 2020), which can have profound impacts over the surface in polar and midlatitude regions.

The meridional circulation of the QBO and the associated temperature anomaly impact the height and temperature of the tropopause in the tropics (Baldwin et al., 2001; Tegtmeier et al., 2020a,b). The easterly phase of the QBO (QBOE) is associated with a higher and colder tropopause in the tropics whereas the westerly phase (QBOW) is observed with lower and warmer tropical tropopause (Tegtmeier et al., 2020a). These variations in the tropopause characteristics, amongst other effects associated with the QBO, have been hypothesized to affect, to different extents, a range of tropical phenomena, and in particular, deep convective systems.

2.5.2 Tropical teleconnections of the QBO

The influence of the QBO on the dynamic and thermodynamic characteristics of the tropical upper-troposphere-lower stratosphere (UTLS) region has raised interest in possible indirect effects of the QBO over tropical deep convection and clouds. Gray (1984) was amongst the first to suggest an influence of the QBO over tropical systems, in particular, that Atlantic tropical cyclone activity was enhanced during QBOW compared to QBOE. Gray et al. (1992) further argued that the anomalous vertical wind shear associated with the QBO affects the strength of convection in monsoonal and convergence zones to the extent that the vertical wind shear can modify ENSO frequency. Their results suggest that El Niño events are favoured during QBOE and La Niña events are more frequent during QBOW.

The evidence by Gray et al. (1992) has motivated further observational and modelling research on QBO tropical teleconnections; some of this research has contested Gray's results (e.g. Chan, 1995; Camargo and Sobel, 2010; Hansen et al., 2016). For example, Giorgetta et al. (1999) was amongst the first to use a global climate model (ECHAM4) to investigate the effects of the QBO over tropical convection. Giorgetta et al. (1999) focused on the role that the QBO plays in modulating the strength of the East Asian and Indian monsoons. Their findings suggest that monsoon variability was partially modulated by the QBO, with the strongest effects associated with the QBO found for cloudiness at 100 hPa. Giorgetta et al. (1999) argued that these

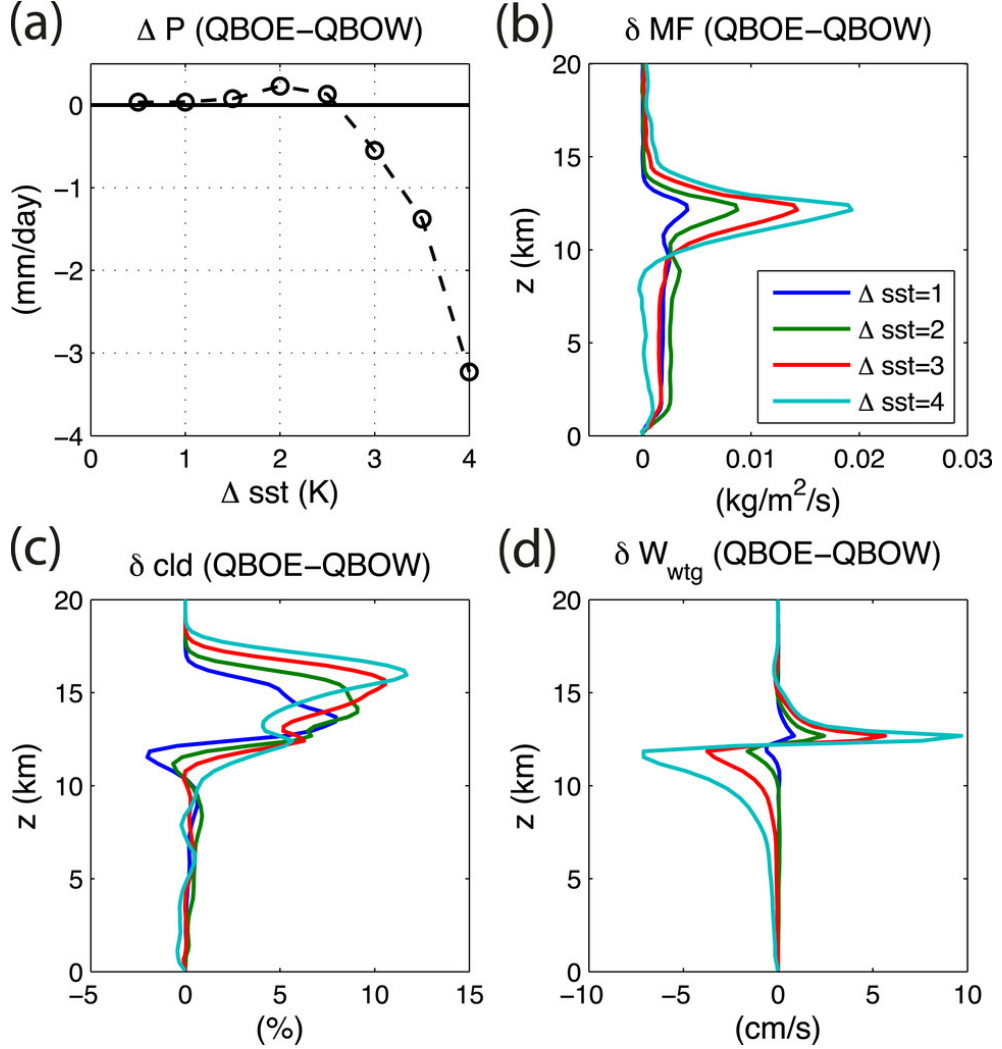


Figure 2.4: (a) QBO anomalous precipitation as a function of SST forcing. The δsst are increments over a baseline of 301 K throughout the whole model domain. (b)–(d) The differences of mass flux in cloud cores, cloud fraction, and the parametrized large-scale vertical velocity derived from the weak temperature gradient approximation, respectively, between experiments with the QBOE and QBOW temperature profiles. Figure 3 from Nie and Sobel (2015).

differences could be explained by the effect of the QBO on the UTLS static stability and a consequent effect over the vertical extent of deep tropical convection.

Further modelling work has been carried out, for instance by Garfinkel and Hartmann (2010) and Garfinkel and Hartmann (2011) that used the Whole Atmosphere Community Climate Model (WACCM) to understand the effect of the QBO over tropical precipitation, the subtropical jets and the wintertime polar vortex. Garfinkel and Hartmann (2010) shows that the canonical ENSO teleconnections to the North

Pacific are stronger during QBO W in WACCM and reanalysis suggesting that the QBO modulates the wave propagation activity associated with ENSO events.

Garfinkel and Hartmann (2011) uses perpetual winter conditions on the WACCM model and further shows that the effect of the QBO on the upper-tropospheric zonal wind in the equator and the strength and location of subtropical jets, particularly at the exit region of the jets. Their experiments show that the QBOE-QBOW zonal wind response in the upper troposphere is zonally asymmetric at the equator but zonally symmetric in the subtropics as the subtropical jet is weakened during QBOE conditions.

The response of convection to the QBO UTLS temperature anomalies was investigated in cloud-resolving model simulations by Nie and Sobel (2015). Their experimental design used the System for Atmospheric Modelling (SAM), varying SST boundary conditions with increments over a baseline SST level of 301 K, the use of the weak-temperature gradient approximation and an idealized vertical temperature profile to simulate the effect of the QBO temperature signal. Figure 2.4 shows that the precipitation and convective features differences between QBO phases depends on the SST forcing.

The precipitation difference QBOE-QBOW is positive under relatively small SST anomalies but in experiments with large SST anomalies this difference becomes negative and overall larger than under small SSTs. The difference in mass flux is also sensitive to the underlying SSTs, as increased mass flux during QBO E is increased for larger SSTs. In other words, the QBO influence on precipitation is non monotonic and largely depends on the underlying SST field.

The cloud fraction in the upper troposphere is increased during QBO E compared to QBO W whereas the ascending motions show peculiar behaviour with stronger ascent above 12 km for QBOE and weaker ascent below 12 km. Their results suggest that the QBO influences convection in two ways that are non-linear and are competing mechanisms. In agreement with previous arguments, Nie and Sobel (2015) finds that the mas flux in the upper troposphere is increased during QBO E but also that this increases the gross moist static stability (GMS) increasing the efficiency of large-scale vertical motions during QBO E for large SSTs, which acts to reduce

precipitation. Secondly, the QBO modifies the fraction of high-level clouds resulting from deep convection which modifies the radiative heating to the column which increases precipitation during QBOE. Figure 2.4a then shows how these competing effects change for different SSTs with the GMS effect dominating for large SSTs.

Various attempts have been made to determine a relationship between the QBO and deep convection in observations. One influential study by Collimore et al. (2003) analysed satellite-derived out-going long-wave radiation (OLR) in the tropics composited by QBO phase. These composites suggest that OLR is significantly different between QBO phases in most monsoon regions, such as Central America and the West Pacific, with an overall indication that convective activity is reduced during QBOW compared to QBOE. This influence, however, was not found to be zonally symmetric and in fact the longitudinal variations of the QBO-related OLR differences were suggestive enough that Collimore et al. (2003) argued for a possible role for the QBO to modulate the Walker circulation, which would explain the lack of zonal symmetry in their results.

Another relevant study by Liess and Geller (2012) found that satellite-derived cloud thickness and frequency and upper-level velocity potential had a significant and longitudinally asymmetric response to the QBO. In particular, their results show increased convective activity during QBOE in the West Pacific but the opposite for the East Pacific. For this reason, Liess and Geller (2012) also argued that the strength of the tropical overturning circulation may be modulated by the QBO, indicating the possible role of both the vertical wind shear and the upper-level static stability to modulate deep convection.

The topic of QBO tropical teleconnections has regained attention due to recent findings suggesting a link between the QBO and the Madden-Julian Oscillation (MJO) (Son et al., 2017) which motivated extensive research (see e.g. Lee and Klingaman, 2018; Wang et al., 2019; Martin et al., 2020) due to the worldwide impact of the MJO. The MJO in observations shows a stronger amplitude and more predictability during QBO E, but further inspection in cloud-permitting and forecast models have not provided conclusive answers to this puzzle (Martin et al., 2019, 2020).

Questions still arise as to whether this tropical link is real or due to chance, for instance Wang et al. (2019) argued that the increased predictability of the MJO under the QBO E phase is included in the initial conditions, and thus not a result of a mechanistic effect of the QBO on the MJO. More generally, whether the QBO has a considerable effect on deep convection in general is debated as several plausible mechanisms exist in the literature (see e.g. Nie and Sobel, 2015) such as the effect of wind shear, the tropopause height, the cold-point temperature, static stability and/or feedbacks with very high cirrus and cumulonimbus clouds.

3

Data and methods

3.1 Observations and reanalysis data

Continuous and reliable observations of Earth's atmosphere and ocean have only been possible in recent decades, due to the advent of satellites. In particular, precipitation analyses have benefited greatly from satellite-derived estimates of precipitation in regions where station-data is non-existent such as oceans. This thesis uses several data sources for precipitation from various gridded precipitation datasets. Several dynamic diagnostics are also used in this thesis, which are taken from the latest reanalysis from the European Centre from European Centre for Medium-Range Weather Forecasts, described below. Table 3.1 summarises relevant information of the observations and reanalysis datasets used in this study.

3.1.1 Gridded precipitation datasets

The Tropical Rainfall Measurement Mission (TRMM) dataset is a multi-satellite multi-sensor infra-red precipitation product that is available on several versions that are made with different algorithms and calibrations with surface rain-gauge data (Huffman et al., 2007). This thesis uses the daily product TRMM version 7 3B42 provided by the Goddard Earth Sciences Data and Information Services Center (Mission, 2011) at https://disc.gsfc.nasa.gov/datasets/TRMM_3B42_7/.

3. Data and methods

Table 3.1: Summary of the datasets used in this study. For each dataset, the acronym used hereafter, the period of coverage, the field used and the horizontal resolution are shown. Some datasets extend further back in time, but only the satellite-era period is used in most of the datasets. The variables used are: precipitation, surface-air temperature ($2mT$), sea-level pressure (SLP), SSTs, the x and y components of the wind (u, v), the lagrangian tendency of air pressure (ω), outgoing longwave radiation (OLR), geopotential height (GPH) and specific humidity (q).

Dataset/ Version	Acronym	Variable	Period	Data type	Resolution	Reference
Global Precipitation Climatology Project v2.3	GPCP	Precipitation	(1979-2018)	Surface and satellite	2.5°x2.5°	(Adler et al., 2003)
Global Precipitation Climatology Centre	GPCC	Precipitation	(1940-2013)	Surface station	0.5°x0.5°	(Becker et al., 2011)
Climate Prediction Center Merged Analysis of Precipitation	CMAP	Precipitation	(1979-2016)	Satellite calibrated with surface rain-gauge	2.5x2.5°	(Xie and Arkin, 1997)
Climatic Research Unit TS v4. Climate Hazards Infrared Precipitation with Stations	CRU4 CHIRPS	Surface temperature Precipitation	(1979-2017) (1981-2018)	Surface rain-gauge and satellite	0.5°x0.5° 0.05°x0.05°	(Harris et al., 2014) (Funk et al., 2015)
Tropical Rainfall Measurement Mission 3B42 V7	TRMM	Precipitation	(1999-2018)	Satellite calibrated with surface station	0.25°x0.25°	(Huffman et al., 2010)
Hadley Centre SST3	HadSST	SST	(1940-2018)	Buoy and satellite	2.5°x2.5°	(Kennedy et al., 2011)
European Centre for Medium-Range Forecasting ERA-5	ERA-5	$2mT$, SLP, u , v , ω , OLR, q , SST, GPH, precipitation	(1979-2018)	Reanalysis	0.75x0.75°	(C3S, 2017; Hersbach et al., 2020)

A set of microwave and infra-red sensors onboard low earth orbit (LEO) satellites, such as the Microwave Imager (TMI) and the Advanced Microwave Scanning Radiometer-Earth Observing System (AMSR-E), provide the main source of information about hydrometeors for TRMM. The microwave sensor data is used to calibrate the infrared data to produce a first estimate of precipitation. However, even using the products of several satellites there is a sparse sampling of time-space precipitation in passive microwave techniques. Therefore, this data is complimented by infrared measurements onboard geosynchronous earth orbit satellites. Other sources of information include a radar onboard TRMM and rain gauge analysis. Details of the research product can be found in Huffman et al. (2007) and Huffman et al. (2010).

The Climate Prediction Center Merged Analysis of Precipitation (CMAP) dataset is a global merged product of satellite and ground based observations but also constrained by a numerical model (Xie et al., 2007). This dataset was first produced at monthly-mean resolution (Xie and Arkin, 1997) but is now available as a collection of products at several temporal scales. The pentad-scale version of CMAP is used in this study.

The Climate Hazards Infrared Precipitation with Stations (CHIRPS) is relatively more recent merged product of precipitation (Funk et al., 2015). This dataset uses high-resolution rain-gauge station data that is complimented by satellite cloud cold duration estimates on regions where station data is sparse. The products are calibrated with TRMM data (Funk et al., 2015), so they are cannot be considered an independent source of information from TRMM.

All these datasets have shortcomings, advantages and unceratainties in their representation of precipitation. The algorithm of merged products such as TRMM to combine different satellite sensors and calibration techniques as well as surface station rain-gauge data results in products that may have shortcomings to accurately depict extreme events (Trejo et al., 2016), As the source data of most of these datasets is shared, the datasets cannot be considered to be fully independent sources of information.

The TRMM dataset has a high horizontal and temporal resolution and was used in several CMIP assessments (Geil et al., 2013; Jones and Carvalho, 2013) as a reliable source of precipitation (Carvalho et al., 2012). Therefore, TRMM is used in this thesis

as the best estimate for the spatial and temporal characteristics of rainfall. However, the period covered by TRMM (1998-2018) is too short to analyse statistically robust teleconnections or variability, so GPCP, GPCC and CHIRPS are used to evaluate longer term variability for their longer period. Although a thorough validation and comparison of these datasets across the AMS domain is missing, several studies have analysed one or more of these datasets in regions of the AMS (e.g. Franchito et al., 2009; Dinku et al., 2010; Trejo et al., 2016).

3.1.2 ERA-5

A reanalysis is a numerical description of the state of the atmosphere in a global or regional scale of full of diagnostics in a gridded product that is available at multiple vertical levels, in other words "maps without gaps" (Hersbach et al., 2020). A reanalysis takes a set of physically consistent blend of observations that are then used to run the forecasting model. Reanalysis are key tools for climate and weather research as they provide full pictures of the atmospheric state for long periods, a feature that could not be possible with our current purely observational tools. For this reason, reanalyses are typically used to validate GCM output.

The latest reanalysis from ECMWF, the fifth generation of their reanalysis, is called ERA5. ERA5 uses the Integrated Forecasting System (IFS) model and a 4D variational data assimilation system (4D-Var), a larger number of data sources for assimilation and also provides output on higher horizontal resolution (Hersbach et al., 2020). The output is available on hourly to monthly-mean frequencies, from 1000 hPa to 0.1 hPa in the vertical and with horizontal resolutions as high as 0.25° . In this thesis, the resolution of all ERA5 data, unless otherwise stated is of 0.75° and all data was downloaded from the Climate Store at <https://climate.copernicus.eu/climate-reanalysis>.

ERA5 presents a notable improvement in the representation of the water cycle, by increasing the mean correlation to precipitation datasets such as GPCP. ERA5, as all reanalysis, resolves precipitation rates in the driving physical model using the convective scheme and parametrisation. However, this reanalysis also assimilates radiances from several satellite instruments such as Global precipitation monitoring

mission Microwave Imager, TMI and ASMR-2 Hersbach et al. (2020). This assimilation of satellite data has improved the representation of the water cycle in ERA5 compared to older reanalysis such as ERA-interim (e.g. Hénin et al., 2018). These improvements are also due to changes to the parametrisations of the microphysics of clouds and rain (Forbes and Ahlgrimm, 2014) and the diurnal cycle of convection (Bechtold et al., 2014).

3.2 The Unified Model of the Met Office Hadley Centre

The UK Met Office Hadley Centre (MOHC) released the first version of the Hadley Centre Global Environmental Model (HadGEM1) in 2006 (Johns et al., 2006), and has since continuously updated the HadGEM model and submitted experiments from the model to the various phases of the Coupled Model Intercomparison Project (CMIP), which is the backbone of the Intergovernmental Panel on Climate Change (IPCC) reports. This section first describes the third generation of the HadGEM model and subsequently describes the experiments from these versions of the model submitted for CMIP6.

3.2.1 The Global Coupled Configurations of HadGEM3

The MOHC Unified Model (UM) is a weather and climate global model that is based on a seamless modelling approach, which means that the UM consists of a dynamical core and parametrization schemes that can be used across a wide range of temporal and spatial scales. The UM version that was used for CMIP6 experiments and is used throughout this thesis employs the Global Coupled (GC) configuration 3.1 (GC3.1) (Williams et al., 2018; Walters et al., 2019) which in turn is composed of the components: Global Atmosphere 7.0 (GA7.0), Global Land 7.0 (GL7.0), Global Ocean 6.0 (GO6.0), and Global Sea Ice 8.0 (GSI8.0). The GC3.1 configuration runs with 85 atmospheric levels, 4 soil levels and 75 ocean levels and can be run with atmospheric horizontal resolutions ranging from 10 - 135 km (at the midlatitudes)

with varying resolutions for the ocean component as well. The model top of GC3.1 is 85 km above sea level (Walters et al., 2019).

The GA7.0 configuration, described in Walters et al. (2019), built on previous configurations principally by updating a number of parametrisation schemes including the rain and ice-cloud treatment as well as the convection scheme. Four critical errors were pinpointed and tackled by GA7.0 which include rainfall deficits in the Indian monsoon, temperature and humidity biases in the tropopause layer, deficiencies in numerical conservation and surface flux biases over the Southern Ocean. The GO6.0 configuration (Storkey et al., 2018) is in turn based on the NEMO ocean model code (version 3.6) and is responsible for determining the sea-ice extent, the ocean mixed-layer depth and deep water formation, amongst other key ocean processes.

In most GCMs, precipitation is a result of two simulated processes. First, precipitation due to grid-scale processes referred to as large-scale precipitation, is estimated by the microphysics, or cloud scheme, that evaluates the cloud fraction and saturation within the grid-box column where precipitation occurs by processes such as warm rain (Walters et al., 2019). The second process that simulates precipitation is associated with convection of varying depths and is considered a sub-grid process calculated by the convection scheme. In GC3.1 the convective scheme follows three stages, according to Walters et al. (2019), first a diagnosis of the boundary layer to establish whether convection should occur at a given time-step and separately diagnosis shallow or deep convection, second, the shallow or deep convection schemes are called and third, a call for mid-level convection.

In other words, the convective scheme first decides whether the thermodynamic profile at each grid-point fits certain parameters that measure the buoyancy of the parcels and vertical velocity profile, which then separates areas of deep and shallow convection. After these routines, the model implements the mid-level convection scheme to remove instabilities from above the shallow convective regions or below the deep convective regions. The closure of the deep convective scheme follows the convective available potential energy (CAPE) closure of Fritsch and Chappell (1980) which regulates the amount, strength and duration of convection based on availability

of buoyant energy. In addition, the scheme couples the detrainment rates of plumes to the column relative humidity and buoyancy as described in Derbyshire et al. (2011). Further details of the GC3 configuration including model description and biases can be found in Williams et al. (2018) and Kuhlbrodt et al. (2018).

3.2.2 The CMIP6 experiments

The MOHC submitted output from several experiments to various projects part of CMIP6 using different variations of the GC3.1 configuration, i.e., varying horizontal resolution and varying representation of processes. The main model, HadGEM3 GC3.1 (hereafter GC3) is the latest version of the HadGEM model, and was run at two horizontal resolutions for CMIP6: a low resolution configuration, labelled as N96, with an atmospheric resolution of $1.875^\circ \times 1.25^\circ$ and a 1° resolution in the ocean model and a medium resolution configuration, labelled N216, with atmospheric resolutions of $0.83^\circ \times 0.56^\circ$ and a 0.25° oceanic resolution (Menary et al., 2018).

The dynamical core the GC3.1 configuration, the core of the GC3 submissions to CMIP6, was used to build a slightly different model, one that aims to better capture ocean-biogeochemical, air-soil and air-chemistry interactions, the UKESM1. The UKESM1 was recently developed aiming to improve the UM climate model adding processes of the Earth System (Sellal et al., 2019). These additional components include ocean biogeochemistry with coupled chemical cycles, tropospheric-stratospheric interactive chemistry which aim to better characterise aerosol-cloud and aerosol-radiation interactions (Mulcahy et al., 2018; Sellal et al., 2019). The physical atmosphere-land-ocean-sea-ice core of the HadGEM3 GC3.1 underpins the UKESM1, so that the UKESM1 and the HadGEM3 have the same dynamical core but the UKESM1 has the additional components mentioned above.

This study uses output from several CMIP6 experiments, which are outlined in Table 3.2. First, the pre-industrial control (piControl) simulations, which are run with constant climate forcing that represents the best estimate for pre-industrial (1850) forcing of aerosols and greenhouse gas levels. Second, historical experiments are 164-yr integrations for 1850-2014 that include historical forcings of aerosol, greenhouse

3. Data and methods

Table 3.2: Summary of the CMIP6 simulations in this study. For each simulation the acronym used hereafter, the experiment and the horizontal resolution are shown. The first 100 years of the piControl simulations are used and for historical experiments the period 1979-2014 is used.

Model	Experiment	Period	Atmospheric (Ocean) resolution	Acronym	Ensemble members	Reference
Hadley Centre Global Environment Model version 3 (HadGEM3)	Pre-industrial control	1850-2350	N96 1.875°x1.25° (1°)	GC3 N96-pi	1	(Menary et al., 2018; Ridley et al., 2018)
HadGEM3	Pre-industrial control	1850-2000	N216 0.83°x0.56° (0.25°)	GC3 N216-pi	1	(Menary et al., 2018; Ridley et al., 2019c)
HadGEM3	Historical	1979-2014	N96 1.875°x1.25° (1°)	GC3-hist	4(r1-r4)	(Andrews et al., 2020; Ridley et al., 2019b)
HadGEM3	Historical	1979-2014	N216 0.83°x0.56° (0.25°)	N216-hist	1	(Ridley et al., 2019c)
HadGEM3	Atmospheric Model Intercomparison (AMIP)	1979-2014	N96 1.875°x1.25° (1°)	GC3-amip	5 (r1-r5)	(Ridley et al., 2019a)
United Kingdom Earth System Model version 1 (UKESM1)	Pre-industrial control	2060-2600	N96 1.875°x1.25° (1°)	UKESM-pi	1	(Tang et al., 2019b)
UKESM1	Historical	1979-2014	N96 1.875°x1.25° (1°)	UKESM-hist	5 (r1-r5)	(Tang et al., 2019a)

gas, volcanic and solar signals since 1850 (Eyring et al., 2016; Andrews et al., 2019). The historical experiments of HadGEM3 and UKESM1 are composed of 4 and 9 ensemble members, respectively, but the results will be presented as the ensemble mean for the 1979-2014 period. These experiments will be referred to as GC3-hist and UKESM1-hist hereafter. For further details, Andrews et al. (2020) extensively describes the historical simulations of HadGEM3-GC3.1.

In contrast to the pre-industrial control experiments, the historical experiments use time-varying aerosol and greenhouse gas emissions and land-use change (Eyring et al., 2016). In Latin-America, land-use change for agricultural purposes has dramatically decreased tree cover in Central America and south-eastern Brazil since the 1950s (Lawrence et al., 2012), thereby affecting the surface energy balance. The regional emissions of carbonaceous aerosols, nitrogen oxides and volatile organic compound in Latin America are also considered in the historical experiments. These emissions are noteworthy, e.g., due to the impact of black carbon emissions by increased biomass burning in the Amazon and northern Central America (Chuvieco et al., 2008).

The Atmosphere Model Intercomparison Project (AMIP) is a CMIP project that uses atmosphere-only (AO) simulations of the climate to understand the role of SST biases, variability and forcing climate signals. The standard AMIP experiment covers the period 1979-2014 and uses the observed SST fields in this period to drive the models with the same forcing as the historical simulations. Other AMIP experiments may use model-driven SSTs of other experiments to disentangle other processes. This thesis uses the five ensemble members of the AMIP experiment from GC3.

3.3 The Moist Static Energy Budget

The moist static energy (MSE) is a key measure of the energy within moist parcel and the analysis of MSE budgets has proven useful in the context of ENSO (e.g. Annamalai, 2020), tropical cyclones (e.g. Wing et al., 2019), axi-symmetric monsoons (e.g. Bordoni and Schneider, 2008) and regional monsoons (e.g. Smyth et al., 2018; Ma et al., 2019). The MSE arises from the first law of thermodynamics which decomposes

the internal energy of a system into two components: one associated with heat in or out of the system and the second component associated with work done by the system.

From the preferred version of the first law of thermodynamics, the changes to several other quantities, known as state variables, can be traced. The MSE, also denoted as h is given by:

$$h = L * q + C_p T + gz = Lq + s \quad (3.1)$$

where C_p is the heat capacity at constant pressure, T is the air temperature, L is the latent heat of vaporization, q is the specific humidity and s is the dry static energy. Equation 3.1 separates the total moist energy of a parcel into a dry component also referred as dry-air enthalpy or heat content (Emanuel, 2007), and the last term is the potential energy associated with the gravitational acceleration. The MSE is conserved under pseudo-adiabatic processes and thus is considered to be a key variable of a moist system, a state variable that is not created or destroyed by convection but rather re-distributed by the coupling of convection with the large-scale circulation (Chou and Neelin, 2004; Emanuel, 2007).

The material derivative of the MSE can therefore be written as:

$$\frac{Dh}{dt} = \frac{\partial h}{\partial t} + \nabla \cdot \vec{u} h_p + \frac{\partial p}{\partial t} \frac{\partial h}{\partial p} \quad (3.2)$$

where \vec{u} is the horizontal wind vector, p is the air pressure used as a vertical coordinate so that $\partial p / \partial t = \omega$. The vertically integrated budget equation arises by rearranging and integrating equation 3.2 in the pressure coordinate which, following Annamalai (2020), leads to:

$$\left\langle \frac{dh}{dt} \right\rangle = - \left\langle \vec{u} \cdot \nabla h_p \right\rangle - \left\langle \omega \frac{\partial h}{\partial p} \right\rangle + F, \quad (3.3)$$

where the angle brackets $\langle \rangle$ denote vertical integrals from the surface pressure level until the 100 hPa level, i.e.:

$$\langle \rangle = \int_{p_0}^{100} dp, \quad (3.4)$$

and the term F denotes the net forcing of MSE which is given by the surface fluxes and the radiative heating of the column:

$$F = LH + SH + \langle LW \rangle + \langle SW \rangle \quad (3.5)$$

where SH and LH are the surface turbulent sensible and latent heat fluxes, respectively, and LW and SW are the column heating rates from longwave and shortwave radiation, respectively.

4

The American monsoon system in UKESM1 and HadGEM3

This chapter evaluates the representation of the AMS in the contributions to CMIP6 from UKESM1 and HadGEM3. The pre-industrial control, historical and AMIP experiments described in section 3.2 are evaluated for their large and regional-scale biases, as well as their representation of key teleconnection patterns. The simulations show a good representation of the seasonal cycle of temperature, although the historical experiments overestimate the observed summer temperature in the Amazon, Mexico and Central America by more than 1.5 K. The seasonal cycle of rainfall and general characteristics of the North American Monsoon in all the simulations agree well with observations, suggesting a notable improvement from previous versions of the HadGEM model. The models reasonably simulate the bimodal regime of precipitation in southern Mexico, Central America and the Caribbean known as the midsummer drought, although with a stronger than observed difference between the two peaks of precipitation and the dry period. Austral summer biases in the modelled Atlantic Intertropical Convergence Zone (ITCZ), cloud cover and regional temperature patterns are noteworthy and influence the simulated regional rainfall in the South American Monsoon. These biases are associated with an overestimation of precipitation in southeastern Brazil and an underestimation of precipitation in the Amazon which are

greatly reduced in the AMIP simulations, highlighting that an accurate simulation of the Atlantic SSTs is key for representing precipitation in the South American Monsoon. El Niño Southern Oscillation (ENSO) teleconnections, of precipitation and temperature, to the AMS are reasonably simulated by all the experiments. The precipitation responses to the positive and negative phase of ENSO in subtropical America are linear in both pre-industrial and historical experiments, in contrast to observations. Overall, the biases in UKESM1 and the low resolution configuration of GC3 are very similar for precipitation, ITCZs and the Walker circulation, i.e., the inclusion of Earth System processes appears to make no significant difference for the representation of the AMS rainfall. In contrast, the medium resolution HadGEM3 N216 simulation outperforms the low-resolution simulations due to improved SSTs and circulation.

4.1 Introduction

The response of regional monsoons to greenhouse forcing remains an open question (Zhou et al., 2016; Pascale et al., 2019) because the observational record is too short to exhibit significant trends but also because biases in GCMs increase uncertainty in future model projections. Although the thermodynamical response to greenhouse forcing in tropics seems to be relatively well constrained, the dynamical response is less clear (Shepherd, 2014). The American Monsoon System (AMS), as most monsoon regions is shaped by regional dynamical features which makes the dynamical biases particularly relevant when understanding the precipitation response to forcing in a monsoon region.

In spite of current recognition as a monsoon, the AMS has received less attention by the modelling community compared to the Asian or African monsoons. The assessment of climate models in monsoon regions is key to understand current and future changes to the water cycle in tropics. However, in the AMS, model assessments are usually only done in a handful of studies per CMIP phase. These studies only provide a wide view of the biases of each generation of models while usually highlighting which biases have improved and which biases remain from previous model generations (see e.g. Geil et al., 2013; Ryu and Hayhoe, 2014). However, a deeper evaluation of individual

models can be used to provide better insight into the processes associated with climatological biases in the large-scale circulation and ultimately better understand the causes for the model biases in AMS rainfall.

For example, in the South American Monsoon, CMIP5 models improved from CMIP3 in the simulated distribution of precipitation during monsoon maturity and exhibited an improved seasonal cycle (Jones and Carvalho, 2013; Yin et al., 2013). However, biases in the South American Monsoon, e.g., the underestimation of rainfall in the central Amazon, have persisted from the first generation of GCMs up until CMIP5 (Li et al., 2006; Yin et al., 2013). The geographic distribution of rainfall during austral fall and several characteristics of the South Atlantic Convergence Zone are also poorly represented in CMIP5. However, these studies provided little evidence as for the reasons for the improvements or the remaining biases in the models. A clear motivation to evaluate models in the South American Monsoon is that the accurate simulation of the geographic distribution and seasonality of rainfall in the Amazon rainforest is a relevant issue due to the impact of the rainforest on climate and society (e.g. Li et al., 2006; Malhi et al., 2009; Yin et al., 2013) and thus more research on the representation of the South American Monsoon is warranted.

Climate research in recent decades has aimed to reduce uncertainty in climate projections by improving GCMs, but different approaches taken by modelling centres are seemingly disconnected (Jakob, 2014). One approach is to reduce horizontal grid spacing down to km resolution to rely less on parametrizations and more on physical laws to represent clouds and convection (Palmer and Stevens, 2019). A second approach aims to include new explicit representation of Earth System processes to better characterise complex land-atmosphere-ocean biogeochemical cycles that may provide a better constraint on large-scale aspects of the climate such as climate sensitivity, a parameter that depends on the carbon cycle (Marotzke et al., 2017; Sellar et al., 2019; Andrews et al., 2019). Finally, recent modelling centres have chosen to include stochastic parametrisations of sub-grid processes since this approach has improved seasonal forecasts and may therefore improve climate projections (Palmer, 2019).

Model validation and assessment is important to analyse the effect of new parametrisations and to highlight missing processes but also evaluate which route provides the more substantial model improvement, stochastic parametrisations, increased resolution or Earth System processes. The focus of this chapter is then to evaluate the CMIP6 experiments from HadGEM3 GC3.1 (GC3) and UKESM1 in the AMS. In this chapter and remainder of the thesis, the AMS is considered to be composed of the North and South American monsoon systems, while also including the Midsummer drought region of southern Mexico and Central America as part of the AMS (as in e.g. Vera et al., 2006; Pascale et al., 2019).

The remainder of this chapter is organised as follows. The following section described the data and methods used in this chapter. Section 4.3 compares modelled and observed climatological temperature, sea-level pressure and low-level wind fields, whereas section 4.4 analyses the Pacific and Atlantic ITCZs. Section 4.5 analyses the spatial and temporal characteristics of rainfall and convection in the AMS while section 4.6 documents the simulated teleconnections of ENSO. A summary and discussion of the results is provided at the end of the chapter.

4.2 Methods and data

The model assessment of this chapter will use a range of experiments from the MOHC. The piControl experiments from GC3 and GC3 N216 are used to evaluate the role of resolution whereas the historical experiments from UKESM1 and GC3 are used to evaluate model skill in reproducing the observed period whereas the AMIP experiment from GC3 is used to highlight the role of SST biases. The historical experiment data is used only in the 1970-2014 period whereas the whole pre-industrial and AMIP available data is used. All the datasets used in this chapter are thoroughly described in chapter 3 but in summary in this chapter, the surface or near-surface air temperature data is taken from the CRU4 dataset and ERA5, whereas precipitation is used from the different datasets described in the previous chapter. The dynamical features such as wind speed and vertical velocity are taken from ERA5.

The climate indices of ENSO and the QBO used in this chapter were obtained by the following process. For ENSO, the deseasonalized and detrended time-series of the area-averaged SSTs (EN3.4 region [190-240°W, 5°S-5°N]) is used as an index to composite months into positive, negative and neutral phases. A month is determined to be in the positive, El Niño, phase when the index is higher than +0.65 K and a negative phase, La Niña, when the index is more negative than -0.65 K. A neutral month is found where the magnitude of the index is smaller than 0.5 K. Other indices, including the use of a 5-month running mean (Trenberth et al., 1998), were tested without significantly changing the results. Previous studies (e.g. Menary et al., 2018; Kuhlbrodt et al., 2018) showed that the MOHC models reasonably simulate several characteristics of ENSO such as the period and SST patterns.

Similarly, for the QBO, the deseasonalized and detrended time-series of the equatorially averaged [10°S-10°N] zonal-mean zonal wind at the 70 hPa level is used as the QBO index for both reanalysis and model data. The westerly phase of the QBO (QBOw) is determined when the index is greater than 2 m s^{-1} and the easterly phase (QBOe) when the index is less than -2 m s^{-1} .

4.3 Climatological temperature and low-level wind biases

This section evaluates the simulated climatological temperature and low-level wind structure in the AMS region. The climatological representation of the near-surface air temperature and low-level winds in the models is compared to ERA5 in Figures 4.1 and 4.2, the climatology of DJF and JJA of ERA5 is shown in Figure 4.1a, b. The biases of the historical experiments, computed as the differences between the model and observed fields, are shown in Figures 4.1c, d) for GC3-hist and e, f) for UKESM1-hist. Only statistically significant differences are shown, according to a Welch t-test (Wilks, 2011), which accounts for the difference in sample size and variance between model and observations/reanalysis data. The significance for simulations with multiple ensemble members is estimated first for each ensemble member and then combined into a single

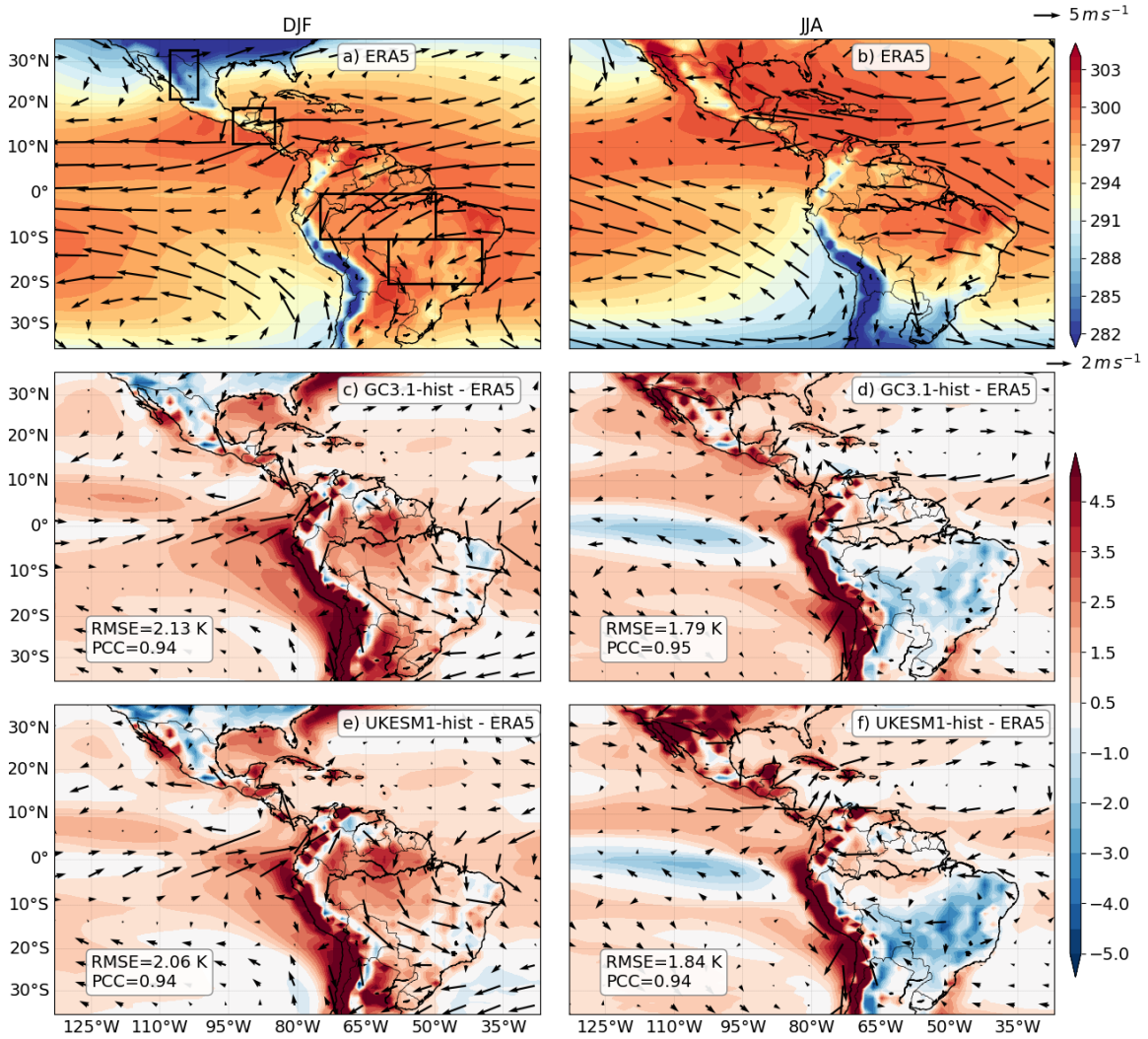


Figure 4.1: (a, b) Temperature (color-contours in K) and wind speed (vectors) at 850 hPa DJF and JJA climatogies in ERA5. The biases are shown as the differences between the ensemble mean from the historical experiment of (c, d) GC3 and (e, f) UKESM1 and ERA5. The climatogies and biases are shown for (a, c, e) boreal winter (DJF) and (b, d, f) boreal summer (JJA). Only differences statistically significant to the 95% level are shown, according to a Welch t-test for each field. The key for the size of the wind vectors is shown in the top right corner of panels b) and d). The root-mean square error (RMSE) and pattern correlation coefficient (PCC) are shown on the bottom left of c-f.

probability or p-value using Fisher's method (Fisher, 1992). Pattern correlations and root-mean square error (RMSE) are shown in Figures 4.1c-f and in Table 4.1.

During DJF, the simulations show a colder-than-observed sub-tropical North America and a warm bias over the Amazon ($\approx +3.5$ K). The west coast of South America also shows a significant warm bias ($> +4$ K) in the historical simulations.

Table 4.1: Root-mean square error (RMSE) and pattern correlation coefficients (PCC) for each season and each model experiment. Near surface air temperature ($t2m$), wind components (u and v) and mean-sea level pressure ($mslp$) are assessed against ERA-5 and precipitation (pr) against TRMM.

Variable	Experiment	DJF	DJF	MAM	MAM	JJA	JJA	SON	SON
		RMSE	PCC	RMSE	PCC	RMSE	PCC	RMSE	PCC
t2m	GC3 N96	1.28	0.98	1.3	0.96	1.38	0.96	1.31	0.96
t2m	GC3 N216	1.05	0.99	1.07	0.98	1.02	0.98	0.98	0.98
t2m	GC3 Hist	2.06	0.94	1.75	0.93	1.73	0.94	2.05	0.92
t2m	UKESM-hist	2.03	0.94	1.77	0.93	1.8	0.94	2.0	0.93
t2m	GC3 AMIP	1.17	0.98	1.12	0.97	1.2	0.97	1.2	0.97
u	GC3 N96	0.78	0.99	0.59	0.99	0.9	0.98	0.87	0.98
u	GC3 N216	0.78	0.99	0.59	0.99	0.9	0.98	0.87	0.98
u	GC3 Hist	1.02	0.98	1.04	0.97	0.92	0.98	0.84	0.98
u	UKESM-hist	1.04	0.98	1.01	0.97	0.91	0.98	0.82	0.98
u	GC3 AMIP	0.96	0.98	0.77	0.99	1.18	0.97	1.09	0.96
v	GC3 N96	0.75	0.93	0.66	0.93	0.65	0.95	0.59	0.94
v	GC3 N216	0.6	0.96	0.5	0.95	0.57	0.96	0.54	0.94
v	GC3 Hist	0.76	0.94	0.72	0.92	0.66	0.95	0.59	0.94
v	UKESM-hist	0.75	0.93	0.69	0.92	0.65	0.95	0.6	0.93
v	GC3 AMIP	0.67	0.95	0.52	0.95	0.68	0.94	0.61	0.93
mslp	GC3 N96	1.33	0.96	1.03	0.97	1.15	0.96	0.95	0.97
mslp	GC3 N216	1.11	0.97	0.9	0.97	1.1	0.96	0.89	0.97
mslp	GC3 Hist	1.31	0.97	1.12	0.96	1.08	0.96	0.94	0.97
mslp	UKESM-hist	1.4	0.97	1.15	0.96	1.14	0.95	0.99	0.97
mslp	GC3 AMIP	1.15	0.97	0.87	0.97	1.09	0.96	0.93	0.97
pr	GC3 N96	2.02	0.79	2.24	0.71	1.62	0.9	1.69	0.86
pr	GC3 N216	1.58	0.88	1.72	0.85	1.4	0.93	1.57	0.89
pr	GC3 Hist	2.05	0.78	2.49	0.64	1.69	0.88	1.69	0.86
pr	UKESM-hist	1.96	0.8	2.39	0.66	1.71	0.88	1.62	0.87
pr	GC3 AMIP	1.42	0.9	1.61	0.88	1.95	0.88	1.8	0.88

The simulated circulation in austral summer in South America has a significant bias in the easterly flow coming from the equatorial and subtropical Atlantic. The low-level wind biases suggest a weaker easterly flow from the Atlantic into southeastern Brazil but also a strong southward flow from northern to southern South America. The South America Low-Level Jet, i.e., the low-level northwesterly flow in Bolivia, observed in Figure 1a, is stronger in the simulations. This stronger than observed jet is suggestive of a stronger moisture transport to the La Plata Basin, which has been associated with a drying of the Amazon and positive precipitation anomalies at the exit region of the jet (Marengo et al., 2012; Jones and Carvalho, 2018).

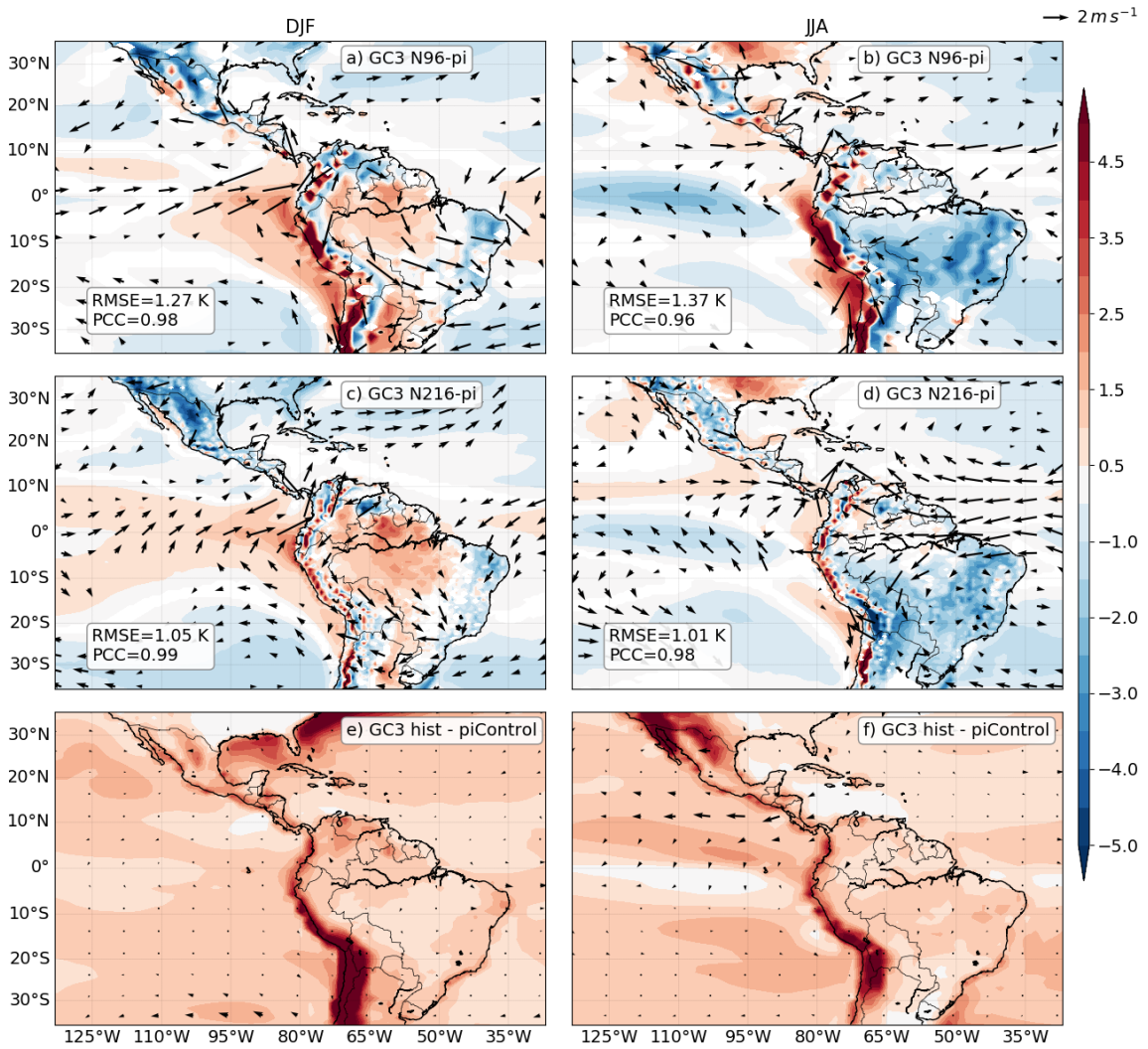


Figure 4.2: As in Figure 4.1, but showing the differences between the piControl simulations of (a, b) GC3 N96-pi and (c, d) GC3 N216-pi, and ERA5. (e, f) show the statistically significant differences between the historical (1979-2014) and piControl experiments of GC3. The RMSE and PCC are shown on the bottom left of a-d.

In turn, in boreal summer (Figures 4.1d, f), positive temperature biases are observed in southwestern North America ($> +3.5$ K), which are higher in UKESM1-hist than in GC3-hist. The easterly flow west of Central America has a negative bias in UKESM1 suggesting a weaker flow that crosses from the Caribbean Sea into the East Pacific Ocean. Also in JJA, the simulated East Pacific surface temperatures are colder than observed for both historical experiments. The inclusion of Earth System processes appears to make no improvement on the low-level circulation biases.

The piControl simulations (Figures 4.2a-d) have some similar biases to the historical simulations. In DJF, the piControl simulations show a similar but smaller positive bias in the Amazon than the historical experiments, as well as a similar bias in the circulation in South America, with the smallest biases in GC3 N216 piControl. In JJA, the piControl simulations do not show the positive temperature bias in northwestern North America. However, the bias in the zonal wind over the easternmost Pacific is present in both piControl and historical simulations.

Figures 4.2e, f show the difference between the historical and piControl experiment of GC3, illustrating the response to historical forcing in GC3. The temperature response in austral summer in South America is observed as 1.5 K whereas in JJA in North America temperatures were 4 K higher in the historical experiment than in the piControl. A very similar temperature pattern response to historical forcing was observed for UKESM1 (not shown) although of slightly different magnitude. The only significant difference in low-level winds, as a response to historical forcing, are the easterlies in the East Pacific Ocean during JJA, which are stronger in the historical simulation.

The seasonal cycle of temperature in key regions (depicted in Figure 4.1a) of the AMS is shown in Figure 4.3, comparing the simulations to ERA5 and the CRU4 dataset. The temperature in the North American Monsoon region ranges from the boreal winter mean temperature of 12°C to a maximum in June close to 27°C. Although the piControl simulated temperatures are colder than observed throughout the year, the models reasonably reproduce the seasonal cycle, which may be relevant for the simulated monsoon onset timing and strength (Turrent and Cavazos, 2009). The historical experiments notably show a colder than observed winter and a warmer than observed summer.

The piControl simulations show a colder-than-observed winter in southern Mexico and northern Central America. The historical experiments show a warming signal, when compared to the piControl simulations, of about 1.5 K in winter and 2 K in the summer in this region. In spite of these biases, all the experiments follow closely the seasonal cycle in North and Central America.

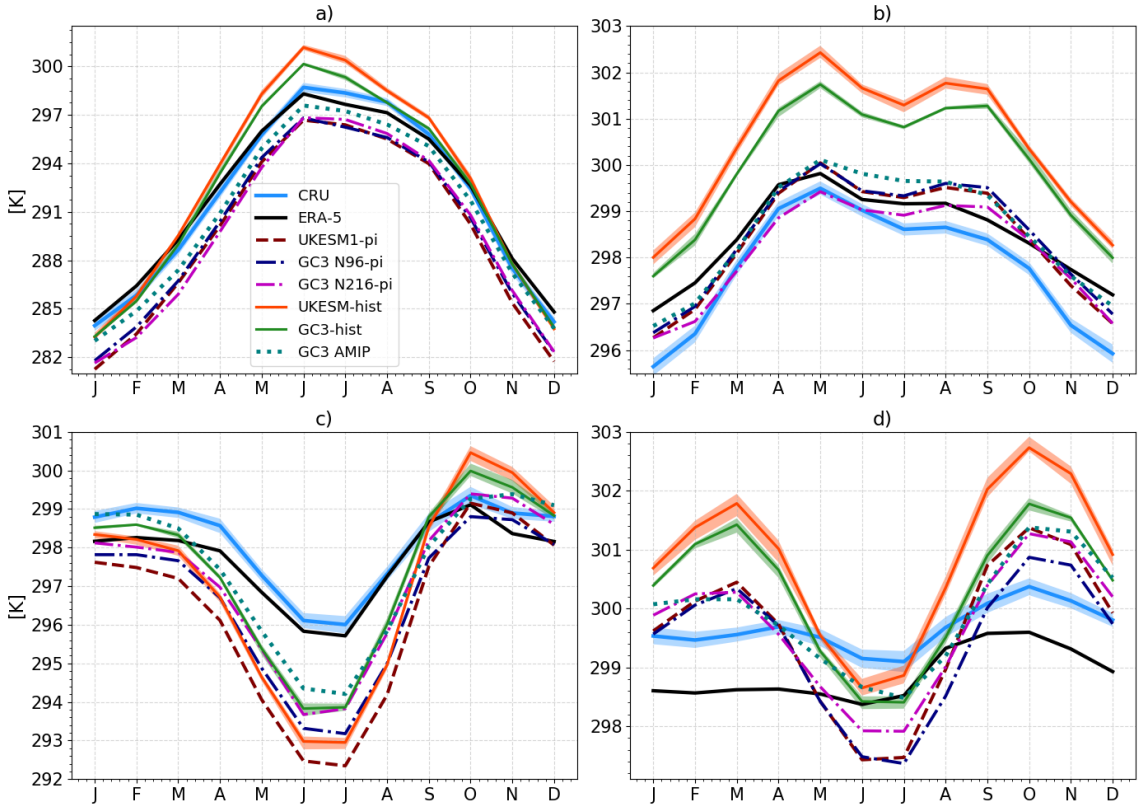


Figure 4.3: Monthly-mean temperature in the (a) North American Monsoon [$19\text{--}35^{\circ}\text{N}, 110\text{--}103^{\circ}\text{W}$], (b) the Midsummer drought [$11\text{--}19^{\circ}\text{N}, 95\text{--}85^{\circ}\text{W}$] (c) Eastern Brazil [$20\text{--}10^{\circ}\text{S}, 60\text{--}40^{\circ}\text{W}$] and (d) the Amazon basin [$-10\text{--}0^{\circ}\text{S}, 75\text{--}50^{\circ}\text{W}$] regions. The shadings for the CRU dataset represents the observational uncertainties and for the historical simulations the shading is the ensemble spread. The regions for this plot are shown in Figure 4.1a.

However, the seasonal cycle in South American regions (Figures 4.3 c, d) of southeastern Brazil and the central Amazon shows notable temperature biases. The simulations show a stronger than observed seasonal cycle, especially the historical experiments. For example, the modelled temperature difference between late austral winter and spring was ≈ 4 K whereas the observed temperature varies by less than 1 K in the same period. The models show a warm bias in the Amazon region (Fig. 4.3 d) which peaks in austral spring (SON), during the development of the monsoon (Marengo et al., 2012). In southeastern Brazil, the seasonal cycle is reasonably well reproduced but with a significant cold bias throughout the year which maximizes during austral winter (JJA), as models (e.g. UKESM1) simulate a temperature 4 K lower than observed. In all panels of Figure 4.3, the historical experiments show

a significant warming signal as a response to historical forcing, which is generally stronger in UKESM1 than in GC3.

4.4 The Atlantic and Pacific ITCZs and the SACZ

The AMS is intertwined with the seasonal migration of the East Pacific and Atlantic ITCZ as the ITCZ largely determines regions of ascending and descending motions, moisture transport and the hemispheric energy balance (Oueslati and Bellon, 2013; Li and Xie, 2014; Zhou et al., 2016; Cai et al., 2019). In particular, the North American monsoon and MSD are mostly influenced by the East Pacific ITCZ whereas the South American monsoon is affected by the strength and position of the Atlantic ITCZ (Yoon and Zeng, 2010; Marengo et al., 2012).

Figure 4.4 shows the observed and modelled climatological rainfall and the ITCZ climatological positions. Three simulations are shown: the ensemble-mean UKESM1-historical, the ensemble mean GC3 AMIP and GC3 N216-pi. Other simulations are not shown as all the coupled low resolution simulations showed very similar precipitation and ITCZ characteristics whereas the AMIP and medium-resolution experiments showed notable differences.

The climatological ITCZ in TRMM (Figure 4.4a) is found, on average, at 8°N in the East Pacific and at 6°N in the Atlantic. All the simulations reasonably represent the climatological position of the East Pacific (EP) ITCZ; however, the modelled Atlantic ITCZ near the coast of Brazil is found south of the equator at 3°S in the coupled model simulations. The location of the ITCZ in GC3 N216-pi and the spatial distribution of rainfall is more consistent with TRMM dataset than the rest of experiments. Rainfall near the Amazon river mouth is significantly larger in the low resolution simulations than in the TRMM dataset. However, the GC3 AMIP shows the best agreement with TRMM in ITCZ position and rainfall distribution.

The seasonal cycle of the ITCZ location, precipitation rates and low-level winds in both basins are shown in Figure 4.5, for TRMM, UKESM1-hist, GC3 AMIP, GC3 N96-pi and GC3 N216-pi. The EP ITCZ in observations (Fig. 4.5a) migrates southwards

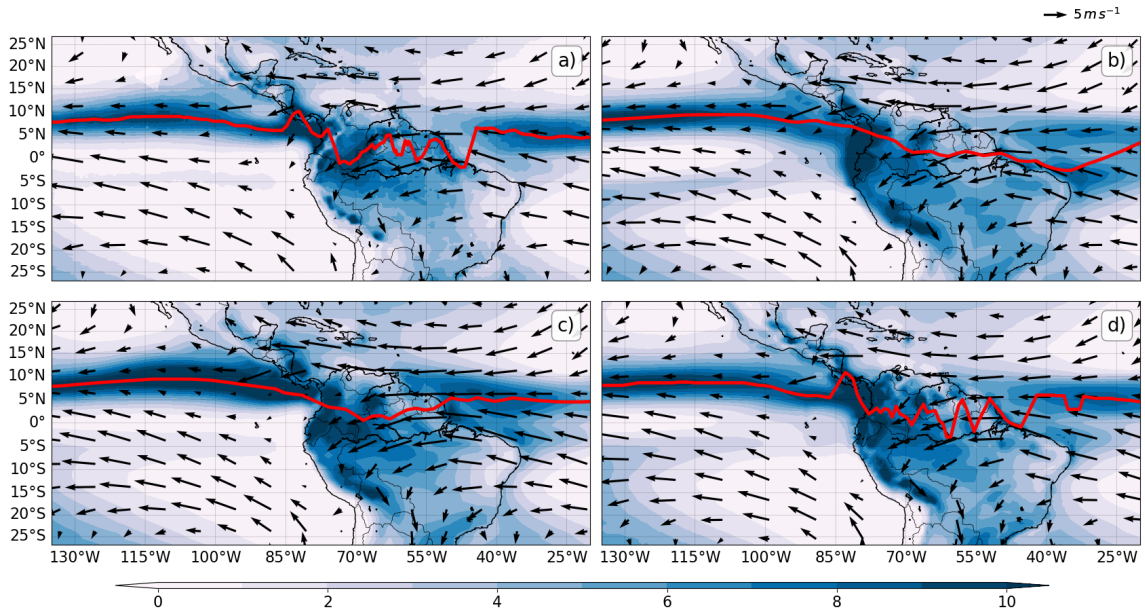


Figure 4.4: Climatological rainfall [mm day^{-1}] and low-level wind speed (850-hPa) in (a) TRMM and ERA-5, (b) the ensemble-mean UKESM-historical, (c) GC3-amip and (d) GC3 N216-pi. The red line highlights the maximum rainfall for each longitude as a proxy for the position of the ITCZ.

during the first days of the year and is weakest and at its southernmost position at 5°N around day 100 (mid-April). During boreal spring, the EP ITCZ migrates northward reaching a peak latitude and maximum rainfall at 10°N by day 250, or early September. The EP ITCZ during boreal winter is weaker than during the rest of the seasons. The low-level winds are predominantly easterly, which are stronger away from the ITCZ and weaker and convergent near the ITCZ position. The position and seasonal migration of the EP ITCZ is reasonably well represented in the four simulations (Figs. 4.5c, e, g, i), but a noticeable bias in precipitation is observed in boreal winter south of the equator in the coupled simulations. The modelled low-level winds in the coupled simulations show significant biases near the ITCZ. These wind biases are observed as stronger wind vectors converging toward the ITCZ during boreal summer and spring and stronger wind vectors diverging away from the equator during boreal winter.

The observed Atlantic ITCZ (Figure 4.5b) has a similar seasonal cycle to the EP ITCZ. The Atlantic ITCZ is close to 4°N at day 1 and migrates southwards at the start of the year reaching its southernmost position at 0° at the end of March. During

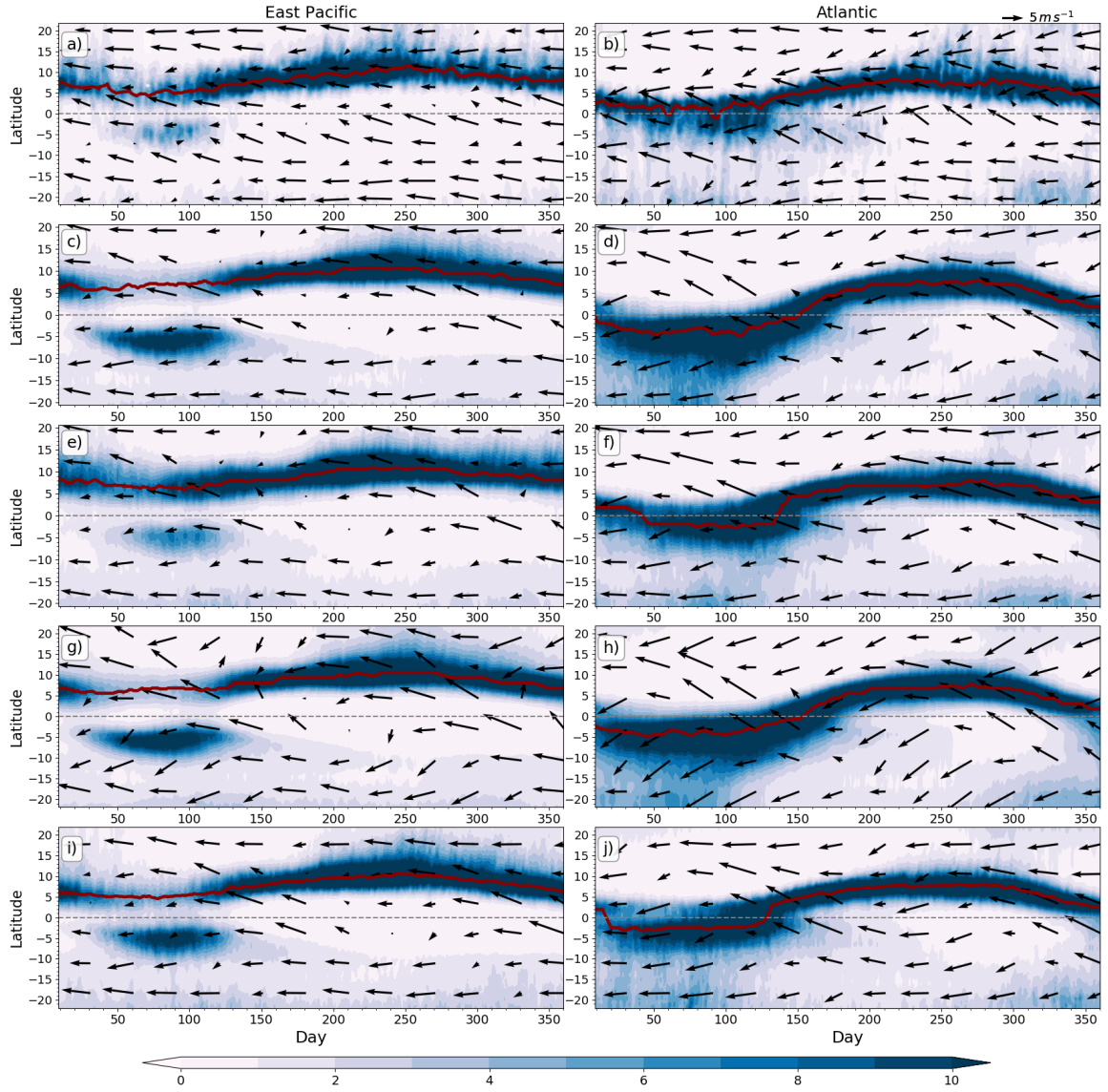


Figure 4.5: Time-Latitude plot of daily mean rainfall (colour contours) and low-level wind speed (850 hPa) longitudinally averaged over the (a, c, e, g) East Pacific [150°W-100°W] and (b, d, f, h) Atlantic [40°W-20°W] Oceans. (a, b) show rainfall from TRMM and winds from ERA-5, (c, d) the ensemble-mean UKESM-historical, (e, f) GC3 AMIP, (g, h) N96-pi and (i, j) GC3 N216-pi. The red solid line shows the ITCZ as the latitude of maximum precipitation.

boreal spring, the Atlantic ITCZ migrates north, reaching 8°N at the start of boreal summer. In contrast to the EP ITCZ, the maximum rainfall in the Atlantic ITCZ does not weaken during any season. The boreal winter position of the modelled ITCZ is displaced south with respect to the observations. The simulated ITCZ crosses south of the equator during boreal winter, as high rainfall rates above 12 mm day⁻¹ covering

the 10S-0 region. After boreal spring, the modelled ITCZ crosses back north of the equator and matches the observed ITCZ reasonably well for boreal summer and fall. Low-level wind vectors near the Atlantic ITCZ (Figures 4.5f and h) suggest a simulated southerly bias north of the equator and a stronger northerly flow south of 10°S.

The biases in the Atlantic ITCZ can also be observed in the overturning circulation (not shown) and the associated Walker circulation as significant negative ω and q biases just north and south of equatorial South America indicative of weaker convective activity. The simulated Atlantic Ocean has a biased negative ω (more ascent) south of the equator and a positive ω bias (less ascent) north of the equator in the low resolution simulations. These biases in the Atlantic ITCZ and overturning circulations described above were found to be of similar magnitude in all the coupled model simulations run at lower resolution, both historical and piControl experiments, however, these biases improved in the medium resolution GC3 N216-pi and in the AMIP simulations (Figures 4.5f, j).

The South Atlantic Convergence Zone (SACZ) is a northwest-southeast oriented band of convection and is a prominent influence on the South American Monsoon mean and extreme rainfall (Carvalho et al., 2004; Marengo et al., 2012; Jorgetti et al., 2014). The SACZ is primarily characterized by convergence oriented northwest-to-southeast that promotes rainfall in southeastern Brazil. The position of the SACZ and strength are an important factor for variability of the South American monsoon on different temporal and spatial scales (Carvalho et al., 2004; Marengo et al., 2012; Jorgetti et al., 2014).

The SACZ in this simulations, defined by the outgoing long-wave radiation empirical orthogonal function analysis (Figure 4.6) closely resembles the pattern found in ERA5. The SACZ active days and the persistence of the SACZ are also compared and found to be in relatively good agreement between reanalysis and model datasets. The simulations from UKESM1, and GC3 N96 and N216 appear to reasonably simulate the spatial pattern of active SACZ days characterized by the low OLR in southeastern Brazil and higher OLR in the La Plata Basin. Similarly, the seasonal cycle of the frequency and persistence of SACZ active days is very well represented by the models with peak activity found from November through January and very little activity

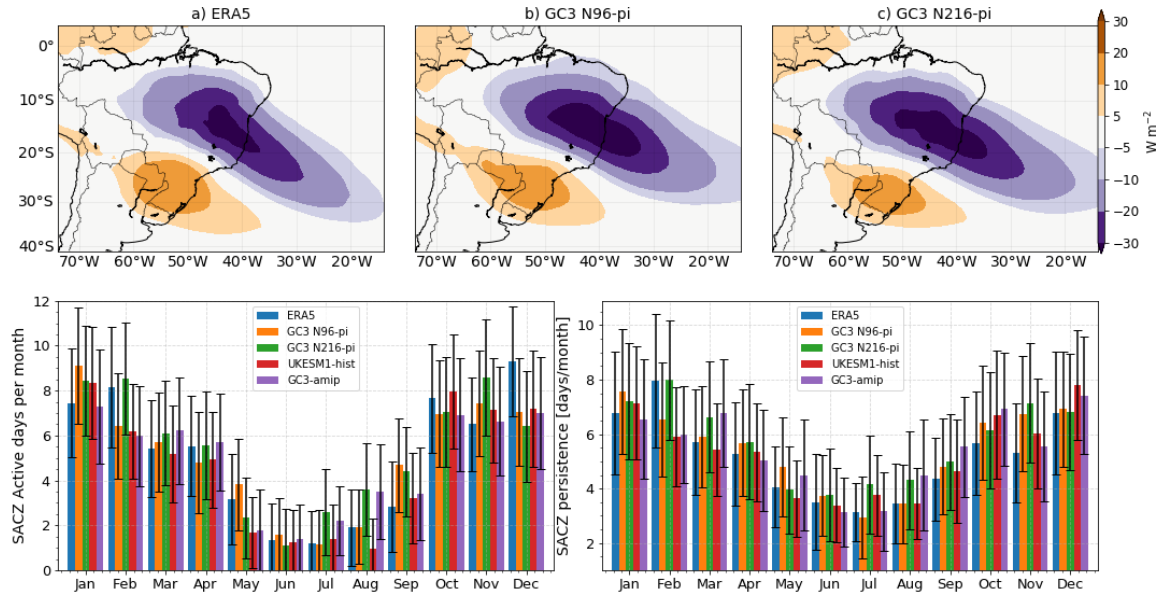


Figure 4.6: (a, b, c) OLR anomalies during active South Atlantic Convergence Zone (SACZ) events. (d, e) Frequency of active SACZ days and length of active SACZ events in reanalysis and model data, the standard deviation is shown as the error bar. The SACZ active days are constructed by first computing the first EOF of the monthly-mean deseasonalized OLR and then the daily OLR, previously filtered to remove periods higher than 99 days, is projected on the EOF pattern to produce a time-series of pseudo-principal components. Active SACZ days are found when this time-series of pseudo-PCs is greater than 1, and the persistence is measured as the number of continuous days where the time-series is greater than 1.

during austral winter. The impact that an accurate representation of the SACZ activity in GCMs has for representing short-scale variability of the South American Monsoon System is an open question, as the SACZ is rarely assessed in CMIP analyses.

4.5 Precipitation and convection in the AMS

4.5.1 Mean seasonal precipitation

The austral summer (DJF) rainfall distribution in South America of the TRMM dataset and the simulations for GC3 N216-pi, UKESM-hist and GC3-amip (Figure 4.7) shows several noteworthy biases in the coupled simulations. The maximum austral summer rainfall in TRMM (Figure 4.7a) is found as a northwest-southeast oriented band of precipitation from the core Amazon region into southeastern Brazil, which is related to the SACZ. The biases are illustrated (Figures 4.7e-h) as the precipitation

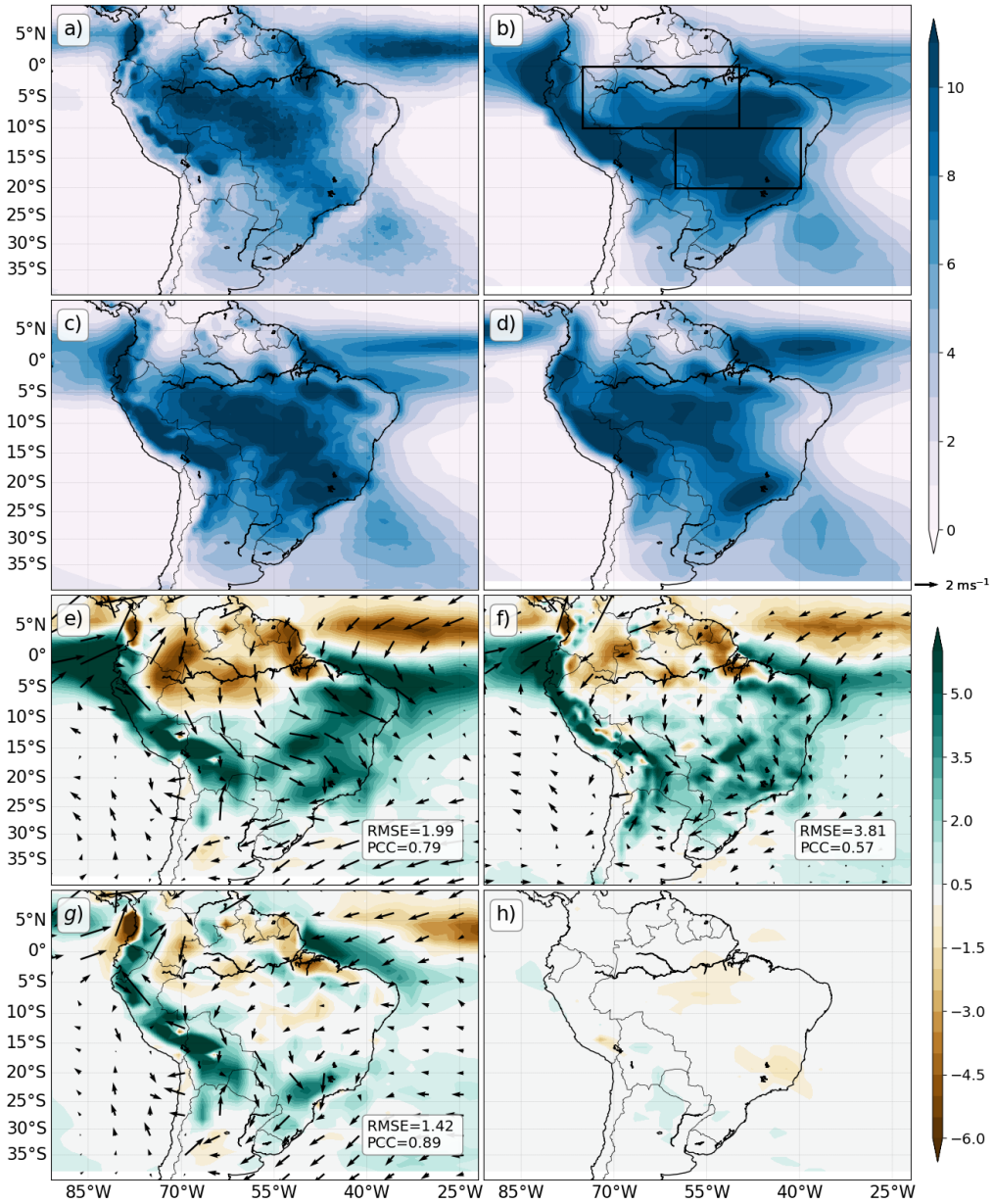


Figure 4.7: DJF mean rainfall [mm day⁻¹] from (a) TRMM, (b) UKESM1-historical, (c) GC3 N216-pi and (d) GC3-amip. (e, f, g) show the statistically significant differences between panels (b, c, d) and (a) TRMM, respectively. (h) Precipitation difference between UKESM-historical and UKESM1-pi, only statistically significant differences (95%) confidence level is shown. The biases in the 850-hPa winds are shown as vectors.

difference between the simulations and TRMM.

The coupled simulations show three main biases. Rainfall in the Atlantic ITCZ in these simulations is displaced southwards, observed as positive (+5 mm day⁻¹) biases south of the equator and negative biases (-5 mm day⁻¹) north of the equator

in the Atlantic. Second, the models underestimate rainfall in the core Amazon basin by -3 mm day^{-1} on average, and the third major bias is that rainfall in southeastern Brazil is overestimated by more than $+5 \text{ mm day}^{-1}$, approximately $+100\%$ of the observed rainfall in this region.

The precipitation biases are associated with a stronger northerly flow in South America, transporting moisture from the Amazon into southeastern Brazil and the La Plata Basin. The magnitude of these biases is smaller in GC3 N216 (Figure 4.7f) than in the low resolution simulations, such as UKESM1-hist. The ensemble mean GC3 AMIP (Figure 4.7d) shows a better representation of the austral summer rainfall and circulation patterns, removing the main circulation biases (Figure 4.7g) of the coupled simulations. The response to historical forcing, illustrated by the difference between UKESM1-hist and UKESM1-pi (Figure 4.7h), is much weaker than the magnitude of the biases and is characterized by a weak drying of the Amazon and southeastern Brazil.

The modelled and observed JJA mean rainfall and biases for Mexico and Central America are shown in Figure 4.8. The main feature is the East Pacific (EP) ITCZ which extends north to 15°N near the western coast of Mexico as a broad band of rainfall ($>11 \text{ mm day}^{-1}$). The modelled EP ITCZ (Figures 4.8e, f, g) rainfall is overestimated by more than 5 mm day^{-1} , especially in GC3-amip. This wet bias is associated with a westerly bias in the low-level circulation, suggesting a weaker flow from the Caribbean into the East Pacific.

The North American Monsoon can be observed as a band of precipitation across western Mexico. In the core monsoon region, near the Sierra Madre Occidental (Adams and Comrie, 1997; Zhou et al., 2016), the JJA-mean rainfall is higher than 8 mm day^{-1} . The distribution of rainfall in the North American Monsoon region is relatively well represented in all the simulations, as only a moderate wet bias ($+2 \text{ mm day}^{-1}$) in western Mexico is observed. The northernmost part of the North American Monsoon (southwestern US) is best simulated by GC3 N216-pi, as the other simulations show a dry bias in this region. The low-resolution simulations (Figure 4.8e) underestimate rainfall (-5 mm day^{-1}) over land in southern Mexico, Guatemala and Belize. Rainfall in the Caribbean islands and Florida is underestimated (-1 mm day^{-1}) in all simulations.

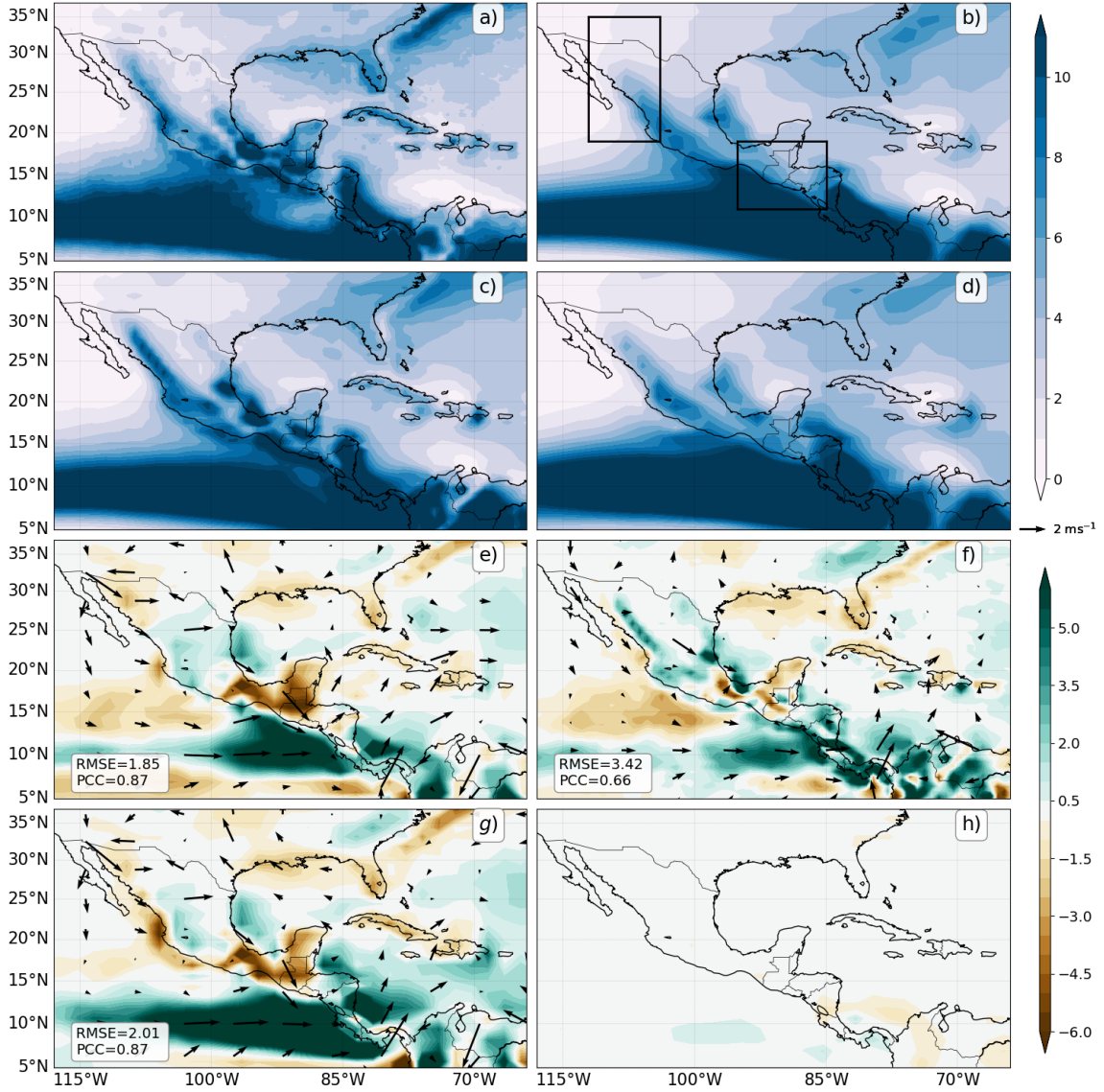


Figure 4.8: As in Figure 4.7 but for JJA in the northern part of subtropical America.

In most cases for JJA in this region, the precipitation and wind biases were reduced in the high-resolution simulation (Figure 4.8f) and little-to-no difference was observed between UKESM1-hist and GC3-hist (not shown). The precipitation response to historical forcing is much lower than the biases (Figure 4.8h) with no significant precipitation differences over land due to the historical forcing.

4.5.2 The annual cycle of rainfall

Figure 4.9 shows the seasonal cycle of rainfall at the pentad (5-day) scale over the North American Monsoon, the Midsummer drought (MSD), the Amazon and eastern Brazil regions. The correlation between TRMM and the model and reanalysis data (ERA5) is also shown in each panel.

The seasonal cycle of precipitation in the MSD region in the simulations is well represented as all the simulations show the characteristic bimodal distribution, a feature that is uncommon for a climate model to be able to reproduce (Ryu and Hayhoe, 2014). However, the characteristics of the simulated MSD are different from observations. For example, the magnitude of the first peak and second peaks in the simulations are different. For instance, most of the first peak simulated magnitudes are higher than TRMM by 4 mm day⁻¹, and the AMIP simulation overestimates the second maximum of rainfall by 2-3 mm day⁻¹. Similarly, the differences between the first peak

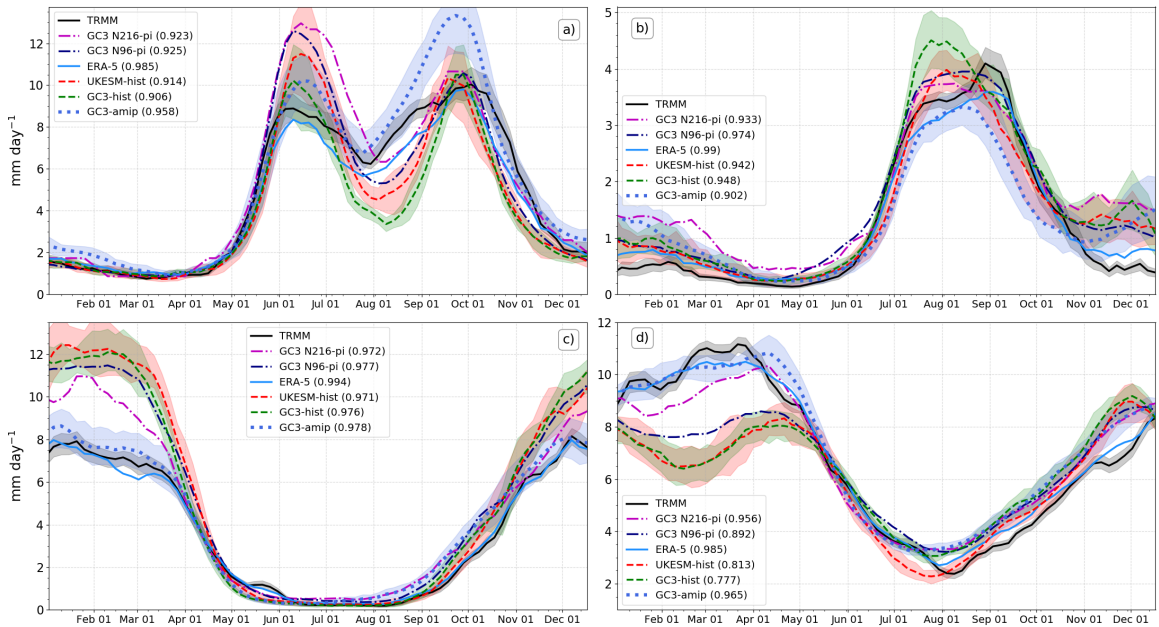


Figure 4.9: Annual cycle of pentad-mean rainfall in the regions (a) the Midsummer drought, (b) the North American Monsoon, (c) Eastern Brazil and (d) the Amazon Basin. The regions are defined as in Figure 4.3 and are illustrated in Figure 4.8b and Figure 4.9b. The shaded regions represent observational uncertainty for TRMM and ensemble spread for the historical experiments. The correlation coefficient for each of the simulated seasonal cycles with TRMM is given in brackets in each panel.

and the MSD and between the MSD and the second peak are more pronounced in the coupled simulations. The timing of the MSD period is different in the models, as the simulations show the driest period taking place 10 days after TRMM and ERA5.

In the North American Monsoon (Figure 4.9b), the observed seasonal cycle is characterized by a very long and dry period ranging from the end of November to the start of June, which is followed by a sharp increase of rainfall around mid-June. The timing of the increase of rainfall in models coincides with observations, suggesting that onset timing and strength is well represented in these models. Moreover, the modelled and observed mean precipitation rates during monsoon maturity are 4 mm day^{-1} , from mid-July until early September, which suggests notable ability of the models to reproduce the peak monsoon rainfall. The historical simulations show a shorter wet season characterised by an earlier retreat of the monsoon rainfall and, as all the simulations, a positive boreal fall rainfall bias ($+1 \text{ mm day}^{-1}$), a feature that has been shown in these models in CMIP5 (Geil et al., 2013).

The seasonal cycle of precipitation in eastern Brazil is characterised by a very wet summer ($\sim 8 \text{ mm day}^{-1}$) compared to a very dry ($\sim 0.2 \text{ mm day}^{-1}$) winter (Figure 4.9c). Rainfall in TRMM and ERA5 increases steadily from austral spring (September) to a maximum found in early January ($\sim 8 \text{ mm day}^{-1}$). Rainfall in this region decreases to $\sim 6 \text{ mm day}^{-1}$ by late March as the monsoon migrates northward and then sharply decreases in austral fall.

The models (Figure 4.9c) show a positive bias during monsoon maturity. This bias was found to be of $+4 \text{ mm day}^{-1}$ and $+2.5 \text{ mm day}^{-1}$ for the low and medium resolution simulations, respectively. This positive bias in the maximum rainfall is consistent with the biases shown in Figure 4.7, which showed that rainfall in southeastern Brazil is overestimated, especially in the low resolution coupled simulations. In contrast to the coupled simulations, GC3-amip shows a very good agreement with the observed maximum summer rainfall and the seasonal cycle ($r=0.978$) throughout the year.

Finally, the seasonal cycle in the Amazon (Figure 4.9d) has a weaker contrast as rainfall greater than 2 mm day^{-1} is found year-round. The coupled simulations show a dry bias during austral summer and a good agreement with the observations

during austral winter. Rainfall rates in the Amazon from January to March, in both TRMM and ERA-5, is close to 10 mm day^{-1} , yet the low resolution simulations show rainfall rates of 8 mm day^{-1} in mid-February, particularly the historical experiments. GC3 N216-pi shows a better agreement with observations but still underestimates summertime rainfall by 1 mm day^{-1} .

This dry Amazon bias has been a known feature of GCMs, including the MOHC models, since CMIP3 (Li et al., 2006; Yin et al., 2013). In these simulations the dry Amazon bias is only alleviated in GC3-amip whose seasonal cycle and maximum summer rainfall agree well with observations. The models, however, represent with reasonable skill the timing of the transition from early austral spring (4 mm day^{-1} in September) to summertime rainfall (6 mm day^{-1} in November).

4.5.3 Characteristics of convective activity

The seasonal cycles of outgoing long-wave radiation (OLR), vertical velocity (ω) and specific humidity (q) are key features of a monsoon since these quantities characterise the strength and height of deep convection, as well as the moisture within the column. shows The pentad-mean annual cycle of OLR, q and ω at the 500-hPa level in four regions of the AMS (Figure 4.10) are used as process oriented diagnostics to further evaluate the biases in the spatial distribution and seasonal cycle of rainfall.

For the North American Monsoon the seasonal cycle of OLR, q and ω is relatively well represented in the simulations. During late boreal winter and early spring, OLR increases steadily as a result of surface warming. However, in early June, near the onset date (Douglas et al., 1993; Geil et al., 2013), OLR sharply decreases reaching a minimum value of 246 W m^{-2} by mid-July. The vertical velocity decreases steadily from January to a minimum in August, indicating ascent from May 1st until September 15th. The models show similar seasonal cycles but overestimate the summertime OLR by $\approx 6 \text{ W m}^{-2}$ and underestimate mid-level moisture by 0.3 g/kg and ω by 0.01 Pa s^{-1} . The simulated shallower convection and drier mid-troposphere is seemingly compensated by stronger mid-level ascent.

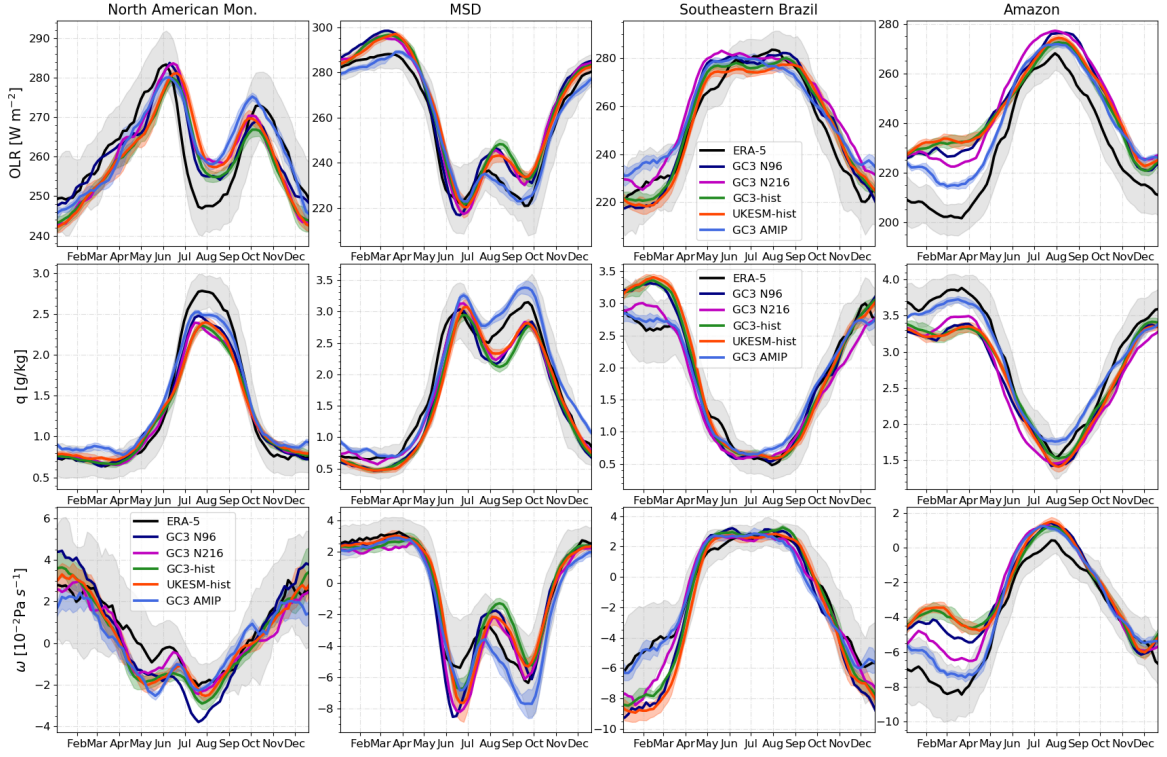


Figure 4.10: Pentad-mean (upper) outgoing long-wave radiation (OLR), (middle) specific humidity at 500-hPa and (lower) ω 500-hPa. These are shown from left to right for the North American Monsoon, the Midsummer drought, southeastern Brazil and the core Amazon. The uncertainty in ERA-5 data, shown as faint gray shading was estimating by bootstrapping with replacement the ERA-5 record 10,000 times.

In the MSD region, OLR and q show signs of convective activity from mid-April, as OLR sharply decreases and moisture increases. The characteristic MSD bimodal distribution of precipitation can also be observed as two peaks of low OLR, high q and low ω . These periods are separated by a period of relatively higher OLR, lower q and weaker ascent from June 15 until late August. Although arguably with a small dry bias with shallower convection after mid-July, the simulations follow closely the observed seasonal cycle.

The simulated conditions during the first peak period show similar OLR and mid-level moisture but stronger ascending motions, which may explain the positive rainfall bias in this period showed in Figure 4.9a. In the period between the first peak and the MSD, the simulated OLR increases more sharply than observations from 220 W m^{-2} (June 15) to 250 W m^{-2} (early August), with similar behaviour in ω and q ,

which may also be related to the strong MSD precipitation differences described in the previous section. The period during the second peak of rainfall in September shows signs of shallower convection and a drier mid-level when compared to ERA5.

In southeastern Brazil, the simulations reasonably follow the timings of the annual cycle of OLR, q and ω of the reanalysis, particularly during austral winter. The moisture q in ERA5 during the dry seasons of austral fall, winter and spring is reasonably simulated by all the experiments. However, during austral summer, the coupled model simulations show significant biases characterised by stronger ascent and increased specific humidity in the mid-levels, although the height of convection (OLR 225 W m $^{-2}$) is only modestly higher in the simulations.

The simulated OLR, q and ω exhibit the highest biases in the Amazon. During austral summer, particularly January and February, the simulated convective activity is shallower (OLR bias of +25 W m $^{-2}$) and weaker (positive ω bias +0.02 Pa s $^{-1}$) and the mid-level troposphere is drier (-0.5 g/kg) than in ERA5. All these biases are in agreement with the dry Amazon bias described in the previous section. In spite of biases in the magnitude of OLR, q and ω during peak convective activity, the seasonal variation is very well simulated so that convective activity, as evidenced by these metrics, starts and ends in the simulations within one or two pentads of the reanalysis. The smallest biases in coupled simulations are those of GC3 N216-pi, not just for the Amazon region but for the other regions as well. The simulated OLR, q and ω in GC3-amp in southeastern Brazil and the Amazon show a much better agreement with the reanalysis during austral summer than the rest of the simulations.

4.6 ENSO Teleconnections

El Niño-Southern Oscillation (ENSO) teleconnections are the prominent source of interannual variability for the AMS (Vera et al., 2006), as summarized in section 2.4. The response to ENSO events in UKESM1 and HadGEM3 is investigated in this section, which first shows the temperature, sea-level pressure (SLP) and precipitation responses to observed and simulated ENSO events in the AMS, to then analyse the

effect of ENSO flavours on the AMS. Finally, results show a possible influence of the QBO for the teleconnections of ENSO.

4.6.1 Canonical teleconnections

The surface temperature and sea-level pressure (SLP) responses to ENSO events are shown in Figure 4.11 for HadGEM3, UKESM1 and ERA5 data during DJF, the season of strongest impact of ENSO events. The characteristic warm anomaly during El Niño events in the East Pacific Ocean does not extend to the east in all the simulations as the observed warm anomaly. In turn, the cold anomalies during La Niña events in the Central Pacific are colder in the simulations than in ERA5. The teleconnection to southern North America, i.e., colder (warmer) conditions in southern (northern) North America during El Niño events is relatively well simulated. For example, the simulated and observed teleconnection patterns to South America, e.g., the cold anomalies during La Niña events in northern South America are well simulated. However, the low resolution simulations show a broader and stronger than observed negative response in southeastern US to El Niño events.

The SLP response in the north Pacific and North America, known as the Pacific North-American pattern, is linked with a displacement of the subtropical jet affecting the eastward propagation of wave activity that reaches the North Atlantic (e.g. Bayr et al., 2019; Jiménez-Esteve and Domeisen, 2020). During El Niño events, the Aleutian Low is strengthened in ERA5, with a strong SLP anomaly (-4 hPa) off the coast of California. The models show a similar but smaller SLP response in the same region. El Niño events events are associated with a negative phase of the North Atlantic Oscillation (NAO), with an opposite response for La Niña events. While the models seem to be able to capture this response of the NAO, the simulated response is weaker than observed. A sensible representation of the ENSO-NAO tropospheric teleconnection may be relevant to then simulate the effect of the NAO on Central American and northern South American rainfall (Giannini et al., 2000, 2004).

The rainfall anomalies associated with ENSO events are shown in Figure 4.12. Three regions in the AMS have a significant precipitation response to ENSO events

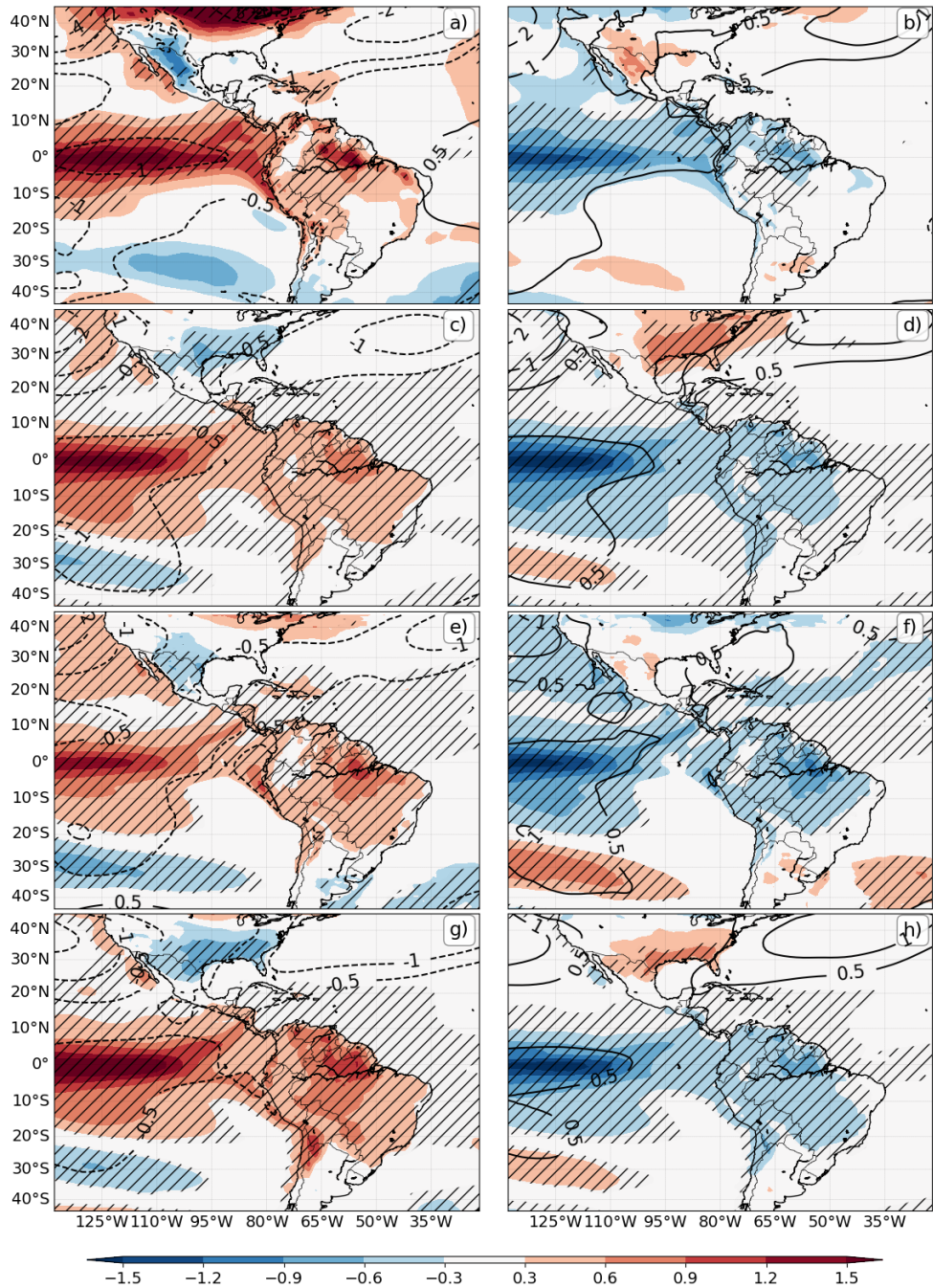


Figure 4.11: DJF Temperature anomalies (colour contours in K) and SLP (line contours in hPa) during (a, c, e, g) El Niño and (b, d, f, h) La Niña events. Results are shown for (a, b) ERA-5, (c, d) UKESM1-hist, (e, f) GC3 N96-pi and (g, h) GC3 N216-pi. The hatched regions denote differences between ENSO phases and the climatological state with significance to the 99% confidence level from a Welch t-test for the temperature field.

in the observations and simulations. In southern North America, rainfall increases (decreases) during El Niño (La Niña) events due to the effects of the PNA pattern

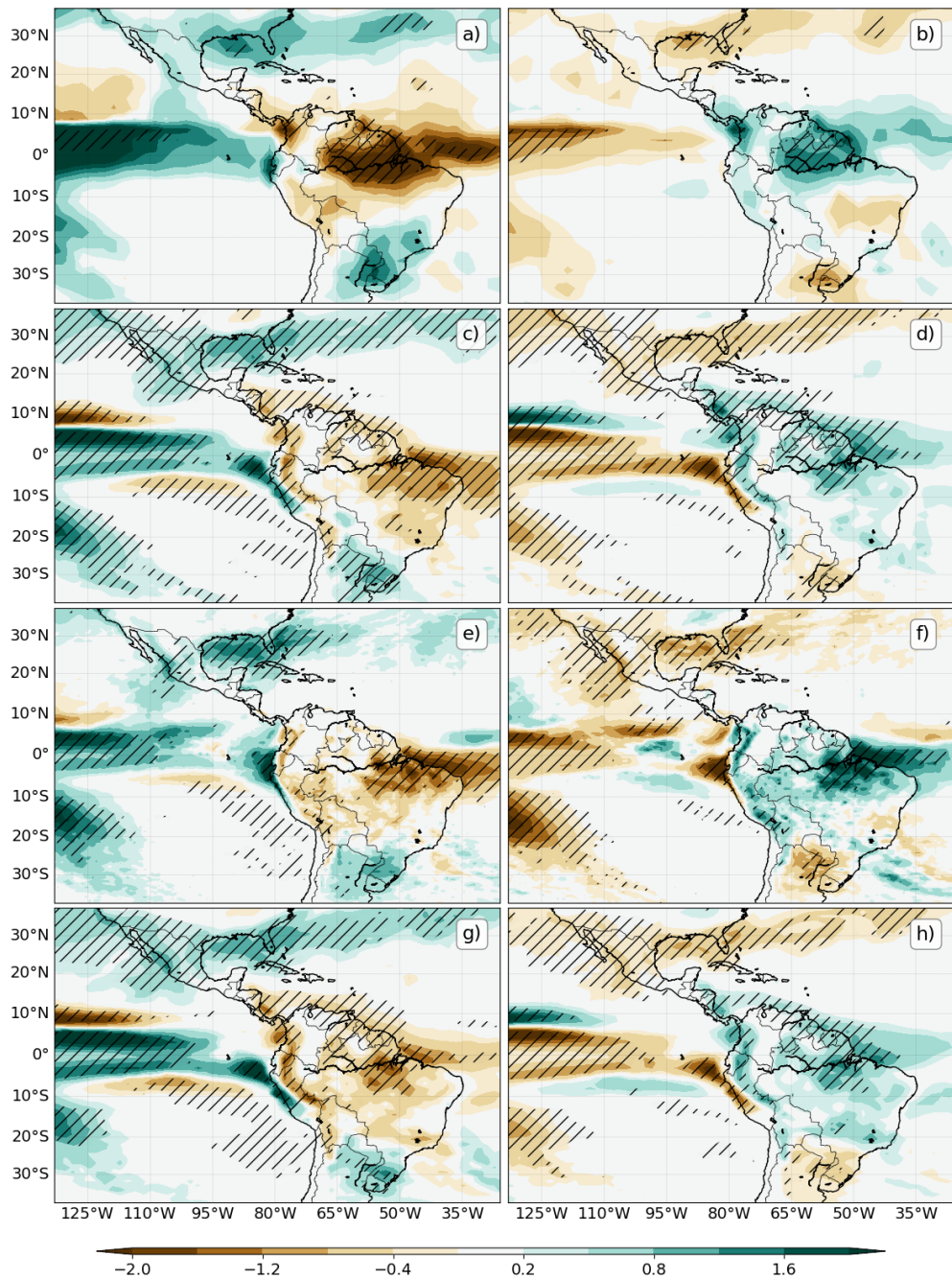


Figure 4.12: As in Figure 4.11 but for the rainfall response [mm day^{-1}] using GPCP as the observational dataset.

on the subtropical jet, which influences the frequency and latitude of propagation of wintertime midlatitude disturbances which are the main source of rainfall in the region during the dry season (Vera et al., 2006; Bayr et al., 2019).

The GPCP dataset (Figure 4.12a, b) shows significant boreal winter rainfall

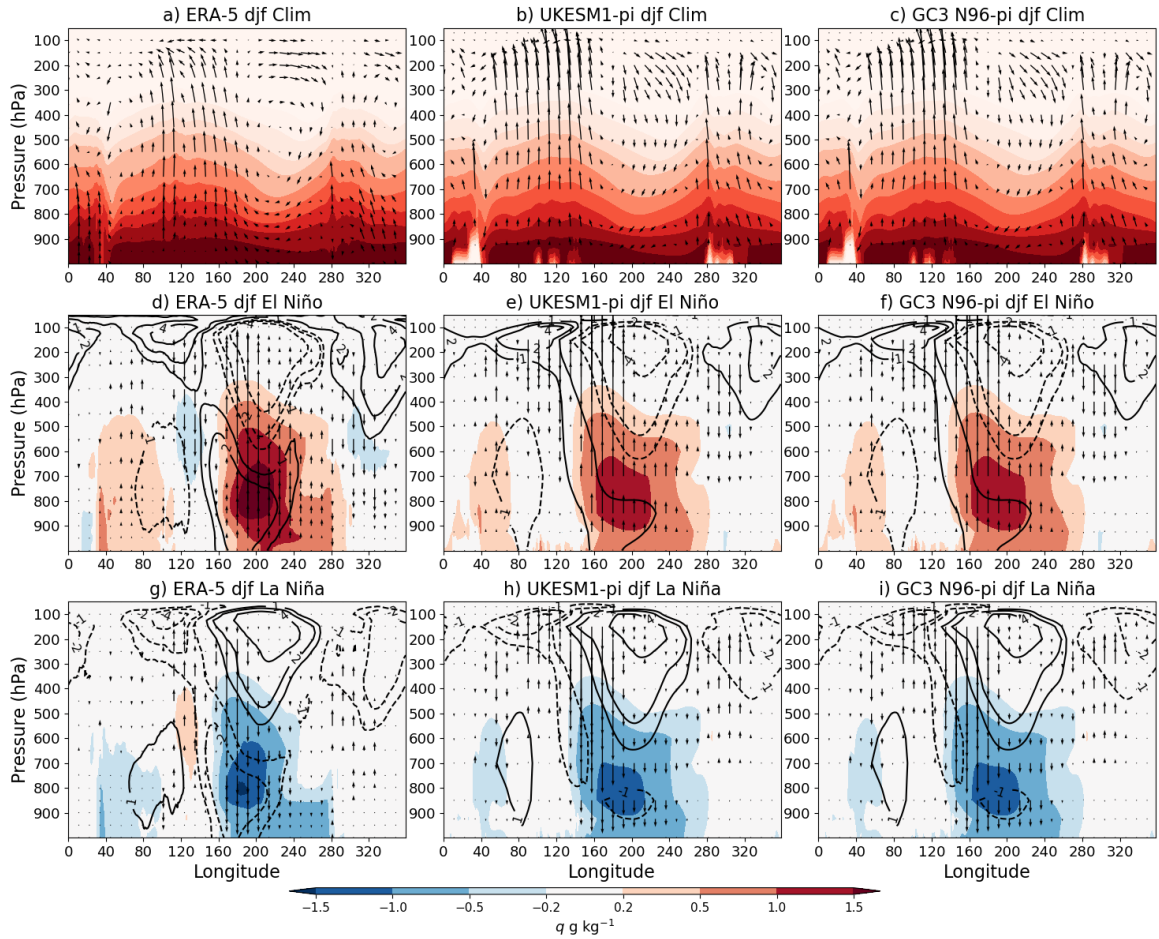


Figure 4.13: DJF Longitude-height Walker circulation anomalies of specific humidity (colour-contours), ω (vectors) and zonal wind (line-contours) during El Niño events (left) and La Niña events (right). Results are shown for ERA-5 (upper), UKESM1-pi (middle) and HadGEM3 piControl (lower).

increases in southeastern US and the Gulf of Mexico during El Niño events, and an opposite response to La Niña phases. All the simulations reproduce this teleconnection rainfall pattern. The models also simulate the observed response in southeastern South America (SESA) of positive anomalies during El Niño and negative anomalies during La Niña events. This teleconnection is also associated with the effect of ENSO on midlatitude and subtropical jet activity, but for the Southern Hemisphere.

The anomalies in the Amazon show the strongest response to ENSO events in the observations. Significant positive (negative) rainfall anomalies during the negative (positive) phase of ENSO in northern South America are observed in GPCP. All the simulations show a very similar and statistically significant response. This

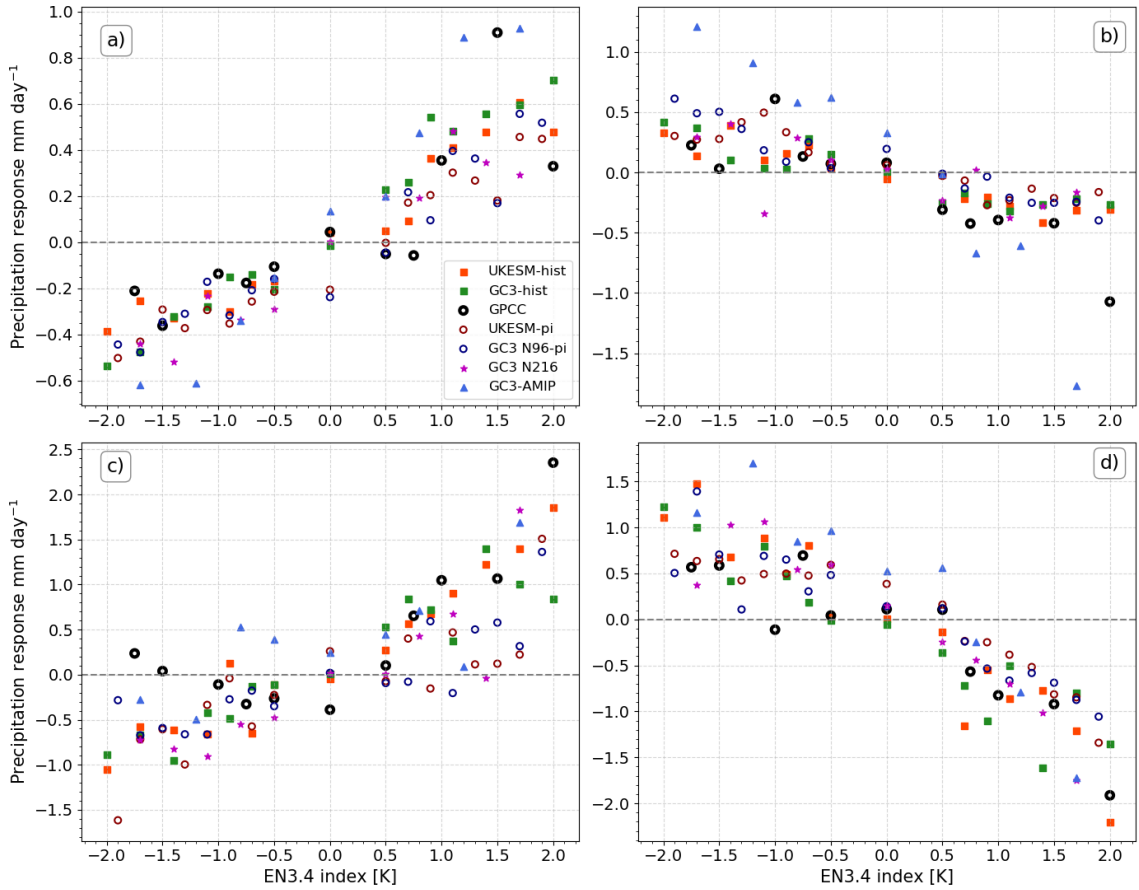


Figure 4.14: Precipitation response [mm day^{-1}] as a function of the El Niño 3.4 index (see text) for (a) southwestern North America [$20\text{-}37^\circ\text{N}, 112\text{-}98^\circ\text{W}$], (b) Central America and southern Mexico [$5\text{-}19^\circ\text{N}, 95\text{-}83^\circ\text{W}$], (c) South Eastern South America [$35\text{-}25^\circ\text{S}, 60\text{-}50^\circ\text{W}$], and (d) the Amazon [$10\text{-}0^\circ\text{S}, 70\text{-}45^\circ\text{W}$]. The observation scatter points are from GPCC in the period of 1940–2013.

teleconnection works through the coupling of ENSO with the Walker circulation (Vera et al., 2006; Cai et al., 2019), which is illustrated in Figure 4.13.

The climatological Walker circulation during DJF shows strong ascent in the $100\text{-}160^\circ\text{E}$ and the $280\text{-}310^\circ\text{E}$ regions, which correspond to the maritime continent and South America (Figure 4.13a). During El Niño events, there is increased specific humidity throughout the lower troposphere in the Central and Eastern Pacific, associated with ascending motions in this region and negative low-level wind anomalies and positive upper-level wind anomalies (Figure 4.13d). In other words, an eastward shift of the Walker circulation. The wind, vertical velocity and specific humidity anomalies are the opposite during La Niña events, indicative of a stronger Walker

circulation, slightly shifted to the west. The models seems to broadly reproduce the observed changes to the Walker circulation during ENSO events (Figure 4.13).

Figure 4.14 shows the observed and simulated precipitation responses in four regions of the AMS to different magnitudes of ENSO events, by binning events for their magnitude of the EN3.4 index and the corresponding precipitation anomaly from the climatology in each region. This figure aims to show the degree of linearity of ENSO teleconnections to the AMS. While the observed response shows some degree of linearity for El Niño events in South America (panels c, d), the majority of the observed responses, particularly to La Niña phases, are not linear.

However, the simulations show several signs of linearity. For instance, consider the historical experiments, UKESM1-hist and GC3-hist, which show that the precipitation responses in southwestern North America, SESA and the Amazon increases roughly linearly as the magnitude of SST anomaly increases. In contrast, some other simulated responses, e.g. to La Niña phases in South America in the piControl simulations, show signs of non-linearity.

4.6.2 The role of ENSO flavours

As described in section 2.4, not all ENSO events are observed with the same SST anomaly pattern in the Pacific Ocean. These different SST patterns for each ENSO event are considered to be a source of non-linearity of ENSO impacts over South America (Sulca et al., 2018; Cai et al., 2020). Principal component analysis has shown that ENSO events may be separated into two categories: Central Pacific (CP) and East Pacific (EP) events (Cai et al., 2020), which highlight where the peak SST anomaly is found in the Pacific Ocean. Figure 4.15 shows that both UKESM1 and GC3 reasonably simulate the observed SST patterns associated with EP and CP El Niño events, although the simulations show CP SST patterns to spread further to the east than the HadSST dataset. The simulations are also able to replicate very broadly the observed differences in the frequency of each event as CP La Niña events are more frequent than EP La Niña events, while the opposite is true for El Niño events.

Furthermore, Figure 4.16 compares the precipitation anomalies for each type of ENSO event in observations with three simulations: GC3 N96-pi, GC3 N216-pi and GC3-amip. The observed precipitation response in the GPCC dataset to EP La Niña over equatorial South America is not significant and is smaller than the strong positive response to CP La Niña events in the same region. However, the simulated response in GC3 N96-pi and GC3 N216 during La Niña events appears to be more independent of the type of event. In contrast, GC3-amip shows different magnitudes of responses to different types of La Niña events, in particular a positive, and significant, anomaly

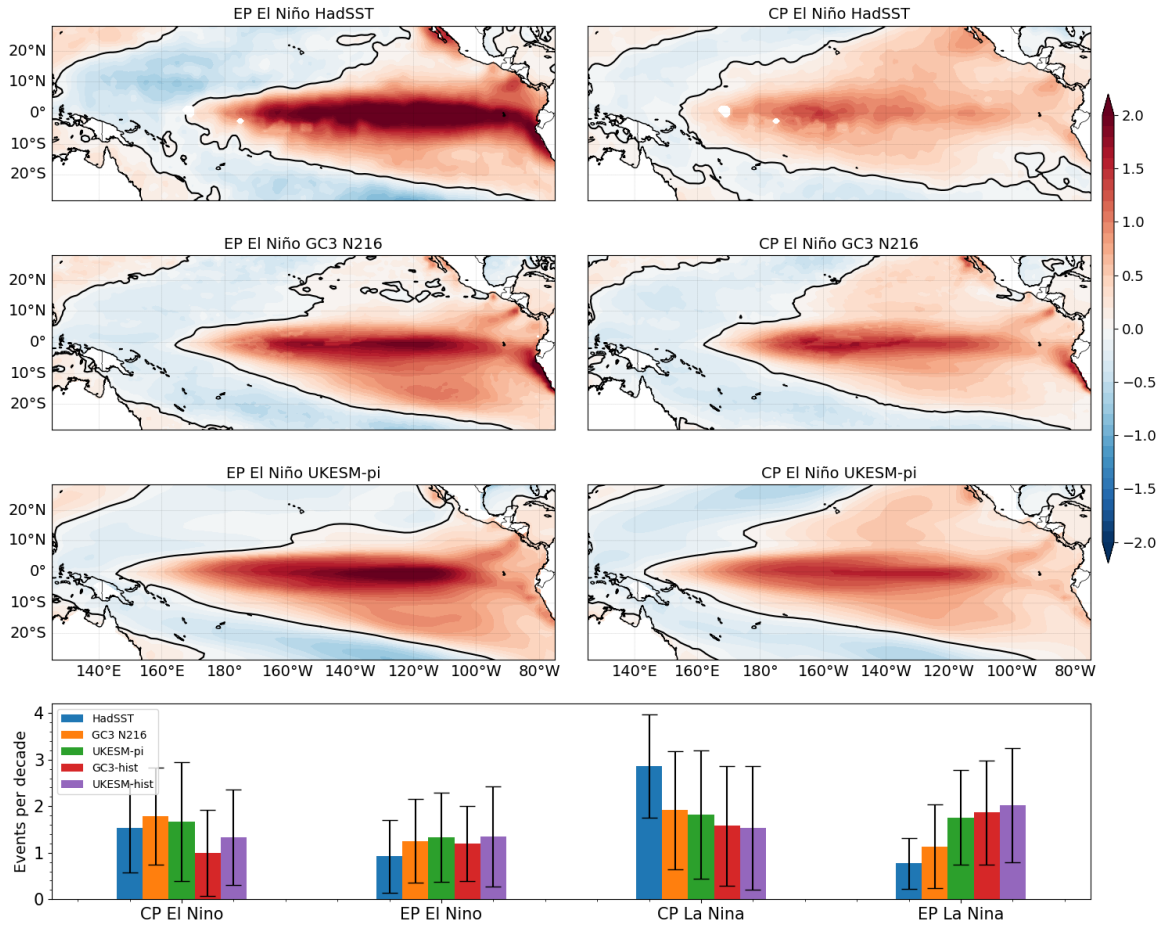


Figure 4.15: SST anomalies [K] for East Pacific (EP) and Central Pacific El Niño events in HadSST, GC3 N216 and UKESM piControl. EP (CP) events were defined where the E-index (C-index) was greater than 1. In the bottom panel, the frequency of events per decade (with standard deviation as error bar) is shown for HadSST and the simulations used in this study. The E-index is computed from $(PC1 - PC2)/\sqrt{2}$ and the C-index from $(PC1 + PC2)/\sqrt{2}$.

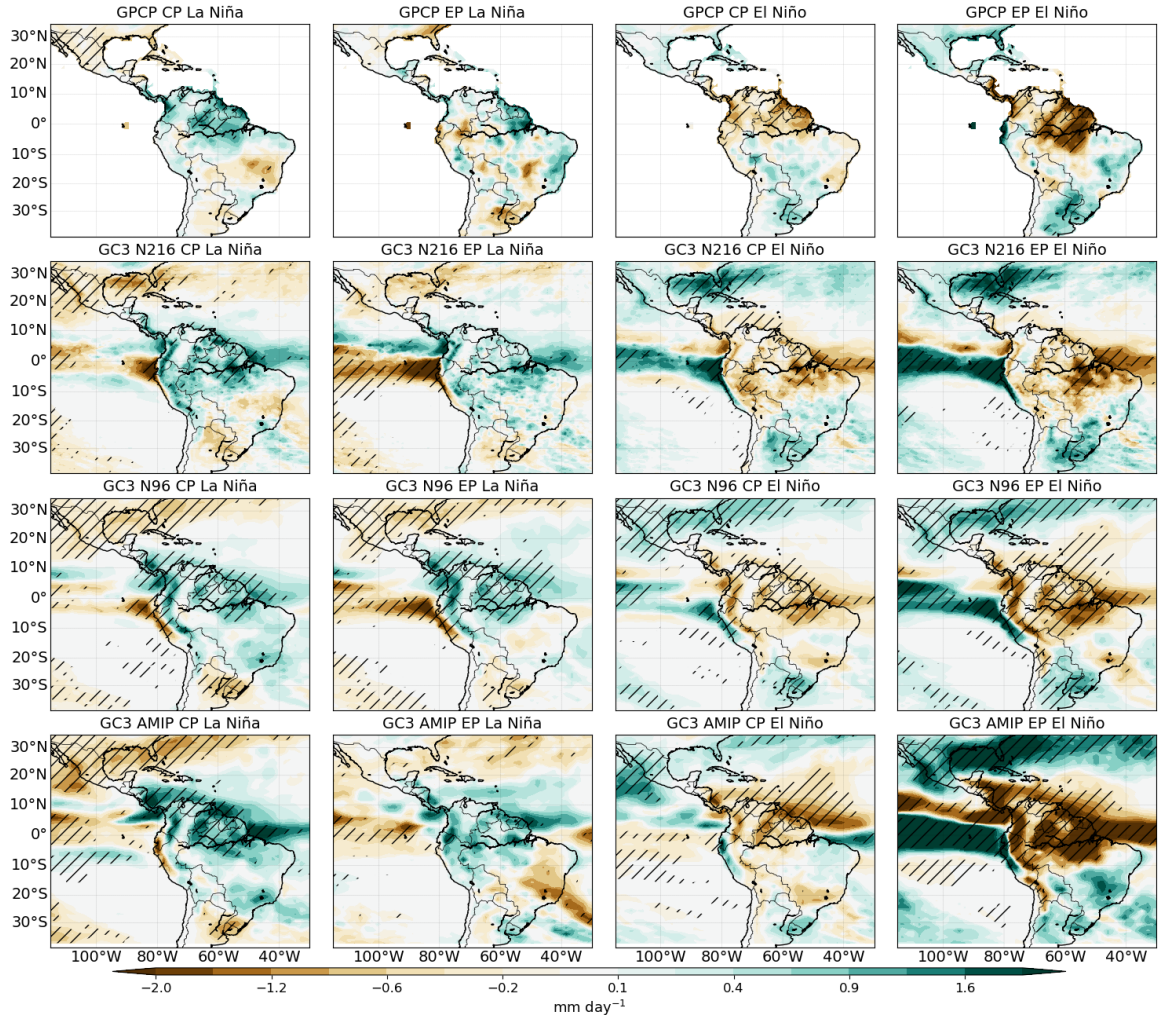


Figure 4.16: Precipitation anomalies in GPCC 1940-2013, GC3 N216-pi, GC3 N96-pi and GC3 AMIP for the four different types of ENSO events, as defined by Cai et al. (2020). Statistically significant anomalies (95% confidence level) are hatched.

for CP La Niña events in the Amazon and weaker and not significant anomalies during EP events, which agrees with observations.

The observed response to El Niño events in GPCC is also dependent on the type of event. EP EL Niño events show significant negative anomalies over the Amazon and positive anomalies over SESA whereas CP events only show significant anomalies (-1 mm day^{-1}) over northeastern South America. While the coupled models (GC3 N96-pi and GC3 N216) do show a stronger response to EP EL Niño events than to CP events, the patterns of the response are very similar. In contrast, the response in GC3-amip agrees with observations. For this experiment, stronger negative responses

to EP El Niño events are observed in the Amazon but the response to CP events is much weaker and is only significant in northeastern South America. In other words, GC3-amip agrees well with the observed non-linear teleconnection patterns whereas the teleconnections in the coupled models do not depend on the type of ENSO event.

4.6.3 A possible influence of the QBO on tropical ENSO teleconnections

Section 2.5 discussed the observational and modelling evidence of the effects on deep convection associated with the stratospheric quasi-biennial oscillation (QBO). In particular, some evidence suggest that the QBO may play a role to determine interannual variability of the Walker circulation and monsoons (Giorgetta et al., 1999; Collimore et al., 2003; Liess and Geller, 2012).

This section evaluates whether the simulations analysed in this chapter, as well as observations, show signs of an influence of the QBO on the AMS. In particular, the analysis aims to understand whether the QBO may be a source of non-linearity and non-asymmetry for the teleconnections of ENSO associated with deep convection and the Walker circulation. In all cases, the phases of the QBO were defined using a 70 hPa zonal mean zonal wind index, with a threshold of $+2 \text{ m s}^{-1}$ for the westerly phase (QBOw) and -2 m s^{-1} for the easterly phase (QBOe).

Composites of the precipitation response to La Niña (LN) events in Figure 4.17 show that the phase of the QBO may be determine the strength and location of the teleconnection. While the precipitation difference in the western Pacific is relatively similar during QBOe than during QBOw in observations and simulations, the teleconnections to Australia, South America and the maritime continent are notably different depending on the QBO phase. In the GPCP dataset, the composite difference QBOe-QBOw during LN events suggests that the characteristic positive precipitation response during LN events in the Amazon, is largely associated with QBOw phases, whereas LN events during QBOe appear to have little effect over South America. A similar result is obtained for GC3 N96-pi.

These precipitation responses are further investigated by changes in the overturning circulation (Figure 4.18). As depicted in Figure 4.13, La Niña events are associated with a westward shift in the Walker circulation with a strengthening of the low-level easterlies in the Pacific Ocean. Figure 4.18 shows that during LN the tropical troposphere cools

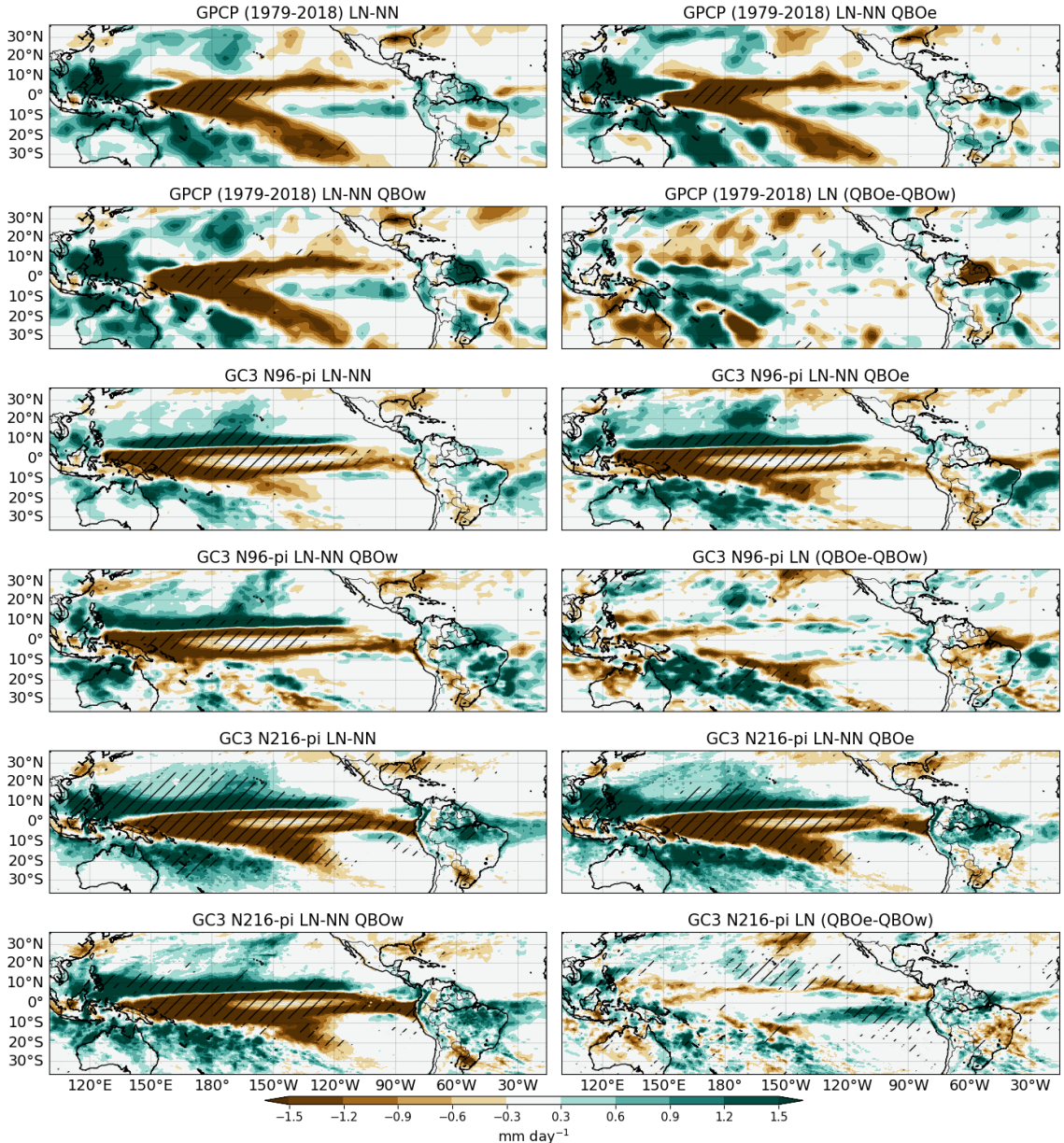


Figure 4.17: Composite precipitation differences during JFMA in GPCP (1979-2018), GC3 N216-pi and GC3 N96-pi between (top) La Niña and Neutral ENSO conditions. The two middle panels show a subset of the top panel, by separating the La Niña composite based on the phase of the QBO. The lower panel shows the differences QBO E-W during La Niña periods. Statistically significant anomalies (95% confidence level) are hatched.

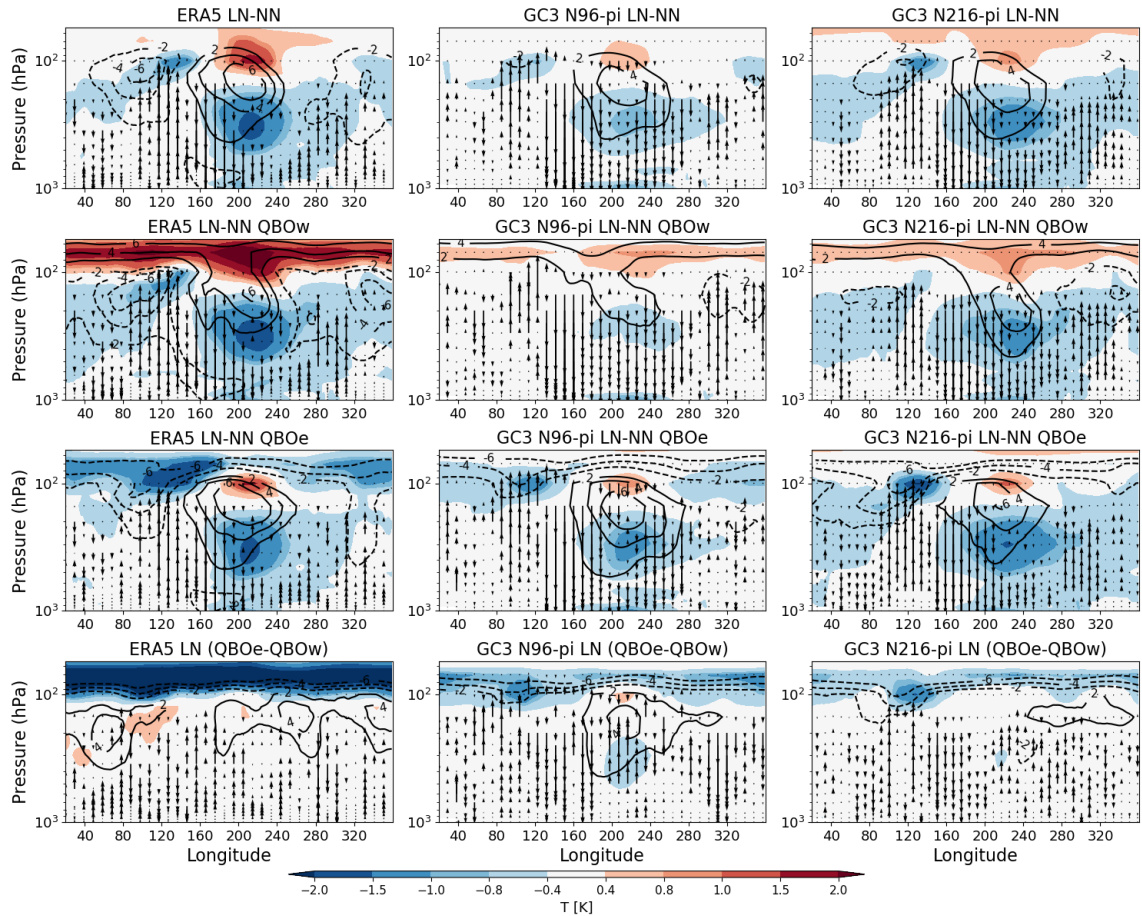


Figure 4.18: Longitude-height differences (JFMA) of equatorial (10S-10N) air temperature (color shading), zonal wind (contours) and vertical velocity (ω - vectors). The differences shown from top to bottom are between all La Niña (LN) periods and Neutral conditions (NN), between LN and NN during QBOw, LN-NN during QBOe, and the difference between LN events on different QBO phases (LN QBOe-QBOw).

and the UTLS region in the Central Pacific warms. These temperature anomalies are weaker in the simulations than in ERA5.

The zonal wind anomalies in the upper-troposphere associated with LN events show different patterns and strengths during QBOw than during QBOe. The mean teleconnections during LN show positive upper-tropospheric anomalies above the Pacific Ocean, but these anomalies are stronger during QBOe than during QBOw in ERA5 and the two simulations shown. In ERA5, most of the upper troposphere shows positive zonal wind differences in the QBOe-QBOw panel.

There are three regions where ascending and descending motions are more greatly

affected by LN events: the maritime continent, the Pacific Ocean and South America. The observed effect of the mean LN teleconnection is the following: anomalous ascent is seen in the maritime continent and in South America, in agreement with a stronger Walker circulation, whereas anomalous descending motions is observed in the Central and eastern Pacific associated with a westward shift of the Walker circulation.

The effect of LN over ascending and descending motions is seemingly also affected by the QBO phase, according to the bottom panels of Figure 4.18. In ERA5 and the simulations, the anomalous ascent observed in South America during LN events is mostly associated with QBOw, whereas only small anomalous ascent is observed during QBOe. However, ERA5 disagrees with the simulations in the western Pacific region (140-180E), as the simulations suggest larger anomalous descent during QBOe than during QBOw, whereas in ERA5 these descending anomalies are larger during QBOw.

A similar analysis was conducted to evaluate the effect of the QBO during the positive and the neutral phases of ENSO. These results are not shown because, although tentative suggestions were found that the QBO may play a role during these other phases of ENSO, there was little agreement between the models and ERA5/observations. Furthermore, the QBO representation in these CMIP6 models is biased in the UTLS region. In particular, the temperature signal associated with circulation of the QBO, most clearly seen in the bottom panels of Figure 4.18, is much weaker in the models.

As suggested by the literature summarised in section 2.5, this temperature signal could be the key aspect of any effect of the QBO on deep convective systems, and as such, the evidence from a short record (ERA5) or models with key biases in possible processes involved presented in this chapter warrants both caution and more work. This topic will be investigated in the next chapters.

4.7 Summary and discussion

This chapter assessed the MOHC models, HadGEM3 and UKESM1, in their pre-industrial control, historical and AMIP experiment contributions to CMIP6 with

specific emphasis on the AMS and associated large-scale tropical circulation. The selected CMIP6 experiments allow to assess the effect of including Earth System processes or increasing resolution for representing regional monsoon rainfall. A schematic in Figure 4.19 shows the primary components of the AMS climate and summarises the main biases found in these simulations and this chapter.

Rainfall in the North American Monsoon was particularly well simulated by the models. The seasonal cycle, peak monsoon rainfall rates and timings of monsoon onset and retreat in the simulations agreed well with TRMM. The historical experiments overestimate the mean temperature in most of the Americas by 1.5 K, but particularly in boreal summer in southwestern North America (+4 K). In spite of this warm bias, the temperature seasonal cycle is well represented by these models.

These results suggest model improvement on the simulation of the North American Monsoon from previous versions of the MOHC models (Arritt et al., 2000), and most of the model cohorts of CMIP3 and CMIP5 (Geil et al., 2013). For example, most of CMIP5 models showed a very wet bias during monsoon maturity whereas rainfall during monsoon maturity in all the experiments of this chapter are within less than 1 mm day⁻¹ of observations, during the maturity stage. However, these models continue to show biases during monsoon retreat as rainfall does not decrease as sharply as in observations after mid-September, which suggests a continued bias in the winter-time precipitation associated with cold-fronts (Adams and Comrie, 1997). Further research into variability of the North American seasonality may be explored using these models given their skillfull representation fo the seasonal cycle.

The Midsummer Drought (MSD) of southern Mexico and Central America is a regional feature of precipitation that most of CMIP5 models had difficulty capturing, with the MOHC models being amongst the few exceptions (Ryu and Hayhoe, 2014). The MSD in UKESM1 and GC3 continues to be relatively well represented; however, the experiments analysed in this chapter showed various differences in the timing and strength of the bimodal cycle when compared to observed gridded-datasets and ERA5.

The models simulate a wetter-than-observed first peak of precipitation and a drier MSD period, therefore simulating a larger difference between the first peak and the

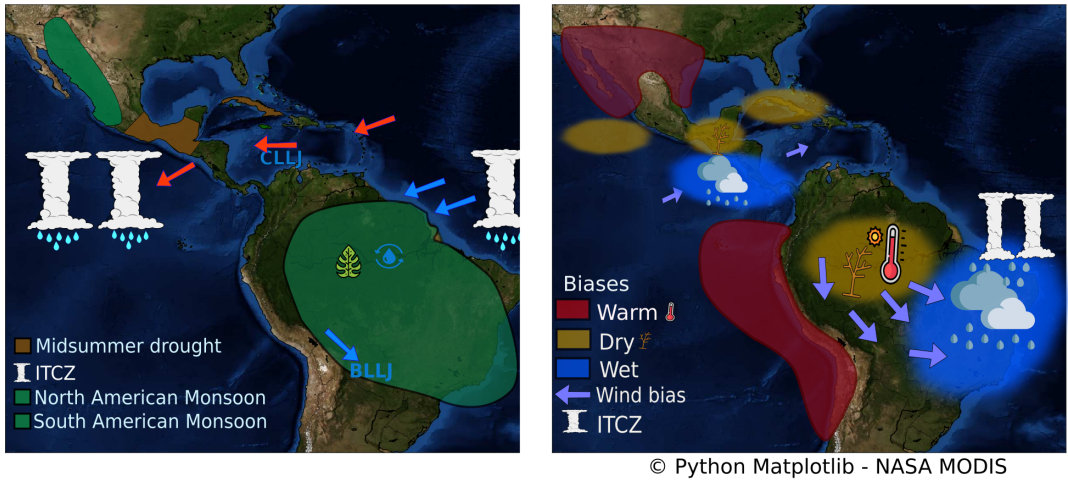


Figure 4.19: Schematics of (a) the main features in the AMS and (b) the main biases in UKESM1 and HadGEM3. In (a) the boreal summer easterlies (red) and austral summer circulation (blue) are shown with the Caribbean and Bolivian Low-level Jets (CLLJ and BLLJ, respectively). In (b) the biases are shown for the respective northern and southern Hemisphere summers. The ITCZ bias in (b) refers to the southward displacement bias of the Atlantic ITCZ in the simulations.

dry period. While in observations this difference between the first peak and the MSD period ranges between 2-3 mm day⁻¹, in the simulations this difference is closer to 6 mm day⁻¹. Rainfall during the first peak has been too wet in these models since CMIP3, suggesting a persistent wet bias in this region, likely associated with the bias in East Pacific ITCZ also shown in this chapter and in recent studies (Ryu and Hayhoe, 2014; Mulcahy et al., 2018). In contrast, the so-called second peak of precipitation, observed in late August, is simulated in close agreement with TRMM, except in the AMIP experiment, which has a wet bias of 2 mm day⁻¹ at this stage.

The skill of UKESM1 and HadGEM to simulate the MSD's bimodal regime of precipitation makes these simulations ideal to understand the mechanisms underpinning the MSD and answer the question of why the MOHC do represent a MSD regime but other models fail. Furthermore, section 2.3 discusses several open questions regarding the mechanisms that cause the observed MSD. These simulations will then be used in future chapters to address the evaluate previous hypotheses of the causes for the MSD.

The East Pacific ITCZ migration and position was shown to be relatively well represented by the models (Figs. 4.4 and 4.5). However, the models showed an

overestimation of boreal summer rainfall near the coast of Central America (Figure 4.9). These biases are associated with an easterly wind bias at low-levels, suggesting a bias in the flow from the Caribbean Sea into the Eastern Pacific (Herrera et al., 2015; Durán-Quesada et al., 2017). The simulations also showed a biased Atlantic ITCZ that was displaced south of the observed ITCZ position during boreal winter (Figure 4.5), particularly in the low resolution coupled simulations.

In the Amazon, the simulations showed a warm bias (+2 K) during austral spring and summer, a bias that existed since CMIP5 (Jones and Carvalho, 2013), and a colder than observed southeastern Brazil. These biases were linked with decreased cloud cover and less rainfall over the Amazon and more convective clouds and rainfall in southeastern Brazil (Figures 4.8 and 4.10). The low cloud cover, warm and dry Amazon biases are intertwined with the low-level circulation from the Atlantic into the South American continent. The biases in the circulation during austral summer were observed as a northerly flow anomaly over the central and southern Amazon, a feature that has been associated with a stronger moisture transport away from the Amazon (Marengo et al., 2012; Jones and Carvalho, 2018).

During the period of maximum rainfall rates in February, the simulations overestimate rainfall by 3 mm day⁻¹ in southeastern Brazil and underestimate rainfall in the Amazon by a similar rate. The historical experiments show a small drying response to historical forcing in the Amazon therefore slightly increasing the magnitude of this dry bias compared to the unforced piControl experiments. The AMIP simulation with the SST biases removed improved the representation of the Atlantic ITCZ and the precipitation, cloud cover and temperature biases over the South American Monsoon. The improvement in the circulation and precipitation biases in the AMIP simulation suggest that the origin of the dry Amazon bias are the biases in the Atlantic SSTs.

The canonical teleconnection responses of temperature, SLP and precipitation in the AMS to ENSO events are well represented in these models. For example, the simulated spatial patterns and strength of the positive (negative) precipitation anomalies observed in northern Mexico and South Eastern South America during El Niño (La Niña) agree well with observations and reanalysis. Similarly, the teleconnection to the Amazon

is well represented for both phases of ENSO, in spite of relevant biases in the mean state of the South American monsoon discussed above.

ENSO teleconnections in these simulations were found to be approximately linear, i.e., the precipitation response is linearly related to the magnitude of the SST perturbation in the EN 3.4 region. These experiments also show signs of symmetric teleconnections as positive and negative phases produce the opposite and equivalent precipitation response in the AMS. In contrast to observations and the GC3 AMIP simulation, the precipitation response in the coupled models appears to be independent of the type or flavour of ENSO events into Central and East Pacific events. The fact that these models show a reasonable representation of ENSO diversity in SST patterns but the models do not replicate the observed non-linear dependance to ENSO events warrants further analysis.

The QBO appears to be a source of non-linearity for ENSO teleconnections to the Amazon. La Niña canonical teleconnections in the Amazon are characterized by a stronger ascent associated with a stronger Walker circulation. This teleconnection pattern occurs in observations and these simulations primarily during the westerly phase of the QBO, whereas the teleconnection during the easterly phase is much weaker and barely different from the climatological mean-state. Whether the stratospheric QBO poses such an important control to the main source of interannual variability for monsoon rainfall in the Amazon merits a separate chapter of this thesis.

The main biases (Fig. 4.19), in these experiments are generally smaller in the medium resolution GC3 N216 compared to the low resolution experiments, which suggests improved model performance with increased horizontal resolution. In contrast, including Earth System processes in the UM model only affects the surface temperature response to historical forcing and not the dynamical biases that drive the precipitation and ITCZ biases.

In short, the main dynamical biases in UKESM1 are very similar to those in GC3 N96 as these two models share the same dynamical core; only when resolution is increased these biases are reduced notably. A noteworthy difference between UKESM1 and GC3 is that warming over the historical period in Mexico and the Amazon

is higher in UKESM1 than in GC3. In general, UKESM1-hist shows a stronger temperature response to forcing than GC3-hist, as UKESM1 has been reported to have a greater climate sensitivity than GC3 (Andrews et al., 2019; Sellar et al., 2019). This differential warming may be a consequence of the land-use change in these regions playing a role in the UKESM1 representation of soil-atmosphere feedbacks.

The improvement in the medium resolution simulation compared to the low-resolution simulations may be associated to the improved dynamics of the ocean or the atmosphere. For example, the Atlantic ITCZ biases have been shown to be directly affected by processes in the convective scheme (Bellucci et al., 2010), such as the treatment of entrainment and moisture-cloud feedbacks (Oueslati and Bellon, 2013; Li and Xie, 2014). The resolution of the ocean model has been shown to impact the eddy heat flux parametrisation and the associated heat uptake and transport of the ocean (Kuhlbrodt et al., 2018). The improvement in the Atlantic SSTs and ITCZ and the associated dynamics in GC3 N216-pi also improves the associated circulation biases and moisture transport in the South American Monsoon. In other words, the oceanic resolution may play an important role in the cross-equatorial heat and moisture transport, SST gradients over the equatorial Atlantic which in turns improves the land-sea circulation over the Amazon during austral summer, a circulation that is key for representing the spatial distribution of rainfall in South America.

5

A wavelet transform method to determine monsoon onset and retreat from precipitation time-series

A new method to determine monsoon onset and retreat timings using wavelet transform methodology applied to precipitation time-series at the pentad scale is described. The principal advantage of this method is its portability, since it can be easily adapted for any region and dataset. The application of the method is illustrated for the North American Monsoon and the Indian Monsoon using four different precipitation datasets and climate model output. The method is shown to be robust across all the datasets and both monsoon regions. The mean onset and retreat dates agree well with previous methods. Spatial patterns of precipitation and circulation anomalies identified around the onset and retreat dates are also consistent with previous work. Several examples illustrate that this method may be used at the grid-box scale, not just over large area-averaged regions. The method is also used to characterise the strength and timing of the Midsummer drought in southern Mexico and Central America. A two peak structure is found to be a robust structure in only in 33% of the years, with other years showing only one peak or no signs of a bimodal distribution. The two-peak structure analysed at the grid-box scale is shown to be a significant signal in several regions of

Central America and southern Mexico. The methodology is also applied to climate model output from the Met Office Hadley Centre UKESM1 and HadGEM3 CMIP6 experiments. The modelled onset and retreat dates agree well with observations in the North American Monsoon but not in the Indian Monsoon. The start and end of the modelled Midsummer drought in southern Mexico and Central America is delayed by one pentad and has a stronger bimodal signal than observed.

5.1 Introduction

The timing and strength of the rainy season are key aspects of the seasonal cycle of monsoon regions such that the length of the rainy season greatly influences sectors such as agriculture (Sultan et al., 2005; Gadgil and Rupa Kumar, 2006; Jain et al., 2015; Harvey et al., 2018) and water management (Turner and Annamalai, 2012; Bussmann et al., 2016). The objective determination of onset and retreat dates is key for climate and weather research aiming to understand the short and long-term variability, trends and predictability of the regional monsoons (e.g. Kitoh and Uchiyama, 2006; Cook and Buckley, 2009; Lucas-Picher et al., 2011; Nieto-Ferreira and Rickenbach, 2011; Htway and Matsumoto, 2011).

For this reason, a plethora of methods have been used to diagnose the onset and retreat dates from a range of variables and datasets. Bombardi et al. (2020) provides a recent review of these methods and highlights the technical differences and purposes of each. Methods can be divided into those that aim to evaluate monsoon onset and retreat on a regional scale (e.g. Webster and Yang, 1992; Fasullo and Webster, 2003; Garcia and Kayano, 2013) or at a local or grid-box scale (e.g. Liebmann and Marengo, 2001; Cook and Buckley, 2009).

Threshold methods are the most commonly used local-scale methods that typically diagnose onset and retreat from a precipitation time-series (Bombardi et al., 2020). These methods evaluate the accumulated (Liebmann and Marengo, 2001) or daily/pentad-mean rainfall rates (Geil et al., 2013) and determine the onset and retreat dates when the time-series exceeds or falls below a pre-defined value (threshold) for a

given amount of time (persistence). The persistence parameter is used to reduce the method's sensitivity to noise in the precipitation time-series. The threshold parameter can be a statistical measure of the seasonal cycle such as the total annual mean rainfall (Arias et al., 2012) but is also frequently subjectively determined or tuned to a specific dataset (e.g. Geil et al., 2013).

The parameters for threshold methods vary distinctly from study to study, first because the wet and dry seasons in each monsoon region have different timings, strengths and dynamical features (Wang et al., 2017). Furthermore, within a given monsoon region, e.g., in the South American Monsoon, several methods are used for different purposes depending on the temporal and spatial scales of interest (see e.g. Liebmann and Marengo, 2001; Marengo et al., 2001; Nieto-Ferreira and Rickenbach, 2011; Carvalho et al., 2011; Garcia and Kayano, 2013). Finally, differences between the datasets used, e.g., in horizontal resolution, can cause differences in the climatological seasonal cycle of rainfall which means that the implementation of threshold methods in different datasets also requires normalization or statistical treatment of the threshold and persistence parameters.

In other words, each threshold method is tailored to a monsoon region using a specific dataset and a specific variable for a given purpose. This characteristic of the threshold methods poses various shortcomings. Firstly, practical shortcomings of the threshold methods, particularly rigid thresholds, include false hits (Moron and Robertson, 2014) or some years not meeting the threshold and persistence criteria (Arias et al., 2012) requiring further relaxation of the parameters. Second, given that threshold methods are tailored to a specific dataset in a given region, statistical corrections are needed to implement the same threshold method in a different dataset or in another region.

The Coupled Model Intercomparison Project (CMIP) assessments of monsoon onset and retreat typically use precipitation threshold methods due to the lack of high temporal or vertical resolution output from all models to estimate vertically integrated quantities required for some methods (e.g. Geil et al., 2013; Zou and Zhou, 2015; Ha et al., 2020). Threshold methods have multiple shortcomings for CMIP assessments

as the persistence and threshold parameters are tuned for observations with a specific seasonal cycle but models have a range of biases in the seasonality, magnitude and spatial distribution of rainfall (Pascale et al., 2019; García-Franco et al., 2020). The use of pre-defined threshold values may also not be suitable to compare different model experiments with changes in forcing where the climatological mean rainfall or the seasonal cycle may change within the model run. These shortcomings are relevant because a proper diagnosis of the seasonal cycle in CMIP assessments is key to understand and diagnose current and future changes to monsoon seasonality as a result of greenhouse forcing (Zhou et al., 2016; Wang et al., 2017).

The objective diagnosis of shorter time-scale rainfall variability, such as bimodal regimes and active and break phases of a monsoon, also requires methods that can separate relatively drier and wetter periods within the rainy season. For example, for the MSD of Central America and the Caribbean (section 2.3) the objective determination of the strength, spatial distribution and robustness of the bimodal signals is not straightforward. For example, the global method used in Bombardi et al. (2020) fails to diagnose the region of southern Mexico, Central America and the Caribbean as a bi-modal regime.

The majority of existing methods to diagnose bimodal signals in this region use geometric or statistical measures of the monthly-mean rainfall that measure the difference between the months of maximum rainfall and the drier months. However, this approach fails to capture the shorter-scale changes that have been shown to occur in both observations and model data, as the MSD does not start or end exactly on given calendar months (Magaña et al., 1999; García-Franco et al., 2020). Zhao and Zhang (2021) review and compare several methods to detect and measure the MSD, finding that using monthly-mean data and prior assumptions of the dates of the first and second peaks can lead to errors.

Only a handful of methods exist that can determine the characteristics of the MSD in Central America on sub-monthly timescales. Anderson et al. (2019) analysed the pentad-mean time-series from the Climate Hazards Infrared Precipitation with Stations (CHIRPS) dataset. After a double temporal smoothing of the time-series, Anderson

et al. (2019) determined the MSD timings through a threshold method with parameters tailored to the CHIRPS dataset. In turn, Zhao et al. (2020) used daily-mean time-series and determined the two-peak structure through linear-regression analysis.

In short, multiple methods exist, each with various parameters fit for different purposes, but these methods present shortcomings for studies that compare results from multiple datasets or investigate model experiments where climatological rainfall and the seasonal cycle change. Similarly, studies that investigate the impact of decadal modes of variability (e.g. Arias et al., 2012), greenhouse warming (e.g Geil et al., 2013) or general trends (e.g. Sahana et al., 2015) rely solely on the output of one single method whereas the use of two or more methods may help to test the sensitivity of their results to the chosen method and parameters. Both the objective determination of monsoon onset and retreat and the timings of bimodal regimes require a method that can analyse temporal changes to precipitation on several scales and that can be used on any gridded dataset.

The goal of this chapter is then to present an objective approach that is more portable across datasets, regions and robust for various purposes, some of which will be further explored in the following chapter. This chapter introduces a wavelet transform method to determine monsoon onset and retreat dates using pentad-mean precipitation time-series. Wavelet algorithms have been extensively used in atmospheric research for multiple purposes, such as the detection of the boundary layer height (e.g. Brooks, 2003), as well as to analyse time-frequency features of a signal (e.g. Whitcher et al., 2000; Dimdore-Miles et al., 2021). In fact, Allen and Mapes (2017) used a wavelet analysis to determine monsoon onset and retreat using daily OLR data. The method is constructed such that the determination of monsoon onset and withdrawal dates is less sensitive to the characteristics of the time-series, i.e., the characteristics of the seasonality of each monsoon or of a given observational dataset. Furthermore, the method is expanded to characterise bimodal regimes which is illustrated for the MSD of southern Mexico, Central America and the Caribbean.

The remainder of this chapter is organised as follows: section 2 describes the methods and datasets. Section 3 shows the results of applying the method to the

Indian and North American Monsoons and the MSD. Section 4 summarises the method and discusses the results.

5.2 Data

5.2.1 Precipitation datasets and reanalysis data

This chapter uses three gridded precipitation datasets described in chapter 3: the TRMM v7 3B42, the CHIRPS, and the CMAP datasets. These three precipitation datasets are merged products, TRMM and CMAP mainly use microwave satellite measurements complimented by several other sensors and calibrated with rain-gauge data whereas CHIRPS uses several products from TRMM, as well as high-resolution station data. These datasets also differ in their end-product horizontal resolutions.

The precipitation output from the latest ECMWF reanalysis, ERA5, is used, which has been shown to exhibit a relatively good representation of the temporal characteristics of rainfall in the american monsoons in chapter 4. Other variables from ERA5 used to diagnose changes to the circulation associated with monsoon onset were daily-mean geopotential height at 500 hPa and wind speed (\vec{u}) at several vertical levels.

5.2.2 Model data

Daily precipitation data from the CMIP6 archive are used, retrieved from: <https://esgf-index1.ceda.ac.uk/projects/cmip6-ceda/>, to illustrate the method using standard climate model output. In particular, we use results from the Met Office Hadley Centre models (MOHC): HadGEM3 GC3.1 and UKESM1 using the pre-industrial control and historical experiments, these simulations and the MOHC models are described in chapter 3. The daily precipitation data were converted to pentad-scales.

5.3 The wavelet transform method

Wavelets are band-limited wave-like functions with specific mathematical properties that include a finite energy and zero-mean (Whitcher et al., 2000; Addison, 2017).

The wavelet function is defined using two parameters, a dilation (a width or temporal scale) and a translation (centroid in time/space).

Wavelet transforms are the result of the inner product (convolution) of a wavelet function with a time-series or a signal (Addison, 2017). The wavelet transform can be thought of as a local comparison between the wavelet function and the observed signal for different frequencies or temporal scales. The information provided by a wavelet transform largely depends on the characteristics of the wavelet function used, thus, different wavelet functions are used for different purposes (Addison, 2017). For the purpose of finding the onset and retreat dates, the wavelet based on the Haar function is useful as this wavelet is suitable to find sudden changes in a signal (Addison, 2017). The Haar wavelet is defined as the non-continuous piece-wise function:

$$\psi\left(\frac{t-b}{a}\right) = \begin{cases} 1 & b \leq t \leq b + \frac{a}{2} \\ -1 & b - \frac{a}{2} \leq t \leq b \\ 0 & elsewhere, \end{cases} \quad (5.1)$$

where a is the dilation coefficient, b is the centre of the wavelet or the translation coefficient and t is the time coordinate.

The wavelet covariant transform is then the inner product of the Haar wavelet with a timeseries (Brooks, 2003), i.e. :

$$W_f(a, b) = \frac{1}{a} \int_{t_i}^{t_f} pr(t) \psi\left(\frac{t-b}{a}\right) dt, \quad (5.2)$$

where $pr(t)$ is a time-series of precipitation, either on daily or pentad scales and $W_f(a, b)$ is the matrix of the covariant transform and t_i and t_f are the start and end time-points. No statistical treatment, normalization or anomaly, *a priori*, is calculated on the precipitation time-series $pr(t)$ so the units of W_f are the same as the precipitation time-series (e.g. mm d⁻¹).

Monsoon timings can be observed as sharp changes to precipitation, i.e., rainfall sharply increases at onset and sharply decreases at retreat. However, measuring these changes can be difficult since precipitation time-series are typically noisy. The Haar wavelet is useful in these cases for signal detection since the wavelet transform

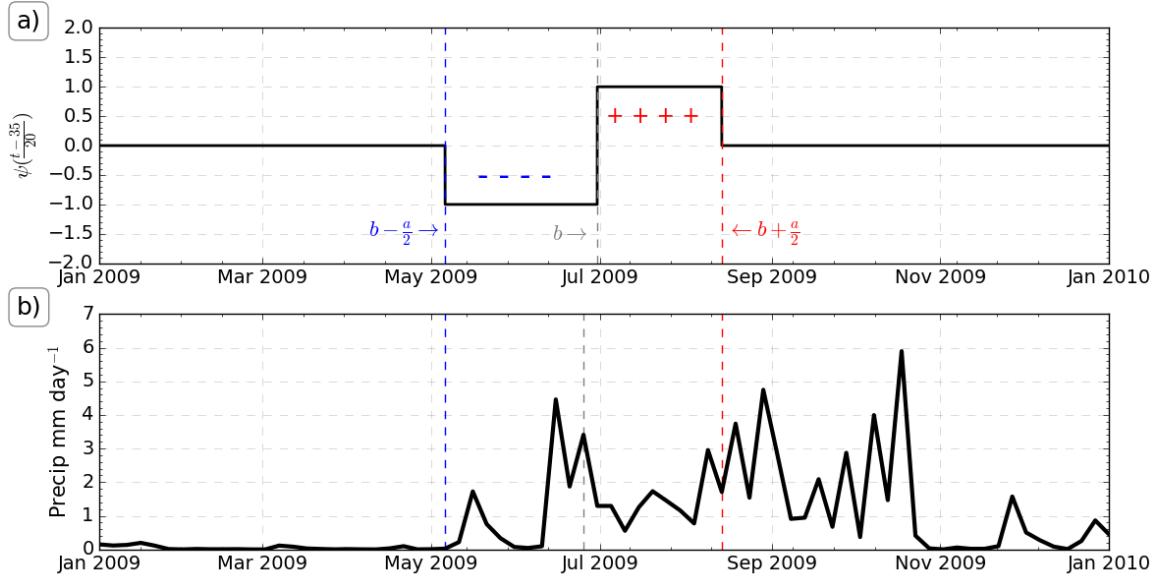


Figure 5.1: (a) Haar wavelet at a dilation $a = 20$ and translation $b = 35$, which is the 35th pentad around June 22. The positive and negative parts of the wavelet are highlighted in red and blue, respectively. (b) CMAP precipitation in 2009 in the North American Monsoon [20-27°N, 110-103°W].

is interpreted as gradients across different temporal scales and can smooth out the high-frequency variability using sufficiently large dilation scales. In other words, the wavelet covariant transform ($W_f(a, b)$) measures gradients on a dilation scale a for each time-step (b).

Figure 5.1 shows the Haar wavelet and one year of observed precipitation in the North American Monsoon from the CMAP dataset. Figure 5.1a illustrates how the wavelet function compares the observed signal in the interval $b < t \leq b + \frac{a}{2}$ with the values of the signal in the interval $b - \frac{a}{2} \leq t < b$ where b in this case is a pentad time step. The wavelet transform coefficient for dilation $a = 20$ pentads at the translation of $b = 35$, i.e., pentad 35, is a measure of the precipitation difference between the sum of the observed rainfall 10 pentads after pentad 35 and the sum of the observed rainfall 10 pentads before pentad 35 as illustrated in Figure 5.1b.

Figure 5.2 shows an example of the wavelet transform (WT) application using the observed climatological precipitation in the North American Monsoon in four different precipitation datasets. The mean climatological rainfall rates (upper panel) differ in their peak summer rainfall rates but qualitatively show similarities in the

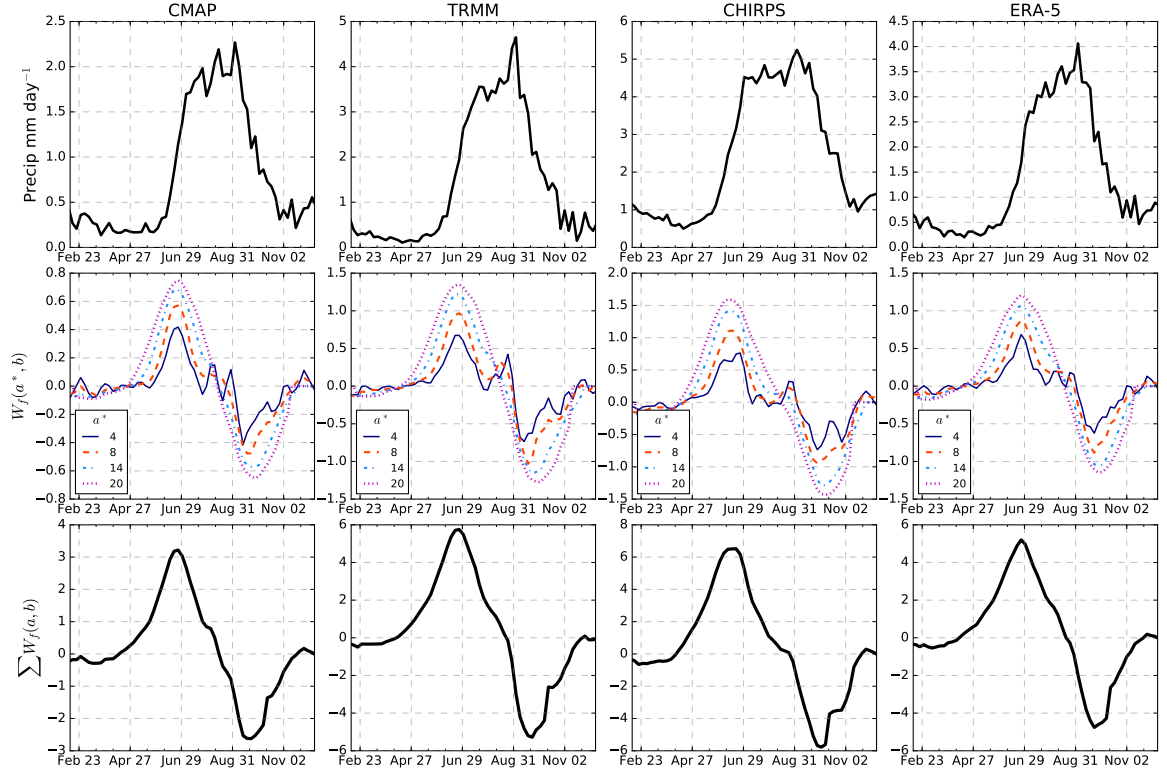


Figure 5.2: (upper) Climatological pentad-mean precipitation in four different observational datasets in the North American Monsoon [19–35°N, 110–103°W]. (middle) The wavelet transform coefficients (mm d^{-1}) for four different dilations a . (lower) The sum of the wavelet transform coefficients (mm d^{-1}) over dilations $a = 4, 8, 14, 20$.

start and end dates of the rainy season. The wavelet transform coefficients ($W_f(a, b)$ in the middle panel) for a small dilation $a = 4$ are relatively noisy but show a clear maximum and minimum that correspond well with the maximum and minimum of longer dilations ($a = 14, 20$). The sum of these four coefficients at each translation or pentad b , highlight a maximum found around June 22 and a minimum found around September 21st, which agree well with previous results of mean onset and retreat dates in the North American Monsoon (e.g. Arias et al., 2012; Geil et al., 2013).

Local maxima in the wavelet transform highlight positive steps in the precipitation time-series with a coherent scale of a pentad steps. This interpretation is then extended to diagnose monsoon onset. The pentad (b^*) corresponding to the maximum of the sum of the transform over a set of scales is defined as monsoon onset (MO), i.e:

$$MO = b^* \Leftrightarrow \sum_{a_0}^{a_f} W_f(a, b^*) = \max \left(\sum_{a_0}^{a_f} W_f(a, b) \right). \quad (5.3)$$

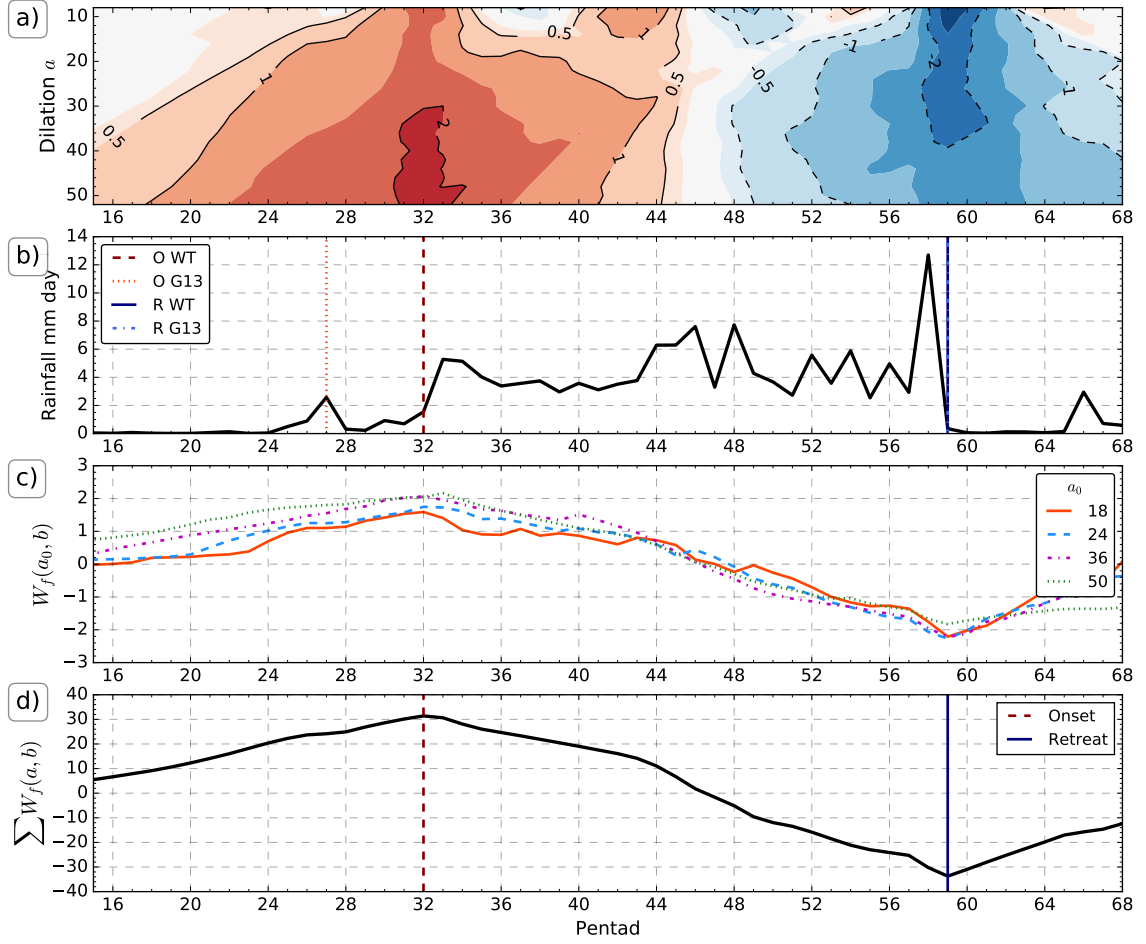


Figure 5.3: Example determination of monsoon onset and retreat dates for the North American Monsoon [20-27°N, 109-103°W] in the TRMM dataset for 2009. (a) Wavelet transform coefficient matrix (mm d^{-1}) as a function of time and dilation coefficient a . The shading is from -3 to 3 mm d^{-1} with an interval of 0.5 mm d^{-1} . (b) Observed precipitation, the onset and retreat dates as determined by the wavelet transform (WT) method (dashed) and Geil et al. (2013)'s threshold method (solid) are shown. (c) The wavelet transform coefficients for different dilations. (d) The sum of the WT ($\sum W_f(a, b)$) (mm d^{-1}); the maximum and minimum are shown in red and blue, representing onset and retreat pentads, respectively.

where a_0 and a_f are the limits of the pentad scales, i.e., the dilation coefficients, b^* is the pentad of maximum $\sum W_f(a, b)$ and the monsoon onset pentad. Similarly, the monsoon retreat pentad is found at the minimum of the sum of the wavelet transforms, i.e.,

$$MR = b^* \Leftrightarrow \sum_{a_0}^{a_f} W_f(a, b^*) = \min \left(\sum_{a_0}^{a_f} W_f(a, b) \right). \quad (5.4)$$

In other words, we seek to find monsoon onset and retreat using the maximum

and minimum the wavelet power spectrum over a range of temporal scales. Several sensitivity tests were performed with different dilation coefficients (a) in the different observational datasets, models and regions and a set or vector of dilation scales was found to be optimal to be used for all purposes. The set of dilation coefficients $\vec{a} = (28, 30, \dots, 54)$ was found to be robust, i.e., was able to capture the onset and retreat dates in all the datasets.

5.3.1 Identification of Monsoon Onset and Retreat

Monsoon onset is defined as the maximum sum of wavelet coefficients, capturing positive gradients within the scales of 14 to 27 pentads (half of the elements of vector a defined above). Monsoon Retreat has a similar definition, capturing the greatest negative gradient of precipitation over the same pentad scales.

For example, Figure 5.3 illustrates the method in the North American Monsoon in the TRMM dataset for 2009. Figure 5.3a shows the WT coefficient matrix, showing the changes in precipitation for dilations ranging from 10 to 40. A clear signal of positive coefficients is observed between pentads 28 to 34 and a similar negative signal observed in pentads 56 to 60. Figure 5.3b shows the time-series of the observed precipitation, which suggests that monsoon onset occurs sometime between pentads 28 and 34. Observed rainfall rapidly decreases after pentad 59 suggesting that monsoon retreat can be diagnosed around this pentad.

Figure 5.3c shows the WT coefficients as a function of pentad for several dilations (a_0). The coefficients for all scales seem to follow a very similar behaviour, increasing during spring to reach a maximum around pentad 32 and thereafter decreasing to a minimum around pentad 59. When the sum of the wavelet transform coefficients across the dilations is computed (Figure 5.3d) this behaviour becomes much clearer. The maximum and minimum are found at pentads 32 and 59, respectively and these pentads define the onset and retreat times. For comparison, the results from the method of Geil et al. (2013) are shown in Figure 5.3b, indicating that this method may have found an earlier onset.

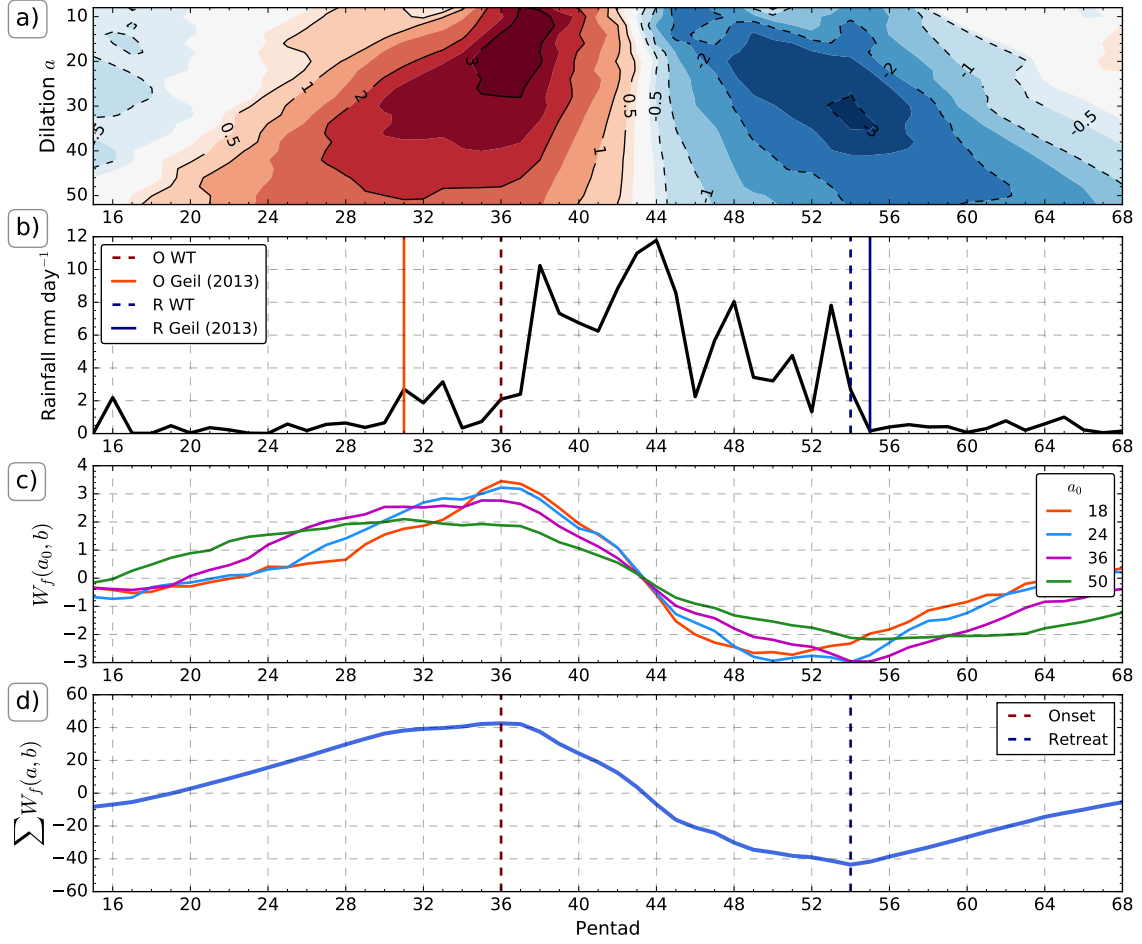


Figure 5.4: As in Figure 5.3, but for a year (1875) in the HadGEMGC3.1 N216 pre-industrial control simulation.

As a proof of concept, Figure 5.4 shows a similar example using precipitation area-averaged in the same region but using model data from the piControl simulation of HadGEM3 GC3.1 N216. The results show that the WT method can capture the onset and retreat dates with relatively high skill and that these dates are different from the dates computed using the method of G13, with the threshold method suggesting an earlier onset and a later retreat.

5.3.2 Extension for Application to the MSD signal

The wavelet method can be extended to characterise the shorter scale variations of precipitation of the MSD in Central America and the Caribbean. First, the monsoon onset and retreat dates are determined in the time-series from the area-averaged

precipitation in the MSD region via the approach described in the previous section. Once the onset and retreat dates are established, an additional wavelet analysis determines the dates in which the MSD starts and ends. The onset and end of the drier period of the MSD can be found by computing the wavelet transform again but using smaller dilations and over a limited temporal range. In particular, the WT is only calculated in the 20 pentads before and after the dates defining monsoon retreat and onset, respectively. The MSD Onset (MSDO) and MSD End (MSDE) are defined as the minimum and maximum, respectively, of the sum of the wavelet transforms (equations 5.3 and 5.4) using dilation coefficients $\vec{a}^* = (10, 12, \dots, 24)$.

Figure 5.5 illustrates the use of the WT method to determine the dates of MSDO and MSDE for the precipitation of 2017 in ERA-5. Figure 5.5a depicts the wavelet covariant transform matrix, showing the W_f coefficients for each dilation a at each pentad b . The onset of rainfall is diagnosed around the time-steps of highest positive W_f coefficients – around pentads 24 to 32 for almost all dilations. These positive coefficients are followed by a period of negative values from pentad 32 to pentad 40, which represent the decrease in precipitation, or relative drought, in the midsummer. The MSD is followed by another period of positive coefficients from pentad 44 to pentad 52, illustrating the so-called second peak of precipitation and, finally, a period of negative coefficients associated with monsoon retreat.

The coefficients of the wavelet transform ($W_f(a_0, b)$) for selected dilations a_0 (Figure 5.5c) show that the smaller dilations are more sensitive to smaller scale variations in the time series and longer dilations better highlight the long-term change of the time series. For example $a_0 = 18$ shows signs of a MSD by showing two local maxima and two local minima, whereas $a_0 = 54$ only shows a local maximum and a local minimum associated with onset and retreat.

The maximum and minimum of the sum over all dilations (Figure 5.5) depict the rainfall onset and retreat dates, respectively. The second wavelet transform $W_f(a^*, b)$ is computed over smaller dilation coefficients (a^*) near the onset and retreat dates as described above to highlight the MSDO and the MSDE. Figure 5.5e shows the sum of the wavelet transform coefficients $W_f(a^*, b)$ and the pentad of the MSDO,

34, and MSDE, 49, corresponding to the minimum and maximum of the sum of these wavelet transform coefficients, respectively.

The strength of the MSD can be measured through the maximum and minimum sum of the coefficients $\sum W_f(a^*, b)$ used to define the start and end dates of the MSD. For example, in Figure 5.5e the minimum of the $\sum W_f(a^*, b)$ was -20 mm d^{-1} found

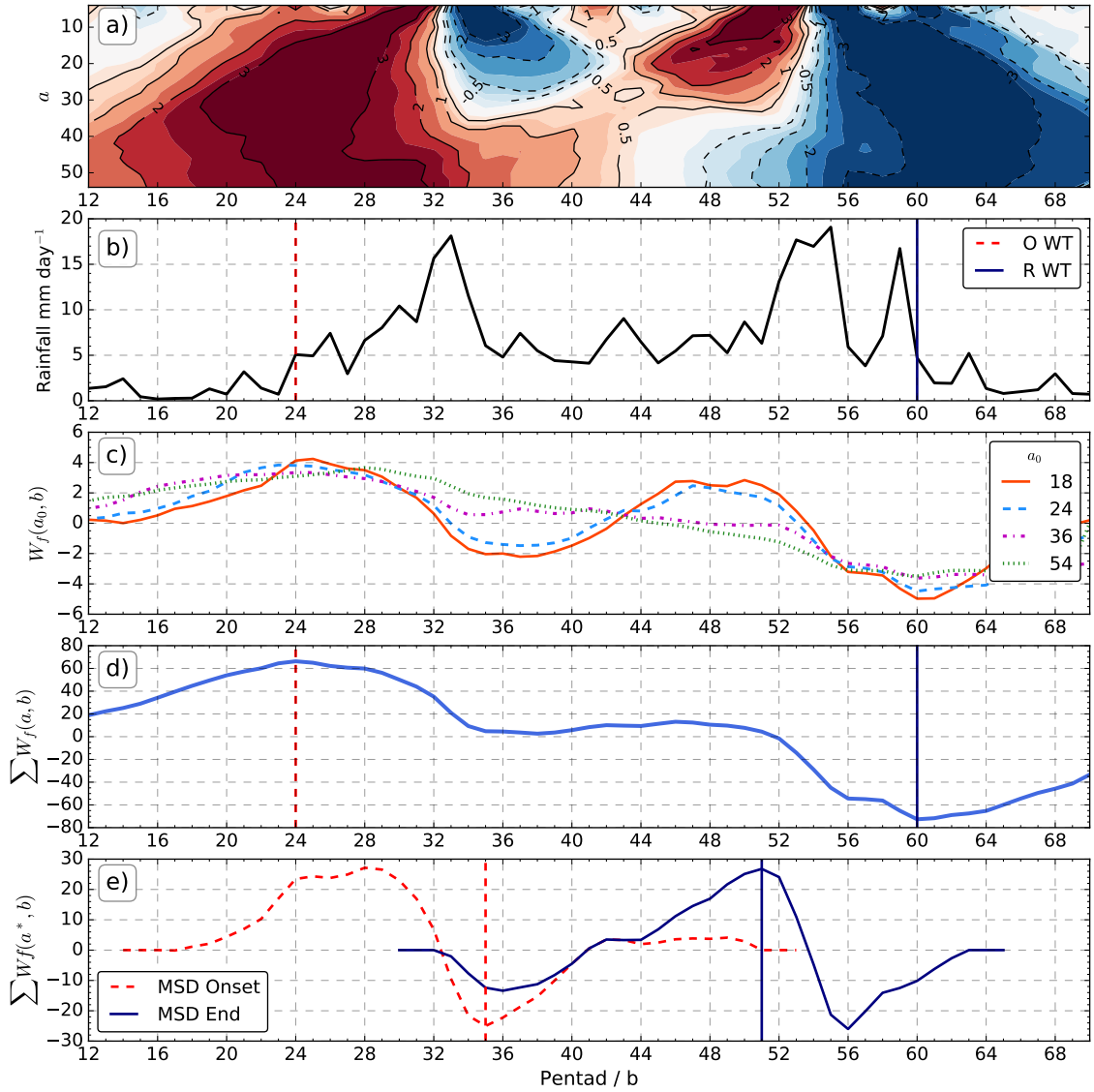


Figure 5.5: Example characterisation of the MSD [11-19°N, 95-85°W] using ERA-5 data for 2017. (a) Wavelet transform spectra, (b) observed precipitation with the onset and retreat pentads shown in red and blue, respectively. (c) Wavelet transform coefficients for four different dilations (mm d^{-1}). (d) The sum of the wavelet transform coefficients (mm d^{-1}) for $a = 28, \dots, 51$. (e) The sum of $W_f(a, b)$ (mm d^{-1}) for dilation coefficients $a = 12, \dots, 24$ showing the start (MSD Onset) and end (MSD End) of the midsummer drought.

at pentad 35 and an opposite local maximum of $+20 \text{ mm d}^{-1}$ at pentad 49. These two values, hereafter *coef1* and *coef2*, provide a quantitative measure of the strength of the MSD for this year in this dataset and will be used to measure the spatial variability of the magnitude of the MSD in the different datasets.

5.3.3 Comparative Methodologies

For validation purposes the wavelet transform method is compared with existing methods that determine onset and retreat in the North American and Indian monsoons. The threshold methods of Geil et al. (2013) (hereafter G13) and Arias et al. (2012) (hereafter A12) are compared to the results of the wavelet transform in the North American Monsoon. G13 used a threshold of 1.3 mm day^{-1} for at least 3 days for onset and 7 days for retreat for daily TRMM observations. In this study we adapt this method for TRMM to the same threshold value, but the onset pentad is the first pentad above the threshold whereas for retreat, we require rainfall to be below the threshold for two consecutive pentads. The method of A12 defines onset with two conditions. The first condition to find the onset pentad is that six out of the eight subsequent pentads must have rain-rates above the annual-mean climatological rainfall. The second condition is that at least six out of the eight previous pentads must be below the annual-mean climatological rainfall. The opposite definition is used to determine the pentad of monsoon retreat.

In the Indian Monsoon region, a commonly used method is known as the hydrologic onset and withdrawal index (HOWI) based on moisture transport over the Arabian Sea (Fasullo and Webster, 2003; Sahana et al., 2015; Chevuturi et al., 2019). To compute the HOWI index, first, the vertically integrated moisture transport (VIMT) is computed from daily ERA-5 data in the Arabian sea, as described by Fasullo and Webster (2003), i.e.:

$$\chi = \frac{1}{g} \int_{p_0}^0 q \mathbf{V} dp, \quad (5.5)$$

where χ is the VIMT, g is the gravitational acceleration, p are the pressure levels, q is the specific humidity and \mathbf{V} is the wind vector. The VIMT is then normalized using the transformation:

$$HOWI = 2 \left(\frac{\chi - \min(\bar{\chi})}{\max(\bar{\chi}) - \min(\bar{\chi})} \right) \quad (5.6)$$

where χ is the unnormalized time-series, $\bar{\chi}$ is the mean seasonal cycle of the unnormalized index and HOWI is the normalized index. The onset date is defined as the first day of each year where the HOWI index is greater than zero and the retreat date is the first day after the onset date that the HOWI index is negative (Fasullo and Webster, 2003; Sahana et al., 2015). The necessary daily data of moisture and wind speed on sufficient vertical levels to compute the HOWI index in the MOHC submissions to CMIP6 was not available, so the HOWI index can only be computed using ERA5 and will be compared to the WT method used on the observational gridded datasets.

5.4 Results

The onset and retreat dates were determined for each year in each observed and model dataset for the Indian, North American and MSD regions using the methods described in the previous section. The calculations were performed for area-averaged precipitation time-series representative of the core regions defining these monsoons. Calculations were also made at grid-box scales to illustrate the spatial distribution of the onset and retreat dates.

5.4.1 The North American Monsoon

Table 5.1 shows the onset and retreat dates of the North American Monsoon estimated using the G13, A12 and WT methods. The table reports the results for three observational datasets, ERA-5 reanalysis and five climate model experiments. The observations generally agree that the onset date is found at pentad 33 (around June 15), according to the WT and the method by G13. However, the method of G13 generally places the retreat date one pentad after the WT method, i.e., around October

Table 5.1: Mean (standard deviation) pentads of monsoon onset (O) and retreat (R) in the North American Monsoon [110°-103°W, 20°-27°N] for observational datasets, reanalysis and model output with the wavelet transform method WT, G13's and A14's method. Pentad 34 corresponds to the period between June 17-22 and pentad 54 to the period Sep 27 - Oct 1. The results from the WT method in the model experiments that are statistically different to both the CMAP and CHIRPS results to the 95% confidence level, according to a Welch's t-test, are shown in bold.

Dataset / Experiment	WT O	WT R	G13 O	G13 R	A12 O	A12 R
TRMM	33.3 [±1.8]	55.8 [±1.9]	33.0 [±1.7]	56.6 [±1.4]	30.4 [±1.7]	53.8 [±2.0]
CMAP	33.2 [±1.6]	55.0 [±2.1]	36.0 [±3.3]	55.7 [±1.8]	31.7 [±3.0]	54.5 [±3.3]
CHIRPS	32.5 [±1.5]	54.7 [±1.9]	33.6 [±1.7]	56.1 [±1.4]	30.1 [±1.7]	53.6 [±2.5]
ERA-5	33.5 [±1.8]	55.5 [±2.0]	33.6 [±1.8]	56.4 [±1.4]	30.9 [±1.7]	53.3 [±2.3]
GC3 N216- pi	33.7 [±2.0]	55.1 [±1.8]	32.6 [±2.5]	55.9 [±2.3]	32.4 [±2.5]	53.8 [±3.8]
GC3 N96-pi	33.7 [±2.2]	55.0 [±2.1]	32.7 [±2.9]	56.3 [±2.0]	31.9 [±2.6]	54.1 [±4.1]
GC3-hist	33.8 [±2.3]	55.1 [±2.1]	33.3 [±2.9]	56.0 [±2.2]	31.9 [±2.6]	53.7 [±4.0]
UKESM-pi	34.5 [±2.1]	54.8 [±2.1]	34.1 [±2.9]	56.1 [±1.9]	33 [±2.6]	53.9 [±4]
UKESM- hist	34.3 [±2.2]	54.3 [±2.2]	34.4 [±3.2]	55.6 [±2.1]	33.1 [±3.0]	53.2 [±4.2]

7th for G13's method and October 2nd for the WT's method. The method by A12 disagrees with G13 and the WT methods on both onset and retreat mean pentads, in both cases finding an earlier onset (pentad 30) and retreat (pentad 54).

The climate models reasonably represent the mean onset and retreat dates, as only the onset dates from two experiments of UKESM1 are statistically different from two of the observational datasets. The similarities in onset and retreat dates confirm that the seasonal cycle is very well represented by these models in the North american monsoon. The method by A12 in the simulations also produces an earlier onset and retreat dates when compared to the other two methods by about 1.5 pentads, but this is within the uncertainty range given by the interannual variability.

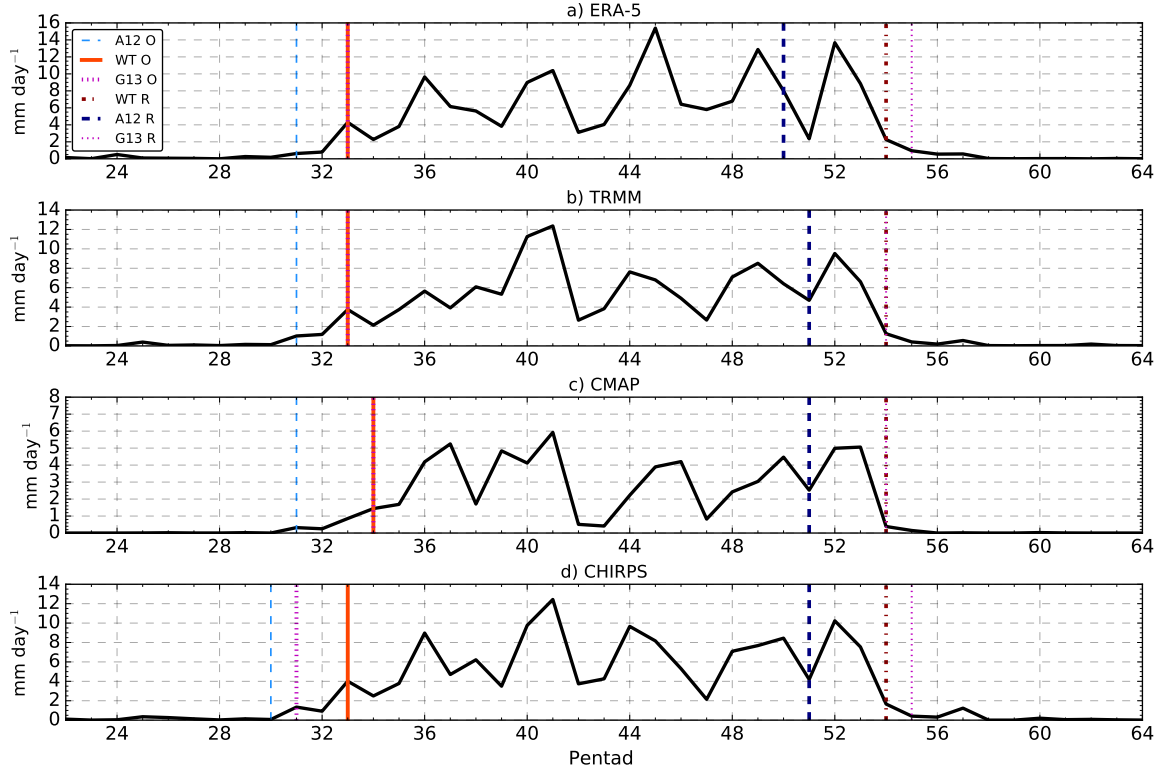


Figure 5.6: Pentad-mean precipitation for the North American Monsoon in 2010 in four precipitation datasets showing the onset and retreat pentads as diagnosed by the WT, the A12 and G13 methods. The area used to average the precipitation is illustrated in in Figure 5.7b).

Figure 5.6 compares the estimated onset and retreat dates using these three methods in the North American Monsoon in 2010 using the three observational datasets and ERA-5. The method by A12 shows an earlier onset and retreat in all the datasets whereas the WT and G13 agree in almost every dataset. The WT method is the only method that estimated the same onset date for all the four datasets and the same retreat date in three of the four datasets, with the fourth dataset delayed by only one pentad.

The meteorological changes associated with onset and retreat in the North American Monsoon are shown in Figure 5.7. The composite differences of the precipitation, wind and geopotential changes 10 days prior and after onset and retreat are compared for the three methods. The impact of monsoon onset in precipitation is slightly stronger using the method by A12 than the WT or G13. The WT method shows a very similar pattern and magnitudes of the anomalies of onset and retreat when compared to the

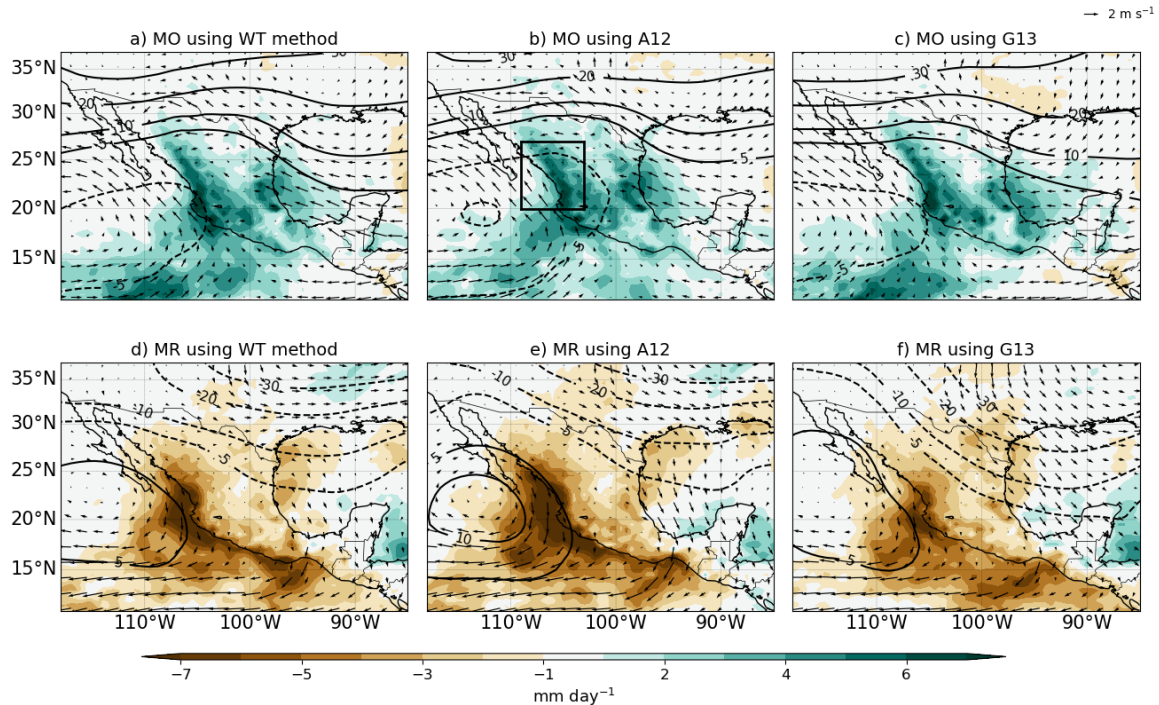


Figure 5.7: Precipitation (color contours), low level wind at 850-hPa and geopotential height (line contours) at 500 hPa anomalies for (a, b, c) the difference between the 10 days after monsoon onset and 10 days prior to onset (MO) using onset dates from (a) the WT (b) Arias et al. (2012) and (c) Geil et al. (2013). (d, e, f) are as in (a, b, c) but for monsoon retreat. The data and dates are obtained from ERA-5, and the area for the average is shown in the box in b).

other two methods. The method by G13 produces the weakest anomalies, particularly of precipitation, but very similar patterns overall.

Figure 5.8 shows the spatial distribution of the mean onset and retreat dates in the North American Monsoon region for various datasets. There is high agreement between TRMM, CHIRPS and ERA5 on the spatial pattern of mean onset and retreat dates. Onset in western Mexico is around pentad 31 (around June 1st) whereas in Chihuahua and Sonora, the rainy season begins shortly after pentad 35 (June 22). The pattern in the medium-resolution simulation GC3 N216 piControl is consistent with observations, particularly during onset. However, the spatial pattern of the mean retreat dates in the northern regions of the monsoon show an earlier than observed retreat, possibly associated with the dry bias in this region in these models (see chapter 4).

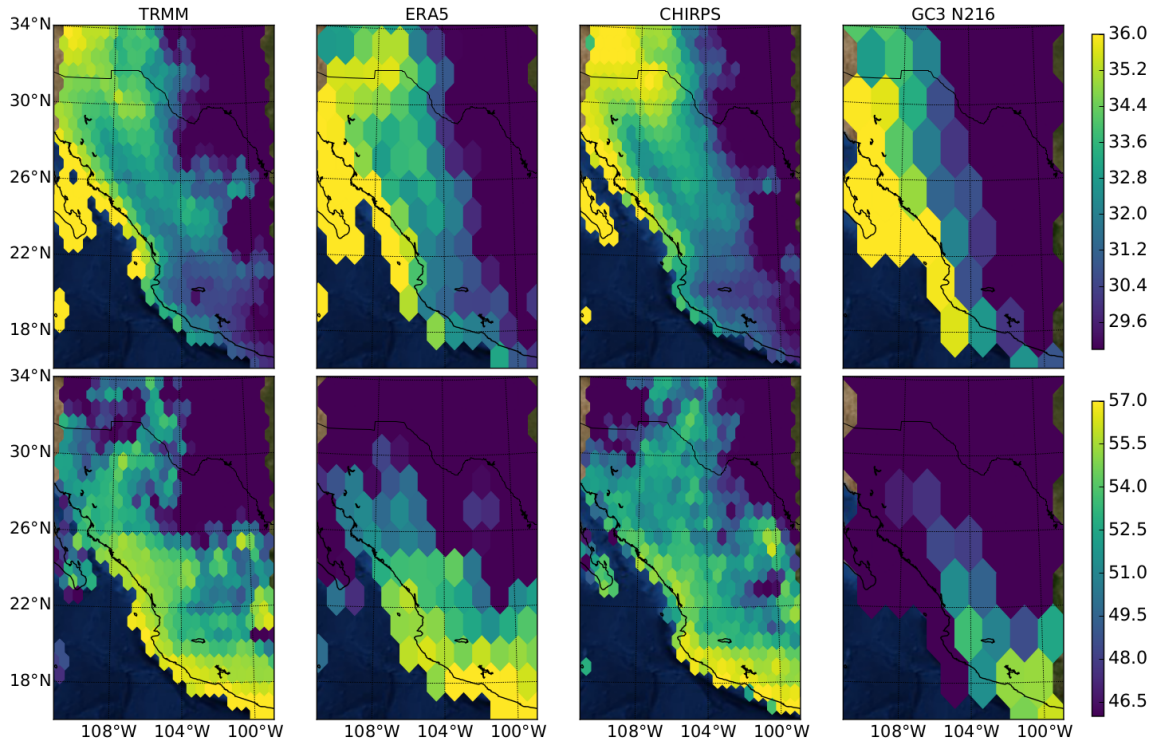


Figure 5.8: Rainfall onset (upper) and retreat (lower) mean pentads in the North American Monsoon for observations and a climate model output using the WT method.

5.4.2 The Indian Monsoon

Table 5.2 compares the mean onset and retreat dates in the Indian Monsoon computed from the HOWI index using ERA5 data and the WT used for gridded precipitation datasets. The onset and retreat dates from the HOWI index were converted from the daily to the pentad-scale to compare with the WT. The mean onset date for the HOWI index is May 27th between pentads 29 and 30, and retreat is between pentads 49 and 50, around September 3rd. The mean onset date found using the WT method for the four observational datasets was close to pentad 32, about two pentads later than the HOWI index. The mean retreat date for the WT method was about one pentad earlier than the HOWI results.

Overall, the models exhibited later than observed onset and retreat dates (4 pentads). The differences between the hydrological determination of onset and retreat dates, through HOWI, and the WT method on gridded datasets is significant, according to a Welch's t-test done between HOWI and all the gridded datasets. These

Table 5.2: Mean (standard deviation) pentads of monsoon onset (O) and retreat (R) in the Indian Monsoon using the WT method on observed, reanalysed and modelled time-series as well as for the HOWI index. The region over which precipitation was area-averaged for the WT method was [75°–83°E, 18°–24°N]. The mean onset and retreat dates that are significantly different to the 99% confidence level to the CMAP dataset are shown in bold.

Dataset	Onset	Retreat
TRMM	31.6 [± 1.8]	53.2 [± 1.9]
CMAP	31.8 [± 1.6]	53.3 [± 2.6]
CHIRPS	31.5 [± 1.4]	53.4 [± 1.9]
ERA-5	31.8 [± 1.9]	52.7 [± 2.6]
GC3 N216-pi	34.4 [± 1.3]	50.5 [± 1.9]
UKESM-pi	36.1 [± 3.1]	51.9 [± 3.2]
UKESM-hist	36.0 [± 3.9]	51.8 [± 3.3]
GC3 N96-pi	35.5 [± 1.8]	51.8 [± 2.3]
GC3-hist	35.7 [± 2.1]	51.5 [± 2.8]
HOWI (ERA5)	29.5 [± 2.3]	49.3 [± 2.4]

differences may be due to the different regions where each method is defined, i.e., HOWI is defined over the whole of the Arabian Sea where an earlier onset and later retreat would be expected when compared to rainfall over mainland India, where the WT method was applied.

Figure 5.9 shows differences between the WT (based on ERA5 precipitation) and HOWI methods, comparing precipitation and moisture fluxes at 850 hPa 10 days prior to and following monsoon onset and retreat. The HOWI index better captures the moisture transport in the Arabian Sea whereas the WT method best captures precipitation differences prior to and following monsoon onset and retreat over mainland India. In contrast, the HOWI index best captures the moisture flux in the Arabian Sea, which may be out-of-phase with precipitation over mainland.

The WT method is also able to capture onset and retreat dates and the associated anomalies within the climate model output. Figure 5.10 shows the precipitation and moisture transport anomalies around the onset and retreat of the Indian monsoon in three different climate model experiments. While the models show significant biases in the timings of the monsoon, according to a Welch's t-test (Table 5.2), the

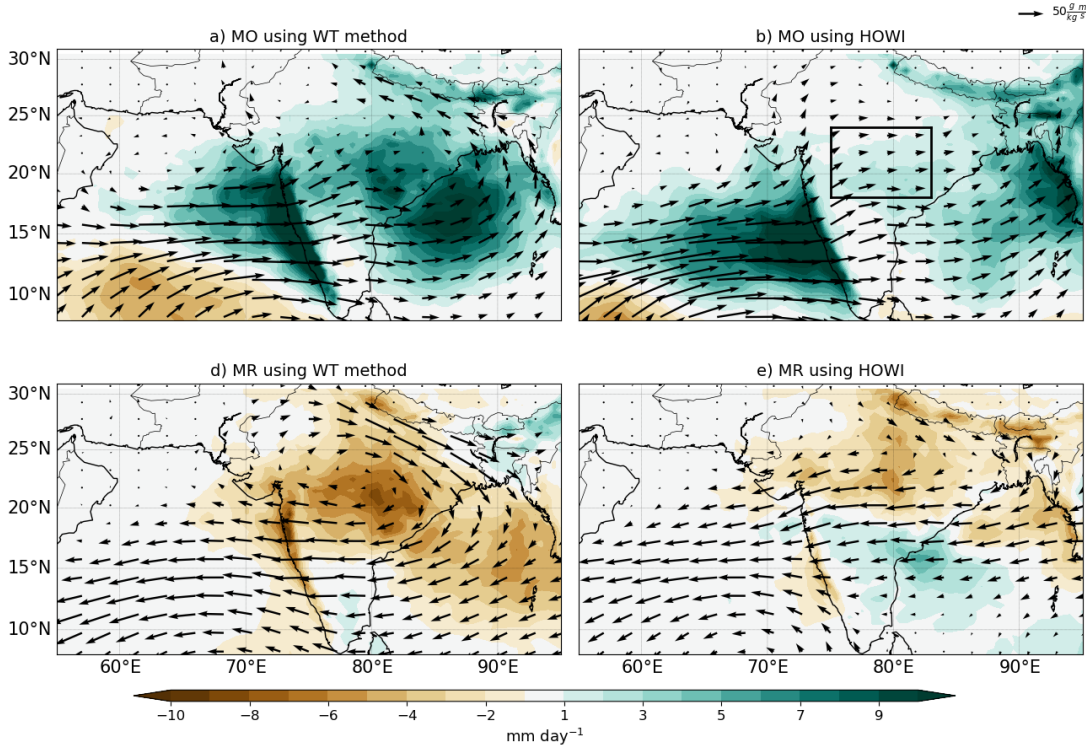


Figure 5.9: Precipitation anomalies (color contours) and the moisture vectors showing the product of specific humidity (q) and wind (\vec{u}) at 850 hPa. (a, b) shows the difference between the 10 days after monsoon onset and 10 days prior to onset (MO) using (a) the wavelet transform method (WT) and (b) the dates estimated using the HOWI index. (c, d) are as in (a, b) but for monsoon retreat. The data and calculations are from ERA-5 over the box in panel b).

patterns of rainfall and moisture transport anomalies to the observations around both onset and retreat agree well with reanalysis.

In the case of the Indian monsoon, Figure 5.11 shows that the mean onset and retreat dates vary greatly spatially on the southern tip of the subcontinent. While most of northern India has a mean onset date around pentad 33, the western coast shows an earlier onset by about one or two pentads. There is high agreement in the onset date in the three observed/reanalysed datasets over mainland India and between TRMM and ERA5 over the western coast of India. Earliest onset is found on the western coast around pentad 25-27 and extending to central India by pentad 31. The GC3 N216 simulation, however, shows a later onset than observed by about two pentads in most regions. In contrast, the spatial pattern for the mean retreat date shows higher spatial

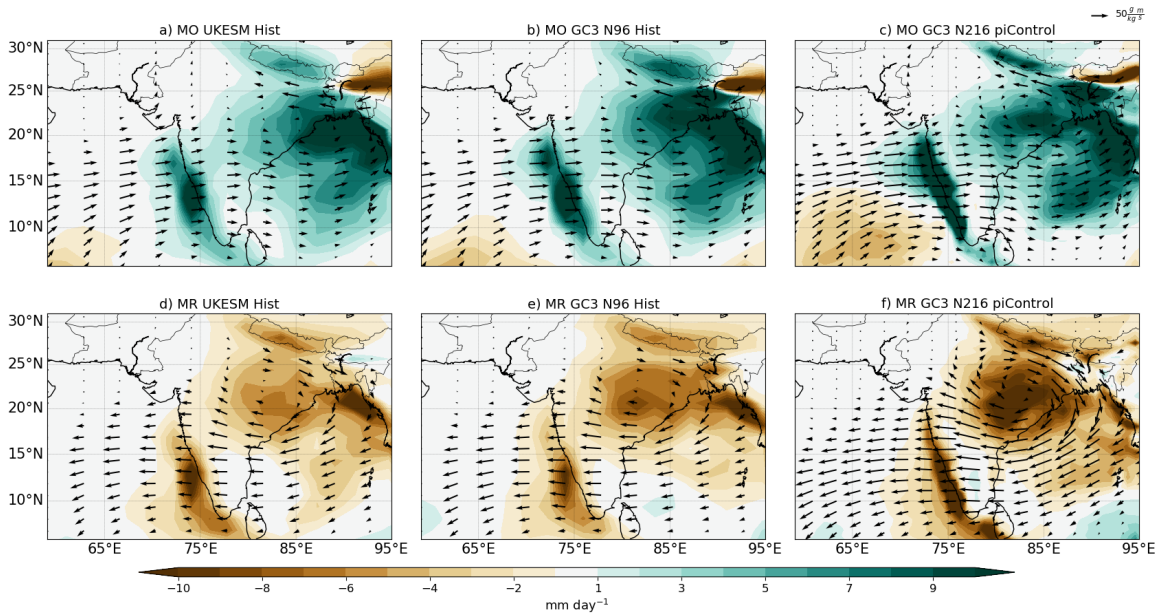


Figure 5.10: As in Figure 4.14 but showing onset and retreat for three different climate model experiments: (a, d) UKESM1 historical, (b) HadGEM3 GC3.1 N96 historical, (c) HadGEM3 GC3.1 N216 piControl.

variability between the western and eastern coasts of India. CHIRPS shows the latest retreat dates over the south-central states when compared to TRMM and ERA-5.

5.4.3 The midsummer drought

Results from the application of the wavelet transform to the MSD, including the mean onset and retreat dates as well as the start and end dates of the MSD period, are reported in Table 5.3. The mean onset date in the observations is around pentad 27 (May 14th), whereas the retreat date is around pentad 61 (October 31st). The end of the so-called first-peak period, or start of the relatively drier period (MSD), is consistently found in all the observed datasets to be around pentad 36 (around June 29th). The end of the drier period or start of the second peak is also consistently determined to be between pentads 48 to 49 in the four observational datasets. In other words, the MSD has a mean duration of 12 pentads, or around two months, from late June to late August. In the MOHC simulations, the MSD starts slightly later than observed by about two pentads, and ends about one pentad later than observed.

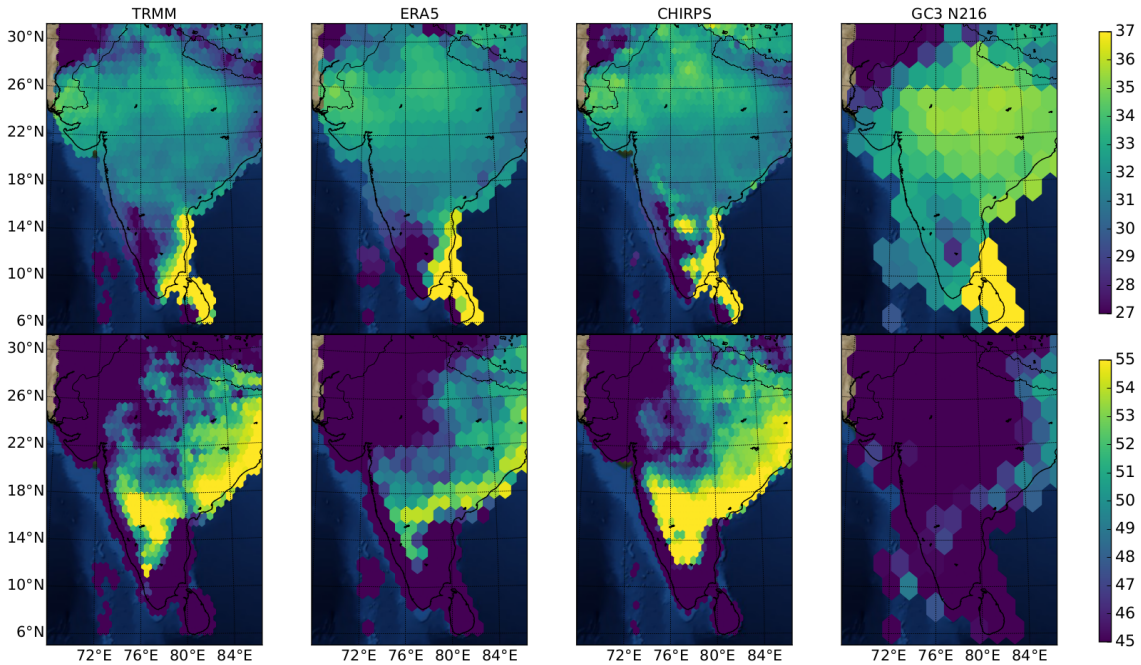


Figure 5.11: As in Figure 5.7 but for the Indian Monsoon.

Figure 5.12 shows the rainfall anomalies associated with the different periods (stages) of the rainy season in southern Mexico and Central America. These include monsoon onset and retreat, and the start and end of the MSD, the MSDO and MSDE, respectively. For each stage, we compared the anomalies computed by separating the stages using the WT method or the dates of the climatological monsoon onset, retreat, MSDO and MSDE as found in Table 5.3. In this way, the ability of the WT method to characterise rainfall variations is tested against a first best guess – the climatological mean dates. Overall, using the dates for MSDO and MSDE from the climatological dates results in weaker anomalies than compositing via the specific dates for each year obtained with the WT method. Even though the area-averaged signal used diagnose the different MSD stages focuses on a small region of southern Mexico and northern Central America, the anomalies associated with the onset and end of the MSD (Figures 5.12f, h) extend across the East Pacific warm pool, most of the western coast of Mexico and into to the Caribbean Sea and Cuba.

The analysis of individual years of observed precipitation in the selected area-averaged time-series showed that not all years showed a bimodal signal in the area-

Table 5.3: Mean pentads of rainfall onset (RO), rainfall retreat (RR), MSD Onset (MSDO) and MSD End (MSDE) in the MSD region [11-19°N, 95-85°W- illustrated in Figure 5.12a.] estimated through the WT method. Pentad 35 corresponds to the period between June 22-27 and pentad 52 to the period Sep 13-18. The model dates shown in bold are statistically different from CMAP and CHIRPS results to the 99% confidence level according to a Welch's t-test.

Dataset	RO	RR	MSDO	MSDE	coef1	coef2
TRMM	25.8 [±2.2]	61.6 [±3.1]	35.9 [±2.4]	49.0 [±4.1]	-9.5 [±4.2]	10.4 [±5.4]
CMAP	26.7 [±1.9]	60.6 [±3.3]	36.5 [±2.6]	48.0 [±4.2]	-7.1 [±4.2]	7.7 [±4.3]
CHIRPS	26.7 [±2.3]	61.4 [±3.1]	36.5 [±2.7]	48.3 [±3.5]	-4.7 [±2.7]	5.5 [±3.2]
ERA-5	26.5 [±2.2]	61.8 [±3.2]	36.1 [±2.7]	48.8 [±3.5]	-10.7 [±5.4]	11.8 [±6.6]
UKESM- pi	27.4 [±2.4]	61.9 [±3.2]	38.2 [±2.7]	49.1 [±2.7]	-18.2 [±8.7]	14.6 [±8.0]
GC3 N96- pi	26.9 [±2.6]	62.3 [±3.5]	37.8 [±2.1]	49.9 [±3.1]	-21.7 [±9.4]	16.8 [±8.0]
GC3 N216- pi	26.9 [±2.3]	62.2 [±3.5]	38.4 [±2.1]	50.0 [±2.7]	-23.5 [±8.0]	14.1 [±6.7]
GC3-hist	26.9 [±2.7]	62.8 [±3.7]	37.8 [±2.4]	50.3 [±2.6]	-19 [±8.7] [±10.1]	17.1 [±8.4]
UKESM- hist	28.5 [±2.7]	62.8 [±3.5]	38.7 [±2.8]	50.1 [±2.7]	-20.3 [±10.1]	14.9 [±8.3]

averaged precipitation (Fig. 5.13) in the supplementary material). In fact, a given year could be classified as having (1) a canonical two-peak structure separated by an MSD, (2) only having a first peak and an MSD but no second peak, (3) only having a second peak but no clear MSD or (4) a plateau-like monsoon season with no MSD-type variations (see Fig. 5.13).

Due to this year-to-year variability in the characteristics of the seasonal cycle, an objective measure was defined to determine whether a signal presented a robust MSD-bimodal signature. For this purpose, the WT algorithm was applied to randomly generated precipitation time-series.

The random time-series are constructed by randomly sampling observations in the wet and dry seasons. The pentad-mean onset and retreat dates from Table 5.3 were used to composite the observations into dry and wet distributions. For a random

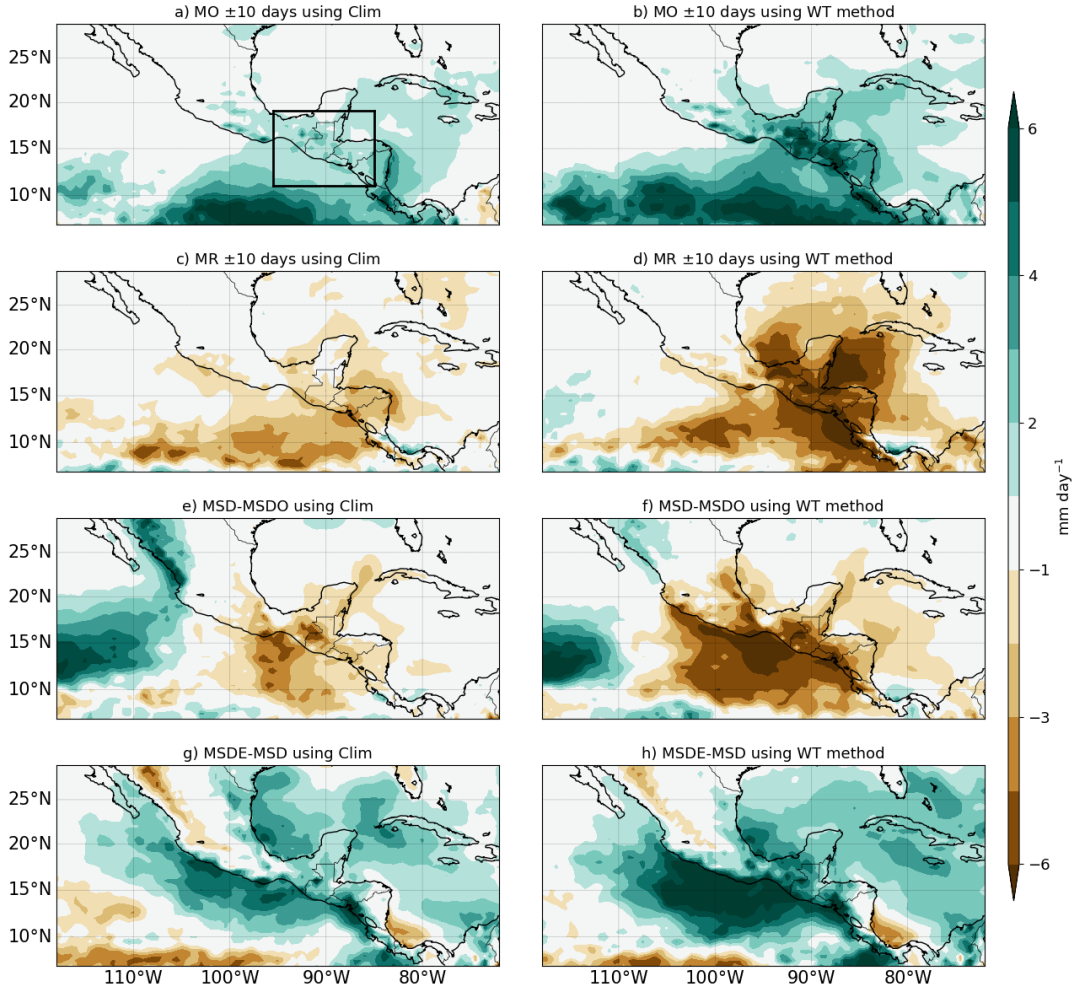


Figure 5.12: Precipitation anomalies for (a, b) the difference between the 10 days after monsoon onset and 10 days prior to onset (MO) using (a) the climatological dates of onset and (b) the dates estimated using the WT method. (c, d) are as in (a, b) but for monsoon retreat. (e, f) Difference between the Midsummer Drought (MSD) and the 10-day mean prior to the onset of the MSD (MSDO). (g, h) as in (e, f) but showing the difference between the end of the MSD (MSDE) and MSD. The data and calculations are from ERA-5. The black rectangle in a) shows the MSD area used to average the precipitation throughout this study.

time-series, the values of each pentad are randomly selected from the dry or wet distributions, depending on the pentad. In this way, the value of a given pentad of the random time-series may have been observed at a different pentad; the only constraint is that the random values come from pentads that were observed in the same season.

This approach has two advantages. First, that the approach imposes the monsoon-like feature of a sharp wet-dry contrast but secondly, the random selection in the wet

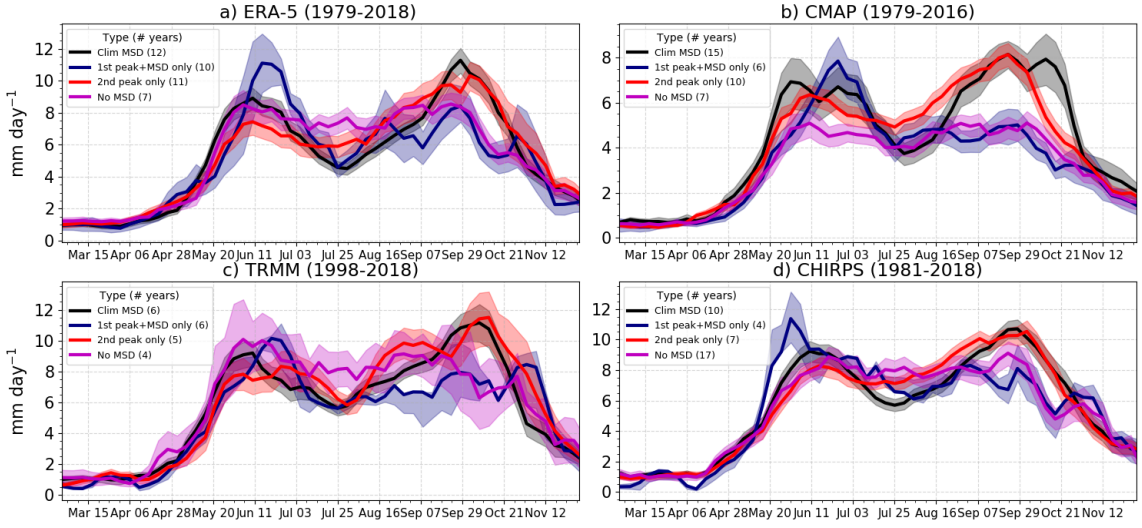


Figure 5.13: Pentad-mean precipitation in years differentiated by MSD characteristics in four datasets: (a) ERA-5, (b) CMAP, (c) TRMM and (d) CHIRPS. The shading for each line represents first to third quantile of the distribution provided a bootstrapping with replacement all the years in each composite 10000 times.

season removes the possible signal of the MSD in the climatological rainfall.

The random time series are then constructed by randomly drawing values at each pentad from the wet or dry season distributions of each dataset. Then, the WT method was used on 10,000 of these random-time series. This approach rendered a distribution of coefficients ($coef1$ and $coef2$) essentially representing the variability of the WT method applied to noise.

Figure 5.14 shows the pentad-mean time-series from two years in the TRMM dataset, and two randomly generated time-series. The coefficients $coef1$ and $coef2$, illustrated in Figure 5.14b, measure the difference in precipitation between the first peak and the MSD period and the MSD and the second peak, respectively. The first quantile of $coef1$ and the third quantile of $coef2$ provide a measure of robustness for the observed $coef1$ and $coef2$. In other words, for a year to be classified as having a robust MSD signal, the resulting $coef1$ and $coef2$ of the WT procedure must be lower and higher, respectively, than those obtained for a random time-series. The analysis of $coef1$ then determines the existence of a first-peak MSD type variability and $coef2$ determines the robustness of a possible second-peak for that year. By this

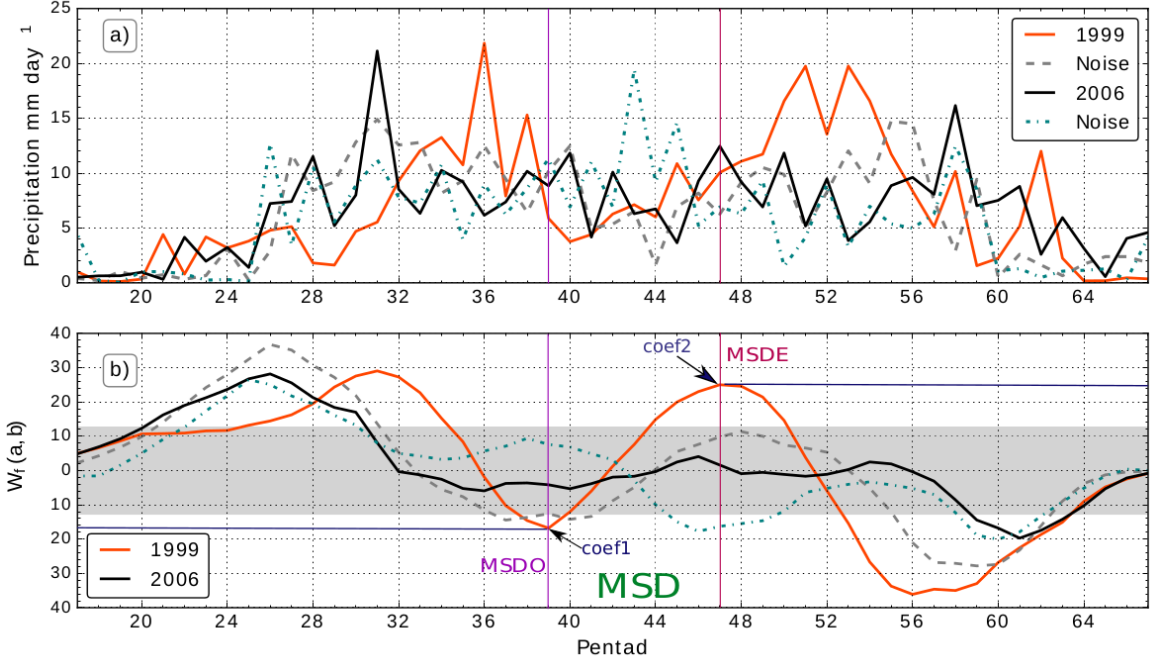


Figure 5.14: (a) Pentad-mean precipitation in two years of TRMM data: 1999 and 2006 and two randomly generated precipitation time-series (see text). (b) Sum of the wavelet transforms of the time series in (a). The shaded region in gray in (b) corresponds to the interval between the first quantile of *coef1* and the third quantile of *coef2* of 10,000 random timeseries constructed with TRMM data. The onset (MSDO) and end (MSDE) of the relatively drier period, as well as the location and values of *coef1* and *coef2* for 1999 are labelled in (b).

procedure, a given year could fit into four categories:

- Canonical MSD: *coef1* lower than the first quantile (25%) of random *coef1* and *coef2* higher than the third quantile (75%) of random *coef2*.
- 1st peak+MSD: *coef1* lower than the first quantile of random *coef1* but *coef2* lower than the third quantile of random *coef2*. In other words, the second peak is not distinguishable from noise.
- 2nd peak only: *coef1* higher than the first quantile of random *coef1* but *coef2* higher than the third quantile of random *coef2*. In other words, the second peak is distinguishable from noise, but there is no first-peak + MSD structure.
- No MSD: *coef1* higher than the first quantile of random *coef1* and *coef2* lower than the third quantile of random *coef2*. In other words, the precipitation

time-series shows no robust signal of an MSD regime, with a first or second peak.

Figure 5.13 shows how separating years into these categories affects the pentad-mean seasonal cycle of precipitation in southern Mexico and Central America in four observational datasets. This figure also validates the above procedure as the WT method is able to robustly separate years into the different categories.

For each dataset we determine those grid-points showing a robust MSD. We use the climatological rainy and wet seasons as above, to construct the random time-series for each grid-point and estimate the random values of $coef1$ and $coef2$, repeating the procedure 10,000 times. A given grid-point is diagnosed to have a MSD when the value of $coef2 - coef1$ is higher than the third quantile of the PDF of the random time series. The value of $coef2 - coef1$ is a measure of the magnitude of the MSD since $coef2$ measures the relative strength of the second-peak compared to the MSD and therefore positive in an MSD grid-point and $coef1$ compares how dry the MSD is relative to the first-peak and thus negative if an MSD regime is observed at that grid point.

Figure 5.15 shows the regions where the climatological rainfall shows a MSD signal that is distinguishable from noise, i.e., regions where the values of $coef2 - coef1$ exceed the third quantile of the distribution composited with random time-series. Cuba, western Central America and most of southern and central-eastern Mexico exhibit a robust MSD signal. This map also shows the MSD amplitude; the strongest MSD signal is found on the western coast of northern Central America and northeastern Mexico. The high correspondence between the three observational datasets shows that the method is robust across datasets. These results agree well with previous studies on the spatial distribution of the MSD (Magaña et al., 1999; Perdigón-Morales et al., 2018; Anderson et al., 2019; Zhao and Zhang, 2021). In particular, the method is able to replicate the previously reported MSD signal in the Pacific Mexican coast and the stronger MSD signal in northeastern Mexico.

Figure 5.16 shows the spatial distribution of the mean onset and retreat pentads and the start and end of the MSD, in the grid-points where the signal is significant

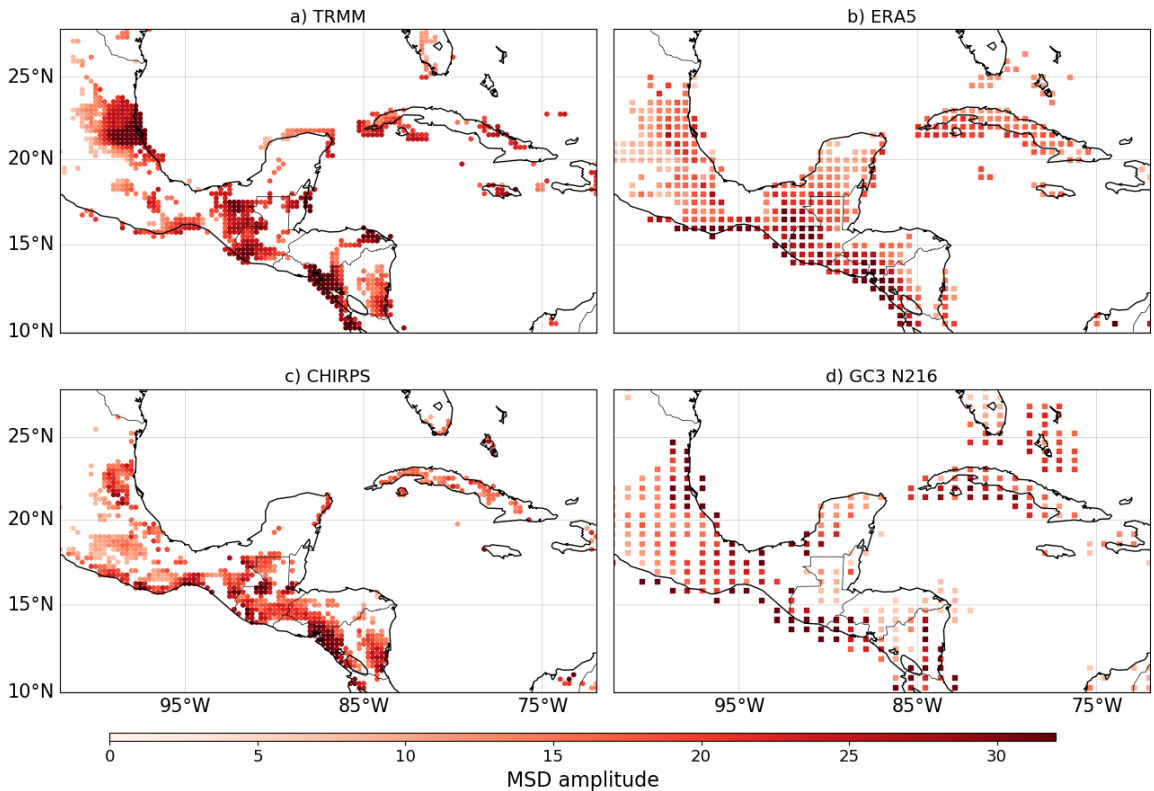


Figure 5.15: Grid points where the MSD is significantly different from noise (see section 3.3) for a) TRMM, b) ERA-5, c) CHIRPS and d) GC3 N16-pi. The magnitude of the MSD, measured as $coef2 - coef1$ is shown in colour shading.

as in Fig. 5.15. The earliest rainfall onset is found on the western coast of southern Mexico, Guatemala and El Salvador, as well as in Cuba, at pentad 25, whereas onset in the Yucatan peninsula is found at pentad 28 and even later, around pentad 31, in the eastern states of Mexico. In contrast, the retreat date seems spatially more homogeneous as northern Central American has a mean retreat date around pentad 59 and central Mexico around pentad 54. The MSD coherently starts over the western coast of Guatemala and Chiapas around pentad 33. In contrast, the MSD on the eastern Mexican states of Veracruz and Campeche begins after pentad 40. The earliest MSD end (Figs. 5.16h-j) is found in central and northeastern Mexico, around pentad 42 whereas the MSD in Guatemala ends around pentad 48.

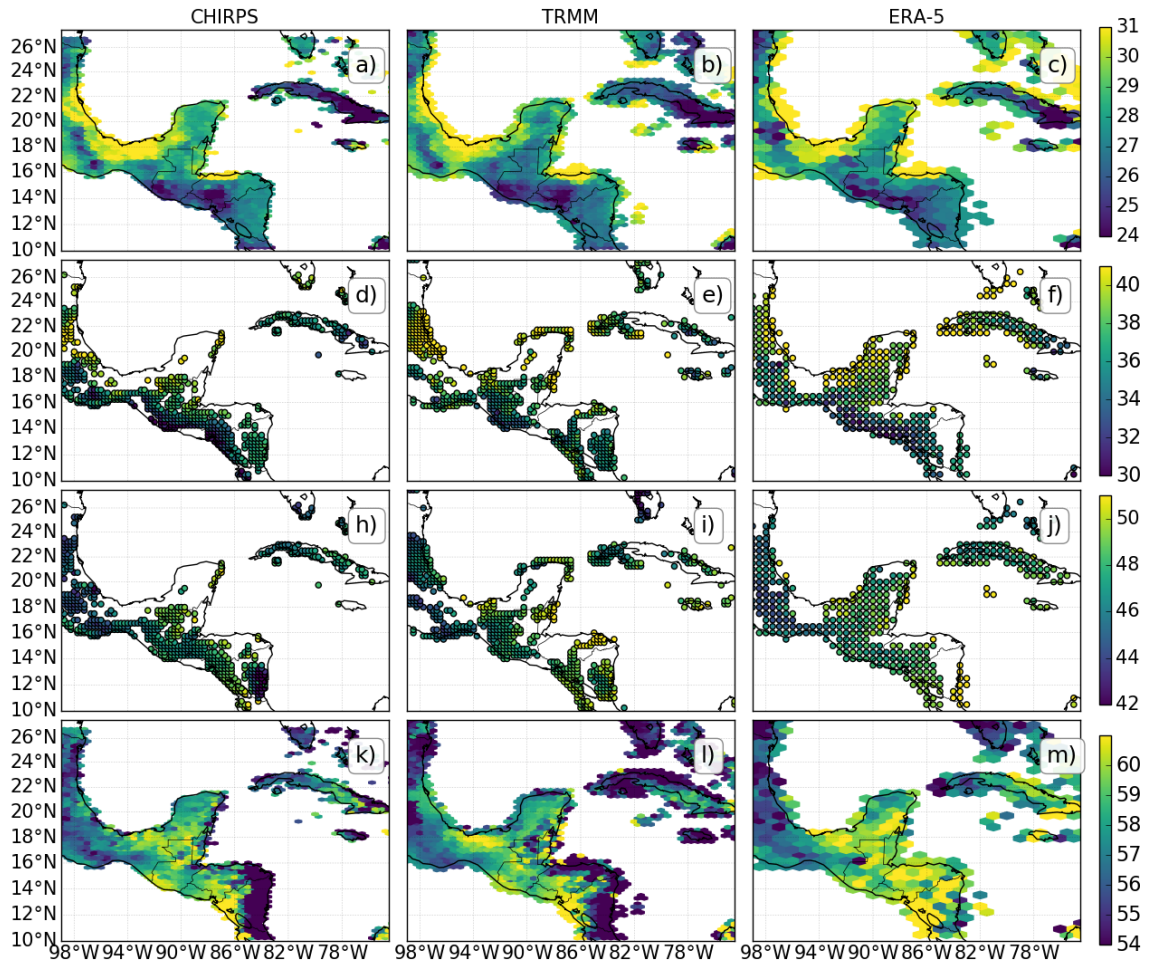


Figure 5.16: Spatial distribution of the MSD (a, b, c) onset strength and (d, e, f) MSD end strength for (a, d) CHIRPS, (b, e) TRMM and (c, f) ERA-5.

5.5 Summary and discussion

The evaluation of the MOHC submissions to CMIP6 in Chapter 4 lacked a robust assessment of the timings of the monsoon systems in the Americas. The principal reason for this was the lack of a robust, wide-spread method to diagnose onset and retreat dates in the various regions of the AMS. This chapter aimed to address this issue by developing a new method to compute onset and retreat dates for the purpose of intercomparison between observational and model data.

The novel method described in this chapter uses pentad-mean precipitation data to compute a wavelet transform over multiple temporal scales from which a set of

coefficient and diagnostics are used to determine onset and retreat dates. The wavelet function used is the Haar wavelet, a wavelet typically used to find abrupt changes in signals. Onset is defined as the maximum of the sum of the coefficients of the wavelet transform computed over a range of temporal scales or dilations. These dilations were found to provide the best results in a range from 28 to 54 pentads. Monsoon retreat is similarly defined but using the minimum of this sum of wavelet transform coefficients. The use of this method is illustrated using multiple observational datasets and climate model output. The method is compared to existing methods to find onset and retreat dates in three monsoon regions.

The method has a similar performance to existing methods that use precipitation thresholds in the North American Monsoon, as shown by the anomalies of precipitation, wind and geopotential anomalies around the onset and retreat dates. The spatial distribution of monsoon onset and retreat in this region was found to be sensibly captured by the wavelet algorithm, illustrating the earlier onset in central western Mexico and the later onset in northwestern Mexico, Arizona and New Mexico. The spatial distribution was shown to be consistent amongst the TRMM, CHIRPS and reanalysis data, suggesting that the method produces similar results in datasets with different climatologies even at the grid-box scale.

The WT method also compares well to a hydrologically defined index (HOWI) in the Indian Monsoon, although the WT better captures the precipitation variations and HOWI the moisture transport. However, the WT method is also able to capture strong differences in moisture transport around the onset and retreat dates, in both models and observations. The WT method obtains a later onset and earlier retreat than in the HOWI index, possibly associated with a lag between the moisture transport in the Arabian Sea (as diagnosed by HOWI) and the actual precipitation over mainland India (as measured by the WT method). The spatial distribution of onset and retreat dates in the Indian Monsoon region using the WT method seem to be relatively consistent and coherent amongst the observational datasets, as the mean onset date in mainland India was found at pentad 32. Onset is earliest on the western coast of India and the onset date appears to be very homogeneous in central India.

The WT method was extended to characterise the timings and strength of the South American Monsoon bi-modal regime of precipitation and the intervening Midsummer Drought (MSD) period, using the same principle but additionally computing the transform over smaller dilations around the onset and retreat dates. By using randomly-generated time-series, the spatial distribution of grid-points with a robust MSD signal was found in Cuba, the northwestern coast of Central America and several regions of south and north-eastern Mexico. The MSD in southern Mexico and northern Central America is found to start around pentads 35 and 36 (last week of June) and end around pentad 48 (mid-August) in most observational datasets and reanalysis. To our knowledge, this extension of the WT method provides one of very few methods to characterise the MSD on sub-monthly scales. This method may be potentially useful when diagnosing changes to the characteristics of the MSD in models or observations.

Current methods that diagnose monsoon onset and retreat using pentad or daily-mean precipitation time-series are typically rigid threshold methods. These threshold methods depend on a number of parameters that need to be tuned for a specific monsoon region and for a specific dataset. For instance, the method by G13 used a threshold value specific for the North American Monsoon and specific for the TRMM dataset but also to the limits of the area used for area-averaging the precipitation. In other words, the persistence and threshold values of most of the threshold methods require normalization, statistical treatment or additional tuning to the parameters to account for climatological differences in the datasets which introduces uncertainty. The method by A12 then uses a climatological mean value as the threshold, but in a climate model with a significantly positive bias in the dry winter season of a monsoon this method would be prone to error as the biased seasonal cycle may impose a biased calculation of monsoon onset and retreat.

The WT method is in many ways similar to the agronomical and threshold methods (e.g. Liebmann and Marengo, 2001; Moron and Robertson, 2014), as the implementation of the method uses a subjective determination of the dilation scales; these scales are comparable to the persistence and window parameters of the threshold methods. However, the WT method presented has three main advantages over most

threshold methods. First, the method produces robust results for the Indian and North American monsoon of onset and retreat, and spatial distributions comparable to previous methods (Moron and Robertson, 2014) while not being subject to 'false-hits' nor years without an identification of the onset and retreat dates. In other words, the method provides robust results without requiring further treatment of years with false-hits or undetermined years.

The second advantage of the method is portability, or utility, as the method shows robust and consistent results for three observational datasets, a reanalysis and climate model experiments with varying climate forcing but without any constraint or treatment of the data beforehand and in three different regions with different seasonal cycles. In other words, this method is robust across datasets and regions. In contrast to rigid threshold techniques (e.g. Liebmann and Marengo, 2001), the identification of onset and retreat for each time-series, e.g. at each grid-point, is based upon coherent temporal changes within each precipitation time-series while not using parameters determined 'a priori' specifically for a region. The WT method then, can be used in any time-series, regardless of the origin of the time-series, without any further change or consideration than those established by the dilations scales determined in section 2.2.1. The portability of the method also means that the method can be implemented as a 'local-scale' method applied at the grid-box scale for high-resolution datasets such as CHIRPS as well as for regional scales using area-averaged time-series.

Third, and in contrast to typical threshold methods, the wavelet method can be applied to climate model output straightforward using the same configuration of dilation scales, a feature of the method that is illustrated by our analysis of several experiments using the Hadley Centre models. The treatment of the data does not require any normalisation or statistical treatment even when used for grid-point time-series for different regions or experiments with varying forcing where the seasonal cycle or total annual rainfall may change notably within the model time-series.

While we do not suggest the WT method is better or superior than any others for all purposes, we argue that the method may be potentially useful for multiple

purposes due to its portability and robustness. For instance, for climate model inter-comparison analyses which require the determination of onset and retreat in data that may have different seasonal cycles, magnitudes and resolutions. In addition to CMIP-style assessments, the method may be used in analyses of the observed trends in mean onset and retreat dates which may benefit from an independent method of validating the results from other methods or may use several datasets to support their findings. In conclusion, the WT method is designed to be multi-purpose, to be used in varying contexts, from a local grid-scale analysis of the 'agronomical' onset or in global-scale analyses of the onset and retreat of the global monsoon while also being useful for the determination of bimodal regimes, such as those found in Central America and the Caribbean.

6

Mechanisms of the Mesoamerican midsummer drought in the Met Office CMIP6 experiments

The physical mechanisms that account for the seasonal cycle of precipitation in southern Mexico and Central America remain debated and this lack of understanding becomes critical with the prospect of greenhouse gas-driven changes to the regional circulation and precipitation patterns, the understanding of these mechanisms for the seasonality of rainfall in the region becomes key for climate awareness and adaptation. This chapter revisits the problem two previously posed physical mechanisms that give rise to the Midsummer drought in the newewst reanalysis ERA5 and a number of CMIP6 experiments from the Met Office Hadley Centre models: HadGEM3 and UKESM1. The roles of the East Pacific sea-surface temperatures and cloud radiative effects, as well as of the Caribbean Low-Level Jet are investigated. A thermodynamic diagnosis of the MSD is also performed via the analysis of the moist static energy budget and the surface entropy on both reanalysis and model data.

6.1 Introduction

A bimodal signal in the climatological seasonal cycle of precipitation has been documented in several regions of southern Mexico, Central America and the Caribbean; most commonly referred to as Midsummer drought MSD (Mosíño and García, 1966; Magaña et al., 1999; Gamble et al., 2008; Perdigón-Morales et al., 2018; Zhao et al., 2020). In spite of several decades of research, a clear depiction of the physical mechanisms that cause the bimodal seasonality of precipitation remains elusive. A relatively large number of hypotheses that argue for different mechanisms causing the MSD, with some studies focusing on the Caribbean MSD (Martinez et al., 2019) and others on the Mesoamerican (Central America and southern Mexico) region (e.g Perdigón-Morales et al., 2018). Section 2.3 provides a literature review of the mechanisms proposed in previous studies, but, in summary, studies disagree on several key aspects such as whether the bimodal signals of the Caribbean and Central America are related, or whether the two-peak structure is a result of two precipitation enhancing mechanisms or just one period of inhibited precipitation.

Amongst the most prominent hypotheses for the MSD is the radiative-convective feedback proposed in Magaña et al. (1999) and Magaña and Caetano (2005), which argues that the East Pacific SST variability controls the seasonal cycle of precipitation in a feedback process involving the incoming shortwave radiation, SSTs, high cloud cover and precipitation. In their framework, the incoming shortwave and the East Pacific SSTs are the dominant control for the bimodal distribution of precipitation.

In turn, Karnauskas et al. (2013) proposes that the MSD is associated with the biannual crossing of the solar declination angle, in a mechanism where the net surface shortwave radiation becomes the key element in controlling the surface temperature and specific humidity, i.e., the surface moist static energy, and thereby convective available potential energy (CAPE) and convection.

In contrast, a large number of studies (see section 2.3) argue that the combined effect of the North Atlantic Sub-tropical high (NASH) and the Caribbean Low-Level Jet (CLLJ) are the key factor that can explain the bimodal seasonal cycle. However,

the precise mechanism that links the CLLJ variability with rainfall in Mesoamerica differs amongst studies. The leading hypothesis suggests that the influence of the CLLJ on the regional moisture transport is the most important effect (Durán-Quesada et al., 2017; Martinez et al., 2019). Nevertheless, the question of how changes to the regional moisture transport by the CLLJ influence the easternmost Pacific and the Mesoamerican region is unclear.

The vast majority of studies of the physical climate of the region are observational and analyzed monthly-mean changes to the precipitation. Little attention has been given to this problem in general circulation models (GCMs) or regional models (e.g. Rauscher et al., 2008; Ryu and Hayhoe, 2014; Fuentes-Franco et al., 2015; Colorado-Ruiz et al., 2018), as most studies focus on future projected changes to rainfall and rarely on the mechanisms of the MSD within the models, possibly due to model biases. For example, Ryu and Hayhoe (2014) shows that out of all the models in the CMIP3 and CMIP5 cohort only a handful of realizations show signs of a bimodal signal, with the Met Office Hadley Centre (HadGEM2) model being amongst the few that could simulate the MSD.

Chapters 4 and 5 show that the CMIP6 MOHC simulations reproduce the timings and strength of the bimodal signal of precipitation with reasonable skill (Figure 6.1), albeit with a stronger first peak and a later onset of the MSD (MSDO). The characterisation of the mechanisms that produce the bimodal signal in these simulations is therefore another avenue to understand the real-world MSD, one that has not been explored to great detail. Furthermore, the analysis of the characteristics of the MSD in a GCM run under different configurations and forcings can highlight the roles of horizontal resolution, aerosol-chemical and land-surface interactions for the representation of the physical mechanisms of the MSD. Similarly, the analysis of simulations with no time-varying forcing (the pre-industrial control simulations) versus forced runs (the historical or scenario experiments) allows us to assess how greenhouse gas forcing may affect the mechanisms behind the MSD in these models.

Therefore, the purpose of this chapter is to examine previously proposed physical mechanisms for the MSD in the ERA5 reanalysis and the MOHC submissions to CMIP6.

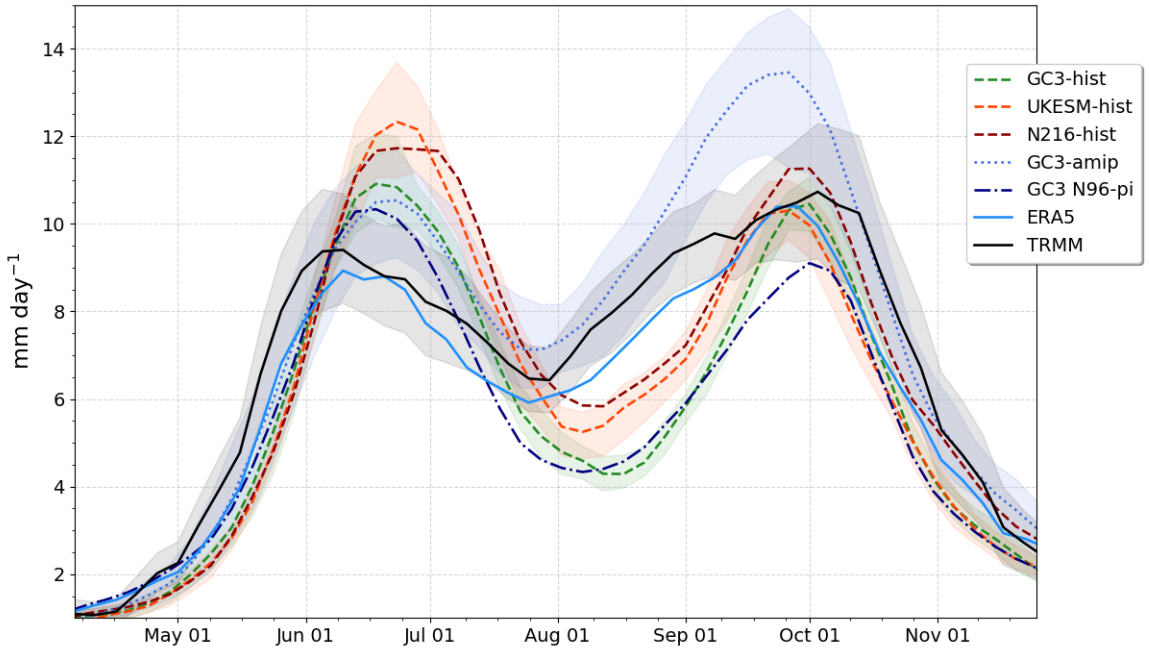


Figure 6.1: Pentad-mean precipitation in southern Mexico and northern Central America [95–86°W, 11–19°N]. The shading for the TRMM dataset is a measure of observational uncertainty obtained by bootstrapping the interannual variability 10000 times whereas the shading for the CMIP6 experiments show the ensemble spread where multiple ensembles were available.

The focus of the chapter is on the region of Mesoamerica, i.e., southern Mexico and Central America, whereas the Caribbean MSD is not directly addressed in this chapter.

The previous chapter provides a useful diagnostic tool to separate the different stages of the MSD, a wavelet transform method (WT) that diagnoses the onset and end of the rainy season, as well as the start and end of the MSD. Similarly, the WT method can provide a robust measure of whether a given year and/or grid-point exhibits a robust bimodal signal. This chapter will use the WT method to separate the different stages of the MSD to better understand how the regional dynamics and thermodynamics varies from one stage of the seasonal cycle to the next.

The remainder of this chapter is presented as follows. Section 2 describes the observational data and the CMIP6 experiments used in this chapter and a general overview of how the WT method is implemented and data is analysed. Then, section 3 evaluates the seasonality and general representation of the key features of the regional climate. Then, several previous hypotheses are tested in the simulations

and contrasted against the reanalysis/observations. The roles of the East Pacific SSTs (section 4), cloud-radiative feedbacks (section 5) and the CLLJ and moisture transport (section 6) have been highlighted in the literature and are investigated with detail in the rest of the chapter.

Convective quasi-equilibrium (CQE) and moist static energy (MSE) budgets have been successfully implemented in monsoon regions to understand mechanisms that drive precipitation changes. The remaining section of this chapter uses MSE and CQE diagnostics to evaluate the role of thermodynamics and ascent within the moist column of the MSD for the seasonal changes to precipitation.

6.2 Data and methods

6.2.1 Observations and reanalysis data

All the data used in this chapter is described in chapter 3. In particular, this chapter relies on the precipitation datasets of TRMM and CHIRPS, as well as the precipitation derived from ERA5. The rest of diagnostics are from ERA5 and unless otherwise specified the diagnostics were downloaded at the 0.75° resolution.

6.2.2 CMIP6 data

This chapter uses the output from the realizations of the HadGEM3 GC3.1 run at two resolutions at N96 and N216 and from UKESM1. These experiments described in section 3.2.2. This chapter follows the terminology and acronyms outlined in section 3.2.2.

6.2.3 Determination of the timings of the MSD

Chapter 5 describes a wavelet transform (WT) method that can determine the timings of the MSD in observational gridded datasets, reanalysis and climate model precipitation time-series. This chapter uses the WT method to determine the onset (MO) and retreat (MR) of the monsoon rainy season, as well as the onset (MSDO) and end (MSDE) of the MSD.

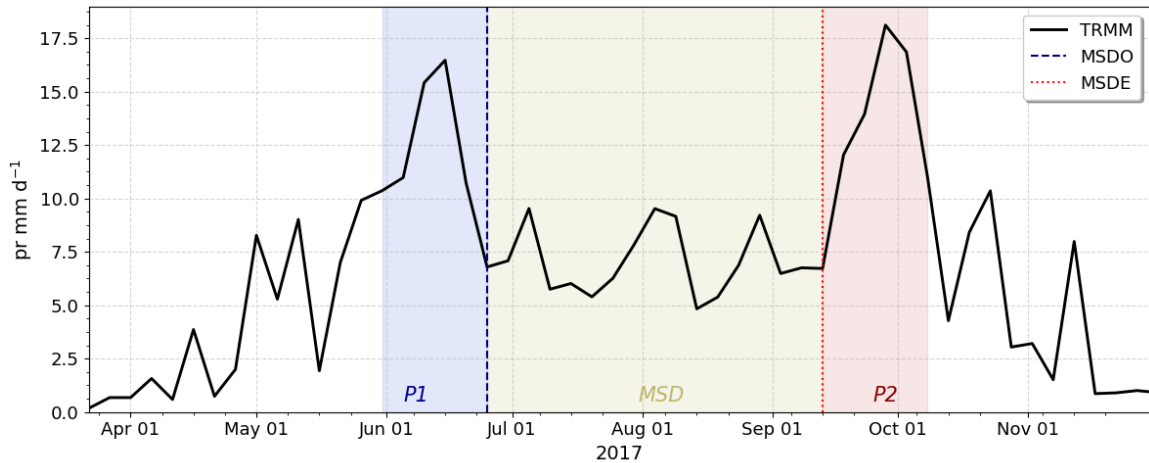


Figure 6.2: Pentad-mean precipitation the study region [95-86°W, 11-19°N] in the TRMM dataset for the summer of 2017. The timings of the onset (MSDO) and end (MSDE) of the MSD, as well as the first (P1) and second (P2) peak periods and the MSD periods are highlighted.

As a brief reminder of the method, MO and MR are determined by the maximum and minimum sum of WT coefficients computed from a dilation scale vector ranging from 24 to 54 pentads. After MO and MR are determined, a second WT is computed with dilation scales to 10 to 24 pentads and the minimum sum of the WT coefficients corresponds to the onset of the MSD and the maximum to the end of the MSD (MSDE). Similarly, the timings of the first (P1) and second (P2) peaks of precipitation are determined from the results of WT method: P1 is defined as the period between the MSDO and the preceding 4 pentads or 20 days, whereas the second peak is defined as the period between the date of MSDE and the subsequent 4 pentads. An example of this separation of the MSD timings for each year is given in Figure 6.2, for precipitation observed from TRMM in 2017 over the study region.

The area of study of this chapter is in southern Mexico and northwestern Central America (depicted in Figure 6.4) a region where Chapter 5 showed to exhibit robust and strong MSD signals. The WT method was implemented on the TRMM, CHIRPS and ERA5 datasets and in the model output over the precipitation time-series area-averaged over the study region.

6.3 Climatological features

The seasonal cycle of precipitation in the region of interest (Figure 6.1) is reasonably well simulated by several experiments of GC3, N216 and UKESM1 and by ERA5. The two-peak structure of the MSD is observed in TRMM and ERA5 as two precipitation maxima, the first peak found during early to mid-June and the second peak at the end of September, separated by a drier period that spans from late June to late August. The precipitation in ERA5 not only closely follows the precipitation variations at the pentad scale but also generally agrees with the magnitude of precipitation during the first peak, the MSD and second peak periods. The MSD in the experiments is observed one or two pentads after TRMM and ERA5 (see the mean values in the previous chapter) and shows a stronger variation of precipitation between the first peak and the Midsummer. In general, the pre-industrial control experiments show a higher magnitude of precipitation during the first peak and the MSD period whereas GC3-amip experiments are characterized by a wetter second peak.

The simulated spatial distribution of the climatological rainfall and the rainfall anomalies associated with the MSD in ERA5 agrees well with TRMM and CHIRPS (Figure 6.3). The simulations reasonably capture rainfall in the regions over land with maximum precipitation rates in the Mexican states of Campeche, Veracruz and Chiapas, as well as in Guatemala and in the East Pacific Ocean. ERA5 shows stronger precipitation differences between the MSD stages, as rainfall in the East Pacific region in ERA5 varies by more than 5 mm day^{-1} between the first peak, the MSD and the second peak. In turn, the simulations (Figure 6.4) have important biases in the magnitude of the precipitation in the East Pacific ITCZ with a positive bias of 3-6 mm day^{-1} depending on the simulation as well as a dry bias over southern Mexico and Central America, documented in chapter 4

The simulations capture the spatial patterns of the variations associated with the MSD stages. In observations and reanalysis (Figure 6.3), the MSD variations have regional scales since even though the timings used to compute the composite difference between the MSD periods were computed using a time-series averaged over

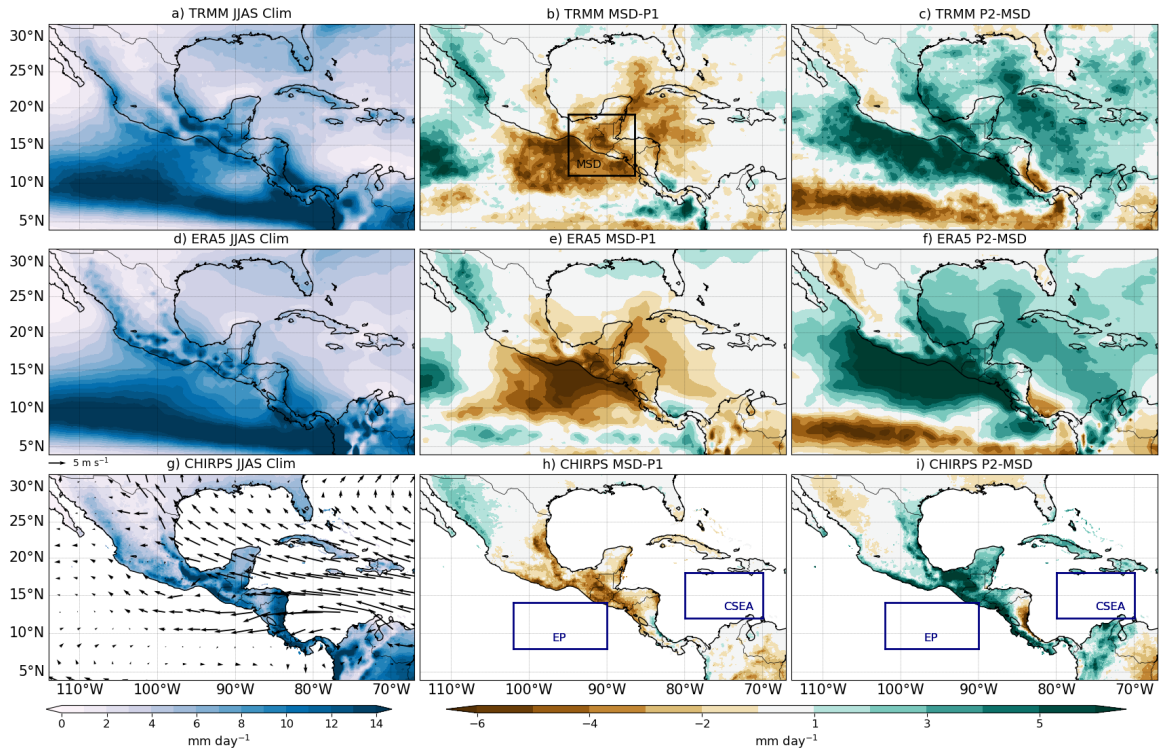


Figure 6.3: (a, d, g) Climatological JJAS rainfall and the difference between (b, e, h) the midsummer drought and the first peak periods and (c, f, i) between the second peak and the midsummer drought periods for (a-c) TRMM, (d-f) ERA5 and (g-i) CHIRPS. The climatological low-level winds (at 850 hPa) for JJAS in ERA5 are shown in c).

the study region, the precipitation differences spread south to the easternmost Pacific Ocean but also east to the Caribbean sea and into the northeastern Mexican states. The simulations also exhibit similar regional-scale patterns of precipitation differences both for the MSDO-MSD and the MSDE-MSD panels, though the precipitation differences associated with the MSD over the ocean in the models are notably larger than in the observations and reanalysis.

The mean rainfall observed in the three periods (P1, P2 and the MSD) in the simulations varied notably between model configurations and with external forcing (Figure 6.5). The scatter of the first and second peak and the MSD mean rainfall rates shows, first, that the mean rainfall in each stage is not linearly related to another, i.e., a larger magnitude of the first peak of precipitation does not necessarily imply a wetter or drier MSD period. The atmosphere-only run, GC3-amip, is a good example of this behaviour as the mean rainfall during P1 is roughly the same as in the rest of

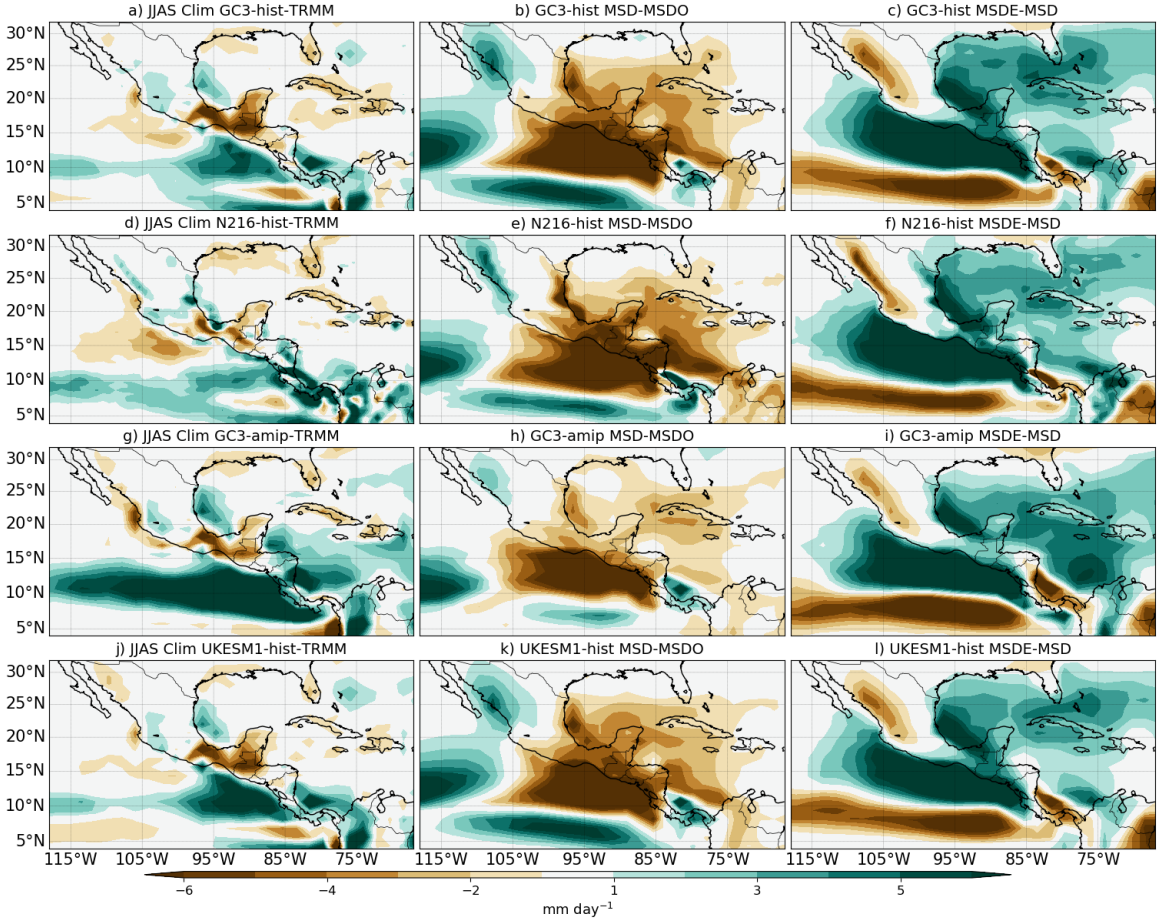


Figure 6.4: (a, d, g, j) JJAS model bias compared to TRMM and the difference between (b, e, h, k) the midsummer drought and the first peak periods and (c, f, i, l) between the second peak and the midsummer drought periods for four different simulations.

the simulations but the mean rainfall during the MSD is slightly larger than in the rest of the simulations and the P2 precipitation is largest in GC3-ampi.

Second, the magnitude of the first decrease in rainfall (MSD-P1) and the late-summer increase (P2-MSD) also show a significant spread amongst experiments, which also suggest that there is no clear association between the magnitude of the MSD and the magnitudes of the two peaks of precipitation in these simulations. The scatter of ERA5 in all panels is notably close to that of TRMM and CHIRPS, which is further evidence that the timings and strength of the MSD is well represented by this reanalysis.

The outgoing long-wave radiation (OLR) and vertical velocity (ω at 500 hPa) differences associated with the MSD (Figure 6.6) also show that the MSD is not a local-scale feature but convective activity varies coherently in neighboring regions.

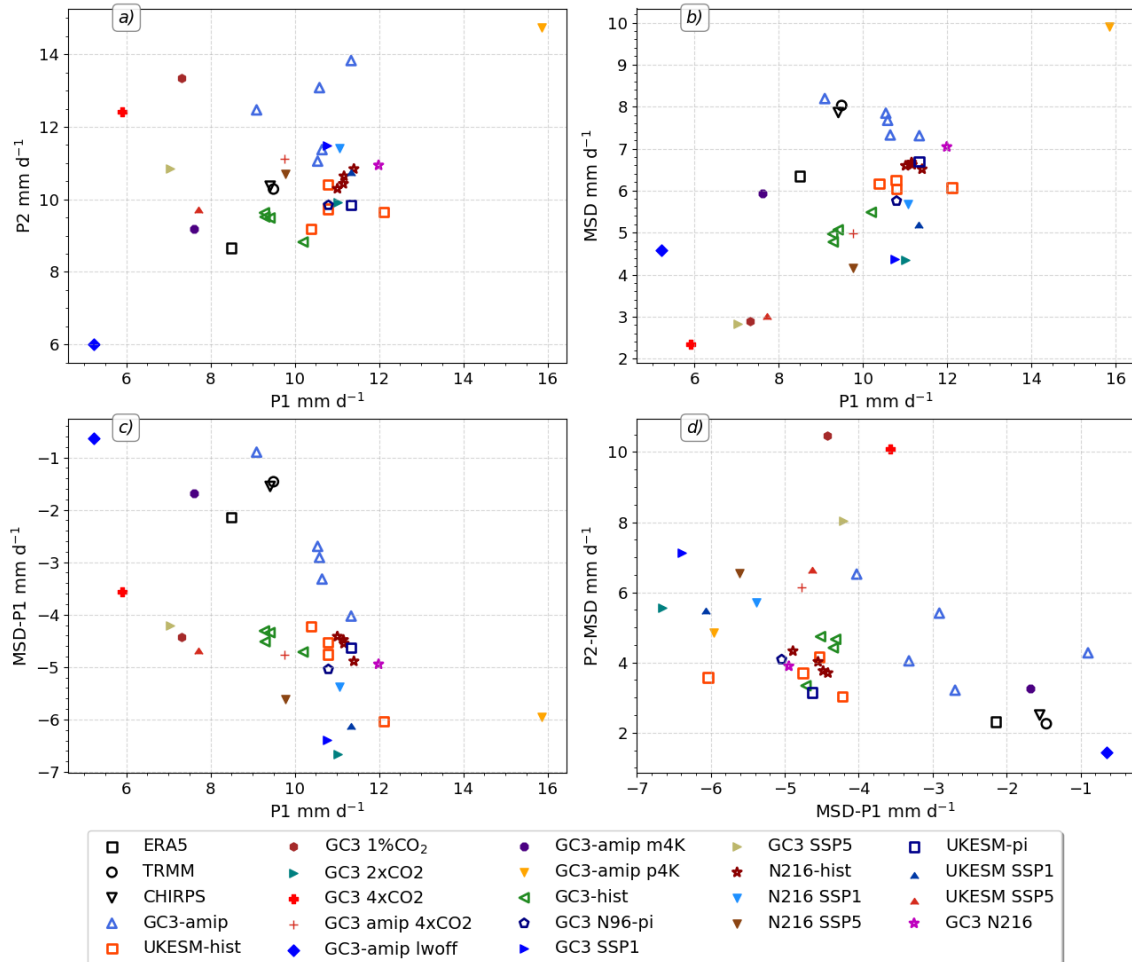


Figure 6.5: (a, b) Scatter plots of the mean values of precipitation [mm day^{-1}] for TRMM, ERA5, CHIRPS and the experiments during the first peak (P1), the MSD and the second peak (P2) periods and (c, d) the precipitation differences between the three periods.

From the MSDO to the MSD, OLR and ω , increase notably in the easternmost Pacific, in southern Mexico and northern Central America and extend into the Caribbean islands and Sea; because ω is defined as $\omega = DP/Dt$ these positive anomalies are indicative of less deep convective activity and weaker convection. The OLR anomalies extend into the North Atlantic.

In contrast, a region several degrees west into the open Pacific Ocean (125°W) and north of the study region into the North American monsoon region show signs of negative OLR and ω anomalies, in the MSD-MSDO panels, which are indication that simultaneously to the onset of the MSD, convection is observed stronger and deeper in the North American Monsoon region and in the Pacific region west of the continent.

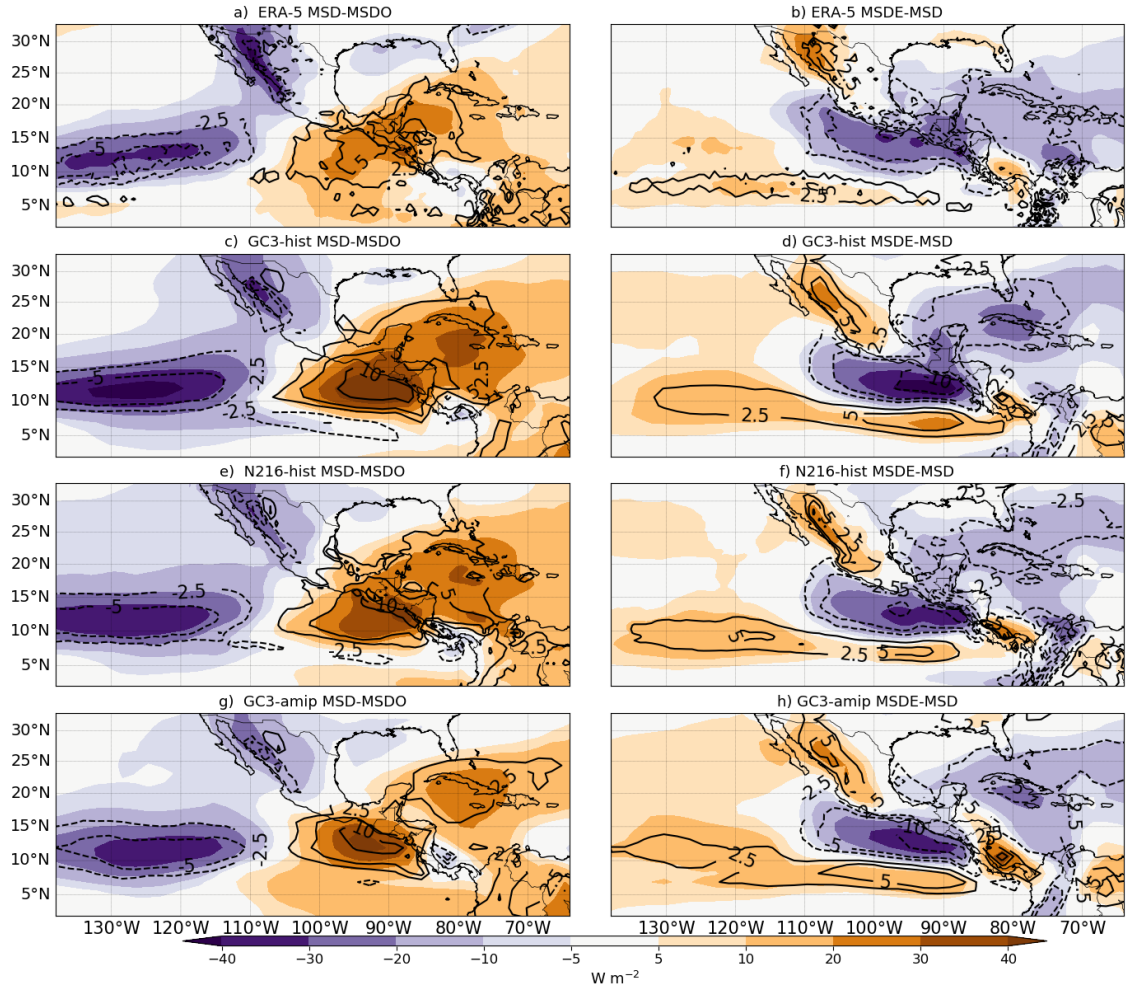


Figure 6.6: Outgoing long-wave radiation (OLR) [W m^{-2}] (shaded) and ω 500-hPa [$10^{-2} \text{ Pa s}^{-1}$] (line contours) differences between the MSD and MSDO and the MSDE and MSD.

The variations at around 125°W were also found by Herrera et al. (2015).

The OLR and ω variations associated with the end of the MSD (MSDE) show a relatively opposite picture to the MSD-MSDO differences. OLR and ω decrease all across the central and south western coast of Mexico and northern Central America extending into the Caribbean Sea whereas positive differences are found in the North American Monsoon region and in the Pacific Ocean at around 125°W .

Several climatological features of the region play key roles for the MSD, according to the various hypothesis in the region. The most prominent factors include the seasonal cycle of the East Pacific (EP) SSTs, the Caribbean Sea SSTs, and the Eastern Pacific wind flow and the CLLJ (Magaña et al., 1999; Amador, 2008; Herrera et al.,

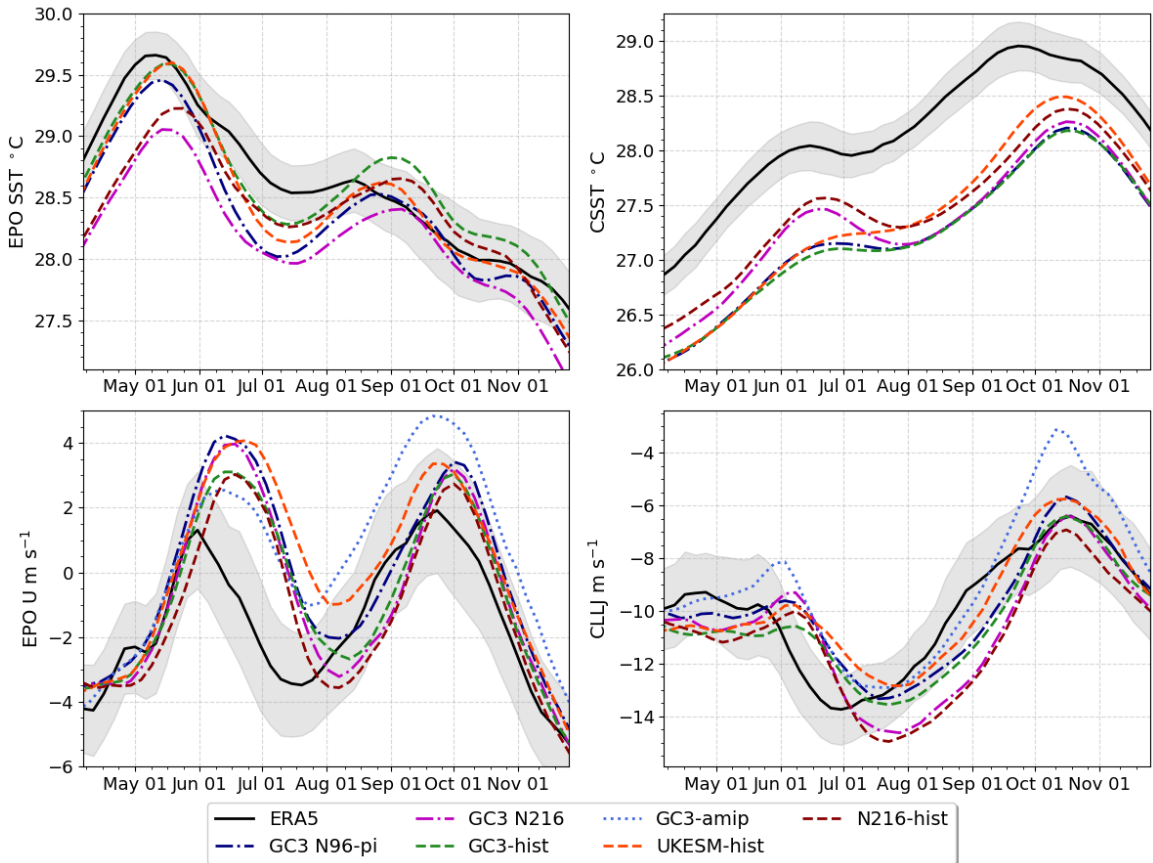


Figure 6.7: Pentad-mean seasonal march of the (a, b) SSTs [$^{\circ}\text{C}$] and (c, d) the low-level (925-hPa) zonal wind flow [m s^{-1}] in (a) the easternmost equatorial Pacific and (b, d) the Caribbean Sea. The transparent shading is as in Figure 6.1.

2015; Straffon et al., 2019; García-Martínez and Bollasina, 2020). The seasonal cycle of these features in ERA5 and the simulations (Figure 6.7) shows that the models are able to replicate the seasonal variations of the SSTs and the zonal wind flow of the region albeit some key biases.

The seasonal cycle of EP SSTs show a maximum peak SST in late May, prior to the first-peak of precipitation in Central America. In contrast, the Caribbean SSTs peak in early fall, about five months later, during late September. After the peak SSTs in late, the EP SSTs decrease to a local minimum found in July both for ERA5 and the simulations. The models, however, show an overall cold bias in the SSTs in both regions, but this bias is most pronounced in the Caribbean Sea where throughout the wet season the SSTs in the models are lower than in ERA5.

The CLLJ seasonal cycle is roughly replicated by the simulations, compared to ERA5, although the peak strength of the CLLJ found in ERA5 during the last week of June is delayed in the simulations by about 1 month, as the simulated CLLJ peaks in mid-July in all the simulations. The low-level wind flow in the EP shows a bimodal regime in both ERA5 and in the simulations. The easterly flow in the EP during the spring becomes weaker turning positive at the end of May and reaching a local maximum in early June in ERA5 and mid-June in the simulations. This local maximum then decreases during June and early July as the zonal wind becomes easterly again and this easterly flow peaks in mid July in ERA5 and about three weeks later in the simulations. The strength of this easterly flow magnitude during the midsummer varies greatly amongst the simulations. After the midsummer easterly flow peak, or zonal wind local minimum, the zonal wind becomes westerly again peaking at the end of September-early August in both ERA5 and simulations.

6.4 The East Pacific SSTs

The East Pacific (EP) SSTs are the key element of the radiative convective feedback of Magaña et al. (1999) as the proposed feedback mechanism suggests that the summer march of the EP SSTs should also exhibit a bimodal signal, similar to that observed for precipitation but out-of-phase, with the SSTs leading the precipitation. The EP SST seasonal cycle (Figure 6.7a) is characterized by peak SSTs in early May, and a subsequent cooling for the rest of the summer.

According to the radiative convective feedback mechanism, the EP SSTs should be reduced prior to the onset of the MSD and then increase at the local minimum or rainfall or MSD period to enhance precipitation and cause the second peak of precipitation in late summer. However, in ERA5 the EP SSTs only very slightly increase during the MSD (Jul-Aug) and rather cool again in late August and September. In fact, the EP SSTs in ERA5 decrease after mid-August, in synchrony with the second peak in deep convection and precipitation. In the models, however, there is indeed a second peak in EP SSTs but the timing of this peak is found in early September and nearly

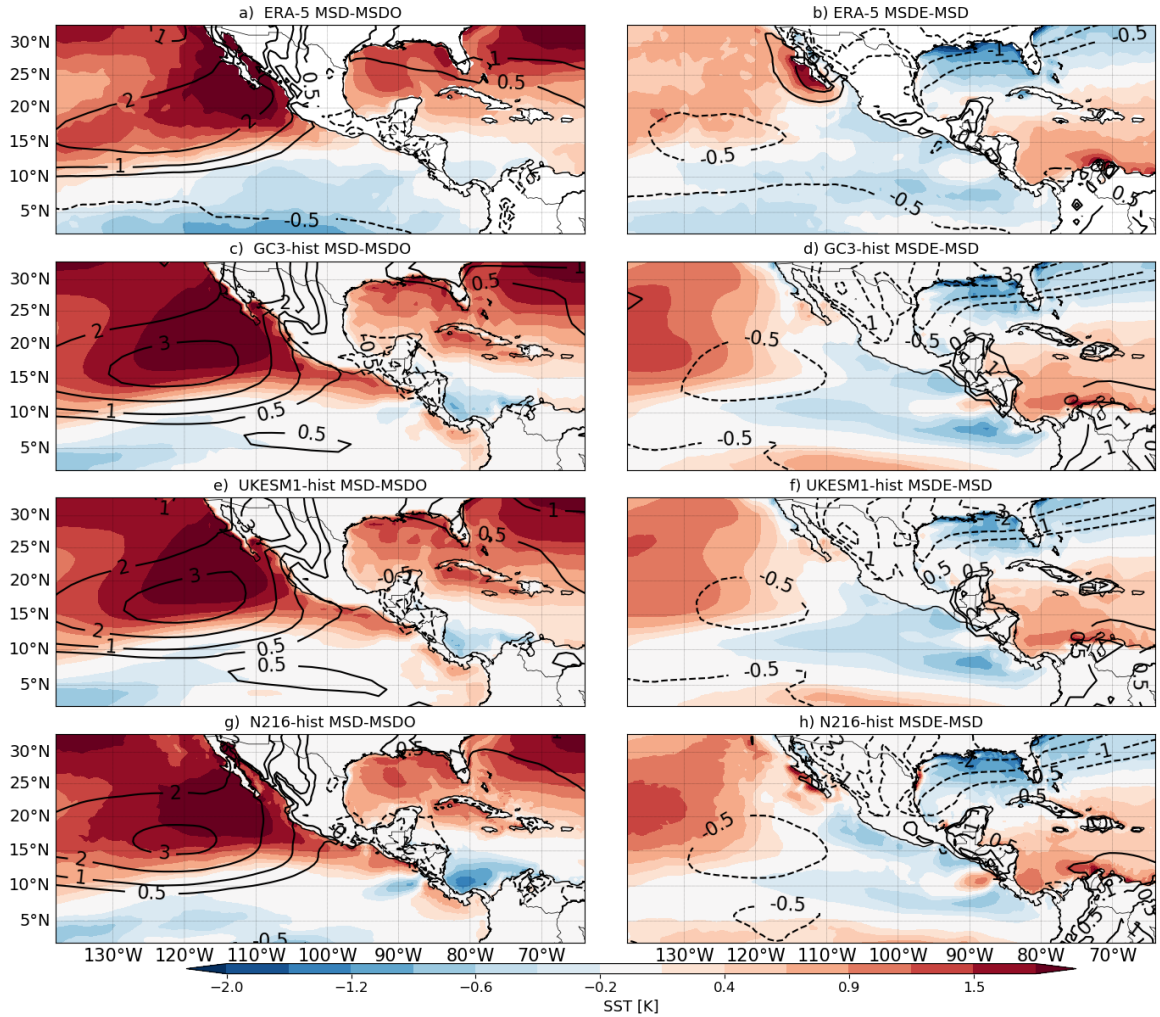


Figure 6.8: As in Figure 6.6 but the anomalies are shown for SSTs [K] (contours) and surface humidity [g kg^{-1}] (line-contours).

synchronous to the second peak in precipitation. The near synchrony of the second peak in EP SST and precipitation as well as the relatively small magnitude of the secondary summer increase in EP SSTs are not clear evidence that the EP SSTs are leading precipitation from the drier MSD to the second peak of rainfall.

The spatial distribution of synchronous SST and surface humidity variations with the MSD timings (Figure 6.8) suggests that little change EP SSTs between the first peak (P1) and the MSD periods, whereas the difference between the MSD period and the second peak (P2) show that SSTs decrease at the end of the MSD. From the P1 to the MSD the most notable change is the warming of the northwester coast of Mexico and of the Gulf of Mexico. From the MSD to the P2 period, the Caribbean SSTs increase,

associated with the peak Caribbean SSTs at the end of the summer (Fig. 6.7b). The historical simulations generally agree with the composite differences of ERA5, with no appreciable warming in the EP region in the MSD-P1 panels, and cooling in the EP and the Gulf of Mexico and warming in the Caribbean Sea in the P2-MSD panels.

A direct implication of the feedback mechanism is that the SST variability would force the surface humidity and ultimately precipitation. The surface humidity in the EP, however, is largely unchanged (less than 0.5 g kg^{-1}) during the various stages of the MSD, even though precipitation varies notably during these periods. Instead, the greatest variations in surface humidity are observed west of Baja California from the P1 to the MSD, and this region of increased surface humidity extends into the North American Monsoon region. Similarly, at the end of the MSD, the most notable variations in surface humidity is the drying of the North American monsoon region. The surface humidity variations in the simulations also agree well with those of ERA5 and are very similar amongst the realizations.

If the EP SSTs play a dominant role in the timings and strength of the MSD, as implied previously (Magaña et al., 1999; Magaña and Caetano, 2005; Herrera et al., 2015), then the simulations that were run using observed-SSTs, i.e., the GC3-amip experiment, may be further explored to evaluate the links between the timings or strength of the MSD in GC3-amip and ERA5. A scatter plot of the dates (pentads) of the MO, MR, MSDO and MSDE (Figure 6.9) for matching years between the CHIRPS dataset and TRMM, ERA5 and the five ensemble members of GC3-amip show that the timings of the MSD in GC3-amip are unrelated to CHIRPS and ERA5, whereas ERA5, in spite of precipitation being largely a model-derived quantity in the reanalysis, produces MSD timings that agree fairly well with the CHIRPS and TRMM datasets. This evidence would suggest that the SSTs forcing the model in GC3-amip are not the dominant factor controlling the timings of the MSD in these atmosphere-only runs.

Alternatively, the interannual variability in ERA5 and the multi-experiment spread of the CMIP6 simulations may be further explored to understand whether the changes to the SSTs are related to changes in the precipitation in the MSD region. For this purpose, composite differences between the P1, MSD and P2 periods were computed

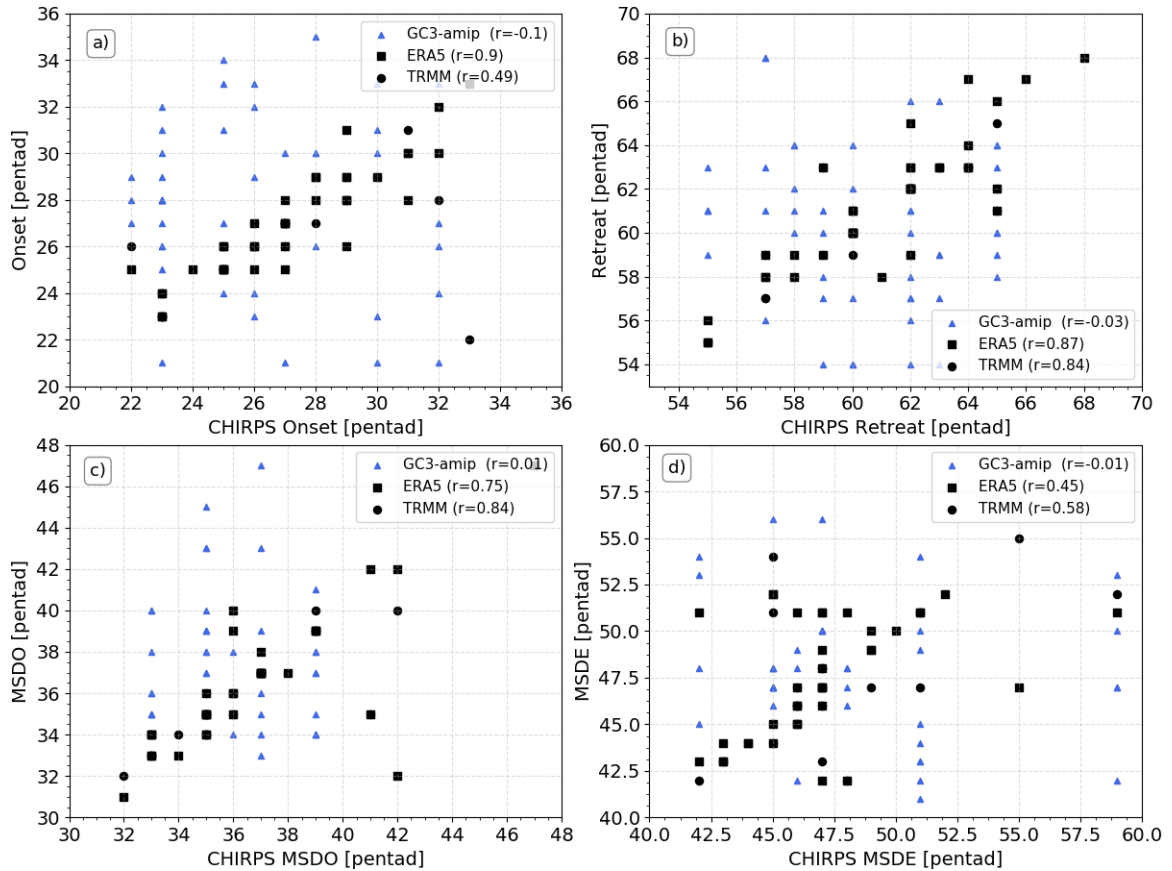


Figure 6.9: Scatterplots of yearly timings in the MSD precipitation time-series diagnosed by the WT method for (a) monsoon onset (MO), (b) monsoon retreat (MR), (c) MSDO and (d) MSDE comparing the results of the CHIRPS dataset with ERA5, TRMM and the GC3-amip simulation. The legend shows the Pearson r coefficient for each comparison.

for each variable for each year in each dataset and then averaged to provide a mean value of change associated with the timings diagnosed by the WT method. For example, the mean difference in SSTs (Figure 6.10a) between the P1 and the MSD periods, show a cooling difference for ERA5, as for the GC3-amip experiments, but a positive difference (warming) for the coupled-model experiments associated (by construction) with a negative precipitation difference in the MSD region.

The warming in the MSD-P1 difference (Figure 6.10a) in the coupled-model experiments agrees well with the seasonal cycle (Fig. 6.7) and suggests that in the model, as precipitation decreases during the MSD, the EP SSTs warm. At the MSDE, the EP SSTs cool (Figure 6.10b) associated with a positive increase in precipitation, suggesting an inverse relationship between EP SSTs and precipitation. However, the

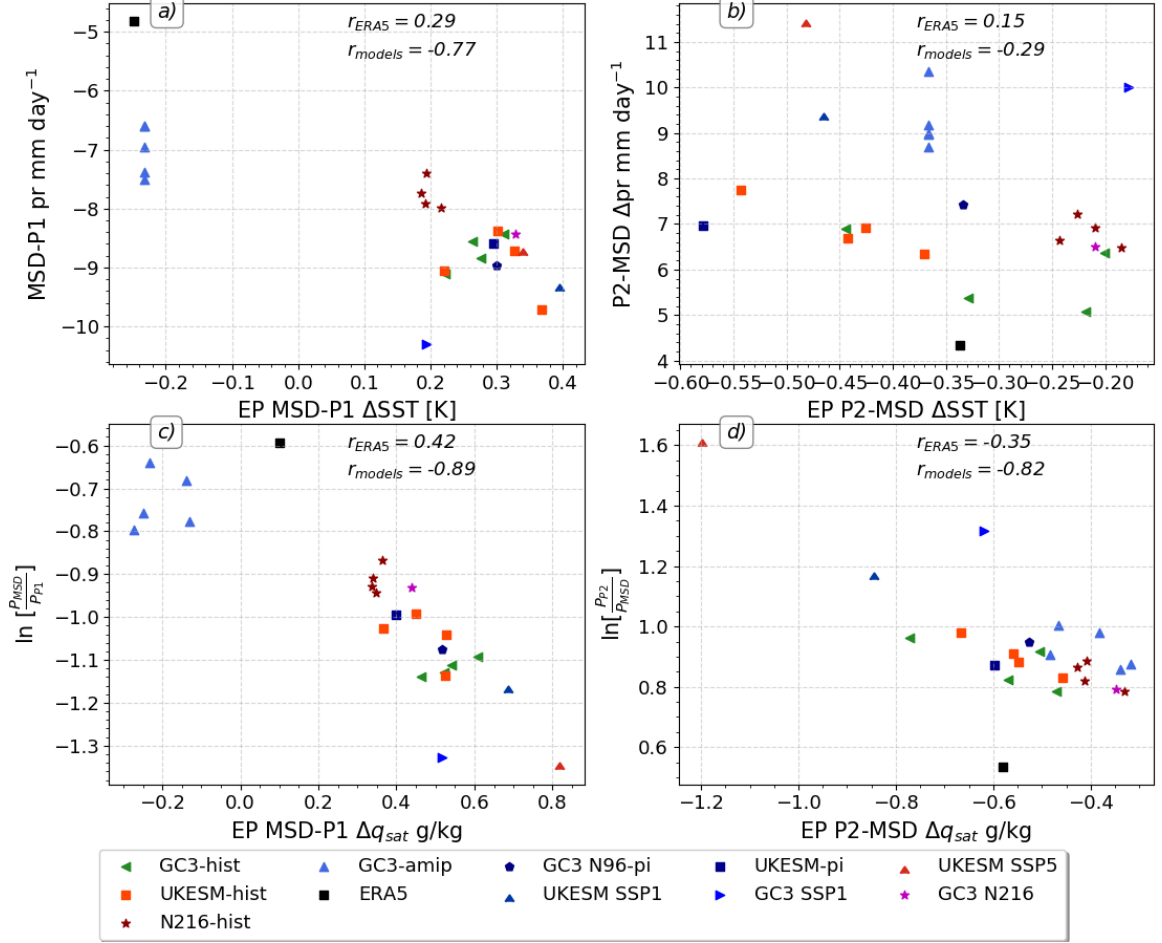


Figure 6.10: Scatterplots of the mean changes in the East Pacific (a, b) sea-surface temperatures (SSTs) and (c, d) surface saturation specific humidity q_{sat} in the x-axis with respect to precipitation variations in the MSD region on the y-axis for the (a, c) MSD-P1 and (b, d) P2-MSD periods. The correlation coefficient of the interannual spread in ERA5 and the multi-experiment correlation coefficient are shown in each panel.

relationship does not seem to explain the inter-experiment spread or the inter-annual variability in ERA5 as the correlation coefficients are low and not significant.

The feedback mechanism of Magaña et al. (1999) suggests that one of the main consequences of the SST changes should also be observed on the evaporation and surface humidity. Furthermore, evidence of tropical precipitation also suggests that the surface saturation specific humidity q_{sat} is not only a measure of the capacity of air to hold moisture but can be used to evaluate the sensitivity of precipitation to SSTs on seasonal time-scales (Yang et al., 2019; Good et al., 2021).

The temporal changes to q_{sat} associated with the MSD timings (Figure 6.10c,d) are

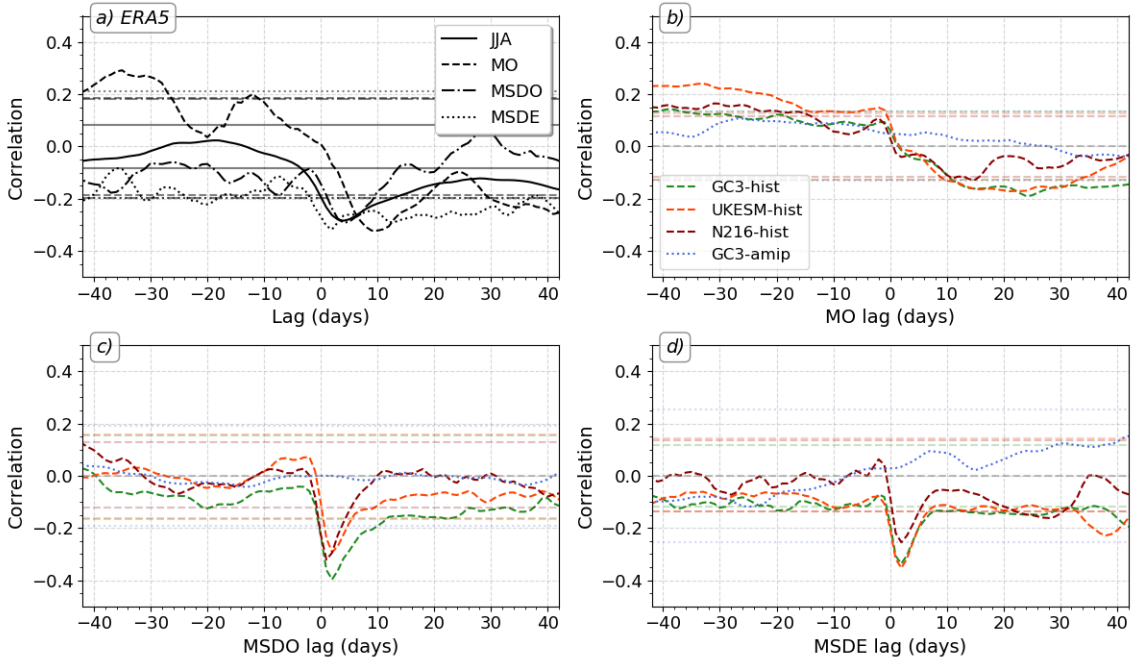


Figure 6.11: Lagged correlations between East Pacific SSTs and precipitation in the MSD region for (a) ERA-5 where the lag 0 date was used in four different ways: first, all the boreal summer JJAS SSTs and precipitation pairings, then lag 0 represents the monsoon onset (MO), MSD onset (MSDO) and MSDE dates. (b-d) as in (a) but for the simulations where the correlations are computed with the SST-precipitation timeseries lagged with respect to the b) monsoon onset date, the c) MSDO date and the d) MSDE date.

not positively related to changes in the precipitation over the MSD region. Although the inter-annual variability of q_{sat} changes during the MSD-P1 period in ERA5 shows a positive correlation, the mean changes to q_{sat} during this stage are very small compared to the differences in the experiments and, furthermore, the relationship for the simulations shows an opposite relationship (negative correlation). For the P2-MSD differences, there is a negative correlation for both ERA5 and the experiments.

The previous results have analysed synchronous changes between the EP SSTs, surface humidity and q_{sat} but the expected relationship may a lead-lag relationship, and as suggested by the radiative-convective feedback mechanism the SSTs should be leading precipitation. Lag-lead correlations (Fig. 6.11) of the EP SSTs and the precipitation in the MSD region show that only during monsoon onset are these two fields significantly positively correlated at lags of \approx -35 days in ERA5 and -40 to -20 days in the historical experiments. In ERA5, the correlation for all the boreal

summer (JJAS) sample is not significant in the SSTs leading precipitation region and is only significant (negative correlation) at lag +5 days, indicative of an inverse SST-precipitation relationship where the SSTs follow precipitation.

In the models (Fig. 6.11b-d), very similar results are shown as significant positive correlations at negative lags, indicative of SSTs leading precipitation, are only found for the MO panel, whereas for MSDO and MSDE, the correlations are only significant at a positive lag and for negative correlations, indicative of the precipitation leading the SSTs on the scale of 3-5 days.

6.5 On the role of cloud-radiative effects

The mechanisms proposed by Magaña et al. (1999) and Karnauskas et al. (2013) suggest that the net shortwave energy absorbed by the surface is key in the driving mechanism of the MSD. Magaña et al. (1999) suggests that tall convective clouds influence the timings and amount of this shortwave flux at the surface (SW), and although not explicitly mentioned as such, Magaña et al. (1999) argues that the cloud-radiative effects (CRE) experience seasonal changes that can explain the MSD. In turn, Karnauskas et al. (2013) argues that the seasonal march of solar insolation characterized by the solar declination angle determines the net shortwave absorbed by the surface. These studies motivate a further inspection of cloud-radiative effects in the simulations to understand whether there is evidence to support previously proposed hypotheses.

Furthermore, CRE effects have been shown to be very important for the timing and strength of regional (Guo et al., 2015) and axi-symmetric (Byrne and Zanna, 2020) monsoons. The long-wave (LW) CRE plays an important role in the convective heating and moistening of the atmospheric column in tropical regions and the short-wave (SW) CRE affects the surface absorption of energy (Allan, 2011). These studies motivate a deeper investigation of the CRE for the MSD timings and strengths in ERA5 and the simulations. The surface cloud radiative effect (CRE_{surf}) is computed from daily-mean fields following Allan (2011), as the sum of the long-wave (LW) and SW CRE, i.e.:

$$\begin{aligned}
 CRE_{surf} &= LWCRE_{surf} + SWCRE_{surf} \\
 &= LDS - LUS - (LDS_{cs} - LUS_{cs}) + SDS - SUS - (SDS_{cs} - SUS_{cs}) \quad (6.1)
 \end{aligned}$$

where the fluxes are depicted as long-wave (L) or short-wave (S) and downwelling (D) or upwelling (U) at the surface (S) and the subscript $_{cs}$ denotes under clear-sky conditions. The long-wave upwelling at the surface (LUS) cancels with the LUS_{cs} because the long-wave emission from the surface is not dependent on the presence of clouds. The net CRE at the surface is then given by:

$$CRE_{surf} = LDS - LDS_{cs} + SDS - SUS - SDS_{cs} + SUS_{cs} \quad (6.2)$$

The net CRE during P1, MSD and P2 periods (Fig. 6.12) is negative and the minimum are found at the East Pacific ITCZ region. The differences between the MSD timings closely follow the precipitation changes during these periods as the

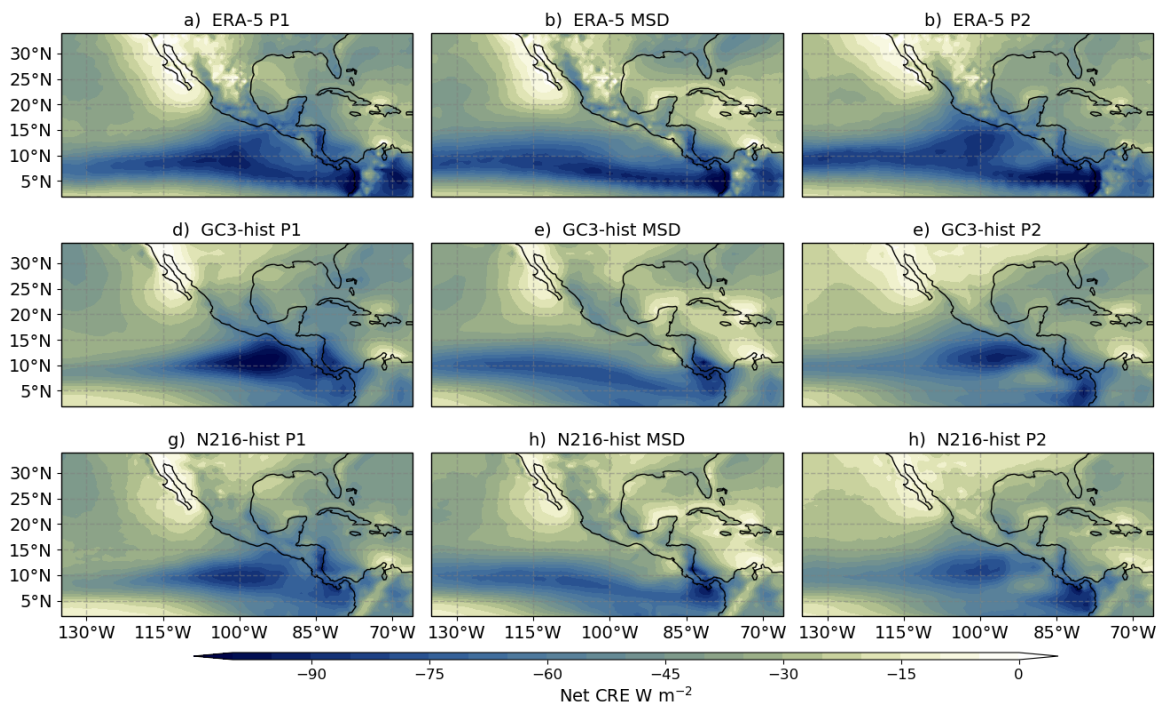


Figure 6.12: Composite mean cloud radiative effect (CRE) [W m^{-2}] during the periods of onset of the MSD, the MSD and the end of the MSD for (a-c) ERA5, and the ensemble mean of (d-f) GC3-hist and (g-h) N216-hist.

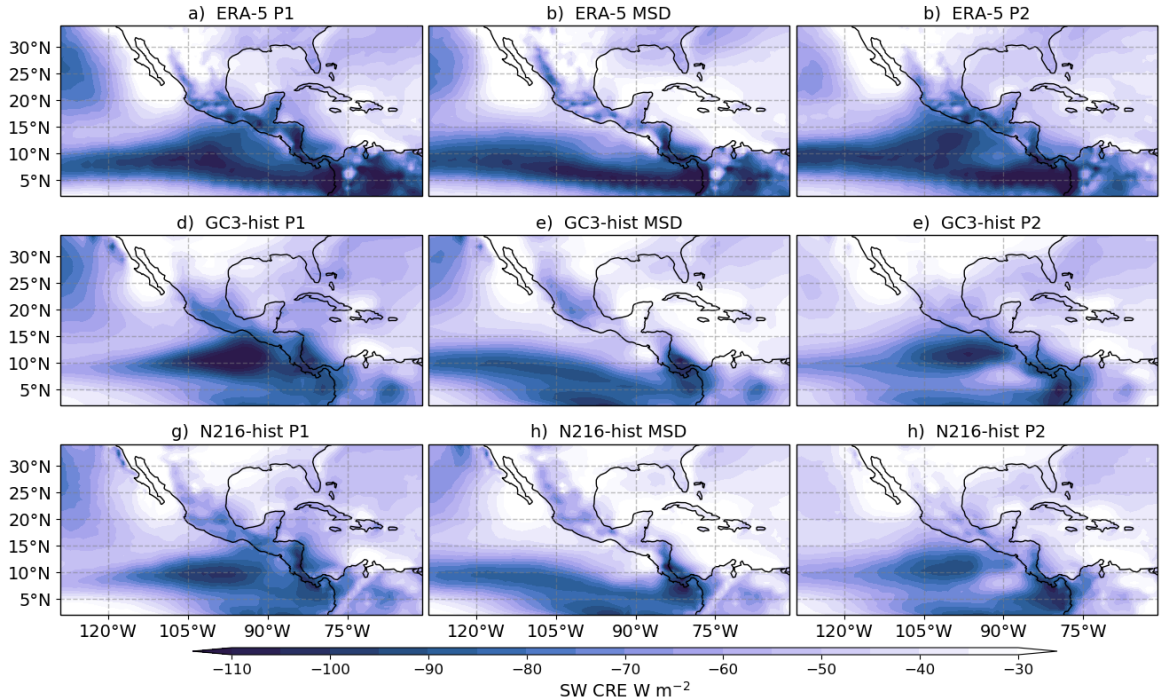


Figure 6.13: As in Fig. 6.12 but for the short-wave radiative effect.

minimum CRE in the EP and the Mesoamerican region is found during the two peaks of precipitation with a reduced value over the continent and nearby coast during the MSD. The smallest CRE is found over the Baja California Peninsula. The two historical ensemble means presented closely follow the results of ERA5, and the only notable difference between the lower (GC3) and the higher (N216) resolution historical experiments is that the CRE is stronger in GC3-hist during the P1 period than in N216-hist.

The individual contributions of the surface SW and LW CREs (Figures 6.13 and 6.14) show that the dominant term in the EP and Mesoamerican regions is the SW term. The negative SW CRE is largest in the EP ITCZ region and the changes associated with the MSD timings are similar to those of the net CRE, i.e., in the MSD region the SW term in ERA5 during P1 and P2 is notably larger ($< -90 \text{ W m}^{-2}$) than during the MSD. The two historical experiments also show that the SW CRE is larger in magnitude in the EP ITCZ region and the show that the SW CRE over land varies notably from P1 to the MSD to the P2 periods.

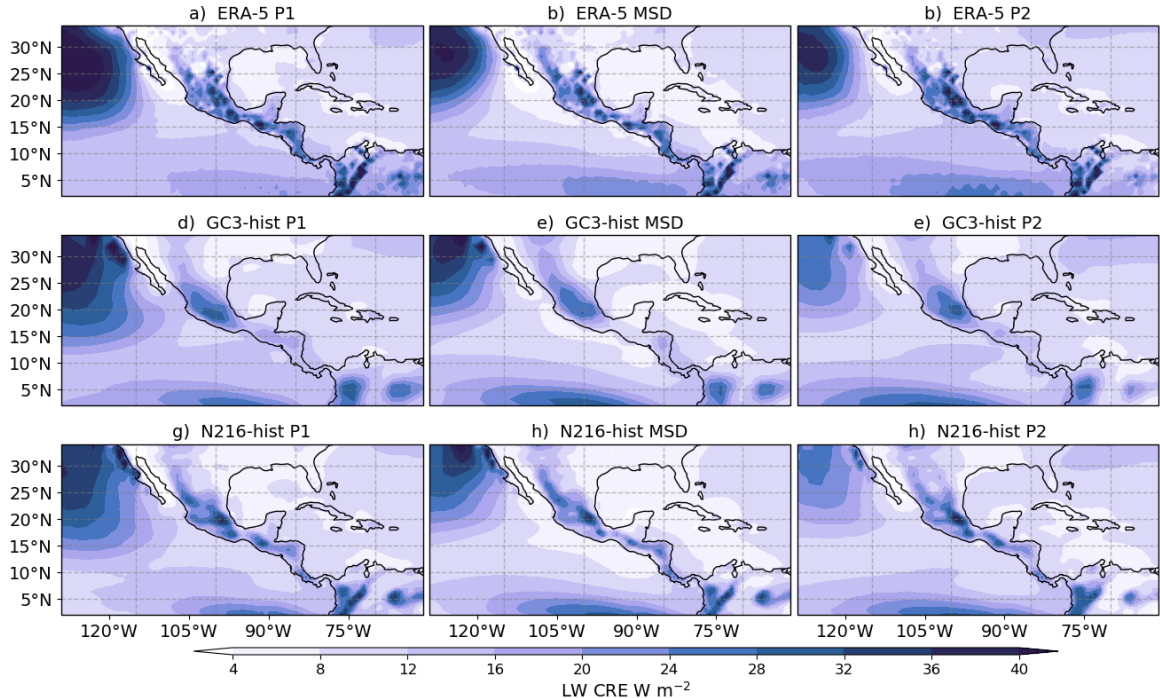


Figure 6.14: As in Fig. 6.12 but for the long-wave CRE.

In contrast, the LW term (Figure 6.14), is generally smaller in magnitude than the SW CRE and is largest over land and in the ocean west of the California with little horizontal gradients over the EP region and the Caribbean Sea. The differences of the LW between the stages of the MSD are smaller than the SW term variations, but both in ERA5 and the simulations, the LW term over the EP and the Caribbean Sea is larger during the two peak periods than during the MSD.

These composites depict how the spatial distribution of the CRE varies with the MSD timings over the larger Intra-American Seas region, but how the seasonal variations in these terms actually changes in the MSD region is not obvious. The seasonal cycles of the SW, LW and net CREs (Figure 6.15a-c) show bimodal signatures characterized by stronger CREs during the two peak periods during June and September and a relative minimum in between found in late July in ERA5 and early August in the simulations.

The simulations reasonably simulate the magnitude of the net and SW CRE during the early summer season but overestimate the decrease in the net, SW and

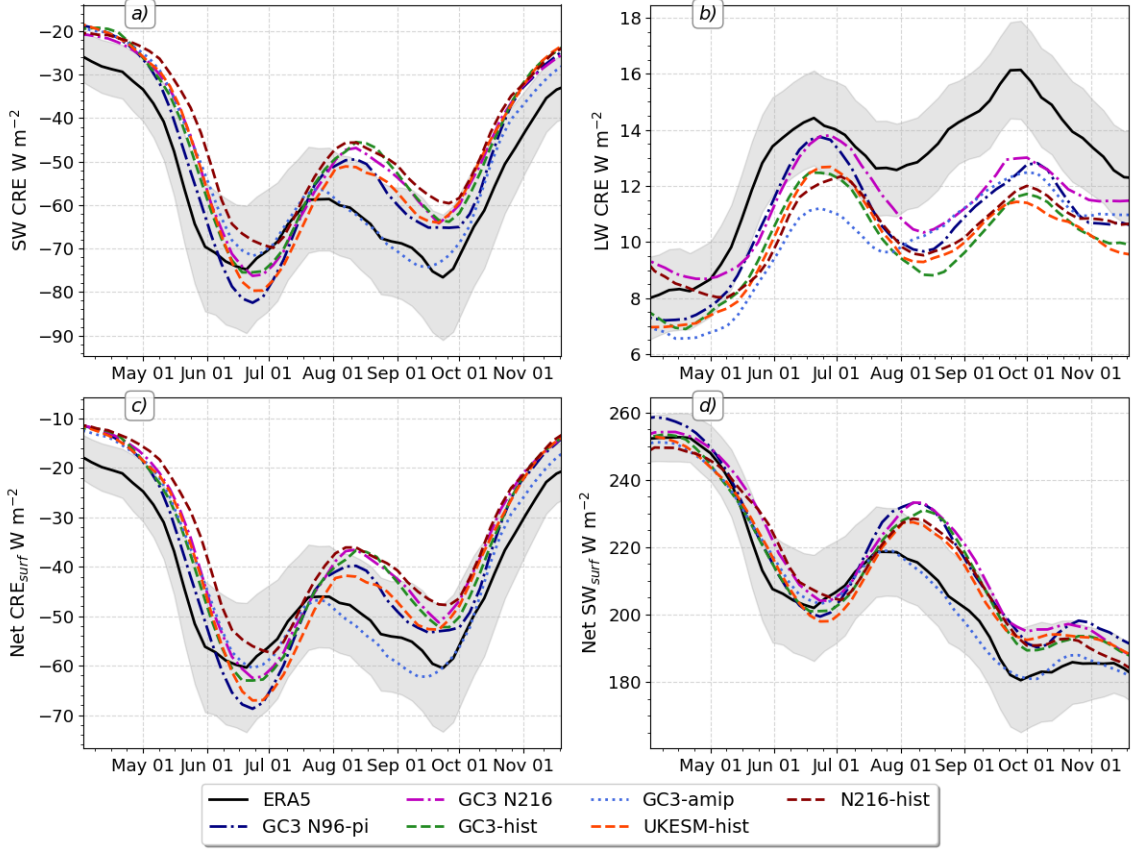


Figure 6.15: Pentad-mean seasonal cycle of the (a) SW and (b) LW CREs, (c) the net CRE, and (d) the net SW at the surface, signed positive to indicate surface absorption of SW radiation.

LW CRE during the midsummer, very likely associated with the underestimation of precipitation over this same period (Figure 6.1).

Both the theories of Magaña et al. (1999) and Karnauskas et al. (2013) suggest that the net SW radiation absorbed at the surface is a key element of the MSD mechanism. Regardless of CREs, the net SW (the difference between upwelling and downwelling shortwave) absorption should also present a bimodal seasonal cycle. In both ERA5 and the simulations the net SW (Figure 6.15d) shows a bimodal local summer cycle characterized by a maximum peak in late May, which coincides with the peak in East Pacific SSTs. This peak in SW is followed by a local minimum during June which is followed by a secondary increase in July in ERA5 and extending to August in the simulations. After this second local maximum in SW, there is another sharp decrease in SW at the end of the summer, which coincides with the the second peak in precipitation.

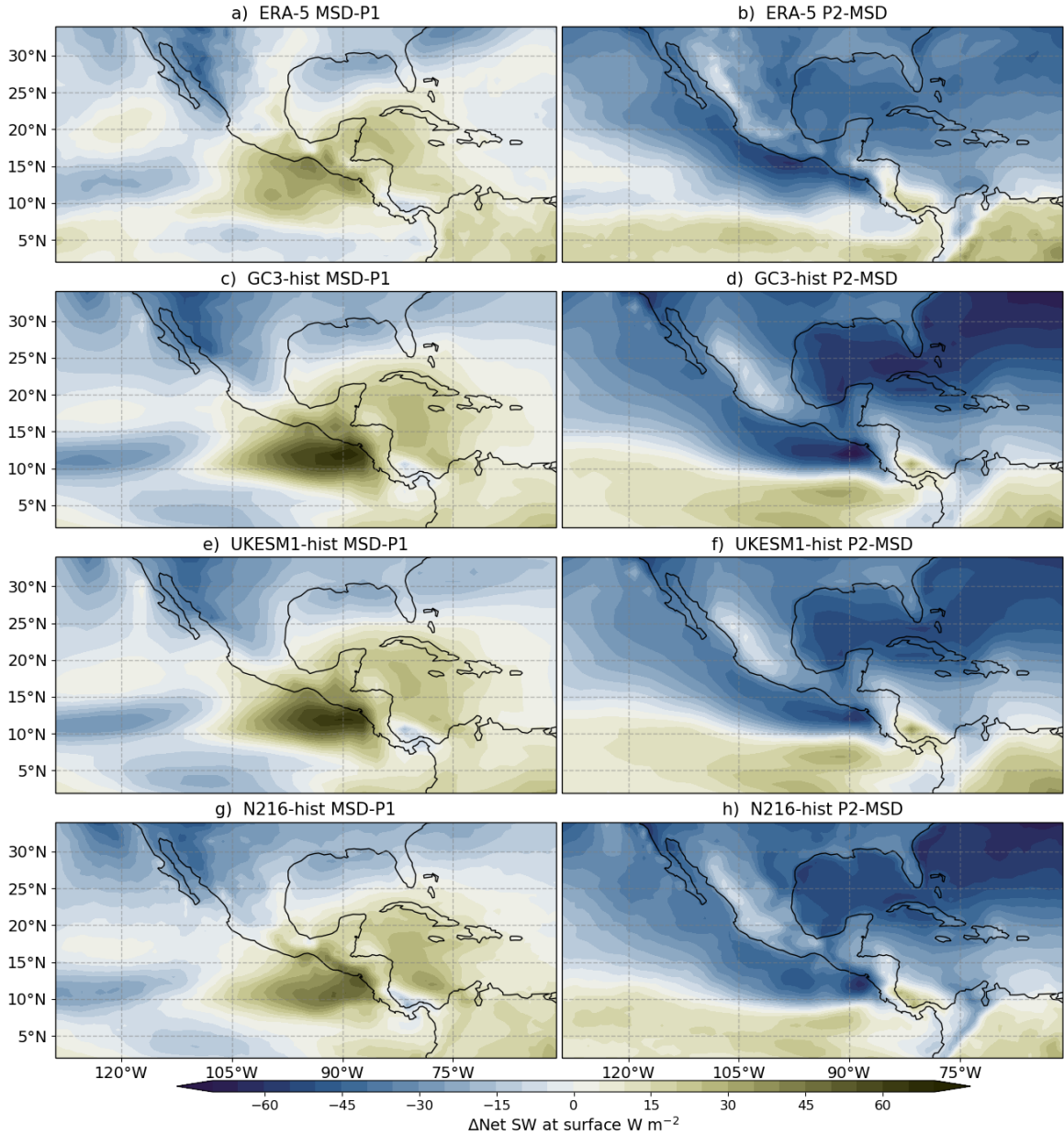


Figure 6.16: As in Fig. 6.6, but for the net shortwave radiation [W m^{-2}] at the surface.

The spatial distribution of the composite mean changes to the net SW absorbed by the surface (Figure 6.16) show that from the first peak to the MSD there is a positive absorption of SW energy (by the surface in the MSD region of about 30 W m^{-2} in ERA5 and 40 W m^{-2} . In contrast, for the P2-MSD differences, a notable reduction in net SW energy is observed throughout the North American continent.

One might reasonably then suspect that the increased SW absorption during the

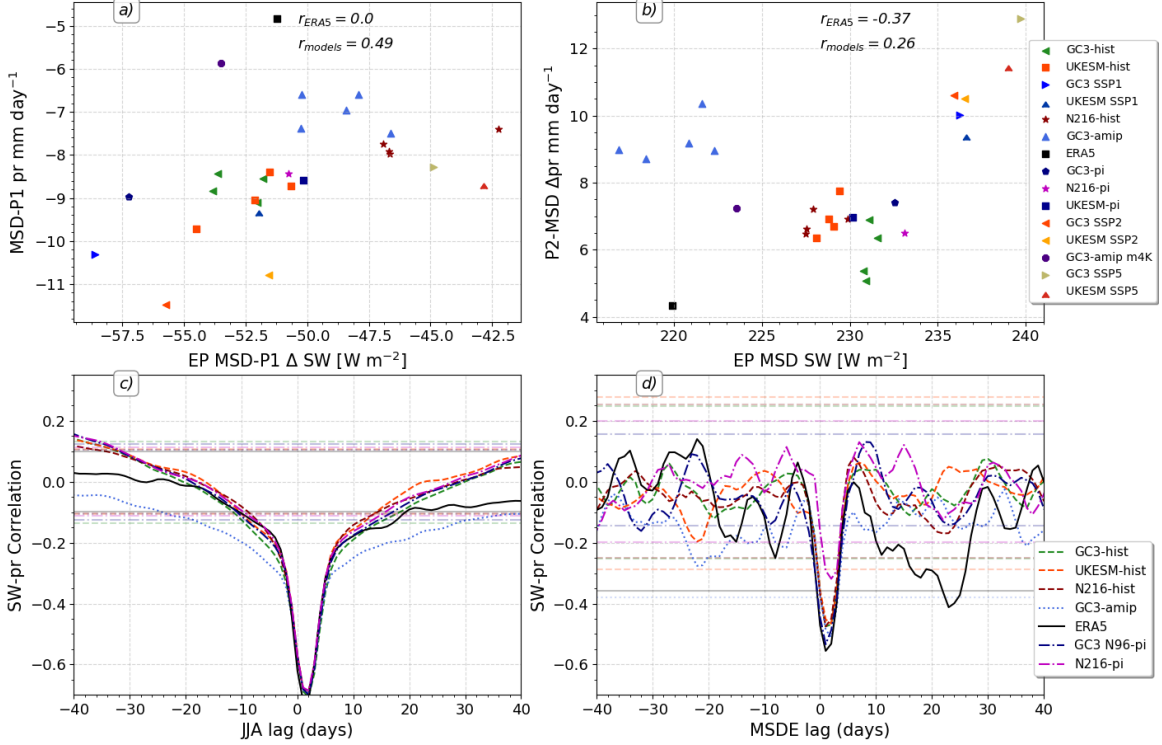


Figure 6.17: Scatter of .

MSD may be the cause for the second peak of precipitation, as suggested by both Magaña et al. (1999) and Karinauskas et al. (2013).

Finally, while the incoming SW has an important role in theories for the MSD, the LW effects have important consequences in general monsoon dynamics. The GC3-amip lwoff experiment is part of the Cloud Feedbacks MIP (CFMIP) is identical to the GC3-amip experiment except that the treatment of the LW in the radiation code in the model is not affected by the presence of clouds, in other words all LW fluxes are assumed to be under clear-sky conditions.

The impact of the LW CRE for precipitation in the Mesomeric region is critical (Figure 6.18). When the LW effects of clouds are ignored, precipitation over the whole domain is greatly reduced (50-80%), ascent becomes weaker and the low-level circulation also weakens. These results are in agreement with previous studies (Guo et al., 2015; Byrne and Zanna, 2020) that show that cloud radiative heating weakens the local and regional circulation in a monsoon. However, these LW appear to be stronger during the MSD and P2 periods than during the P1 period.

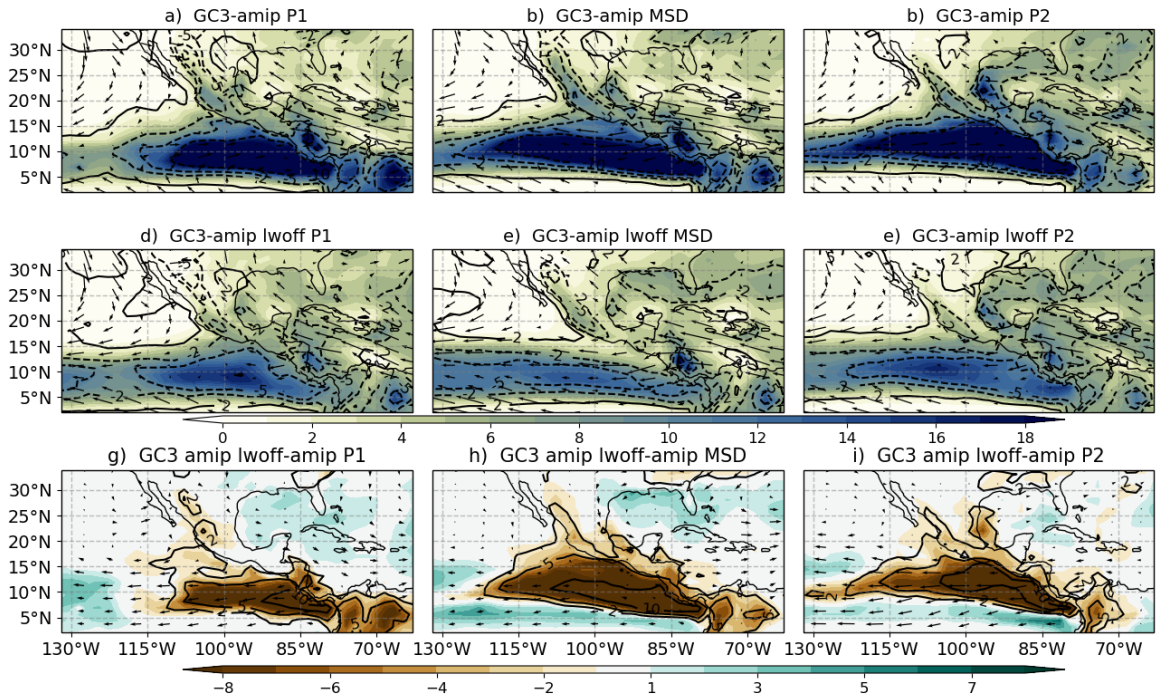


Figure 6.18: Composite mean precipitation (shading), vertical velocity (contours) and 850 hPa wind speed (vectors) for the P1, MSD and P2 periods in the (a-c) GC3-amip and (d-f) GC3-amip lwoff experiment. (g-i) shows the difference between the lwoff-amip and the amip experiments.

6.5.1 On the role of the Caribbean Low-Level Jet

After the MSD, the western coast of the Baja California Peninsula continues to warm and the East Pacific continues to cool, in contrast to previous suggestions (Magaña et al., 1999; Magaña and Caetano, 2005; Herrera et al., 2015). Meanwhile, the Caribbean Sea warms by 1 K and the northern Gulf of Mexico slightly cools down. The incoming shortwave differences show a regional-scale decrease in incoming shortwave, as the summer draws to an end. These SST differences indicate that the meridional SST gradient in both the EP and Caribbean Sea and Gulf of Mexico is greatly modified during the stages of the MSD.

The main dynamical argument put forth to explain the MSD is centred around variations in the moisture flux convergence (MFC), argued to be driven by the Caribbean-Low Level Jet (see e.g. Gamble et al., 2008; Herrera et al., 2015; Martinez et al., 2019). The MFC and zonal wind variations in each stage of the MSD is shown

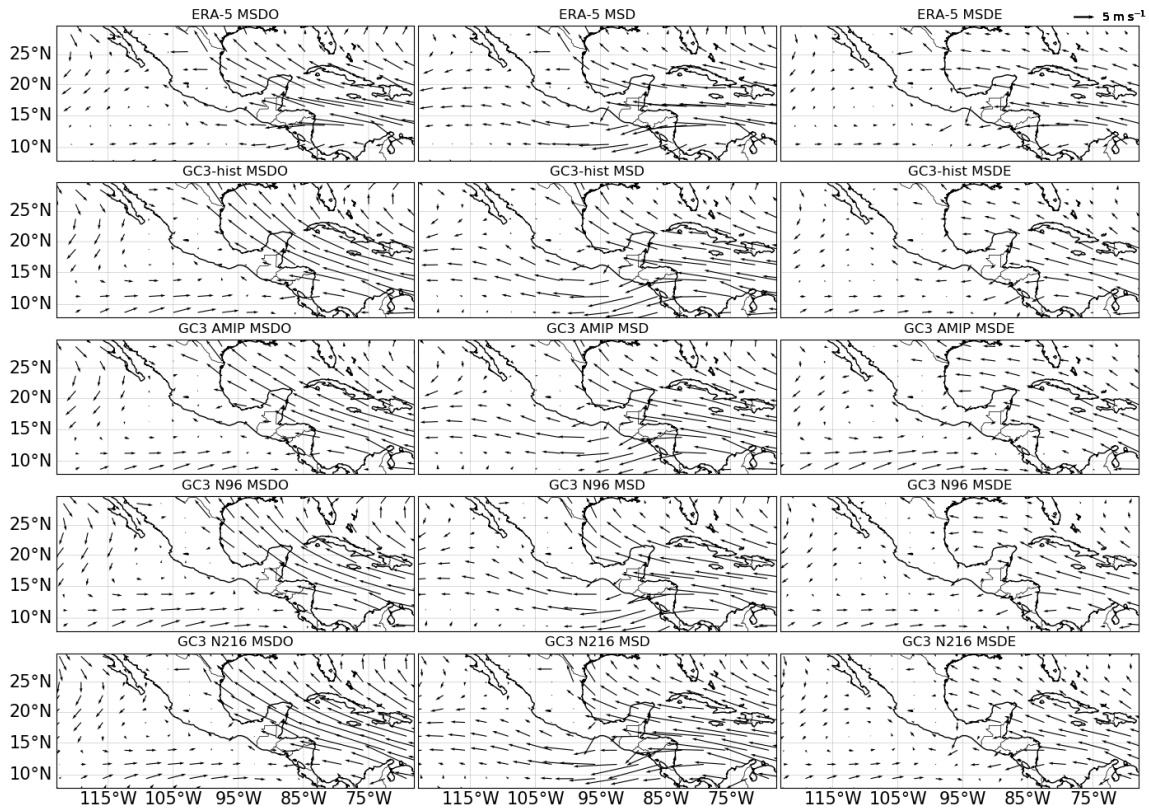


Figure 6.19: As in Figure ?? but showing wind vectors at the 850 hPa level.

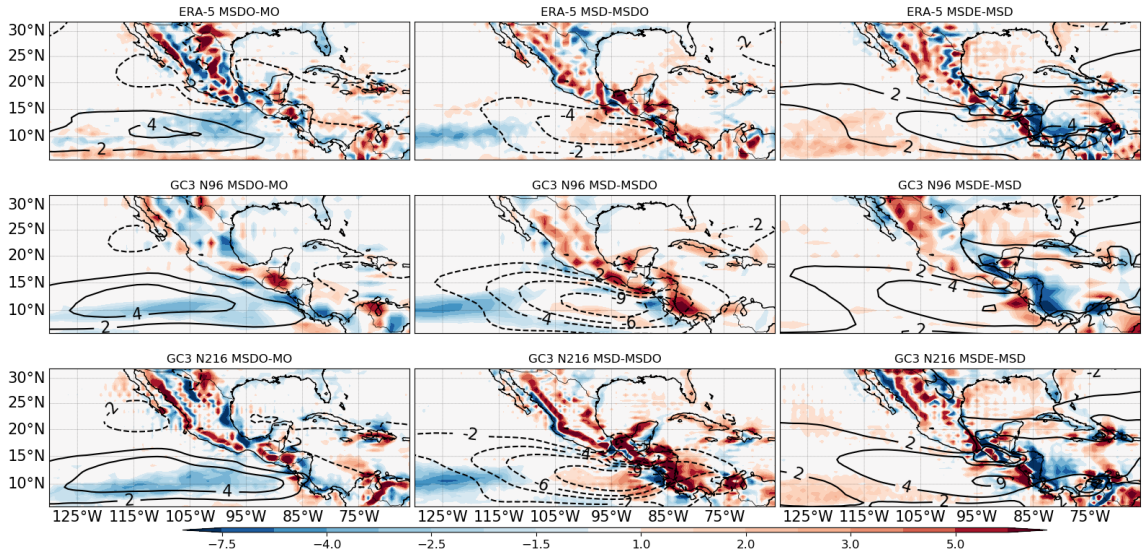


Figure 6.20: As in Figure ?? but showing in shading, moisture flux divergence $\nabla \cdot \vec{u}q$ at the 850 hPa level with units of $10^{-7} \text{ s}^{-1} \text{ kg} / \text{kg}$ and zonal wind anomalies (line contours) in m s^{-1} .

in Figure 6.20 for ERA-5 and two simulations. The low-level MFC increases from monsoon onset (MO) to the first peak period (MSDO) in the EP. This anomaly in MFC corresponds to a region of positive zonal wind anomalies indicative of weaker easterly flow. This zonal wind anomaly from MSD to MSDO is much stronger in the models. The MSD-MSDO difference shows a strong positive MFC anomaly across southern Mexico and most of Central America.

In turn, the MFC anomalies associated with the end of the drier period, observed as the MSDE-MSD anomalies, show negative values, suggesting increased moisture flux, over southern Mexico and northern Central America. Increased moisture flux during the transition from the MSD to the second peak agrees well with the precipitation differences during these periods. The MSDE-MSD zonal wind anomalies in the EP show positive zonal wind anomalies, suggesting a weakened easterly wind flow (see also Fig. 6.19).

The MSD in Central America and southern Mexico has been strongly linked to the strengthening of the CLLJ (Herrera et al., 2015). The maximum zonal wind observed in the CLLJ is found at the very end of July (Fig. 6.7e), synchronized with the start of the MSD. The zonal wind anomalies in the MSD-MSDO panels in Figure 6.20 show that easterlies in the Caribbean Sea do not strengthen by more than 2 m s^{-1} from the first peak to the MSD. Only in the models is there a modest negative anomaly at the westernmost Caribbean Sea. In other words, while the peak of the climatological CLLJ coincides with the climatological timing of the onset of the MSD, these composite analyses constructed by more specifically separating the MSD periods does not show relevant variations in the zonal wind of the Caribbean Sea. The drier MSD period does coincide with stronger easterly flow over the eastern Pacific, which may be associated with the weaker MFC over land.

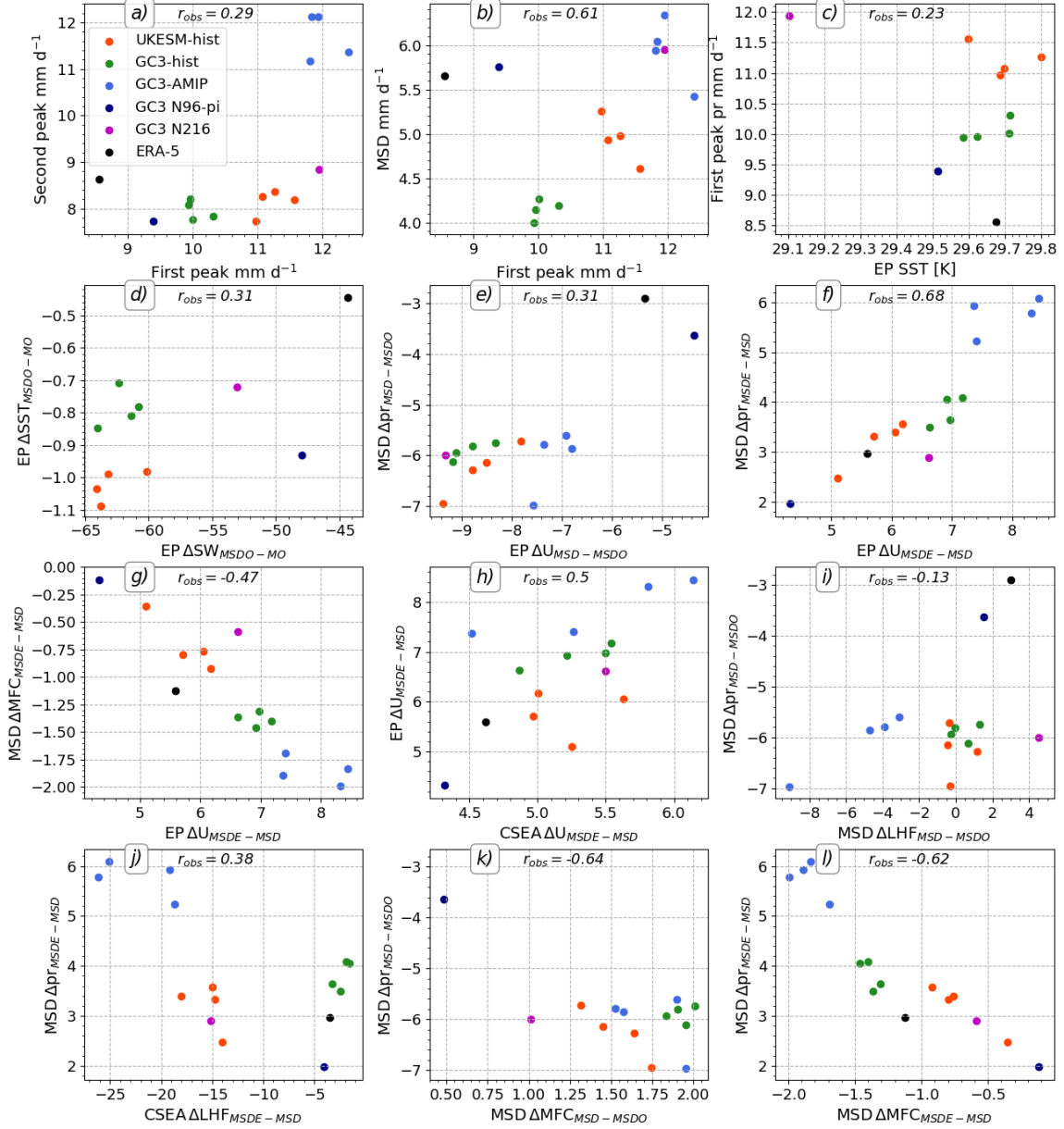


Figure 6.21: Scatter plot of the (a, b) area-averaged precipitation over land (Box in Figure 4.8) during the different stages of the MSD. (c) scatter of the East Pacific SSTs against the precipitation over land during the first peak period. (d-l) show the scatter differences in several variables between the different stages of onset of the MSD (MSDO), the drier MSD and the end of the MSDE. The differences are shown for area-averaged quantities in the East Pacific (EP), the Caribbean Sea (CSEA) and overland (MSD) as above. The units for ΔU are $[\text{m s}^{-1}]$, ΔMFC $[10^{-11} \text{s}^{-1}]$, ΔSW and ΔLHF $[\text{W m}^{-2}]$ and $\Delta pr \text{ mm d}^{-1}$. The Pearson correlation coefficient for the 38 yr of reanalysis or observations (r_{obs}) is shown for each panel.

6.5.2 A look at the MSD through the lense of the moist static energy budget

6.6 Summary and discussion

The midsummer drought is a prominent feature of the seasonal cycle of rainfall of southern Mexico, northern Central America and the Caribbean. The average 20% decrease during the midsummer compared to the wetter periods of early and late summer is a rare feature of monsoon regions that has important implications for agriculture and water management (Hellin et al., 2017; de Sousa et al., 2018; Harvey et al., 2018).

Climate predictions of the MSD, particularly those concerning whether this "drought" will become more pronounced in the following years, are not trustworthy because of several reasons. One factor is the current limitation in the understanding of the physical processes that cause the MSD (section ??) as debate still exists over which large or regional-scale processes are most important to explain the increases and decreases of precipitation over intraseasonal time-scales. Secondly, methods used to diagnose the timing and strength of the MSD typically deal with monthly-scale metrics, which would obscure subtle trends and processes that have an effect on shorter time-scales. Also relevant is the fact that climate models used to produce the predictions show significant biases in the EP ITCZ and the seasonal cycle of rainfall in the region, in fact, most CMIP3 and CMIP5 models did not show a bimodal signature in the seasonal cycle. Models that do not have a climatological MSD cannot provide a prediction for this regime in future climate.

For these reasons, this section analysed the CMIP6 simulations from the Met Office models, UKESM1 and HadGEM3, aiming to understand the causes of the biases in the seasonal cycle. Furthermore, these models are better compared to CMIP3 and CMIP5 cohorts since UKESM1 and HadGEM3 actually simulate a bimodal precipitation regime in these regions. The purpose of this investigation is to use these climate models to better diagnose the relevant biases for the representation of the MSD but

also understand the processes that these models are capturing leading to the MSD, in order to, hopefully, also highlight the dynamics of the MSD in general.

The wavelet transform method was developed to determine the pentads of onset and end of the MSD. For instance, Figures 6.21a,b show the scatter of the mean precipitation during the first peak against second peak and first peak against MSD in all the simulations and ERA5. The magnitude of the first and second peaks appear to be unrelated in these models and in observations, which would suggest that the processes driving each peak are not exactly the same. Similarly, composite analysis of various diagnostics during the different stages of the seasonal cycle was done, for instance, OLR composites showed that the MSD is not a local feature in a small region of southern Mexico but extends throughout a wide range of North America, from central Mexico through Belize, Guatemala, El Salvador, Honduras, Nicaragua, and northern Costa Rica.

This composite approach also allowed to test previously proposed hypotheses by analysing the differences between model experiments and the observed variability in the characteristics of the precipitation at each stage of the MSD. For example, Magaña et al. (1999) proposed a mechanism that explains the MSD through SST-cloud feedbacks. In this hypothesis, shortwave, SSTs and precipitation are strongly coupled in the EP Ocean. The first peak of precipitation in southern Mexico and Central America would then be associated with the EP SSTs prior to the onset of rainfall. Figure 6.21c shows that EP SSTs prior to onset do not explain the inter-model differences in the magnitude of the first peak nor do they show a strong relationship in the observed interannual variability of the first peak mean precipitation. Similarly, Figure 6.21d shows that surface incoming shortwave variations are only weakly related to SSTs variations in the EP, in both models and reanalysis, during the first peak period.

The feedback mechanism also suggests that the second peak is a result of a second increase in surface incoming shortwave that occurs as cloud cover decreases during the drier MSD. This increase in incoming shortwave then increases EP SSTs and thus increasing convective activity. Although the incoming shortwave does show a bimodal behaviour (Figure 6.7d), the SSTs in the East Pacific do not increase during the MSD

period, but in fact cool during the end of the MSD. Furthermore, as in Figure 6.21d, variations in incoming shortwave were not strongly related to SST changes in any of the stages of the MSD (not shown). This suggests that the SSTs are not only dependent on the incoming shortwave in both models and reanalysis.

The low-level winds (Figure 6.19) show notable changes between the onset of the MSD (MSDO), the MSD and the end of the MSD (MSDE). Weak westerlies in the EP are found during the wetter periods but the zonal wind becomes a modest easterly flow during the drier MSD period. The MSDO appears to be synchronized with the strengthening of the Caribbean Low-Level Jet (Fig. 6.7e). During the MSD, the strong zonal flow in the Caribbean crosses Central America into the central-eastern Pacific. This easterly flow during the MSD converges to 125°W in the EP Ocean, a region that also shows increased ascent during the MSD.

Figure 6.21e, f show the relationships between the zonal flow in the EP Ocean and precipitation in southern Mexico and Central America. The changes in the wind flow between the first and the MSD are not related to the drying response over land during the same period. However, the differences between the second peak and the MSD in the wind flow and precipitation show a strong relationship both in observed interannual variability as well as in the model spread. Simulations with a stronger EP zonal wind anomaly show the strongest increment in precipitation over land. The zonal wind change in the EP from the MSD to the second peak period is also modestly related to the MFC over the continent (Fig. 6.21g) with weaker easterly winds in the EP associated with more convergence over land in the models and reanalysis.

The easterly flow in the EP has been associated with the strength of the CLLJ (Herrera et al., 2015). The zonal wind changes in the MSDE-MSD difference in the EP shows a modest linear relationship with the zonal flow in the Caribbean Sea (Fig. 6.21h). During the other periods, the relationship between the CLLJ and the EP zonal component of the wind is even weaker in both models and observations (not shown).

A potentially relevant bias found in the models was stronger-than-observed surface latent heat fluxes (LHF) (Figure 6.7g, h) compared to the reanalysis. Changes in the surface energy balance and the surface temperature in historical versus pre

industrial control simulations may also be responsible for the precipitation differences between these experiments. However, the variations in the LHF_s, both MSD-MSDO and MSDE-MSD either in the Caribbean Sea or over land (Figure 6.21i,j) are not related to precipitation over land.

The main factor associated with the precipitation variations in the seasonal cycle appears to be the low-level moisture flux convergence (MFC) (Figure 6.21k, l). The variations in the MFC over land explain intermodel differences and observed interannual variability in precipitation, particularly in the positive rainfall increment from the MSD to the second peak. From the first peak to the MSD, moisture flux decreases and increases again from the MSD to the second peak.

Bibliography

- Adams, D. K. and Comrie, A. C. (1997), ‘The north American monsoon’, *Bulletin of the American Meteorological Society* **78**(10), 2197–2214.
- Adams, D. K., Gutman, S. I., Holub, K. L. and Pereira, D. S. (2013), ‘GNSS observations of deep convective time scales in the Amazon’, *Geophysical Research Letters* **40**(11), 2818–2823.
- URL:** <https://agupubs.onlinelibrary.wiley.com/doi/abs/10.1002/grl.50573>
- Addison, P. S. (2017), *The illustrated wavelet transform handbook: introductory theory and applications in science, engineering, medicine and finance*, CRC press.
- Adler, R. F., Huffman, G. J., Chang, A., Ferraro, R., Xie, P.-P., Janowiak, J., Rudolf, B., Schneider, U., Curtis, S., Bolvin, D., Gruber, A., Susskind, J., Arkin, P. and Nelkin, E. (2003), ‘The version-2 global precipitation climatology project (gpcp) monthly precipitation analysis (1979–present)’, *Journal of hydrometeorology* **4**(6), 1147–1167.
- Allan, R. P. (2011), ‘Combining satellite data and models to estimate cloud radiative effect at the surface and in the atmosphere’, *Meteorological Applications* **18**(3), 324–333.
- Allen, T. L. and Mapes, B. E. (2017), ‘The late spring Caribbean rain-belt: climatology and dynamics’, *International Journal of Climatology* **37**(15), 4981–4993.
- Amador, J. A. (2008), ‘The intra-americas sea low-level jet: Overview and future research’, *Annals of the New York Academy of Sciences* **1146**(1), 153–188.
- Anderson, T. G., Anchukaitis, K. J., Pons, D. and Taylor, M. (2019), ‘Multiscale trends and precipitation extremes in the Central American Midsummer Drought’, *Environmental Research Letters* **14**(12), 124016.
- Andrews, D. G., Holton, J. R. and Leovy, C. B. (1987), *Middle atmosphere dynamics*, Vol. 40, Academic press.
- Andrews, M., Ridley, J., Wood, R., Andrews, T., Blockley, E., Booth, B., Burke, E., Dittus, A., Florek, P., Gray, L., Haddad, S., Hardiman, S., Hermanson, L., Hodson, D., Hogan, E., Jones, G., Knight, J., Kuhlbrodt, T., Misios, S. and Sutton, R. (2020), ‘Historical simulations with hadgem3-gc3.1 for cmip6’, *Journal of Advances in Modeling Earth Systems*.
- Andrews, T., Andrews, M. B., Bodas-Salcedo, A., Jones, G. S., Kuhlbrodt, T., Manners, J., Menary, M. B., Ridley, J., Ringer, M. A., Sellar, A. A., Senior, C. A. and Tang, Y. (2019), ‘Forcings, feedbacks, and climate sensitivity in hadgem3-gc3. 1 and ukesm1’, *Journal of*

- Advances in Modeling Earth Systems* **11**(12), 4377–4394.
- Angeles, M. E., González, J. E., Ramírez-Beltrán, N. D., Tepley, C. A. and Comarazamy, D. E. (2010), ‘Origins of the caribbean rainfall bimodal behavior’, *Journal of Geophysical Research: Atmospheres* **115**(D11).
- Annamalai, H. (2020), ‘Enso precipitation anomalies along the equatorial pacific: Moist static energy framework diagnostics’, *Journal of Climate* **33**(21), 9103–9127.
- Arias, P. A., Fu, R. and Mo, K. C. (2012), ‘Decadal variation of rainfall seasonality in the north american monsoon region and its potential causes’, *Journal of Climate* **25**(12), 4258–4274.
- URL:** <https://doi.org/10.1175/JCLI-D-11-00140.1>
- Arritt, R. W., Goering, D. C. and Anderson, C. J. (2000), ‘The north american monsoon system in the hadley centre coupled ocean-atmosphere gcm’, *Geophysical Research Letters* **27**(4), 565–568.
- Ashok, K. and Yamagata, T. (2009), ‘The el niño with a difference’, *Nature* **461**(7263), 481–484.
- Ávila, A., Justino, F., Wilson, A., Bromwich, D. and Amorim, M. (2016), ‘Recent precipitation trends, flash floods and landslides in southern brazil’, *Environmental Research Letters* **11**(11), 114029.
- Baldwin, M., Gray, L., Dunkerton, T., Hamilton, K., Haynes, P., Randel, W., Holton, J., Alexander, M., Hirota, I., Horinouchi, T. et al. (2001), ‘The quasi-biennial oscillation’, *Reviews of Geophysics* **39**(2), 179–229.
- Barlow, M., Nigam, S. and Berbery, E. H. (1998), ‘Evolution of the north american monsoon system’, *Journal of Climate* **11**(9), 2238–2257.
- Bayr, T., Domeisen, D. I. and Wengel, C. (2019), ‘The effect of the equatorial pacific cold sst bias on simulated enso teleconnections to the north pacific and california’, *Climate Dynamics* pp. 1–19.
- Bechtold, P., Semane, N., Lopez, P., Chaboureau, J.-P., Beljaars, A. and Bormann, N. (2014), ‘Representing equilibrium and nonequilibrium convection in large-scale models’, *Journal of Atmospheric Sciences* **71**(2), 734–753.
- Becker, A., Finger, P., Meyer-Christoffer, A., Rudolf, B. and Ziese, M. (2011), ‘Gpcc full data reanalysis version 6.0 at 1.0: monthly land-surface precipitation from rain-gauges built on gts-based and historic data’, *Global Precipitation Climatology Centre (GPCC): Berlin, Germany*.
- Bellucci, A., Gualdi, S. and Navarra, A. (2010), ‘The double-itcz syndrome in coupled general circulation models: The role of large-scale vertical circulation regimes’, *Journal of Climate* **23**(5), 1127–1145.
- Biasutti, M., Voigt, A., Boos, W. R., Braconnot, P., Hargreaves, J. C., Harrison, S. P., Kang, S. M., Mapes, B. E., Scheff, J., Schumacher, C. et al. (2018), ‘Global energetics

- and local physics as drivers of past, present and future monsoons', *Nature Geoscience* **11**(6), 392–400.
- Bischoff, T. and Schneider, T. (2016), 'The Equatorial Energy Balance, ITCZ Position, and Double-ITCZ Bifurcations', *Journal of Climate* **29**(8), 2997–3013.
URL: <https://doi.org/10.1175/JCLI-D-15-0328.1>
- Bjerknes, J. (1969), 'Atmospheric teleconnections from the equatorial pacific', *Mon. Wea. Rev* **97**(3), 163–172.
- Blanford, H. F. (1886), 'Rainfall of india', *Monsoon Monograph – India Meteorological Department* **3**(658).
- Bombardi, R. J. and Carvalho, L. M. (2011), 'The South Atlantic dipole and variations in the characteristics of the South American Monsoon in the WCRP-CMIP3 multi-model simulations', *Climate Dynamics* **36**(11-12), 2091–2102.
- Bombardi, R. J., Moron, V. and Goodnight, J. S. (2020), 'Detection, variability, and predictability of monsoon onset and withdrawal dates: A review', *International Journal of Climatology* **40**(2), 641–667.
URL: <https://rmets.onlinelibrary.wiley.com/doi/abs/10.1002/joc.6264>
- Boos, W. R. (2015), 'A review of recent progress on tibet's role in the south asian monsoon', *CLIVAR Exch* **19**(66), 23–27.
- Boos, W. R. and Korty, R. L. (2016), 'Regional energy budget control of the intertropical convergence zone and application to mid-holocene rainfall', *Nature Geoscience* **9**(12), 892–897.
- Bordoni, S. and Schneider, T. (2008), 'Monsoons as eddy-mediated regime transitions of the tropical overturning circulation', *Nature Geoscience* **1**(8), 515–519.
- Brooks, I. M. (2003), 'Finding boundary layer top: Application of a wavelet covariance transform to lidar backscatter profiles', *Journal of Atmospheric and Oceanic Technology* **20**(8), 1092–1105.
- Bussmann, A., Elagib, N. A., Fayyad, M. and Ribbe, L. (2016), 'Sowing date determinants for sahelian rainfed agriculture in the context of agricultural policies and water management', *Land Use Policy* **52**, 316 – 328.
URL: <http://www.sciencedirect.com/science/article/pii/S0264837715003981>
- Byrne, M. P. and Zanna, L. (2020), 'Radiative effects of clouds and water vapor on an axisymmetric monsoon', *Journal of Climate* **33**(20), 8789–8811.
- C3S (2017), 'ERA5: Fifth generation of ECMWF atmospheric reanalyses of the global climate.', *Copernicus Climate Change Service Climate Data Store (CDS)* . date of access: 18 March 2019, <https://climate.copernicus.eu/climate-reanalysis>.
- Cai, W., McPhaden, M., Grimm, A., Rodrigues, R., Taschetto, A., Garreaud, R., Dewitte, B., Poveda, G., Ham, Y.-G., Santoso, A., Ng, B., Anderson, W., Wang, G., Geng, T., Jo, H., Marengo, J., Alves, L., Osman, M., Li, S. and Vera, C. (2020), 'Climate impacts of

- the El Niño–Southern Oscillation on South America’, *Nature Reviews Earth & Environment* **1**(4), 215–231.
- Cai, W., Wu, L., Lengaigne, M., Li, T., McGregor, S., Kug, J.-S., Yu, J.-Y., Stuecker, M. F., Santoso, A., Li, X., Ham, Y.-G., Chikamoto, Y., Ng, B., McPhaden, M. J., Du, Y., Dommenech, D., Jia, F., Kajtar, J. B., Keenlyside, N., Lin, X., Luo, J.-J., Martín-Rey, M., Ruprich-Robert, Y., Wang, G., Xie, S.-P., Yang, Y., Kang, S. M., Choi, J.-Y., Gan, B., Kim, G.-I., Kim, C.-E., Kim, S., Kim, J.-H. and Chang, P. (2019), ‘Pan-tropical climate interactions’, *Science* **363**(6430), eaav4236.
- Camargo, S. J. and Sobel, A. H. (2010), ‘Revisiting the influence of the quasi-biennial oscillation on tropical cyclone activity’, *Journal of Climate* **23**(21), 5810–5825.
- Caramanica, A., Mesia, L. H., Morales, C. R., Huckleberry, G., Quilter, J. et al. (2020), ‘El Niño resilience farming on the north coast of Peru’, *Proceedings of the National Academy of Sciences* **117**(39), 24127–24137.
- Carvalho, L. M., Jones, C. and Liebmann, B. (2004), ‘The South Atlantic convergence zone: Intensity, form, persistence, and relationships with intraseasonal to interannual activity and extreme rainfall’, *Journal of Climate* **17**, 88–108.
- Carvalho, L. M., Silva, A. E., Jones, C., Liebmann, B., Dias, P. L. S. and Rocha, H. R. (2011), ‘Moisture transport and intraseasonal variability in the South America monsoon system’, *Climate dynamics* **36**, 1865–1880.
- Carvalho, L. M. V., Jones, C., Posadas, A. N. D., Quiroz, R., Bookhagen, B. and Liebmann, B. (2012), ‘Precipitation characteristics of the South American Monsoon System derived from multiple datasets’, *Journal of Climate* **25**(13), 4600–4620.
- URL:** <https://doi.org/10.1175/JCLI-D-11-00335.1>
- Chan, J. C. (1995), ‘Tropical cyclone activity in the western North Pacific in relation to the stratospheric quasi-biennial oscillation’, *Monthly Weather Review* **123**(8), 2567–2571.
- Chao, W. C. and Chen, B. (2001), ‘The origin of monsoons’, *Journal of the Atmospheric Sciences* **58**(22), 3497–3507.
- Chen, J., Wilson, C., Tapley, B., Yang, Z. and Niu, G. (2009), ‘2005 drought event in the Amazon River basin as measured by GRACE and estimated by climate models’, *Journal of Geophysical Research: Solid Earth* **114**(B5).
- Chevuturi, A., Turner, A. G., Woolnough, S. J., Martin, G. M. and MacLachlan, C. (2019), ‘Indian summer monsoon onset forecast skill in the UK Met Office initialized coupled seasonal forecasting system (GLOSEA5-GC2)’, *Climate dynamics* **52**(11), 6599–6617.
- Chou, C. and Neelin, J. D. (2004), ‘Mechanisms of global warming impacts on regional tropical precipitation’, *Journal of Climate* **17**(13), 2688–2701.
- Christensen, H., Berner, J., Coleman, D. R. and Palmer, T. (2017), ‘Stochastic parameterization and El Niño–Southern Oscillation’, *Journal of Climate* **30**(1), 17–38.
- Chuvieco, E., Opazo, S., Sione, W., Valle, H. d., Anaya, J., Bella, C. D., Cruz, I., Manzo, L.,

- López, G., Mari, N., González-Alonso, F., Morelli, F., Setzer, A., Csiszar, I., Kanpandegi, J. A., Bastarrika, A. and Libonati, R. (2008), 'Global burned-land estimation in Latin-America using MODIS composite data', *Ecological Applications* **18**(1), 64–79.
URL: <https://esajournals.onlinelibrary.wiley.com/doi/abs/10.1890/06-2148.1>
- Collimore, C. C., Martin, D. W., Hitchman, M. H., Huesmann, A. and Waliser, D. E. (2003), 'On the relationship between the qbo and tropical deep convection', *Journal of climate* **16**(15), 2552–2568.
- Colorado-Ruiz, G., Cavazos, T., Salinas, J. A., De Grau, P. and Ayala, R. (2018), 'Climate change projections from coupled model intercomparison project phase 5 multi-model weighted ensembles for mexico, the north american monsoon, and the mid-summer drought region', *International Journal of Climatology* **38**(15), 5699–5716.
- Cook, B. I. and Buckley, B. M. (2009), 'Objective determination of monsoon season onset, withdrawal, and length', *Journal of Geophysical Research: Atmospheres* **114**(D23).
URL: <https://agupubs.onlinelibrary.wiley.com/doi/abs/10.1029/2009JD012795>
- Cook, B. and Seager, R. (2013), 'The response of the North American Monsoon to increased greenhouse gas forcing', *Journal of Geophysical Research: Atmospheres* **118**(4), 1690–1699.
- Corrales-Suastegui, A., Fuentes-Franco, R. and Pavia, E. G. (2020), 'The mid-summer drought over mexico and central america in the 21st century', *International Journal of Climatology* **40**(3), 1703–1715.
- Curtis, S. and Gamble, D. W. (2008), 'Regional variations of the caribbean mid-summer drought', *Theoretical and Applied Climatology* **94**, 25–34.
- de Sousa, K., Casanoves, F., Sellare, J., Ospina, A., Suchini, J. G., Aguilar, A. and Mercado, L. (2018), 'How climate awareness influences farmers' adaptation decisions in central america?', *Journal of Rural Studies* **64**, 11–19.
- Derbyshire, S., Maidens, A., Milton, S., Stratton, R. and Willett, M. (2011), 'Adaptive detrainment in a convective parametrization', *Quarterly Journal of the Royal Meteorological Society* **137**(660), 1856–1871.
- Devereux, S. (2007), 'The impact of droughts and floods on food security and policy options to alleviate negative effects', *Agricultural Economics* **37**(s1), 47–58.
URL: <https://onlinelibrary.wiley.com/doi/abs/10.1111/j.1574-0862.2007.00234.x>
- Dilley, M. (1996), 'Synoptic controls on precipitation in the Valley of Oaxaca, Mexico', *International Journal of Climatology: A Journal of the Royal Meteorological Society* **16**(9), 1019–1031.
- Dimdore-Miles, O., Gray, L. and Osprey, S. (2021), 'Origins of multi-decadal variability in sudden stratospheric warmings', *Weather and Climate Dynamics* **2**(1), 205–231.
- Dinku, T., Ruiz, F., Connor, S. J. and Ceccato, P. (2010), 'Validation and intercomparison of satellite rainfall estimates over Colombia', *Journal of Applied Meteorology and*

- Climatology* **49**(5), 1004–1014.
- Domeisen, D. I., Garfinkel, C. I. and Butler, A. H. (2019), ‘The teleconnection of el niño southern oscillation to the stratosphere’, *Reviews of Geophysics* **57**(1), 5–47.
- Dominguez, F., Kumar, P. and Vivoni, E. R. (2008), ‘Precipitation recycling variability and ecoclimatological stability—a study using narr data. part ii: North american monsoon region’, *Journal of Climate* **21**(20), 5187–5203.
- Dommenget, D., Bayr, T. and Frauen, C. (2013), ‘Analysis of the non-linearity in the pattern and time evolution of el niño southern oscillation’, *Climate Dynamics* **40**(11-12), 2825–2847.
- Donohoe, A., Marshall, J., Ferreira, D. and Mcgee, D. (2013), ‘The Relationship between ITCZ Location and Cross-Equatorial Atmospheric Heat Transport: From the Seasonal Cycle to the Last Glacial Maximum’, *Journal of Climate* **26**(11), 3597–3618.
URL: <https://doi.org/10.1175/JCLI-D-12-00467.1>
- Douglas, M. W., Maddox, R. A., Howard, K. and Reyes, S. (1993), ‘The mexican monsoon’, *Journal of Climate* **6**(8), 1665–1677.
- Durán-Quesada, A. M., Gimeno, L. and Amador, J. (2017), ‘Role of moisture transport for central american precipitation’, *Earth System Dynamics* **8**(1), 147–161.
URL: <https://www.earth-syst-dynam.net/8/147/2017/>
- Ebdon, R. (1960), ‘Notes on the wind flow at 50 mb in tropical and sub-tropical regions in january 1957 and january 1958’, *Quarterly Journal of the Royal Meteorological Society* **86**(370), 540–542.
- Emanuel, K. (2007), ‘Quasi-equilibrium dynamics of the tropical atmosphere’, *The Global Circulation of the Atmosphere* **186**, 218.
- Emanuel, K. A. et al. (1994), *Atmospheric convection*, Oxford University Press on Demand.
- Eyring, V., Bony, S., Meehl, G. A., Senior, C. A., Stevens, B., Stouffer, R. J. and Taylor, K. E. (2016), ‘Overview of the Coupled Model Intercomparison Project Phase 6 (CMIP6) experimental design and organization’, *Geoscientific Model Development (Online)* **9**.
- Fasullo, J. and Webster, P. (2003), ‘A hydrological definition of indian monsoon onset and withdrawal’, *Journal of Climate* **16**(19), 3200–3211.
- Faulk, S., Mitchell, J. and Bordoni, S. (2017), ‘Effects of rotation rate and seasonal forcing on the itcz extent in planetary atmospheres’, *Journal of the Atmospheric Sciences* **74**(3), 665–678.
- Fereday, D., Chadwick, R., Knight, J. and Scaife, A. (2020), ‘Tropical rainfall linked to stronger future enso-nao teleconnection in cmip5 models’, *Geophysical Research Letters* **47**(22), e2020GL088664.
- Fisher, R. A. (1992), Statistical methods for research workers, in ‘Breakthroughs in statistics’, Springer, pp. 66–70.
- Forbes, R. M. and Ahlgrimm, M. (2014), ‘On the representation of high-latitude boundary

- layer mixed-phase cloud in the ecmwf global model', *Monthly Weather Review* **142**(9), 3425–3445.
- Franchito, S. H., Rao, V. B., Vasques, A. C., Santo, C. M. and Conforte, J. C. (2009), 'Validation of TRMM precipitation radar monthly rainfall estimates over Brazil', *Journal of Geophysical Research: Atmospheres* **114**(D2).
- Fritsch, J. and Chappell, C. (1980), 'Numerical prediction of convectively driven mesoscale pressure systems. part i: Convective parameterization', *Journal of Atmospheric Sciences* **37**(8), 1722–1733.
- Fuentes-Franco, R., Coppola, E., Giorgi, F., Pavia, E. G., Diro, G. T. and Graef, F. (2015), 'Inter-annual variability of precipitation over southern mexico and central america and its relationship to sea surface temperature from a set of future projections from cmip5 gcms and regcm4 cordex simulations', *Climate Dynamics* **45**(1-2), 425–440.
- Funk, C., Peterson, P., Landsfeld, M., Pedreros, D., Verdin, J., Shukla, S., Husak, G., Rowland, J., Harrison, L., Hoell, A. and Michaelsen, J. (2015), 'The climate hazards infrared precipitation with stations—a new environmental record for monitoring extremes', *Scientific data* **2**, 150066.
- Gadgil, S. (2018), 'The monsoon system: Land–sea breeze or the itcz?', *Journal of Earth System Science* **127**(1), 1.
- Gadgil, S. and Rupa Kumar, K. (2006), *The Asian monsoon — agriculture and economy*, Springer Berlin Heidelberg, Berlin, Heidelberg, pp. 651–683.
- Gamble, D. W., Parnell, D. B. and Curtis, S. (2008), 'Spatial variability of the caribbean mid-summer drought and relation to north atlantic high circulation', *International Journal of Climatology* **28**(3), 343–350.
- Gan, M., Kousky, V. and Ropelewski, C. (2004), 'The South America monsoon circulation and its relationship to rainfall over west-central Brazil', *Journal of climate* **17**, 47–66.
- García-Franco, J. L., Gray, L. J. and Osprey, S. (2020), 'The american monsoon system in hadgem3 and ukesm1', *Weather and Climate Dynamics* **1**(2), 349–371.
- URL:** <https://wcd.copernicus.org/articles/1/349/2020/>
- García-Martínez, I. M. and Bollasina, M. A. (2020), 'Sub-monthly evolution of the caribbean low-level jet and its relationship with regional precipitation and atmospheric circulation', *Climate Dynamics* pp. 1–18.
- Garcia, S. R. and Kayano, M. T. (2013), 'Some considerations on onset dates of the rainy season in western-central brazil with antisymmetric outgoing longwave radiation relative to the equator', *International Journal of Climatology* **33**(1), 188–198.
- URL:** <https://rmets.onlinelibrary.wiley.com/doi/abs/10.1002/joc.3417>
- Garfinkel, C. I. and Hartmann, D. (2010), 'Influence of the quasi-biennial oscillation on the north pacific and el niño teleconnections', *Journal of Geophysical Research: Atmospheres* **115**(D20).

- Garfinkel, C. I. and Hartmann, D. L. (2011), ‘The influence of the quasi-biennial oscillation on the troposphere in winter in a hierarchy of models. part ii: Perpetual winter waccm runs’, *Journal of the Atmospheric Sciences* **68**(9), 2026–2041.
- Geen, R., Bordoni, S., Battisti, D. S. and Hui, K. (2020), ‘Monsoons, itczs and the concept of the global monsoon’, *Reviews of Geophysics* p. e2020RG000700.
- Geen, R., Lambert, F. H. and Vallis, G. K. (2019), ‘Processes and timescales in onset and withdrawal of “aquaplanet monsoons”’, *Journal of the Atmospheric Sciences* **76**(8), 2357–2373.
- Geil, K. L., Serra, Y. L. and Zeng, X. (2013), ‘Assessment of cmip5 model simulations of the north american monsoon system’, *Journal of Climate* **26**(22), 8787–8801.
- Giannini, A., Kushnir, Y. and Cane, M. A. (2000), ‘Interannual variability of Caribbean rainfall, ENSO, and the Atlantic Ocean’, *Journal of Climate* **13**, 297–311.
- Giannini, A., Saravanan, R. and Chang, P. (2004), ‘The preconditioning role of tropical Atlantic variability in the development of the ENSO teleconnection: Implications for the prediction of Nordeste rainfall’, *Climate Dynamics* **22**, 839–855.
- Gill, A. E. (1980), ‘Some simple solutions for heat-induced tropical circulation’, *Quarterly Journal of the Royal Meteorological Society* **106**(449), 447–462.
- Giorgetta, M. A., Bengtsson, L. and Arpe, K. (1999), ‘An investigation of qbo signals in the east asian and indian monsoon in gcm experiments’, *Climate dynamics* **15**(6), 435–450.
- Good, P., Chadwick, R., Holloway, C. E., Kennedy, J., Lowe, J. A., Roehrig, R. and Rushley, S. S. (2021), ‘High sensitivity of tropical precipitation to local sea surface temperature’, *Nature* **589**(7842), 408–414.
- Gray, L. J., Anstey, J. A., Kawatani, Y., Lu, H., Osprey, S. and Schenzinger, V. (2018), ‘Surface impacts of the quasi biennial oscillation’, *Atmospheric Chemistry and Physics* **18**(11), 8227–8247.
- URL:** <https://www.atmos-chem-phys.net/18/8227/2018/>
- Gray, W. M. (1984), ‘Atlantic seasonal hurricane frequency. part i: El niño and 30 mb quasi-biennial oscillation influences’, *Monthly Weather Review* **112**(9), 1649–1668.
- Gray, W. M., Sheaffer, J. D. and Knaff, J. A. (1992), ‘Influence of the stratospheric qbo on enso variability’, *Journal of the Meteorological Society of Japan. Ser. II* **70**(5), 975–995.
- Grimm, A. M. (2011), ‘Interannual climate variability in south america: impacts on seasonal precipitation, extreme events, and possible effects of climate change’, *Stochastic Environmental Research and Risk Assessment* **25**(4), 537–554.
- Guo, Z., Zhou, T., Wang, M. and Qian, Y. (2015), ‘Impact of cloud radiative heating on east asian summer monsoon circulation’, *Environmental Research Letters* **10**(7), 074014.
- Ha, K.-J., Moon, S., Timmermann, A. and Kim, D. (2020), ‘Future changes of summer monsoon characteristics and evaporative demand over asia in cmip6 simulations’, *Geophysical Research Letters* **47**(8), e2020GL087492.

- Halley, E. (1687), ‘An historical account of the trade winds, and monsoons, observable in the seas between and near the tropicks, with an attempt to assign the physical cause of the said winds’, *Philosophical Transactions of the Royal Society of London* **16**(183), 153–168.
- URL:** <https://royalsocietypublishing.org/doi/abs/10.1098/rstl.1686.0026>
- Hansen, F., Matthes, K. and Wahl, S. (2016), ‘Tropospheric qbo–enso interactions and differences between the atlantic and pacific’, *Journal of Climate* **29**(4), 1353–1368.
- Harris, I., Jones, P. D., Osborn, T. J. and Lister, D. H. (2014), ‘Updated high-resolution grids of monthly climatic observations—the cru ts3. 10 dataset’, *International journal of climatology* **34**(3), 623–642.
- Hartmann, D. L. (2015), *Global physical climatology*, Vol. 103, Newnes.
- Harvey, C. A., Saborio-Rodríguez, M., Martínez-Rodríguez, M. R., Viguera, B., Chain-Guadarrama, A., Vignola, R. and Alpizar, F. (2018), ‘Climate change impacts and adaptation among smallholder farmers in central america’, *Agriculture & Food Security* **7**(1), 57.
- Hastenrath, S. L. (1967), ‘Rainfall distribution and regime in central america’, *Archiv für Meteorologie, Geophysik und Bioklimatologie, Serie B* **15**(3), 201–241.
- Hellin, J., Cox, R. and López-Ridaura, S. (2017), ‘Maize Diversity, Market Access, and Poverty Reduction in the Western Highlands of Guatemala’, *Mountain Research and Development* **37**(2), 188 – 197.
- Hénin, R., Liberato, M. L., Ramos, A. M. and Gouveia, C. M. (2018), ‘Assessing the use of satellite-based estimates and high-resolution precipitation datasets for the study of extreme precipitation events over the iberian peninsula’, *Water* **10**(11), 1688.
- Herrera, E., Magaña, V. and Caetano, E. (2015), ‘Air–sea interactions and dynamical processes associated with the midsummer drought’, *International Journal of Climatology* **35**(7), 1569–1578.
- Hersbach, H., Bell, B., Berrisford, P., Hirahara, S., Horányi, A., Muñoz-Sabater, J., Nicolas, J., Peubey, C., Radu, R., Schepers, D., Simmons, A., Soci, C., Abdalla, S., Abellan, X., Balsamo, G., Bechtold, P., Biavati, G., Bidlot, J., Bonavita, M., De Chiara, G., Dahlgren, P., Dee, D., Diamantakis, M., Dragani, R., Flemming, J., Forbes, R., Fuentes, M., Geer, A., Haimberger, L., Healy, S., Hogan, R. J., Hólm, E., Janisková, M., Keeley, S., Laloyaux, P., Lopez, P., Lupu, C., Radnoti, G., de Rosnay, P., Rozum, I., Vamborg, F., Villaume, S. and Thépaut, J.-N. (2020), ‘The era5 global reanalysis’, *Quarterly Journal of the Royal Meteorological Society* **1**(n/a).
- URL:** <https://rmets.onlinelibrary.wiley.com/doi/abs/10.1002/qj.3803>
- Higgins, R., Yao, Y. and Wang, X. (1997), ‘Influence of the North American monsoon system on the US summer precipitation regime’, *Journal of Climate* **10**(10), 2600–2622.
- Hill, S. A. (2019), ‘Theories for past and future monsoon rainfall changes’, *Current Climate Change Reports* **5**(3), 160–171.

- Holton, J. R. and Tan, H.-C. (1980), 'The influence of the equatorial quasi-biennial oscillation on the global circulation at 50 mb', *Journal of the Atmospheric Sciences* **37**(10), 2200–2208.
- Hoskins, B., Yang, G.-Y. and Fonseca, R. (2020), 'The detailed dynamics of the june–august hadley cell', *Quarterly Journal of the Royal Meteorological Society* **146**(727), 557–575.
- Htway, O. and Matsumoto, J. (2011), 'Climatological onset dates of summer monsoon over myanmar', *International Journal of Climatology* **31**(3), 382–393.
- Huffman, G. J., Adler, R. F., Bolvin, D. T. and Nelkin, E. J. (2010), The trmm multi-satellite precipitation analysis (tmpa), in 'Satellite rainfall applications for surface hydrology', Springer, pp. 3–22.
- Huffman, G. J., Bolvin, D. T., Nelkin, E. J., Wolff, D. B., Adler, R. F., Gu, G., Hong, Y., Bowman, K. P. and Stocker, E. F. (2007), 'The TRMM Multisatellite Precipitation Analysis (TMPA): Quasi-Global, Multiyear, Combined-Sensor Precipitation Estimates at Fine Scales', *Journal of Hydrometeorology* **8**(1), 38–55.
- URL:** <https://doi.org/10.1175/JHM560.1>
- Jain, M., Naeem, S., Orlove, B., Modi, V. and DeFries, R. S. (2015), 'Understanding the causes and consequences of differential decision-making in adaptation research: Adapting to a delayed monsoon onset in gujarat, india', *Global Environmental Change* **31**, 98 – 109.
- URL:** <http://www.sciencedirect.com/science/article/pii/S0959378014002179>
- Jakob, C. (2014), 'Going back to basics', *Nature Climate Change* **4**(12), 1042.
- Jiménez-Esteve, B. and Domeisen, D. I. V. (2020), 'Nonlinearity in the tropospheric pathway of ENSO to the North Atlantic', *Weather and Climate Dynamics* **1**(1), 225–245.
- URL:** <http://www.weather-clim-dynam.net/1/225/2020/>
- Jobbová, E., Helmke, C. and Bevan, A. (2018), 'Ritual responses to drought: An examination of ritual expressions in classic maya written sources', *Human Ecology* **46**(5), 759–781.
- Johns, T. C., Durman, C. F., Banks, H. T., Roberts, M. J., McLaren, A. J., Ridley, J. K., Senior, C. A., Williams, K., Jones, A., Rickard, G. et al. (2006), 'The new hadley centre climate model (hadgem1): Evaluation of coupled simulations', *Journal of climate* **19**(7), 1327–1353.
- Jones, C. and Carvalho, L. M. (2002), 'Active and break phases in the South American monsoon system', *Journal of Climate* **15**, 905–914.
- Jones, C. and Carvalho, L. M. (2013), 'Climate change in the South American monsoon system: present climate and CMIP5 projections', *Journal of Climate* **26**(17), 6660–6678.
- Jones, C. and Carvalho, L. M. (2018), 'The influence of the Atlantic multidecadal oscillation on the eastern Andes low-level jet and precipitation in South America', *npj Climate and Atmospheric Science* **1**(1), 1–7.
- Jorgetti, T., da Silva Dias, P. L. and de Freitas, E. D. (2014), 'The relationship between

- south atlantic sst and sacz intensity and positioning', *Climate dynamics* **42**(11-12), 3077–3086.
- Karnauskas, K. B., Seager, R., Giannini, A. and Busalacchi, A. J. (2013), 'A simple mechanism for the climatological midsummer drought along the Pacific coast of Central America', *Atmósfera* **26**, 261–281.
- Kennedy, J., Rayner, N., Smith, R., Parker, D. and Saunby, M. (2011), 'Reassessing biases and other uncertainties in sea surface temperature observations measured in situ since 1850: 2. biases and homogenization', *Journal of Geophysical Research: Atmospheres* **116**(D14).
- Kitoh, A. and Uchiyama, T. (2006), 'Changes in onset and withdrawal of the east asian summer rainy season by multi-model global warming experiments', *Journal of the Meteorological Society of Japan. Ser. II* **84**(2), 247–258.
- Kuhlbrodt, T., Jones, C. G., Sellar, A., Storkey, D., Blockley, E., Stringer, M., Hill, R., Graham, T., Ridley, J., Blaker, A., Calvert, D., Copsey, D., Ellis, R., Hewitt, H., Hyder, P., Ineson, S., Mulcahy, J., Siahaan, A. and Walton, J. (2018), 'The low-resolution version of HadGEM3 GC3. 1: Development and evaluation for global climate', *Journal of advances in modeling earth systems* **10**(11), 2865–2888.
- Lawrence, P. J., Feddema, J. J., Bonan, G. B., Meehl, G. A., O'Neill, B. C., Oleson, K. W., Levis, S., Lawrence, D. M., Kluzeck, E., Lindsay, K. and Thornton, P. E. (2012), 'Simulating the Biogeochemical and Biogeophysical Impacts of Transient Land Cover Change and Wood Harvest in the Community Climate System Model (CCSM4) from 1850 to 2100', *Journal of Climate* **25**(9), 3071–3095.
- Lee, J. C. K. and Klingaman, N. P. (2018), 'The effect of the quasi-biennial oscillation on the madden–julian oscillation in the met office unified model global ocean mixed layer configuration', *Atmospheric Science Letters* **19**(5), e816.
URL: <https://rmets.onlinelibrary.wiley.com/doi/abs/10.1002/asl.816>
- Li, D., Shine, K. and Gray, L. (1995), 'The role of ozone-induced diabatic heating anomalies in the quasi-biennial oscillation', *Quarterly Journal of the Royal Meteorological Society* **121**(524), 937–943.
- Li, G. and Xie, S.-P. (2014), 'Tropical biases in cmip5 multimodel ensemble: The excessive equatorial pacific cold tongue and double itcz problems', *Journal of Climate* **27**(4), 1765–1780.
- Li, T. and Hsu, P.-c. (2018), *Fundamentals of tropical climate dynamics*, Springer.
- Li, W., Fu, R. and Dickinson, R. E. (2006), 'Rainfall and its seasonality over the Amazon in the 21st century as assessed by the coupled models for the IPCC AR4', *Journal of Geophysical Research: Atmospheres* **111**(D2).
- Liebmann, B. and Marengo, J. (2001), 'Interannual variability of the rainy season and rainfall in the brazilian amazon basin', *Journal of Climate* **14**(22), 4308–4318.

- Liess, S. and Geller, M. A. (2012), 'On the relationship between qbo and distribution of tropical deep convection', *Journal of Geophysical Research: Atmospheres* **117**(D3).
- Lorenz, E. N. (1967), *The nature and theory of the general circulation of the atmosphere*, Vol. 218, World Meteorological Organization Geneva.
- Lu, H., Hitchman, M. H., Gray, L. J., Anstey, J. A. and Osprey, S. M. (2020), 'On the role of rossby wave breaking in the quasi-biennial modulation of the stratospheric polar vortex during boreal winter', *Quarterly Journal of the Royal Meteorological Society*.
- Lucas-Picher, P., Christensen, J. H., Saeed, F., Kumar, P., Ashraf, S., Ahrens, B., Wiltshire, A. J., Jacob, D. and Hagemann, S. (2011), 'Can regional climate models represent the indian monsoon?', *Journal of Hydrometeorology* **12**(5), 849–868.
- URL:** <https://doi.org/10.1175/2011JHM1327.1>
- Ma, D., Sobel, A. H., Kuang, Z., Singh, M. S. and Nie, J. (2019), 'A moist entropy budget view of the south asian summer monsoon onset', *Geophysical Research Letters* **46**(8), 4476–4484.
- Machado, L., Laurent, H., Dessay, N. and Miranda, I. (2004), 'Seasonal and diurnal variability of convection over the amazonia: A comparison of different vegetation types and large scale forcing', *Theoretical and Applied Climatology* **78**(1-3), 61–77.
- Magaña, V., Amador, J. A. and Medina, S. (1999), 'The midsummer drought over Mexico and Central America', *Journal of Climate* **12**, 1577–1588.
- Magaña, V. and Caetano, E. (2005), 'Temporal evolution of summer convective activity over the Americas warm pools', *Geophysical Research Letters* **32**(2).
- Maldonado, T., Alfaro, E., Rutgersson, A. and Amador, J. A. (2017), 'The early rainy season in central america: the role of the tropical north atlantic ssts', *International Journal of Climatology* **37**(9), 3731–3742.
- Malhi, Y., Aragão, L. E. O. C., Galbraith, D., Huntingford, C., Fisher, R., Zelazowski, P., Sitch, S., McSweeney, C. and Meir, P. (2009), 'Exploring the likelihood and mechanism of a climate-change-induced dieback of the Amazon rainforest', *Proceedings of the National Academy of Sciences* **106**(49), 20610–20615.
- URL:** <https://www.pnas.org/content/106/49/20610>
- Mapes, B. E., Liu, P. and Buenning, N. (2005), 'Indian monsoon onset and the americas midsummer drought: Out-of-equilibrium responses to smooth seasonal forcing', *Journal of Climate* **18**(7), 1109–1115.
- Marengo, J. A., Liebmann, B., Grimm, A. M., Misra, V., Silva Dias, P. L., Cavalcanti, I. F. A., Carvalho, L. M. V., Berbery, E. H., Ambrizzi, T., Vera, C. S., Saulo, A. C., Nogues-Paegle, J., Zipser, E., Seth, A. and Alves, L. M. (2012), 'Recent developments on the South American monsoon system', *International Journal of Climatology* **32**, 1–21.
- Marengo, J. A., Liebmann, B., Kousky, V. E., Filizola, N. P. and Wainer, I. C. (2001), 'Onset and end of the rainy season in the brazilian amazon basin', *Journal of Climate*

- 14(5), 833–852.
- Marotzke, J., Jakob, C., Bony, S., Dirmeyer, P., O’Gorman, P., Hawkins, E., Perkins-Kirkpatrick, S., Quéré, C., Nowicki, S., Paulavets, K., Seneviratne, S., Stevens, B. and Tuma, M. (2017), ‘Climate research must sharpen its view’, *Nature climate change* 7(2), 89–91.
- Martin, Z., Vitart, F., Wang, S. and Sobel, A. (2020), ‘The impact of the stratosphere on the mjo in a forecast model’, *Journal of Geophysical Research: Atmospheres* 125(4), e2019JD032106. e2019JD032106 2019JD032106.
- URL:** <https://agupubs.onlinelibrary.wiley.com/doi/abs/10.1029/2019JD032106>
- Martin, Z., Wang, S., Nie, J. and Sobel, A. (2019), ‘The Impact of the QBO on MJO Convection in Cloud-Resolving Simulations’, *Journal of the Atmospheric Sciences* 76(3), 669–688.
- URL:** <https://doi.org/10.1175/JAS-D-18-0179.1>
- Martinez, C., Goddard, L., Kushnir, Y. and Ting, M. (2019), ‘Seasonal climatology and dynamical mechanisms of rainfall in the caribbean’, *Climate dynamics* 53(1-2), 825–846.
- Menary, M. B., Kuhlbrodt, T., Ridley, J., Andrews, M. B., Dimdore-Miles, O. B., Deshayes, J., Eade, R., Gray, L., Ineson, S., Mignot, J., Roberts, C. D., Robson, J., Wood, R. A. and Xavier, P. (2018), ‘Preindustrial control simulations with hadgem3-gc3. 1 for cmip6’, *Journal of Advances in Modeling Earth Systems* 10(12), 3049–3075.
- Mestas-Nuñez, A. M., Enfield, D. B. and Zhang, C. (2007), ‘Water vapor fluxes over the intra-americas sea: Seasonal and interannual variability and associations with rainfall’, *Journal of Climate* 20(9), 1910–1922.
- Mission, T. R. M. (2011), ‘Trmm (tmpa/3b43) rainfall estimate l3 1 month 0.25 degree×0.25 degree v7’, Version, Greenbelt, MD, Goddard Earth Sciences Data and Information Services Center (GES DISC) . Accessed: [12-Jan-2019].
- URL:** https://disc.gsfc.nasa.gov/datasets/TRMM_3B42_7/summary
- Moron, V. and Robertson, A. W. (2014), ‘Interannual variability of indian summer monsoon rainfall onset date at local scale’, *International journal of climatology* 34(4), 1050–1061.
- Mosíño, A. and García, E. (1966), Evaluación de la sequía intraestival en la república mexicana, in ‘Proc. Conf. Reg. Latinoamericana Unión Geogr. Int’, Vol. 3, pp. 500–516.
- Mulcahy, J. P., Jones, C., Sellar, A., Johnson, B., Boutle, I. A., Jones, A., Andrews, T., Rumbold, S. T., Molland, J., Bellouin, N., Johnson, C. E., Williams, K. D., Grosvenor, D. P. and McCoy, D. T. (2018), ‘Improved aerosol processes and effective radiative forcing in HadGEM3 and UKESM1’, *Journal of Advances in Modeling Earth Systems* 10(11), 2786–2805.
- Muñoz, E., Busalacchi, A. J., Nigam, S. and Ruiz-Barradas, A. (2008), ‘Winter and summer structure of the caribbean low-level jet’, *Journal of Climate* 21(6), 1260–1276.
- Neelin, J. D. (2007), ‘Moist dynamics of tropical convection zones in monsoons,

- teleconnections, and global warming'.
- Neelin, J. D., Battisti, D. S., Hirst, A. C., Jin, F.-F., Wakata, Y., Yamagata, T. and Zebiak, S. E. (1998), 'ENSO theory', *Journal of Geophysical Research: Oceans* **103**(C7), 14261–14290.
- Nie, J., Boos, W. R. and Kuang, Z. (2010), 'Observational evaluation of a convective quasi-equilibrium view of monsoons', *Journal of Climate* **23**(16), 4416–4428.
- Nie, J. and Sobel, A. H. (2015), 'Responses of tropical deep convection to the qbo: Cloud-resolving simulations', *Journal of the Atmospheric Sciences* **72**(9), 3625–3638.
- Nieto-Ferreira, R. and Rickenbach, T. M. (2011), 'Regionality of monsoon onset in South America: a three-stage conceptual model', *International Journal of Climatology* **31**(9), 1309–1321.
- Ordoñez, P., Nieto, R., Gimeno, L., Ribera, P., Gallego, D., Ochoa-Moya, C. A. and Quintanar, A. I. (2019), 'Climatological moisture sources for the western north american monsoon through a lagrangian approach: their influence on precipitation intensity', *Earth System Dynamics* **10**(1), 59–72.
- Oueslati, B. and Bellon, G. (2013), 'Convective entrainment and large-scale organization of tropical precipitation: Sensitivity of the cnrm-cm5 hierarchy of models', *Journal of climate* **26**(9), 2931–2946.
- Palmer, T. (2019), 'Stochastic weather and climate models', *Nature Reviews Physics* **1**(7), 463–471.
- Palmer, T. and Stevens, B. (2019), 'The scientific challenge of understanding and estimating climate change', *Proceedings of the National Academy of Sciences* **116**(49), 24390–24395.
- Pascale, S., Carvalho, L. M., Adams, D. K., Castro, C. L. and Cavalcanti, I. F. (2019), 'Current and Future Variations of the Monsoons of the Americas in a Warming Climate', *Current Climate Change Reports* pp. 1–20.
- Perdigón-Morales, J., Romero-Centeno, R., Barrett, B. S. and Ordoñez, P. (2019), 'Intraseasonal variability of summer precipitation in mexico: Mjo influence on the midsummer drought', *Journal of Climate* **32**(8).
- Perdigón-Morales, J., Romero-Centeno, R., Ordóñez, P. and Barrett, B. S. (2018), 'The midsummer drought in mexico: perspectives on duration and intensity from the chirps precipitation database', *International Journal of Climatology* **38**, 2174–2186.
- Plumb, R. A. and Bell, R. C. (1982), 'A model of the quasi-biennial oscillation on an equatorial beta-plane', *Quarterly Journal of the Royal Meteorological Society* **108**(456), 335–352.
- Rauscher, S. A., Giorgi, F., Diffenbaugh, N. S. and Seth, A. (2008), 'Extension and intensification of the Meso-American mid-summer drought in the twenty-first century', *Climate Dynamics* **31**, 551–571.
- Reed, R. (1964), 'A tentative model of the 26-month oscillation in tropical latitudes',

- Quarterly Journal of the Royal Meteorological Society* **90**(386), 441–466.
- Ribera, P., Peña-Ortiz, C., Garcia-Herrera, R., Gallego, D., Gimeno, L. and Hernández, E. (2004), ‘Detection of the secondary meridional circulation associated with the quasi-biennial oscillation’, *Journal of Geophysical Research: Atmospheres* **109**(D18).
- Ridley, J., Menary, M., Kuhlbrodt, T., Andrews, M. and Andrews, T. (2018), ‘Mohc hadgem3-gc31-ll model output prepared for cmip6 cmip picontrol’.
- URL:** <https://doi.org/10.22033/ESGF/CMIP6.6294>
- Ridley, J., Menary, M., Kuhlbrodt, T., Andrews, M. and Andrews, T. (2019a), ‘Mohc hadgem3-gc31-ll model output prepared for cmip6 cmip amip’.
- URL:** <https://doi.org/10.22033/ESGF/CMIP6.5853>
- Ridley, J., Menary, M., Kuhlbrodt, T., Andrews, M. and Andrews, T. (2019b), ‘Mohc hadgem3-gc31-ll model output prepared for cmip6 cmip historical’.
- URL:** <https://doi.org/10.22033/ESGF/CMIP6.6109>
- Ridley, J., Menary, M., Kuhlbrodt, T., Andrews, M. and Andrews, T. (2019c), ‘Mohc hadgem3-gc31-mm model output prepared for cmip6 cmip picontrol’.
- URL:** <https://doi.org/10.22033/ESGF/CMIP6.6297>
- Rodrigues, R. R., Haarsma, R. J., Campos, E. J. and Ambrizzi, T. (2011), ‘The impacts of inter-el niño variability on the tropical atlantic and northeast brazil climate’, *Journal of Climate* **24**(13), 3402–3422.
- Ropelewski, C. F. and Halpert, M. S. (1986), ‘North american precipitation and temperature patterns associated with the el niño/southern oscillation (enso)’, *Monthly Weather Review* **114**(12), 2352–2362.
- Ropelewski, C. F. and Halpert, M. S. (1987), ‘Global and regional scale precipitation patterns associated with the el niño/southern oscillation’, *Monthly weather review* **115**(8), 1606–1626.
- Ryu, J.-H. and Hayhoe, K. (2014), ‘Understanding the sources of Caribbean precipitation biases in CMIP3 and CMIP5 simulations’, *Climate dynamics* **42**(11-12), 3233–3252.
- Sahana, A. S., Ghosh, S., Ganguly, A. and Murtugudde, R. (2015), ‘Shift in indian summer monsoon onset during 1976/1977’, *Environmental Research Letters* **10**(5), 054006.
- Schneider, T., Bischoff, T. and Haug, G. H. (2014), ‘Migrations and dynamics of the Intertropical Convergence Zone’, *Nature* **513**(7516), 45.
- Sellar, A. A., Jones, C. G., Mulcahy, J., Tang, Y., Yool, A., Wiltshire, A., O’Connor, F. M., Stringer, M., Hill, R., Palmieri, J., Woodward, S., de Mora, L., Kuhlbrodt, T., Rumbold, S., Kelley, D. I., Ellis, R., Johnson, C. E., Walton, J., Abraham, N. L., Andrews, M. B., Andrews, T., Archibald, A. T., Berthou, S., Burke, E., Blockley, E., Carslaw, K., Dalvi, M., Edwards, J., Folberth, G. A., Gedney, N., Griffiths, P. T., Harper, A. B., Hendry, M. A., Hewitt, A. J., Johnson, B., Jones, A., Jones, C. D., Keeble, J., Liddicoat, S., Morgenstern, O., Parker, R. J., Predoi, V., Robertson, E., Siahaan, A., Smith, R. S.,

- Swaminathan, R., Woodhouse, M. T., Zeng, G. and Zerroukat, M. (2019), 'UKESM1: Description and evaluation of the UK Earth System Model', *Journal of Advances in Modeling Earth Systems* **0**(ja).
- URL:** <https://agupubs.onlinelibrary.wiley.com/doi/abs/10.1029/2019MS001739>
- Shepherd, T. G. (2014), 'Atmospheric circulation as a source of uncertainty in climate change projections', *Nature Geoscience* **7**(10), 703–708.
- Small, R. J. O., De Szeke, S. P. and Xie, S.-P. (2007), 'The central american midsummer drought: Regional aspects and large-scale forcing', *Journal of Climate* **20**(19), 4853–4873.
- Smyth, J. E., Hill, S. A. and Ming, Y. (2018), 'Simulated responses of the west african monsoon and zonal-mean tropical precipitation to early holocene orbital forcing', *Geophysical Research Letters* **45**(21), 12–049.
- Smyth, J. E. and Ming, Y. (2020), 'Characterizing drying in the south american monsoon onset season with the moist static energy budget', *Journal of Climate* **33**(22), 9735–9748.
- Son, S.-W., Lim, Y., Yoo, C., Hendon, H. H. and Kim, J. (2017), 'Stratospheric control of the Madden–Julian oscillation', *Journal of Climate* **30**(6), 1909–1922.
- Stensrud, D. J., Gall, R. L. and Nordquist, M. K. (1997), 'Surges over the gulf of california during the mexican monsoon', *Monthly Weather Review* **125**(4), 417–437.
- Storkey, D., Blaker, A. T., Mathiot, P., Megann, A., Aksenov, Y., Blockley, E. W., Calvert, D., Graham, T., Hewitt, H. T., Hyder, P. et al. (2018), 'UK Global Ocean GO6 and GO7: A traceable hierarchy of model resolutions', *Geoscientific Model Development* **11**(8), 3187–3213.
- Straffon, A., Zavala-Hidalgo, J. and Estrada, F. (2019), 'Preconditioning of the precipitation interannual variability in southern mexico and central america by oceanic and atmospheric anomalies', *International Journal of Climatology* .
- Sulca, J., Takahashi, K., Espinoza, J.-C., Vuille, M. and Lavado-Casimiro, W. (2018), 'Impacts of different ENSO flavors and tropical Pacific convection variability (ITCZ, SPCZ) on austral summer rainfall in South America, with a focus on Peru', *International Journal of Climatology* **38**(1), 420–435.
- Sultan, B., Baron, C., Dingkuhn, M., Sarr, B. and Janicot, S. (2005), 'Agricultural impacts of large-scale variability of the west african monsoon', *Agricultural and Forest Meteorology* **128**(1), 93 – 110.
- URL:** <http://www.sciencedirect.com/science/article/pii/S0168192304001923>
- Takahashi, K. (2004), 'The atmospheric circulation associated with extreme rainfall events in piura, peru, during the 1997–1998 and 2002 el niño events'.
- Tang, Y., Rumbold, S., Ellis, R., Kelley, D., Mulcahy, J., Sellar, A., Walton, J. and Jones, C. (2019a), 'Mohc ukesm1.0-ll model output prepared for cmip6 cmip historical'.
- URL:** <https://doi.org/10.22033/ESGF/CMIP6.6113>
- Tang, Y., Rumbold, S., Ellis, R., Kelley, D., Mulcahy, J., Sellar, A., Walton, J. and Jones,

- C. (2019b), 'Mohc ukcsm1.0-ll model output prepared for cmip6 cmip picontrol'.
URL: <https://doi.org/10.22033/ESGF/CMIP6.6298>
- Tedeschi, R. G., Grimm, A. M. and Cavalcanti, I. F. (2015), 'Influence of central and east enso on extreme events of precipitation in south america during austral spring and summer', *International Journal of Climatology* **35**(8), 2045–2064.
- Tegtmeier, S., Anstey, J., Davis, S., Dragani, R., Harada, Y., Ivanciu, I., Pilch Kedzierski, R., Krüger, K., Legras, B., Long, C., Wang, J. S., Wargan, K. and Wright, J. S. (2020a), 'Temperature and tropopause characteristics from reanalyses data in the tropical tropopause layer', *Atmospheric Chemistry and Physics* **20**(2), 753–770.
URL: <https://www.atmos-chem-phys.net/20/753/2020/>
- Tegtmeier, S., Anstey, J., Davis, S., Ivanciu, I., Jia, Y., McPhee, D. and Pilch Kedzierski, R. (2020b), 'Zonal asymmetry of the qbo temperature signal in the tropical tropopause region', *Geophysical Research Letters* **47**(24), e2020GL089533. e2020GL089533
2020GL089533.
URL: <https://agupubs.onlinelibrary.wiley.com/doi/abs/10.1029/2020GL089533>
- Thompson, D. W., Baldwin, M. P. and Solomon, S. (2005), 'Stratosphere–troposphere coupling in the southern hemisphere', *Journal of Atmospheric Sciences* **62**(3), 708–715.
- Trejo, F. J. P., Barbosa, H. A., Peñaloza-Murillo, M. A., Moreno, M. A. and Farías, A. (2016), 'Intercomparison of improved satellite rainfall estimation with CHIRPS gridded product and rain gauge data over Venezuela', *Atmósfera* **29**(4), 323–342.
- Trenberth, K. E. (1997), 'The definition of el nino', *Bulletin of the American Meteorological Society* **78**(12), 2771–2778.
- Trenberth, K. E., Branstator, G. W., Karoly, D., Kumar, A., Lau, N.-C. and Ropelewski, C. (1998), 'Progress during TOGA in understanding and modeling global teleconnections associated with tropical sea surface temperatures', *Journal of Geophysical Research: Oceans* **103**(C7), 14291–14324.
- Troup, A. (1965), 'The ‘southern oscillation’', *Quarterly Journal of the Royal Meteorological Society* **91**(390), 490–506.
- Turner, A. G. and Annamalai, H. (2012), 'Climate change and the south asian summer monsoon', *Nature Climate Change* **2**(8), 587–595.
- Turrent, C. and Cavazos, T. (2009), 'Role of the land-sea thermal contrast in the interannual modulation of the north american monsoon', *Geophysical Research Letters* **36**(2).
- Vera, C., Higgins, W., Amador, J., Ambrozzi, T., Garreaud, R., Gochis, D., Gutzler, D., Lettenmaier, D., Marengo, J., Mechoso, C. R., Nogues-Paegle, J., Dias, P. L. S. and Zhang, C. (2006), 'Toward a unified view of the American monsoon systems', *Journal of Climate* **19**(20), 4977–5000.
- Walker, G. T. (1924), 'Correlations in seasonal variations of weather. i. a further study of world weather', *Mem. Indian Meteorol. Dep.* **24**, 275–332.

- Walker, G. T. (1932), 'World weather v memories r.', *Meteor. Soc.* **4**, 53–84.
- Walters, D., Boutle, I., Brooks, M., Melvin, T., Stratton, R., Vosper, S., Wells, H., Williams, K., Wood, N., Allen, T., Bushell, A., Copsey, D., Earnshaw, P., Edwards, J., Gross, M., Hardiman, S., Harris, C., Heming, J., Klingaman, N., Levine, R., Manners, J., Martin, G., Milton, S., Mittermaier, M., Morcrette, C., Riddick, T., Roberts, M., Sanchez, C., Selwood, P., Stirling, A., Smith, C., Suri, D., Tennant, W., Vidale, P. L., Wilkinson, J., Willett, M., Woolnough, S. and Xavier, P. (2019), 'The Met Office Unified Model global atmosphere 7.0/7.1 and JULES global land 7.0 configurations', *Geoscientific Model Development* **12**(5), 1909–1963.
- Wang, C. and Picaut, J. (2004), 'Understanding ENSO physics—A review', *Earth's Climate: The Ocean–Atmosphere Interaction, Geophys. Monogr.* **147**, 21–48.
- Wang, P. X., Wang, B., Cheng, H., Fasullo, J., Guo, Z., Kiefer, T. and Liu, Z. (2017), 'The global monsoon across time scales: Mechanisms and outstanding issues', *Earth-Science Reviews* **174**, 84–121.
- Wang, S., Tippett, M. K., Sobel, A. H., Martin, Z. and Vitart, F. (2019), 'Impact of the qbo on prediction and predictability of the mjo convection', *J. Geophys. Res. Atmos.*
- Webster, P. J. (2020), *Dynamics of the Tropical Atmosphere and Oceans*, John Wiley & Sons.
- Webster, P. J. and Yang, S. (1992), 'Monsoon and enso: Selectively interactive systems', *Quarterly Journal of the Royal Meteorological Society* **118**(507), 877–926.
- URL:** <https://rmets.onlinelibrary.wiley.com/doi/abs/10.1002/qj.49711850705>
- Whitcher, B., Guttorp, P. and Percival, D. B. (2000), 'Wavelet analysis of covariance with application to atmospheric time series', *Journal of Geophysical Research: Atmospheres* **105**(D11), 14941–14962.
- Wilks, D. S. (2011), *Statistical methods in the atmospheric sciences*, Vol. 100, Academic press.
- Williams, K. D., Copsey, D., Blockley, E. W., Bodas-Salcedo, A., Calvert, D., Comer, R., Davis, P., Graham, T., Hewitt, H. T., Hill, R., Hyder, P., Ineson, S., Johns, T. C., Keen, A. B., Lee, R. W., Megann, A., Milton, S. F., Rae, J. G. L., Roberts, M. J., Scaife, A. A., Schiemann, R., Storkey, D., Thorpe, L., Watterson, I. G., Walters, D. N., West, A., Wood, R. A., Woollings, T. and Xavier, P. K. (2018), 'The Met Office global coupled model 3.0 and 3.1 (GC3. 0 and GC3. 1) configurations', *Journal of Advances in Modeling Earth Systems* **10**(2), 357–380.
- Wing, A. A., Camargo, S. J., Sobel, A. H., Kim, D., Moon, Y., Murakami, H., Reed, K. A., Vecchi, G. A., Wehner, M. F., Zarzycki, C. et al. (2019), 'Moist static energy budget analysis of tropical cyclone intensification in high-resolution climate models', *Journal of Climate* **32**(18), 6071–6095.
- Xie, P. and Arkin, P. A. (1997), 'Global precipitation: A 17-year monthly analysis based on

- gauge observations, satellite estimates, and numerical model outputs', *Bulletin of the American Meteorological Society* **78**, 2539–2558.
- Xie, P., Arkin, P. A. and Janowiak, J. E. (2007), *CMAP: The CPC Merged Analysis of Precipitation*, Springer Netherlands, Dordrecht, pp. 319–328.
- Yang, B., Zhang, Y., Qian, Y., Song, F., Leung, L. R., Wu, P., Guo, Z., Lu, Y. and Huang, A. (2019), 'Better monsoon precipitation in coupled climate models due to bias compensation', *NPJ Climate and Atmospheric Science* **2**(1), 1–8.
- Yin, L., Fu, R., Shevliakova, E. and Dickinson, R. E. (2013), 'How well can cmip5 simulate precipitation and its controlling processes over tropical south america?', *Climate Dynamics* **41**(11–12), 3127–3143.
- Yoon, J.-H. and Zeng, N. (2010), 'An Atlantic influence on Amazon rainfall', *Climate dynamics* **34**(2), 249–264.
- Zeng, X. and Lu, E. (2004), 'Globally unified monsoon onset and retreat indexes', *Journal of Climate* **17**(11), 2241–2248.
- Zhai, J. and Boos, W. (2015), 'Regime transitions of cross-equatorial hadley circulations with zonally asymmetric thermal forcings', *Journal of the Atmospheric Sciences* **72**(10), 3800–3818.
- Zhang, S. and Wang, B. (2008), 'Global summer monsoon rainy seasons', *International Journal of Climatology: A Journal of the Royal Meteorological Society* **28**(12), 1563–1578.
- Zhao, Z., Holbrook, N. J., Oliver, E. C., Ballesteros, D. and Vargas-Hernandez, J. M. (2020), 'Characteristic atmospheric states during mid-summer droughts over central america and mexico', *Climate Dynamics* pp. 1–21.
- Zhao, Z. and Zhang, X. (2021), 'Evaluation of methods to detect and quantify the bimodal precipitation over central america and mexico', *International Journal of Climatology* **41**, E897–E911.
- Zhou, T., Turner, A. G., Kinter, J. L., Wang, B., Qian, Y., Chen, X., Wu, B., Liu, B., Zou, L. and Bian, H. (2016), 'GMMIP (v1. 0) contribution to CMIP6: global monsoons model inter-comparison project', *Geoscientific Model Development* **9**, 3589–3604.
- Zou, L. and Zhou, T. (2015), 'Asian summer monsoon onset in simulations and cmip5 projections using four chinese climate models', *Advances in Atmospheric Sciences* **32**(6), 794–806.